MEASUREMENTS AND ANALYSIS OF GAMMA-RAY STREAMING THROUGH CONCRETE LINED DUCTS

by

DAVID LEE STUCKER

B.S., Nuclear Engineering
Kansas State University
Manhattan, Kansas
1977

A MASTER'S THESIS

submitted in partial fulfillment of the

requirements of the degree

MASTER OF SCIENCE

Department of Nuclear Engineering
KANSAS STATE UNIVERSITY
Manhattan, Kansas

1980

Approved by:

Robert Simons
Major Professor

Spec. Coll.
LD
2668
.T4
1980
S88
c.2

TABLE OF CONTENTS

Page

LIST OF FIGURES ii

LIST OF TABLES v

1.0 INTRODUCTION 1

2.0 THEORY 11
- 2.1 Compton Cross Section 13
- 2.2 Gamma Flux-to-Exposure Rate Conversion Factor. 13
- 2.3 Klein-Nishina Cross Section 17
- 2.4 Buildup Factor 18
- 2.5 Lip Scattering 19
- 2.6 Duct Wall Scattering 26
- 2.7 Lip Penetration Correction 31

3.0 DISCUSSION OF EXPERIMENTAL FACILITY 42

4.0 DISCUSSION OF INSTRUMENTATION 72

5.0 EXPERIMENTAL RESULTS 98

6.0 CALCULATIONS AND COMPARISONS 130

7.0 CONCLUSIONS 142

8.0 RECOMMENDATIONS 144

9.0 ACKNOWLEDGEMENTS 145

10.0 LITERATURE CITED 146

APPENDICES . . . . . .
- A. Exposure Rate versus Position Plots for 100 cm Wall 147
- B. Exposure Rate versus Position Plots for 150 cm Wall 181
- C. Computer Package 202

LIST OF FIGURES

Figure		Page
1.1	Map of shielding facility	7
1.2	Concrete source pad and associated facilities	8
2.1	General model geometry	12
2.2	Scaled lip scattering geometry	20
2.3	Duct region blowup for lip scattering	21
2.4	Scaled duct wall scattering geometry	27
2.5	Duct region blowup for duct wall scattering	29
2.6	Lip penetration correction geometry	32
2.7	$\sigma(B)$ versus B	41
3.1	Partially completed 50.8 cm thick shielding wall containing the 21.1 cm diameter straight circular duct.	44
3.2	Front view of the 50.8 cm thick duct-bearing wall . . .	45
3.3	Experimental arrangement used for the benchmark measurements made in the 50.8 cm thick wall	47
3.4	Concrete shielding-wall blocks	49
3.5	Duct blocks used to mockup the 41.9-cm diameter duct in the 50.8-cm thick wall	52
3.6	Duct and fill blocks for the 21.1-cm diameter duct mockup in the 50.8-cm thick wall	53
3.7	Collection of ducts and annuli	54
3.8	Source position with respect to lip of steel clad source housing	56
3.9	Irradiator position relative to test wall	58
3.10	Horizontal sectional view through the sources and collimator above irradiator	60
3.11	Shadow shield position relative to source and collimator	61

3.12 Gamma-ray source housing, collimator, and shadow shield 62

3.13 Gamma ray source positioned on the concrete pad 63

3.14 Reflecting room configuration 65

3.15 Front view of the shielding wall area used for the reflecting room experiment 66

3.16 Reflecting room constructed adjacent to the shielding shielding wall 67

3.17 Reflecting wall geometry 71

4.1 Energy sensitivity of the Reuter-Stokes high pressure ionization chamber 73

4.2 Ion chamber traverse system located inside the instrumentation building 75

4.3 Ion chamber mounted to the traverse system 76

4.4 Z traverse drive rods and bearings 78

4.5 Bottom view of z-dimension motorized drive plate and ionization chamber 80

4.6 Top view of x-dimension motorized drive plate, rods, bearings, and supports 81

4.7 Bottom view of x-dimension motorized drive plate . . . 82

4.8 Ion chamber traverser control electronics 84

4.9 Block diagram of X and Z contour-encoder control system 86

4.10 Linear relationship between the Z dimension position indicator reading and the actual ion chamber position 88

4.11 Linear relationship between the X dimension position indicator reading and the actual ion chamber position 89

4.12 Side view of traverser drive assembly 90

4.13 Instrument room 92

4.14 Front panel of control console 93

4.15 Block diagram of data acquisition system 95

5.1 Benchmark gamm ray streaming geometry 99

5.2 Normalized exposure rate as a function of c and d for the 100 cm thick wall with a 20 cm duct 104

5.3 Normalized exposure rate as a function of d and y for the 100 cm thick wall with a 20 cm duct 105

5.4 Normalized exposure rate as a function of d and duct diameter 106

5.5 Normalized exposure rate as a function of d and θ for the 100 cm thick wall with a 20 cm duct 107

5.6 Normalized exposure rate as a function of distance from a 100-cm thick wall with a 20 cm duct, θ = 33° . . 112

5.7 Normalized exposure rate as a function of distance from a 100 cm thick wall with a 20 cm duct, θ = 45° . . 113

5.8 Isodose plot for the 100 cm thick wall with a 40 cm diameter duct and an angle of incidence of 45° 114

5.9 Isodose plot for the 100 cm thick wall with a 20 cm diameter duct and an angle of incidence of 45° 115

5.10 Isodose plot for the 100 cm thick wall with a 20 cm diameter duct and an angle of incidence of 33° 116

5.11 Isodose plot for the 100 cm thick wall with a 40 cm diameter duct and an angle of incidence of 33° 117

5.12 Isodose plot for the 100 cm thick wall with a 40 cm diameter duct and an angle of incidence of 33°, measured at y = -76 cm 118

5.13 Top view of detector traverse area and the 50.8 cm thick shielding wall 123

5.14 Instrument reading for the exposure rate from the experimental data acquisition system versus exposure rate as measured diectly from the Reuter-Stokes area monitor 126

6.1 Duct radius versus source angle 133

6.2 Source angle versus duct radius 134

6.3 Duct radius versus source angle 137

6.4 Source angle versus duct radius 138

LIST OF TABLES

Table		Page
1.1	Summary of benchmark gamma-ray streaming configurations with straight circular ducts in ordinary concrete	3
1.2	Summary of benchmark gamma-ray streaming configurations with straight annular ducts in ordinary concrete	4
1.3	Summary of benchmark gamma-ray streaming configurations with straight rectangular ducts in ordinary concrete	5
1.4	Summary of benchmark gamma-ray streaming solid wall background measurements	5
2.1	Compton cross section comparison	14
2.2	$K_d(E)$ versus photon energy	16
2.3	$\zeta(\theta_s,r)$ versus θ_s and r	35
2.4	$\zeta(\theta_s,r)$ fit parameters	37
3.1	Dimensions of concrete blocks used to construct the duct openings in the concrete shielding walls . . .	50
3.2	Dimensions of annuli used with the concrete shielding walls	51
3.3	^{60}Co source identification and intercalibration data	57
3.4	Cobalt-60 source strengths	57
3.5	Summary of reflecting room measurements made using 0.5 Ci source and the 101.6 cm thick wall with a 21.1 cm diameter duct	69
5.1	Selected raw digital experiment x-z traverse data for the 100 cm thick wall using the Co-60 source of nominal strenght 10 Ci	101
5.2	Selected background digital experiment x-z traverse data for the 100 cm thick wall using the Co-60 source of nominal strength 10 Ci	102

5.3 Reduced x-z traverse data for the 100 cm thick wall using the Co-60 source of nominal strength 10 Ci . . . 103

5.4 Selected raw digital experimental C traverse data for the 100 cm thick wall with a 20 cm diameter duct using the Co-60 source of nominal strength 10 Ci 109

5.5 Selected background digital experimental C traverse data for the 100 cm thick wall using the Co-60 source of nominal strength 10 Ci 110

5.6 Reduced C traverse data for the 100 cm thick wall using the Co-60 source of nominal strength 10 Ci . . . 111

5.7 Startup checklist used for daily operation 120

5.8 Displacement of the center of the ion chamber from the y = 0 plane for the detector at the center and along the periphery of the x-z traversing area 124

5.9 Estimated percentage error in the normalized exposure rate for various duct penetration exposure rates 129

6.1 Peak $(\frac{C}{E})$'s for wall length, l = 100 cm 135

6.2 Peak $(\frac{C}{E})$'s for wall length, l = 150 cm 139

1. INTRODUCTION

The accurate calculation of the radiation that penetrates through a duct in a shield wall is generally quite difficult and expensive. Typically, computerized Monte Carlo or albedo techniques are used as the basis of most duct streaming calculations. However, in many routine duct analyses, the potential accuracy afforded by these sophisticated methods is often not needed. It has become apparent that there is a great need for the development of simplified, inexpensive, engineering methods for estimating the radiation fields from photon penetration through ducts. While such simplified methods may not be as accurate as the transport-theory based methods, they would serve as an important preliminary analysis tool for the shielding analyst.

One of the major impediments to the development of such simplified, semi-empirical, duct-penetration models has been the dearth of experimental data against which the validity of simplified models can be tested. Thus the primary motivation for this study was to obtain benchmark-quality data for the streaming of gamma photons through ducts in concrete walls.

The objective of the experimental phase of the project was to provide a sufficient wealth of radiation penetration data to permit the development of simplified engineering models for predicting gamma photon scattering through straight ducts. In the experimental program, the opening of a duct constructed in a solid concrete wall was illuminated by gamma radiation from a point ^{60}Co source. The spatial distribution of the exposure rate arising from radiation that penetrated through the duct was measured.

The primary emphasis of the experimental program was to obtain benchmark gamma-ray streaming data for twenty-two open duct and three closed duct (solid wall background) configurations. These ducts were built into walls made of ordinary concrete. Three wall thicknesses were studied--50.8 cm, 101.6 cm, and 152.4 cm. Each wall was nominally 3.1 m high and 3.6 m long.

Point ^{60}Co gamma-ray sources were positioned at various locations with respect to the duct opening so that the duct was illuminated at various angles of incidence. A polar ρ-θ coordinate system was used to describe the source position with the origin at the center of the duct mouth. Limits on ρ and θ were 100 to 400 cm and 22.5^{o} to 60^{o}, respectively. A collimator was placed around the source to minimize air scattered (skyshine) radiation components; however, the duct mouth and a sufficient area of the adjacent wall were always fully illuminated so as to obtain the total duct penetration radiation component.

Gamma-ray exposure rates were measured behind the duct-bearing wall using a high pressure ionization chamber attached to an automated traversing mechanism. Three dimensional exposure rate mappings were measured for each duct configuration. Acquisition of traverse data involved moving the detector in the x dimension (parallel to the wall) at discrete distances, c, measured from the back of the wall, and at fixed elevations relative to the duct centerline (y dimension).

The straight duct and annular configurations studied are listed in Tables 1.1 - 1.2. Detailed information is presented for each of these general arrangements of duct size and wall thickness.

Table 1.1 Summary of Benchmark Gamma-Ray Streaming Configurations with Straight Circular Ducts in Ordinary Concrete.

Configuration Number	Diameter cm	Diameter in	Length cm	Length in	Conditions
1	21.1	8.3	50.8	20	Shield Wall
2	41.9	16.5	50.8	20	" "
3	4.76	1.88	101.6	40	" "
4	10.3	4.06	101.6	40	" "
5	21.1	8.3	101.6	40	" "
6	41.9	16.5	152.4	60	" "
7	10.3	4.06	152.4	60	" "
8	21.1	8.3	152.4	60	" "
9	41.9	16.5	152.4	60	" "
10	10.3	4.06	101.6	40	Reflecting Wall
11	21.1	8.3	101.6	40	Reflecting Room
12	10.3	4.06	152.4	60	Iron Liner

Table 1.2 Summary of Benchmark Gamma-Ray Streaming Configurations with Straight Annular Ducts in Ordinary Concrete.

Configuration Number	Outside Diameter		Core Diameter		Length	
	cm	in	cm	in	cm	in
13	21.1	8.3	6.03	2.38	101.6	40
14	21.1	8.3	10.16	4.0	101.6	40
15	41.9	16.5	27.62	10.88	101.6	40
16	41.9	16.5	32.39	12.75	101.6	40
17	21.1	8.3	6.03	2.38	152.4	60
18	21.1	8.3	10.16	4.0	152.4	60
19	41.9	16.5	27.62	10.88	152.4	60
20	41.9	16.5	32.39	12.75	152.4	60

In addition to straight ducts and annuli, rectangular ducts and solid wall (background) configurations were studied. Specifications for these configurations of ducts dimensions and wall thickness are presented in Tables 1.3 and 1.4.

Table 1.3 Summary of Benchmark Gamma-Ray Streaming Configurations with Straight Rectangular Ducts in Ordinary Concrete.

Configuration Number	Height		Width		Length	
	cm	in	cm	in	cm	in
21	15.2	6	30.5	12	101.6	40
22	30.5	12	30.5	12	101.6	40

Table 1.4 Summary of Benchmark Gamma-Ray Streaming Solid Wall Background Measurements.

Configuration Number	Wall thickness	
	cm	in
23	50.8	20
24	101.6	40
25	152.4	60

Source geometry requirements necessitated moving the gamma-ray source (with its 2000 kg storage cask) several times during the sequence of measurements for each duct configuration. The source also had to be moved into a storage building adjacent to the experimental area during non-working hours. Use of a forklift provided a simple solution for both positioning the source on the concrete pad and moving it to and from its storage building. Morever, since the source rested on metal rails, radial position changes were quickly made by manually rolling the source to the desired location.

The experimental program was conducted at the Kansas State University (KSU) Radiation Shielding Facility. This facility is a 710 hectare site located 8 KM west of the University campus in Riley County, Kansas. The site was purchased in 1962 by the State of Kansas for use by the KSU Nuclear Engineering Department, and has been used for numerous radiation shielding/dosimetry studies. A map of this unique university facility is presented in Fig. 1.1.

The northeast corner of the KSU Radiation Shielding Site was selected for development of the desired gamma-ray streaming facility. This area contained a large metal building on relatively level terrain. The building was necessary because the ionization chamber traverse system and the associated control and data acquisition instrumentation required a dust-free, temperature controlled environment. As shown in Fig. 1.2, the instrumentation building contained two rooms. The smaller one, called the instrument room, was used for the data acquisition electronics. The larger room in the building was used to house the ionization chamber traverse system.

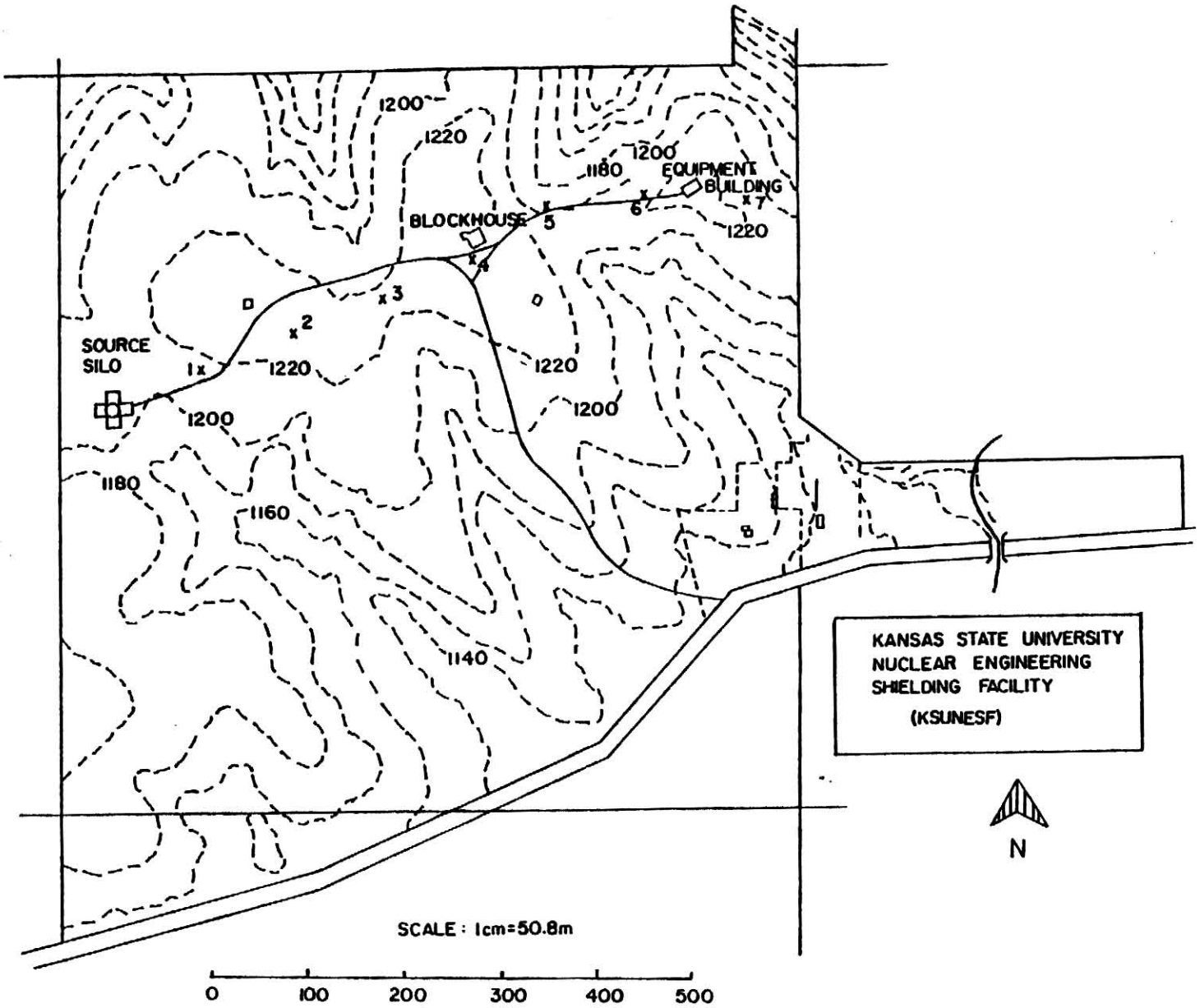

Fig. 1.1 Map of Shielding Facility

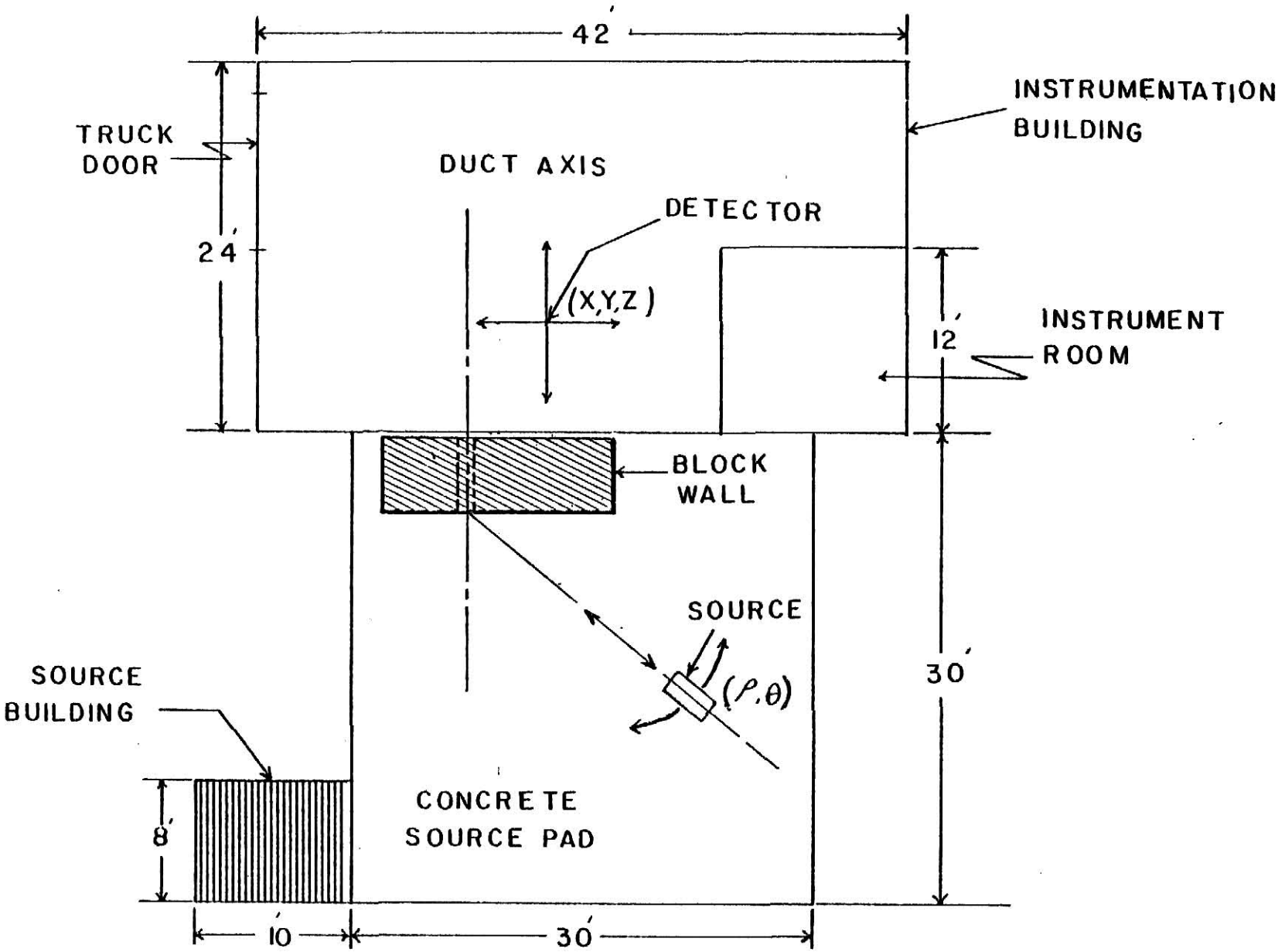

Fig. 1.2. Concrete source pad and associated facilities.

SCALE 1" = 10'

The purpose of the analytical phase of this research was to develop engineering models of the duct scattering. Additionally, the computational codes resulting from these models do not require numerical integration or other iterative techniques and are of a size and simplicity such they will fit on a small programmable calculator such as the HP 67/97 series.

Gamma radiation scattering and transmission phenomena are broken down into three basic components--duct wall scattered, lip scattered and direct penetration. Within the two scattering components, only single scatters are considered. The scattering models calculate the scattering as if it occurred from a single point within the duct region. The scattering points were chosen based on experimental measurements, GGG, and MORSE calculations (9) . The models also assume the detector to be a point detector.

An empirical lip penetration correction for the wall scattering component is also derived. This model corrects the wall scattering model's assumption of an opaque duct lip for the physically reality in contradiction to that assumption. The correction applied to the wall scattering model is dependent upon illumination angle and duct radius. The constants within the correction have been determined based on the data collected and therefore are implicitly valid only for ^{60}Co gamma rays. However, sufficient background is given to formulate constants for other source energies.

The last of the three basic components, identified in this research, is direct penetration. The potential importance of this contribution is realized, however the major thrust of this research has been in measurement and prediction of scattered gamma rays. Techniques used

to estimate direct penetration, while similar to those of scattered radiation, are fundamentally different from scattered techniques and therefore are not discussed.

2.0 THEORY

Radiation streaming through cracks and ducts in shield walls has long been recognized to be one of the most formidable analytical challenges within the realm of radiation shielding. Historically, most analyses of potential streaming problems have been met with excessive computational effort to insure the accuracy of the calculation. The methods involved in this computational overexertion are transport and albedo techniques, frequently using Monte Carlo solution techniques. These methods are elaborate, expensive to run, and typically provide more accuracy than is required of a first-pass design code. Engineering models are developed within to bridge the analytical gap between transport/albedo code solutions and hand calculations.

The analytical approach to this problem entailed reducing spatially dependent exposure rates into two major components. These components are: 1) lip scattering from the duct entrance, and 2) duct wall scattering within the duct. The models presented use point scattering kernels to approximate the scattering in and about the duct region and point detectors to measure the scattered radiation. The problem of direct penetration was not addressed.

The general geometry of this analysis is presented in Fig. 2.1. Notice that the duct is modelled as a parallel slot as opposed to the actual duct with curved walls, top, and bottom. Results of this study (see Chapter 6) show that this approximation is adequate for centerline calculations where the source and detector are at the same elevation. However, if this vertical symmetry is lost, i.e.,

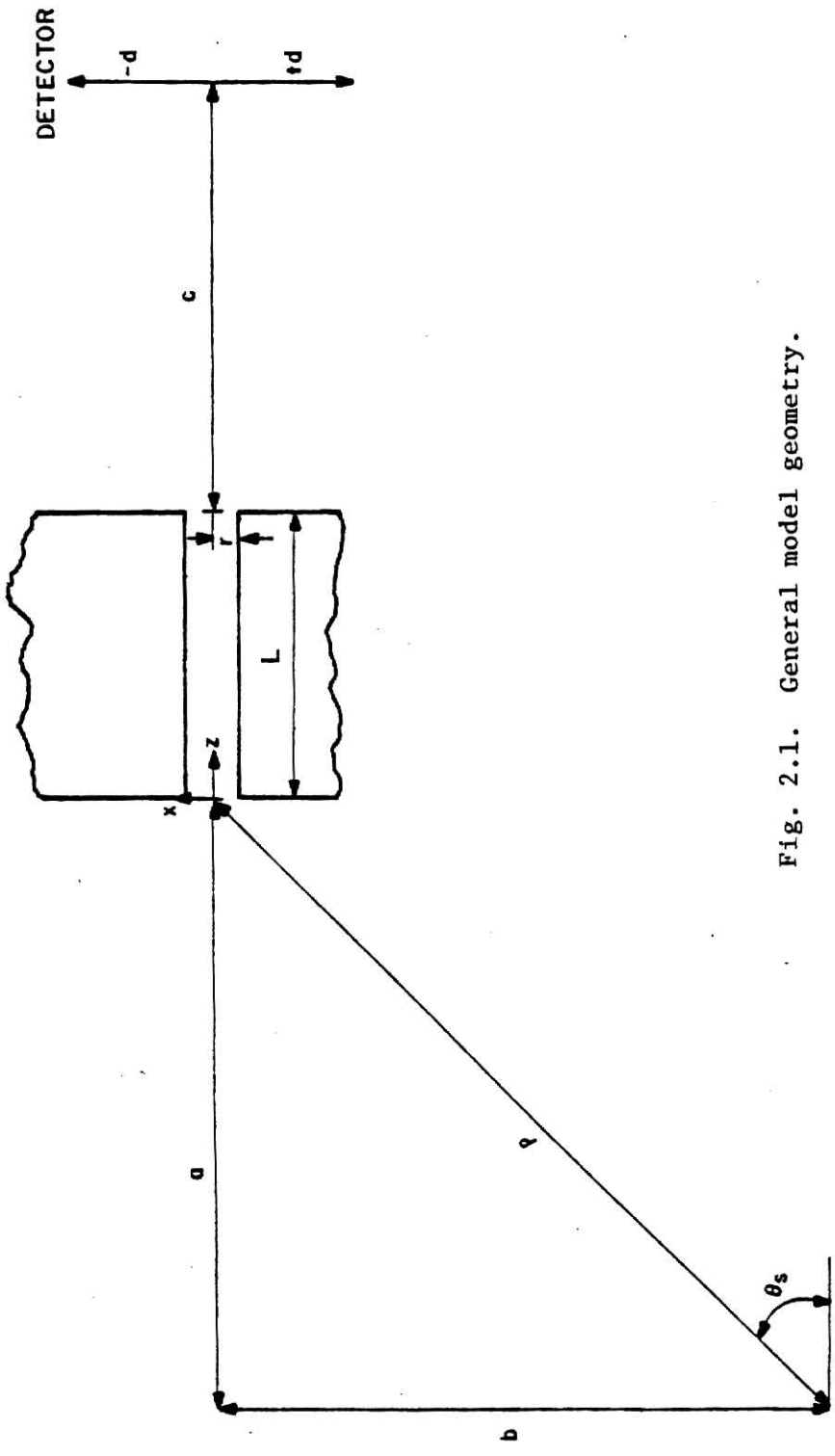

Fig. 2.1. General model geometry.

in off-centerline calculations, the duct top and bottom would become significant contributors and this approximation could be invalid.

Presented next are those general facets of radiation shielding calculations that are common to both component models. These facets include: 1) an empirical fit to the Compton mass absorption cross section, 2) presentation of the flux-to-exposure rate conversion factor, 3) the Klein-Nishina angular differential cross section, and 4) an energy dependent Berger buildup factor for a collimated source.

2.1 Compton Cross Section

The cross section used throughout these models is approximated by the Compton cross section. This approximation is justified since within the photon energy range of interest, from 1.33 Mev to around 200 keV, the Compton interactions in concrete are by far the most dominant mechanism for scattering and attenuation. Within this energy range, the Compton cross section is represented approximately by (9):

$$\frac{\mu_c}{\rho} = 0.0625\ E^{-0.467}\ \left(\frac{cm^2}{g}\right) \qquad (2.1)$$

where E is equal to the photon energy (MeV).

Table 2.1 compares the tabulated total absorption cross section for concrete (10), the calculated cross section using Eq. 2.1, and the relative error between the two.

2.2 Flux-to-Exposure Rate Conversion Factor

The flux-to-exposure rate conversion factor, common to both models, is developed using the following equation for the exposure rate in air,

Table 2.1. Comparison of tabulated and calculated cross sections over the energy range of interest in this investigation.

Photon Energy (MeV)	Tabulated[a] Cross Section (cm^2/g)	Calculated[b] Compton Cross Section (cm^2/g)	Relative Error (%)
1.5	0.0518	0.0517	-0.16
1.0	0.0636	0.0625	-1.73
0.8	0.0707	0.0694	-1.89
0.6	0.0805	0.0793	-1.44
0.5	0.0870	0.0864	-0.71
0.4	0.0954	0.0959	0.50
0.3	0.1070	0.1097	2.49
0.2	0.1230	0.1325	7.74

[a] See Ref. 10.

[b] Calculated using Eq. 2.1.

D_{air}, expressed in units of μR/h

$$D_{air} = \Phi \; E \; K_d(E) \tag{2.2}$$

where

Φ - photon flux of energy E $\left(\frac{\text{photons}}{\text{cm}^2 \text{ s}}\right)$

E - photon energy (MeV)

$K_d(E)$ - flux-to-exposure rate conversion factor for photons of energy E $\left(\frac{\mu\text{R cm}^2 \text{ s}}{\text{MeV photon h}}\right)$.

Using the following physical contants, $K_d(E)$ can be expressed in the desired units:

1 h = 3600 s

1 MeV = 1.6021916×10^{-6} erg

1 μrad = $100 \times 10^{-6} \frac{\text{erg}}{\text{g}}$

1 μR = 0.877 μrad in air

and, $\left(\frac{\mu_{en}}{\rho}\right)_{air}$ is the mass energy absorption coefficient for photons in air with the units of $\left(\frac{\text{cm}^2}{\text{g}}\right)$. Substitution of the above constants gives

$$K_d(E) = \left(\frac{\mu_{en}}{\rho}\right)_{air} \frac{(1.6021916 \times 10^{-6}) \; (3600)}{(0.877) \quad (100 \times 10^{-6})} \left(\frac{\mu\text{R cm}^2 \text{ s}}{\text{MeV photon h}}\right) \tag{2.3}$$

or, more simply

$$K_d(E) = 65.77 \left(\frac{\mu_{en}}{\rho}\right)_{air}. \tag{2.4}$$

Table 2.2 presents $K_d(E)$ in tabular form for photon energies from 200 keV to 1 MeV. As illustrated in Table 2.2, $K_d(E)$ is reasonably constant and can be represented approximately by

$$K_d(E) = 1.90 \quad \text{for} \quad 0.20 \leq E \leq 1.00 \text{ MeV}. \tag{2.5}$$

Table 2.2. Values of flux-to-exposure rate conversion factor, $K_d(E)$.

Photon Energy (MeV)	$K_d(E)$ $\left(\frac{\mu R\ cm^2\ s}{MeV\ photon\ h}\right)$
1.00	1.842
0.80	1.901
0.60	1.947
0.50	1.953
0.40	1.947
0.30	1.894
0.20	1.763

2.3 Klein-Nishina Cross Section

The Klein-Nishina angular differential cross section is the basis for the calculation of the probability for scatter through a given scattering angle and, hence, the spatial dependence of these models. The Klein-Nishina cross section $\frac{d\sigma}{d\Omega}$ is presented in general form as

$$\frac{d\sigma}{d\Omega} = \frac{3}{16\pi} (0.665)\ y^2 \left[\frac{1}{y} + y - \sin^2(\theta_{sc})\right] \left[\frac{b}{\text{elec sr}}\right] \tag{2.6}$$

where

$$y = \frac{E_s}{E_i}$$

and,

E_s - scattered photon energy

E_i - source photon energy

θ_{sc} - scattering angle.

Since these models assume that all scatters are Compton interactions, the expression for E_s in terms of E_i and θ_{sc} is

$$E_s = \frac{E_i}{1 + \frac{E_i}{0.511}\left[(1 - \cos(\theta_{sc})\right]} . \tag{2.7}$$

For convenience, the Klein-Nishina cross section should have units of cm^{-1}. Representing this quantity as $k(\theta_{sc})$, it is defined as

$$k(\theta_{sc}) = \frac{\rho Z N_A}{A} \frac{d\sigma}{d\Omega} \tag{2.8}$$

where

ρ - medium density $\left(\frac{g}{cm^3}\right)$

Z - electrons per molecule

N_A - Avogadro's number $\left(\frac{particles}{g\text{-}mole}\right)$

A - molecular mass $\left(\frac{g}{g\text{-}mole}\right)$.

Additionally, since ordinary concrete was assumed to consist solely of SiO_2, the following value of $(\frac{Z}{A})$ was used in the determination of $k(\theta_{sc})$

$$(\frac{Z}{A}) = 0.5. \tag{2.9}$$

2.4 Buildup Factor

Buildup factors are used throughout shielding calculations to correct simple exponential attenuation for scatter and the resulting photon energy degradation. These buildup factors correct the uncollided gamma flux density for energy spectrum degradation based on the number of mean free paths of material encountered, incident energy of the photon, and medium composition and geometry. The buildup factor used in this model is a Berger type with energy dependent constants. The general form of the Berger equation is given as follows (11)

$$BUF(\lambda,E) = 1 + \xi\lambda\exp(\delta\lambda) \tag{2.10}$$

where

λ - number of mean free paths

$\delta = \delta(E)$, and $\xi = \xi(E)$ and are energy dependent fit parameters.

Eisenhauer and Simmons (8) have measured the buildup factor for an infinite wall. Results of these measurements have been empirically fit to the energy dependent Berger equation given by

$$BUF(\lambda,E) = 1 + \lambda K_1 E^{K_2} \exp(\lambda K_3 \exp(K_4 E)) \qquad (2.11)$$

where

$K_1 = 1.23$

$K_2 = -0.466$

$K_3 = 0.0812$

$K_4 = -0.848.$

However, it would be inappropriate to use an infinite medium buildup factor for development of the subject models since the gamma-ray source was collimated and by no means approximated a bare source. Experiments were performed during the course of this research to estimate the departure of the measured exposure rates from those calculated using the infinite medium buildup factor. Details of these experiments have shown that the correction for a collimated source can be obtained by reducing K_1 by a factor of two (12).

2.5 Lip Scattering

Lip scattering is defined as those scatters that occur in the wall but near enough to the duct region that the scattered photons emerge in the duct region. Refer to Figs. 2.2 and 2.3 for the specific geometric details of this model. The basic assumptions for this model are:

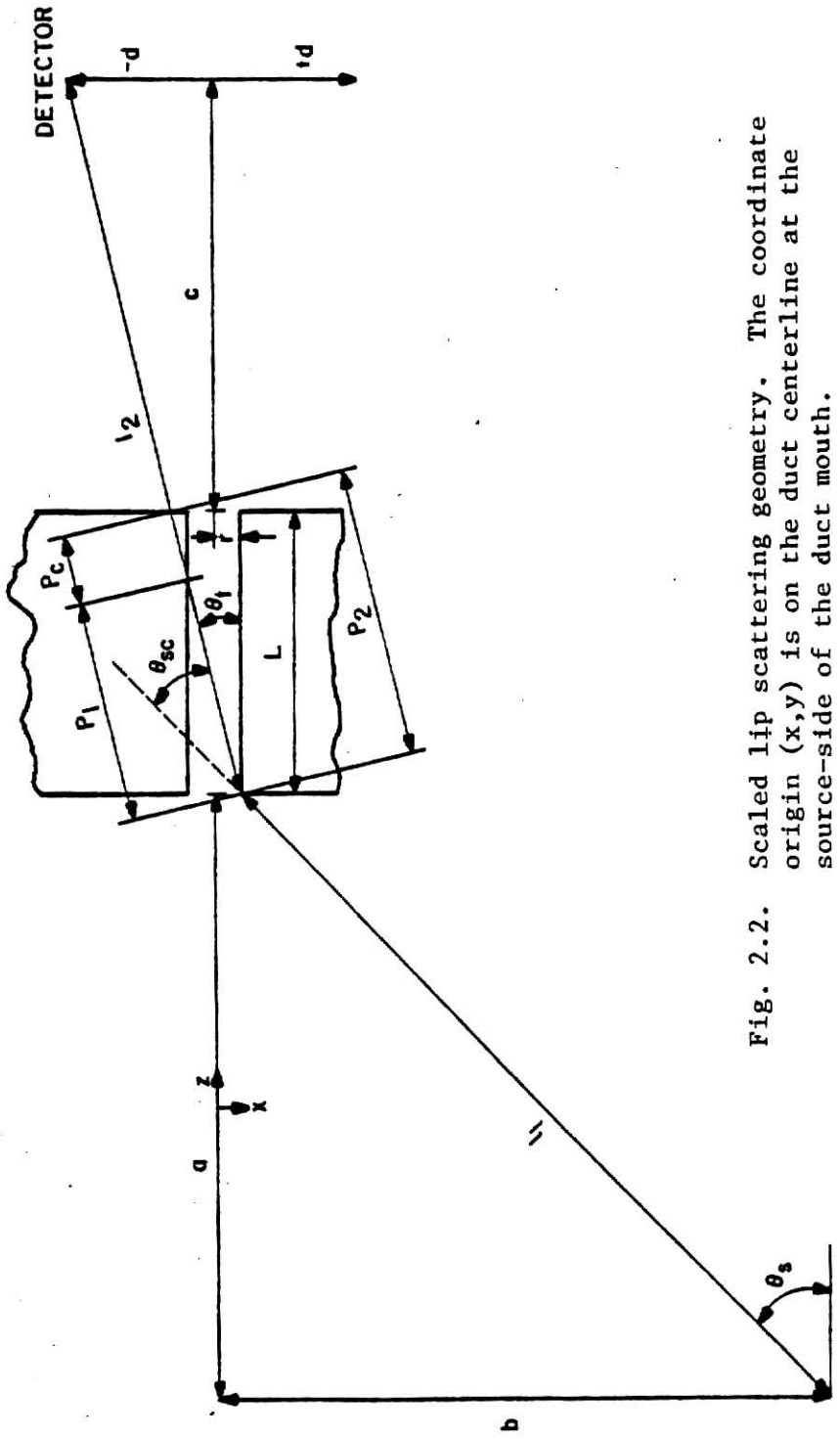

Fig. 2.2. Scaled lip scattering geometry. The coordinate origin (x,y) is on the duct centerline at the source-side of the duct mouth.

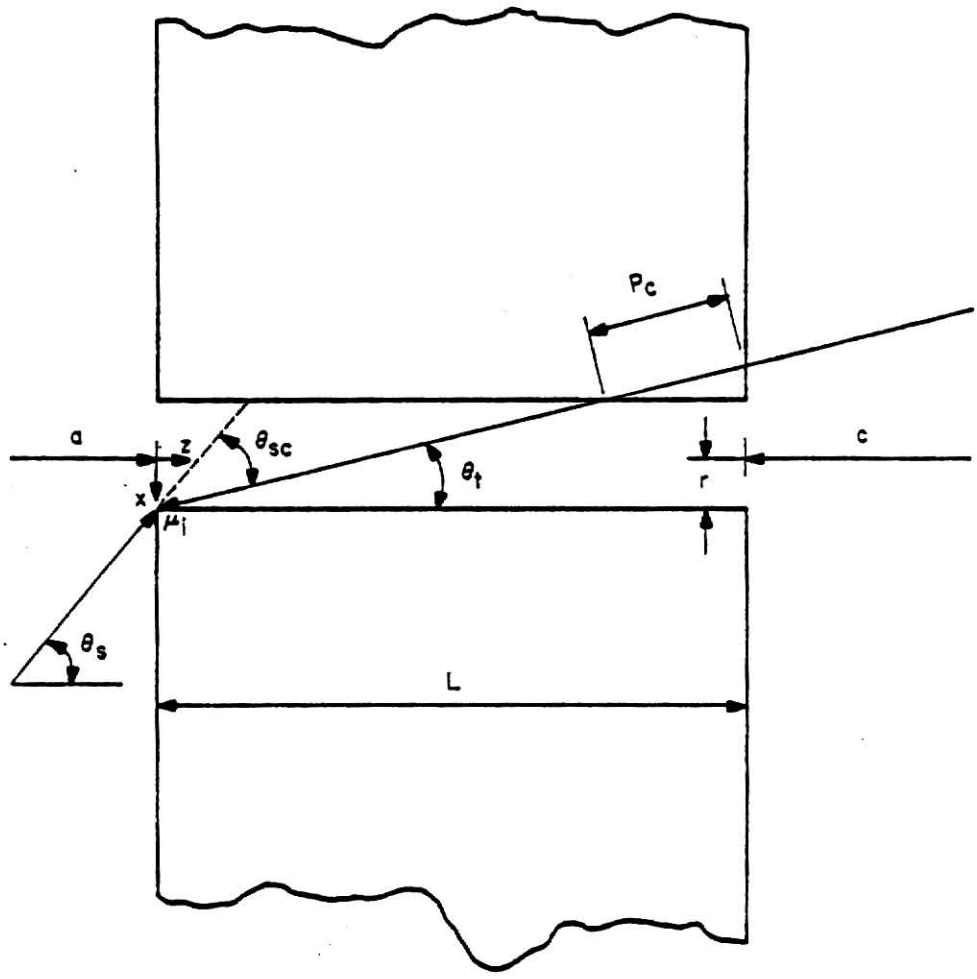

Fig. 2.3. Expanded view of duct region used to develop the lip scattering model.

1) The duct lip can be represented by an annular element of the shield wall surrounding the duct closest to the source,

2) Scattering occurs very close to the edges of the duct such that the geometric attenuation can be assumed to be constant and the scatters occur at x=r and z=0,

3) The angles θ_s, θ_t and θ_{sc} are constant throughout the scattering volume of significance,

4) The wall is thick enough that the number of free paths for direct penetration is very large, i.e., $\mu_i L >> 1$.

The most general form of the equation describing the exposure rate of the detector due to lip scattering D_ℓ, is given by

$$D_\ell = \int_0^L \int_r^\infty \frac{(3.7 \times 10^{10})\ S\ n}{4\pi \ell_1^2}\ dV\ k(\theta_{sc})\ \exp\left(\frac{-\mu_i\ z}{\cos(\theta_s)}\right)\ BUF_2$$

$$\exp\left(\frac{-\mu_s\ (x-r)}{\sin(\theta_t)}\right)\ BUF_c\ \exp(-\mu_s P_c)\ \frac{E_s\ K_d(E_s)}{\ell_2^2} \qquad (2.13)$$

where

S - source intensity (Ci)

n - number of photons per disintegration

μ_i - linear attenuation coefficient at source energy (cm^{-1})

μ_s - linear attenuation coefficient at scattered energies (cm^{-1})

P_c - path length in far lip (cm)

BUF_c - buildup factor for far lip

BUF_2 - buildup factor in scattering lip

and dV is the differential scattering volume for the lip given by:

$$dV = \pi x \, dx \, dz.$$

The coordinate system origin for this model was on the duct centerline at the duct mouth closest to the source. The scattering volume is defined only for the semi-circular annulus closest to the source.

The following substitutions were made to simplify the algebra in Eq. (2.13)

$$\alpha = \frac{\mu_i}{\cos(\theta_s)}, \quad \beta = \frac{\mu_s}{\sin(\theta_t)} \quad \text{and} \quad \lambda = \beta(x-r). \tag{2.14}$$

Recognizing that λ (in Eq. 2.14) is the number of mean free paths in the lip, after scatter, the buildup factor can now be applied for this scattering leg as described in Section 2.4. From the preceding definition of λ, the change of variables from x to λ is

$$x = \frac{\lambda}{\beta} + r \tag{2.15}$$

and

$$dx = \frac{d\lambda}{\beta} . \tag{2.16}$$

Additionally, this model assumes that θ_s and θ_t (and therefore θ_{sc}) are constant in the range where the integrand of Eq. (2.13) is significant. Therefore, substituting Eqs. (2.14)-(2.16) into Eq. (2.13) yields

$$D_\ell = \frac{G}{\beta} \int_0^\infty \int_0^L \left(\frac{\lambda}{\beta} + r\right) \exp(-\alpha z) \, [1 + \xi\lambda\exp(\delta\lambda)] \exp(-\lambda) \, dz \, d\lambda \tag{2.17}$$

where

$$G \equiv \frac{(3.7 \times 10^{10})\ S\ n}{4\ \ell_1^2\ \ell_2^2}\ k(\theta_{sc})\ K_d(E)\ E_s\ BUF_c\ \exp(-\mu_s P_c). \tag{2.18}$$

Further simplification is gained by separating and defining the λ and z dependent terms as shown in the following expression for D_ℓ

$$D_\ell = \frac{G}{\beta}\ I_1\ I_2 \tag{2.19}$$

where the λ dependent term I_1, is

$$I_1 = \int_0^\infty d\lambda\ (\frac{\lambda}{\beta} + r)\ [1 + \xi\lambda\exp(\delta\lambda)]\ \exp(-\lambda) \tag{2.20}$$

and the z dependent term I_2 has the form

$$I_2 = \int_0^L dz\ \exp(-\alpha z). \tag{2.21}$$

Both of these integrals are easily evaluated analytically. Since in this analysis $\alpha L >> 1$, I_2 can be expressed as

$$I_2 = \frac{1 - \exp(-\alpha L)}{\alpha} \simeq \frac{1}{\alpha}\ .$$

Integration of Eq. 2.20 by parts gives:

$$I_1 = \frac{1}{\beta} + \frac{2\xi}{\beta(1 - \delta)^3} + r + \frac{r\xi}{(1 - \delta)^2} \tag{2.23}$$

To express the δ and ξ dependence of Eq. 2.23 in terms of the parameters of the problem, compare δ and ξ to the specific form of the buildup factor developed in Sec. 2.4. This comparison shows

that ξ and δ can be expressed as:

$$\xi = K_1 E^{K_2} \quad \text{and} \quad \delta = K_3 \exp(K_4 E). \tag{2.24}$$

Substituting Eqs. 2.22 and 2.23 into Eq. 2.19 yields

$$D_\ell = \frac{G}{\alpha\beta}\left[\frac{1}{\beta} + \frac{2\xi}{\beta(1-\delta)^3} + r + \frac{r}{(1-\delta)^2}\right] . \tag{2.25}$$

Next, the expression for G (Eq. 2.19) will be evaluated explicitly in terms of the parameters of this problem. The scattering point for geometric attenuation considerations is chosen to be located at x=r and z=0, i.e., on the horizontal diameter chord of the duct at the corner of the lip closest to the source. As illustrated in Fig. 2.3,

$$\ell_1^2 = a^2 + (b - r)^2 \tag{2.26}$$

$$\ell_2^2 = (L + c)^2 + (r - d)^2 \tag{2.27}$$

$$\theta_s = \tan^{-1}\left[\frac{b - r}{a}\right] \tag{2.28}$$

$$\theta_t = \cos^{-1}\left[\frac{L + c}{\ell_2}\right] \tag{2.29}$$

and

$$\theta_{sc} = \theta_s - \theta_t. \tag{2.30}$$

The only quantity in the expression for G remaining to be evaluated is P_c. Referring to Fig. 2.2, the path length in the far lip, P_c, is given as the difference of P_2 and P_1. These two path lengths can be defined in terms of two direction cosines, γ_d and α_d, where:

$\gamma_d \equiv$ the direction cosine for path ℓ_2 with respect to the z axis, and

$\alpha_d \equiv$ the direction cosine for path ℓ_2 with respect to the x axis.

Or, in terms of the same parameters used previously, as

$$\gamma_d = \frac{L + c}{\ell_2} \tag{2.31}$$

$$\alpha_d = \frac{r - d}{\ell_2} \, . \tag{2.32}$$

P_c then becomes

$$P_c = P_2 - P_1 = \frac{\ell}{\gamma_d} - \frac{2r}{\alpha_d} \quad \text{for } \cos^{-1}(\gamma_d) \geq \tan^{-1}\left(\frac{2r}{L}\right)$$

or

$$P_c = 0 \qquad \text{for } \cos^{-1}(\gamma_d) \leq \tan^{-1}\left(\frac{2r}{L}\right). \tag{2.33}$$

The entire expression for the lip scattering exposure rate can now be written explicitly for the geometry defined as

$$D_\ell = \frac{(3.7 \times 10^{10})\ S\ n}{4\ \ell_1^2\ \ell_2^2}\, k(\theta_{sc})\ K_d(E_s)\ E_s\ BUF_c[\mu(E_s)P_c, E_s]\ \exp(-\mu(E_s)P_c)$$

$$\frac{1}{\alpha\beta}\left[\frac{1}{\beta} + \frac{2K_1E_i^{K_2}}{(1 - K_3\ \exp(K_4E_i))^3} + r + \frac{rK_1E_i^{K_2}}{(1 - K_3\ \exp(K_4E_i))^2}\right] . \tag{2.34}$$

2.6 Duct Wall Scattering

The duct wall scattered component of the exposure rate behind the shield wall is considered in this section. Figure 2.4 illustrates the basic geometric details of this model. The basic assumptions for this model are:

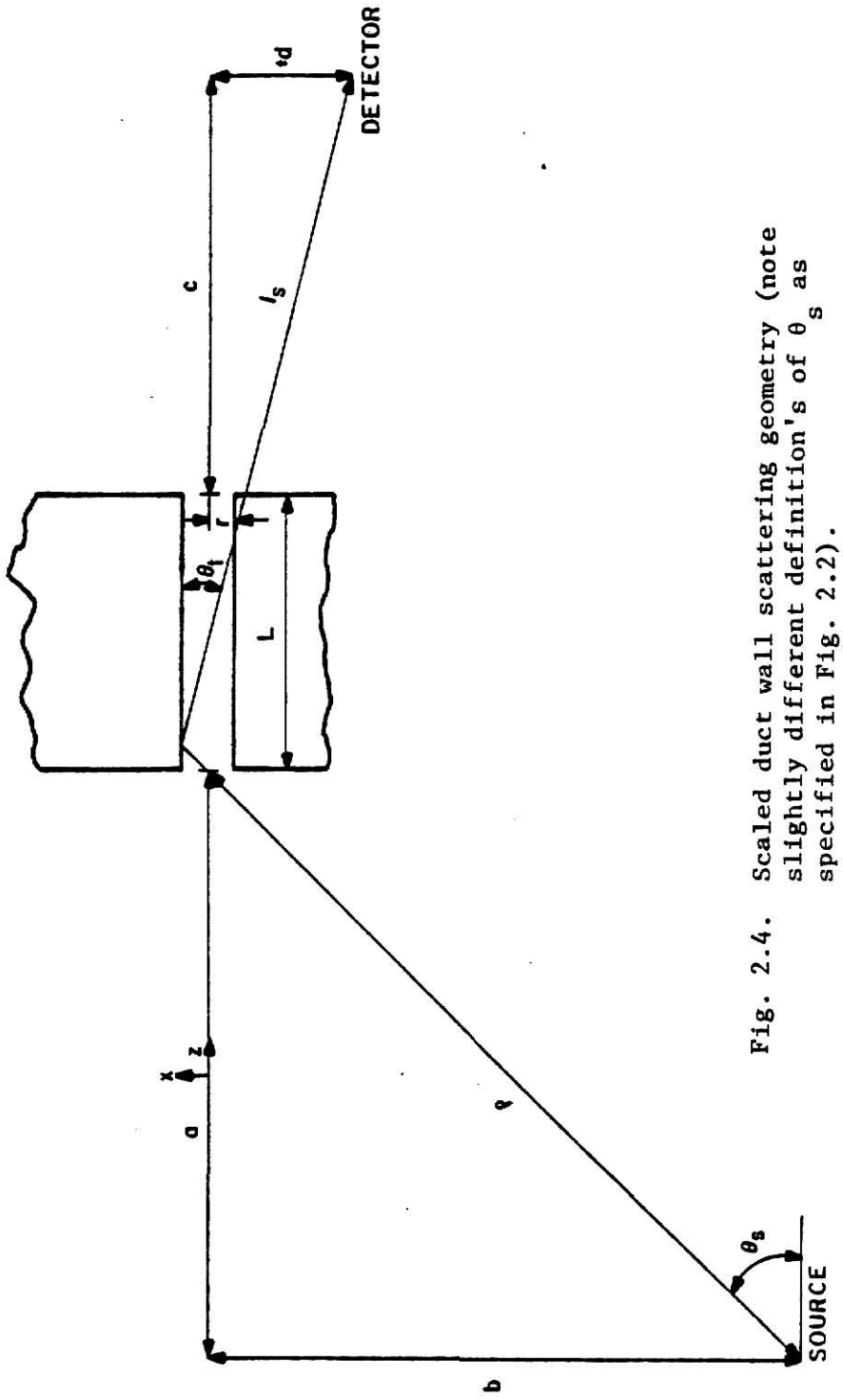

Fig. 2.4. Scaled duct wall scattering geometry (note slightly different definition's of θ_s as specified in Fig. 2.2).

1. There is no line-of-sight path from the source to the detector,
2. Scattering occurs only in the duct wall opposite the source on the horizontal plane diameter chord,
3. The duct can be modelled as a parallel slot of separation 2r,
4. The duct lip is totally opaque (this assumption will be relaxed later), and
5. Scattering occurs a distance x into the duct wall where $x << r$.

With these assumptions the exposure rate at the detector due to duct wall scattering, D_w, is given by

$$D_w = \frac{N_{in}\ P\ B\ K_d(E_s)\ E_s}{\ell_s^2} \tag{2.35}$$

where

N_{in} - number of photons entering the duct mouth

E_s - scattered photon energy (MeV)

B - buildup factor for scattered leg (initially assumed to be a constant, B = 2.0)

P - probability per steradian that a photon will scatter through an angle θ_{sc} and exit the duct wall

ℓ_s - distance from the scatter point (assumed to be on the duct wall surface) to the detector (cm).

Using the specific geometry shown in Fig. 2.5, the number of photons which enter the duct mouth is

$$N_{in} = \frac{(3.7 \times 10^{10})\ S\ n\ \pi r^2\ \cos(\theta_s)}{4\pi(a^2 + b^2)} \tag{2.36}$$

where

S - source strength (Ci)

n - number of photons per disintegration.

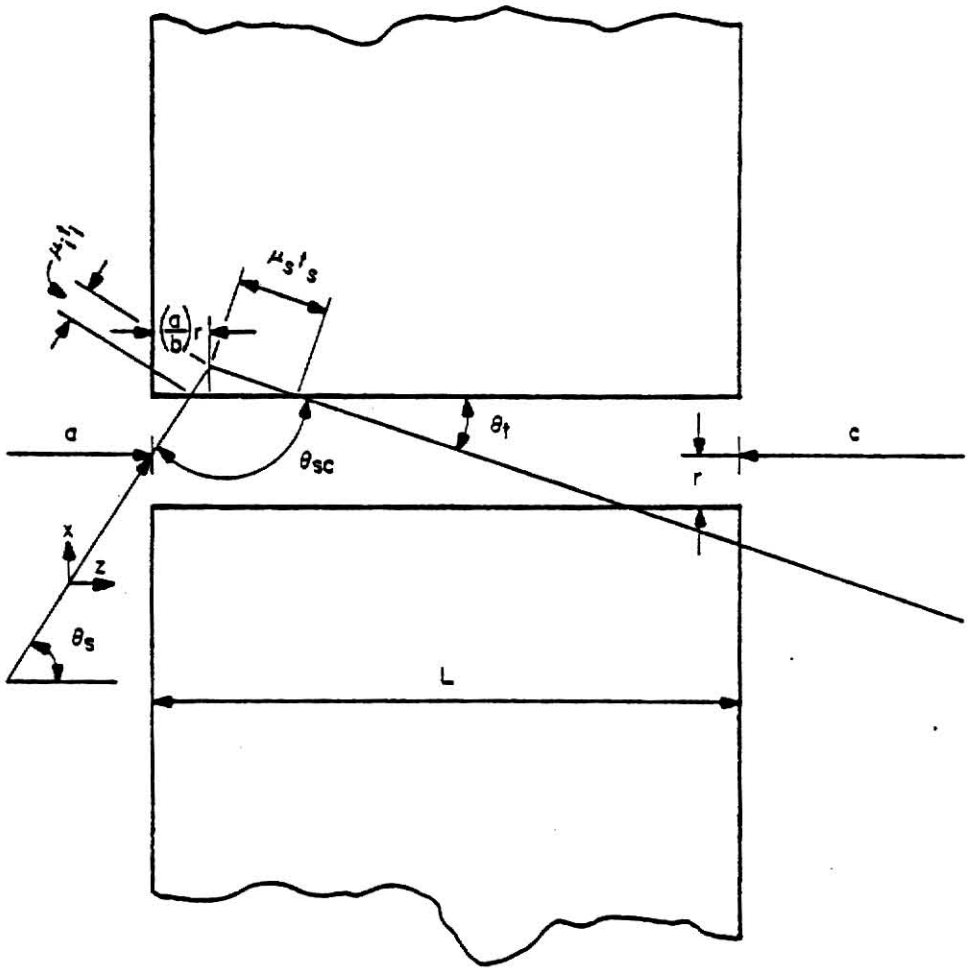

Fig. 2.5. Expanded view of the duct wall scattering model.

Explicit determination of P requires specification of the scattering region. Scattering is assumed to take place on a line perpendicular to the intersection of the source beam centerline and the far duct wall. Furthermore, photon scattering is assumed to occur in the duct wall on the line

$$z = \frac{ar}{b} \quad . \tag{2.37}$$

Based upon these assumptions, the expression for P can be shown to be

$$P = \int_0^\infty dt_i \; k(\theta_{sc}) \; \exp(-\mu_i t_i) \; \exp(-\mu_s t_s) \quad . \tag{2.38}$$

Or in terms of x,

$$P = \int_0^\infty \frac{dx}{\sin(\theta_s)} \; k(\theta_{sc}) \; \exp\left(\frac{-\mu_i x}{\sin(\theta_s)}\right) \quad \exp\left(\frac{-\mu_s x}{\sin(\theta_t)}\right) . \tag{2.39}$$

where x is the perpendicular distance into the duct wall.

The traveled path in the wall, i.e., t_i and t_s increase very rapidly with x. GGG calculations (9) show that the important scattering volume for this component to be where $0 \leq x \leq 0.25$ cm. Within this range, θ_s, θ_t, and θ_{sc} are assumed to be constant. Therefore, Eq. 2.39 can be approximated as follows

$$P \simeq \frac{k(\theta_{sc})}{\sin(\theta_s)} \left[\frac{\mu_i}{\sin(\theta_s)} + \frac{\mu_s}{\sin(\theta_t)}\right]^{-1} \tag{2.40}$$

where

$$\theta_t = \tan^{-1}\left(\frac{r + d}{c + \ell - \frac{ar}{b}}\right) \quad . \tag{2.41}$$

Referring to Fig. 2.4, θ_{sc} and ℓ_s^2 are defined as

$$\theta_{sc} = \theta_s + \theta_t \tag{2.42}$$

and

$$\ell_s^2 = (c + L - \frac{ar}{b})^2 + (r + d)^2 \quad . \tag{2.43}$$

The entire equation for duct wall scattering can now be written explicitly as follows:

$$D_w = \frac{(3.7 \times 10^{10})\ S\ n\ \pi r^2 \cos(\theta_s)\ B\ K_d(E_s)\ E_s}{4\pi(a^2 + b^2)\ [(c + \ell - \frac{ar}{b})^2 + (r + d)^2]} \frac{k(\theta_{sc})}{\sin(\theta_s)}$$

$$\left(\frac{\mu_i}{\sin(\theta_s)} + \frac{\mu_s}{\sin(\theta_t)}\right)^{-1} \quad . \tag{2.44}$$

After combining all terms, the final equation used to calculate the duct wall scattered exposure rates is

$$D_w = \frac{(3.7 \times 10^{10})\ S\ n\ r^2}{4(a^2 + b^2)\ \ell_s^2} \left(\frac{b}{a}\right) k(\theta_{sc}) \frac{B\ K_d(E_s)\ E_s}{\left(\frac{\mu_i}{\sin(\theta_s)} + \frac{\mu_t}{\sin(\theta_t)}\right)} \quad . \tag{2.45}$$

2.7 Lip Penetration Correction

Earlier it was stated that the assumption of a completely opaque duct lip could be relaxed. Certainly this assumption must be relaxed as photons obviously do enter the duct by penetrating the small amount of material at the edge of the duct lip. Figure 2.6 illustrates the general geometric layout of this analysis.

Initial calculations, assuming the duct lip to be opaque and a buildup factor B equal to 2.0, showed good results for acute

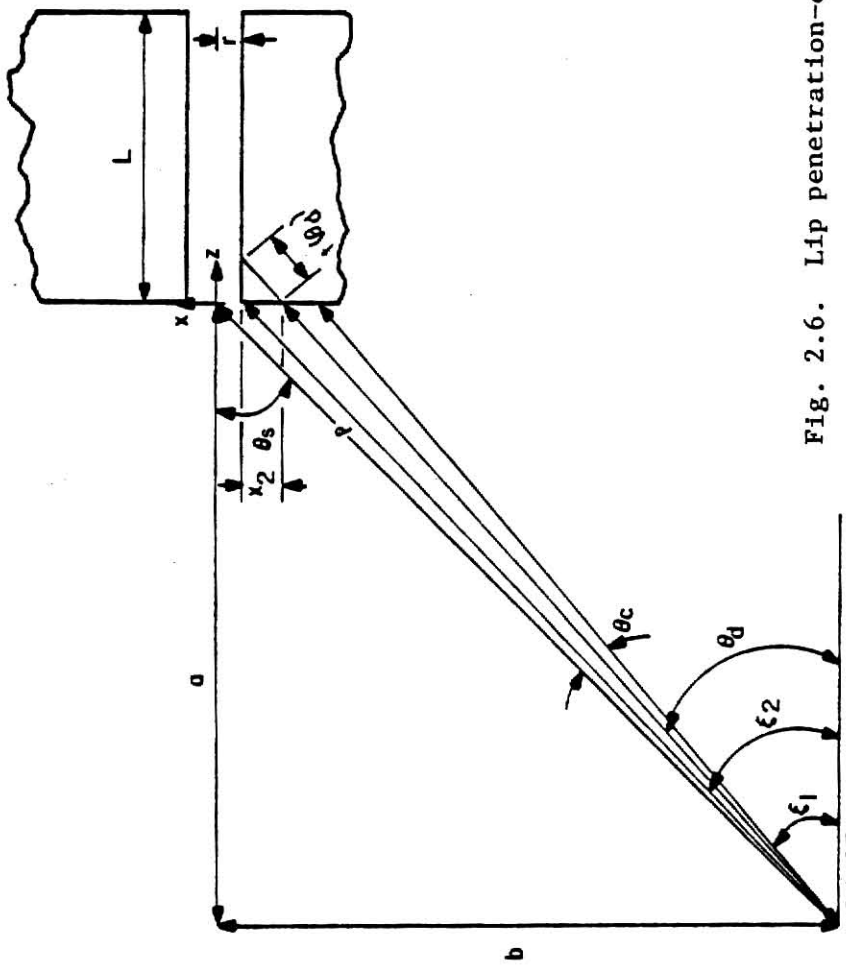

Fig. 2.6. Lip penetration-correction geometry.

angles of illumination. Increasingly poorer results were obtained for shallower angles. It is at these angles where the lip penetration contribution to the duct wall scattering should be the largest. However, the model consistently predicted the proper relative spatial distribution. These two items lead to a correction for lip penetration that modifies the source term of the duct wall scattering model to reflect the true number of photons incident at the scatter point.

Generally, the number of photon penetrating the lip can be represented by

$$N'_{in} = \frac{S'}{4\pi} \int_{\xi_1}^{\xi_2} d\Omega \exp(-\mu_i t(\theta_d)) \qquad (2.46)$$

where

$t(\theta_d)$ - path length for photons in the duct lip emitted from the source at an angle, θ_d, in the horizontal plane

μ_i - attenuation coefficient for source energy photons (cm^{-1})

$d\Omega$ - solid angle defining illumination by source.

The terms listed above will now be defined explicitly in terms of the parameters of the model,

$$t(\theta_d) = \frac{x_2}{\sin(\theta_d)} \qquad (2.47)$$

$$t(\theta_d) = \frac{b - r - a \tan(\theta_d)}{\sin(\theta_d)} \qquad (2.48)$$

$$\xi_1 = \theta_s - \theta_c \qquad (2.49)$$

$$\xi_2 = \tan^{-1} \left(\frac{b - r}{a} \right) \qquad (2.50)$$

and

$$S' = (3.7 \times 10^{10}) \, Sn \qquad (2.51)$$

where

θ_c - horizontal angle defining the horizontal collimator edge

S' - source strength (Ci)

n - number of photons per disintegration.

Since the duct is modelled as a parallel slot, the collimator solid angle, $d\Omega$, is dependent only on θ_d, therefore

$$d\Omega = \frac{dA}{\rho^2} \tag{2.52}$$

and

$$d\Omega = \frac{(\rho d\theta_d)\ [\rho\ \tan(\theta_v)]}{\rho^2} . \tag{2.53}$$

After simplification,

$$d\Omega = \tan(\theta_v)\ d\theta_d \tag{2.54}$$

where θ_v is the vertical angle defining the top and bottom collimator penumbra. Substituting Eqs. 2.48, 2.51, and 2.54 into 2.46 yields the following equation in terms of the parameters of the problem

$$N'_{in} = \frac{S'\tan(\theta_v)}{4\pi} \int_{\xi_1}^{\xi_2} d\theta_d \exp\left(-\mu_i \left[\frac{b - r - a\ \tan(\theta_d)}{\sin(\theta_d)}\right]\right). \tag{2.55}$$

Equation 2.55 was numerically evaluated for four different angles and duct radii. Results of these calculations are presented in Table 2.3 in terms of the quantity, $\zeta(\theta_s,r)$ where:

$$\zeta(\theta_s,r) = \frac{N'_{in}\ 4\pi\rho^2}{S'\cos(\theta_s)\pi r^2} . \tag{2.56}$$

The function $\zeta(\theta_s,r)$ is the ratio of source photons which penetrate the duct lip per photon entering the duct mouth.

Table 2.3. The ratio of source photons which penetrate the duct lip per photon entering the duct mouth, $\zeta(\theta_s, r)$.

Source Angle, θ_s (deg)	$\zeta(\theta_s, r)$			
	Duct Radius, r (cm)			
	5.0	10.0	15.0	20.0
22.5	1.5322	0.3719	0.1600	0.08684
33.0	2.2606	0.5613	0.2455	0.1378
45.0	3.0441	0.7683	0.3445	0.1953
60.0	3.8849	0.9944	0.4524	0.2605

This method of representing $\zeta(\theta_s,r)$ allows the lip penetration correction $\alpha_c\zeta(\theta_s,r)$ to be applied such that the corrected exposure rate prediction, D_w' is:

$$D_w' = D_w\ (1 + \alpha_c\ \zeta(\theta_s,r)) \tag{2.57}$$

where

α_c is a fit parameter to be determined.

Further simplification is achieved by defining

$$D_u = \frac{D_w}{B} \tag{2.58}$$

where D_u is the duct wall scattered prediction independent of B. This relation simplifies the following development since B is a parameter to be determined and D_u need only be calculated once.

The objective of the model development has been to keep the calculational complexity at such a level that a small programmable calculator could practically execute the resulting codes. Clearly, codes involving numerical integration are outside this objective. Therefore, the values of $\zeta(\theta_s,r)$ as tabulated in Table 2.3 were least square fitted as an empirical function of θ_s and r of the form

$$\zeta(\theta_s,r) = r^{C_1\ \theta_s^{(C_2 + C_3 r)}}\ . \tag{2.59}$$

Where the quantities in Eq. 2.59 are defined as follows:

r - duct radius

θ_s - source illumination angle

and, C_1, C_2, and C_3 are the fit parameters tabulated in Table 2.4.

Table 2.4. $\zeta(\theta_s,r)$ fit parameters, C_n.

C_1	-1.954
C_2	0.8933
C_3	0.01144

These values are implicitly appropriate only for the range of parameters encountered during the experiment. The parameters are: ^{60}Co photon energies, vertical collimator angle, and the range of duct radii and source angles listed in Table 2.3. However, test calculations of $\zeta(\theta_s,r)$ for different horizontal collimator angles have shown that $\zeta(\theta_s,r)$ is insensitive to changes in θ_c past the first few centimeters of wall illumination.

The term, α_c, in Eq. 2.59 is annotated differently since it is considered to be a free parameter. This is because it is realized that θ_v is an obvious misrepresentation of the vertical component of the true solid angle represented by the duct lip. Experimental data obtained during the measurement program were used to provide the necessary information to determine the value of α_c. The method used for determining α_c and a revised value of B demand that the mean of $(\frac{C}{E})$ for a selected data set equal one and that the standard deviation of $(\frac{C}{E})$, $\sigma(B)$, for the same data set be minimum. The ratio of calculated to experiment is expressed as:

$$(\frac{C}{E})_i = \frac{D_{w,i}\ (1 + \alpha_c\ \zeta(\theta_{s,i}r)}{E_i} \qquad (2.60)$$

where

$(\frac{C}{E})_i$ - ratio of calculation to experiment for the i-th case at the component peak

E_i - experimental measurement for the i-th case at the component peak.

The condition on the mean of $(\frac{C}{E})$ can be expressed generally as

$$\frac{\sum_i \left(\frac{C}{E}\right)_i}{\sum_i i} = 1.00. \qquad (2.61)$$

All four source angles for the 20 cm diameter (r = 10.0) duct were used for this fit in the 100 cm thick wall. These points were chosen for the wealth of experimental data that exist from the experimental program and for the confidence in the validity of these data. The equation demanding the condition on the mean can be written explicitly for this case as:

$$\frac{D'_{w,1}}{E_1} + \frac{D'_{w,2}}{E_2} + \frac{D'_{w,3}}{E_3} + \frac{D'_{w,4}}{E_4} = 4.00 \qquad (2.62)$$

where for simplicity;

$$D'_{w,i} = BD_{u,i}\ (1 + \alpha_c\ \zeta(\theta_s, r)). \qquad (2.63)$$

Equation 2.62 was solved for α_c in terms of B. The resulting relation is

$$\alpha_c(B) = \frac{\gamma_1}{B} + \gamma_2 \qquad (2.64)$$

where γ_1 and γ_2 were solved from the explicit relation resulting from solution of Eq. 2.62. The values of γ_1 and γ_2 that satisfy the condition on the mean are listed below

$$\gamma_1 = 5.8257 \quad \text{and} \quad \gamma_2 = -2.2344.$$

These values of γ_n were then substituted back into Eq. 2.64 and the resulting value of α_c for a given value of B was further substituted into Eq. 2.60.

The standard deviation of $(\frac{C}{E})$ defined as $\sigma(B)$, was then calculated for the same data set used earlier and the result was plotted as a function of B and graphically minimized. Figure 2.7 shows the plot of this function. The resulting values for B and α_c are tabulated below for the conditions given throughout this derivation

$$B = 1.5625 \quad \text{and} \quad \alpha_c = 1.4940.$$

The preceding correlation has reduced the spread of $(\frac{C}{E})$ ratios from -100% and +200% to typically $\pm$50%.

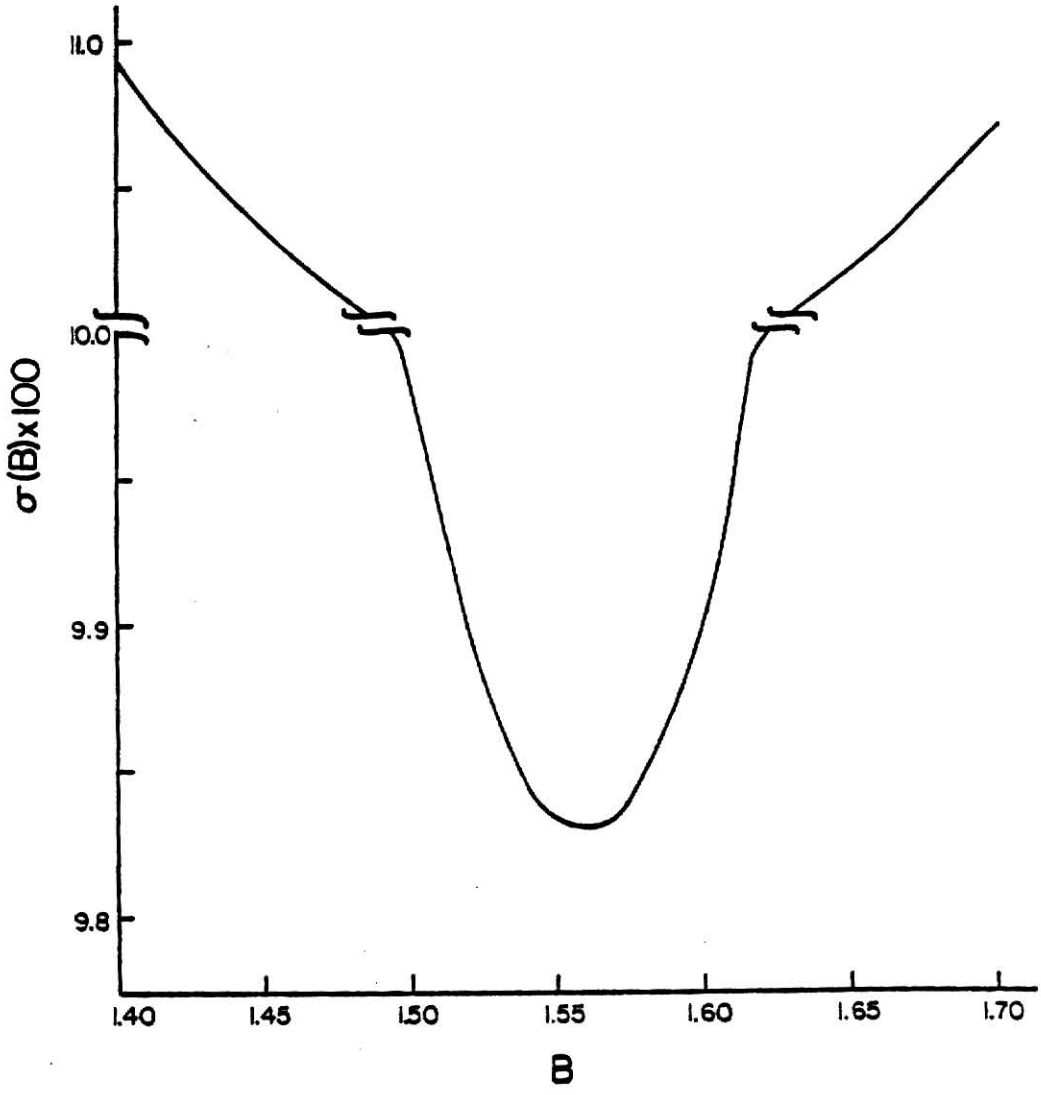

Fig. 2.7. σ(B) versus B.

3. DISCUSSION OF RESEARCH FACILITY

The gamma-ray streaming facility, developed at the Kansas State University Radiation Shielding Site by members of the Nuclear Engineering Department, is described in this chapter. It should be emphasized that the only type of radiation considered, during the design of this facility, were gamma rays. Although only ^{60}Co sources have been used in this facility, other energy gamma-ray sources could easily be accommodated. In addition, shielding walls of virtually any thickness and composition could be installed in place of the existing concrete walls. Flexibility also exists in the sizes and compositions of the ducts which could be mocked up in shielding walls.

This facility was designed to satisfy the following objective -- obtain benchmark gamma-ray streaming data for many different straight ducts in thick concrete walls. In view of this objective, consideration had to be given to the flexibility of changing duct configurations, positioning the source, and measuring the exposure rate throughout a large area behind the shielding walls. Because measurements for a large number of different duct configurations were required in this project, frequent duct changes were required. An important system design consideration was the convenience in making the required configuration changes. It was, therefore, vital that the time required to change from one duct configuration to the next not be excessive. This ability to change configurations rapidly was accomplished by building into each shielding wall a large duct-block opening. Smaller insert duct blocks were then easily placed into the opening to establish the desired duct configuration.

Adjacent to the building, a level, 15 cm. thick, 10 x 10 meter concrete pad was constructed to provide a base for the shielding walls and to accommodate the gamma-ray source. Shielding walls were stacked at the side of the pad next to the building. The concrete pad also contained a 2.5 x 3.25-m extension upon which a source-storage building was built. Sufficient space was also available on the pad to allow room for maneuvering the source-handling forklift from the source storage building to the desired source locations.

Experimental measurements were made in three phases, each phase concentrated on a separate thickness of the shielding wall. The first task of each phase involved constructing the designated wall from concrete blocks. Data were then acquired for each specified duct configuration. Stacking patterns for these duct-bearing free-standing walls, fabrication of the concrete shielding wall blocks and the concrete duct blocks, and specifications for each type of block are described in this section.

Shielding walls were constructed by stacking individual concrete blocks. The first wall investigated (Phase I) was 50.8 cm thick. Additional wall thicknesses were obtained by adding blocks in front of the previously studied wall. A partially completed, 50.8 cm thick, wall is shown in Fig. 3.1 with the 21.1-cm diameter duct installed. This figure also shows the relative position of the shielding wall with respect to the instrumentation building. The block stacking pattern for the completed 50.8-cm thick wall is shown in Fig. 3.2.

Each wall consisted of close-packed blocks with only a rectangular duct section left unfilled. The duct opening centerline elevation was fixed at the height of the ^{60}Co gamma-ray sources used for these benchmark duct measurements. Moreover, the center of the duct opening was

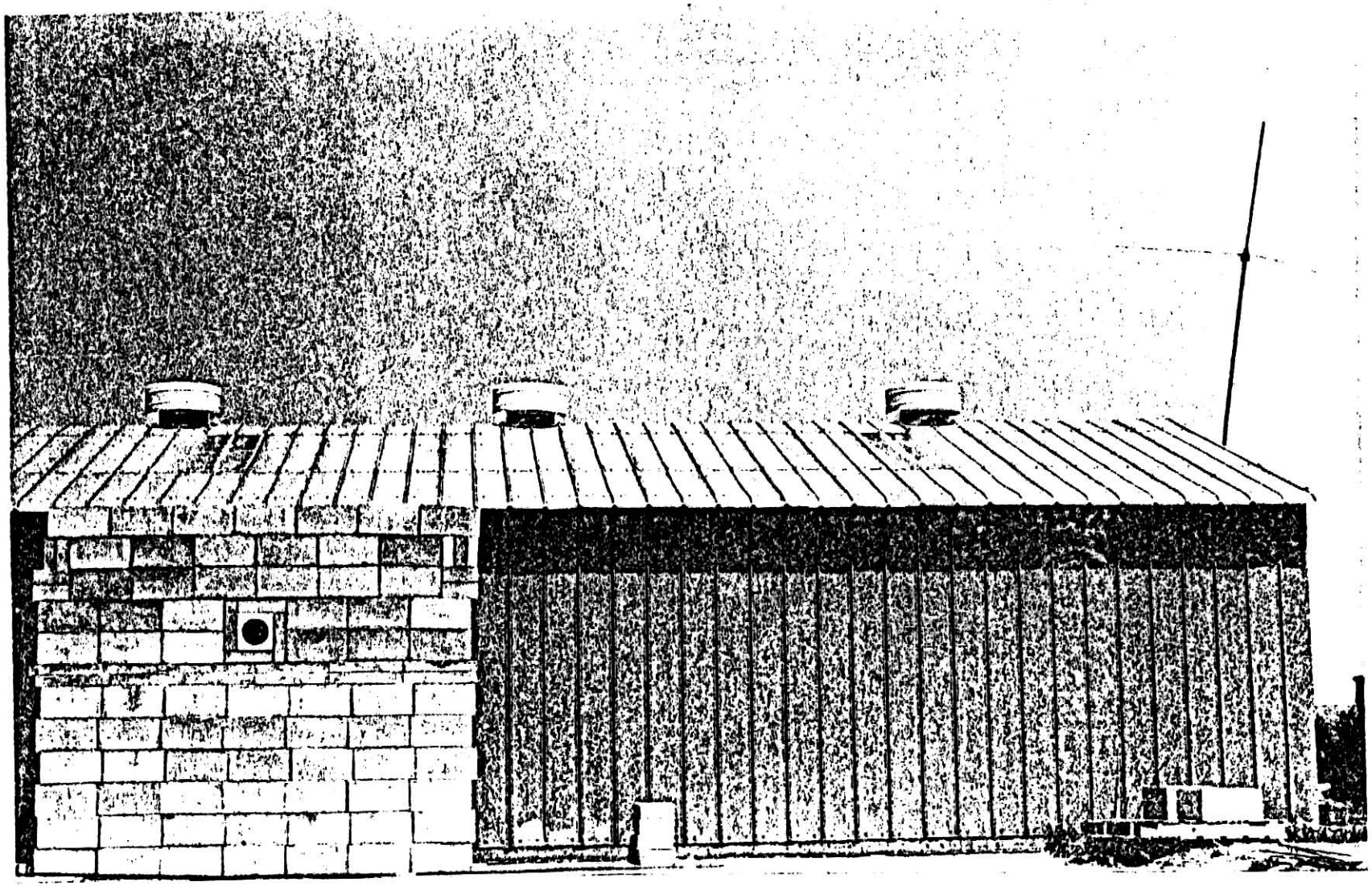

Fig. 3.1 Partially completed 50.8 cm. thick experimental shielding wall containing the 21.1 cm. diameter straight circular duct. Building behind the wall housed the ion chamber and associated instrumentation.

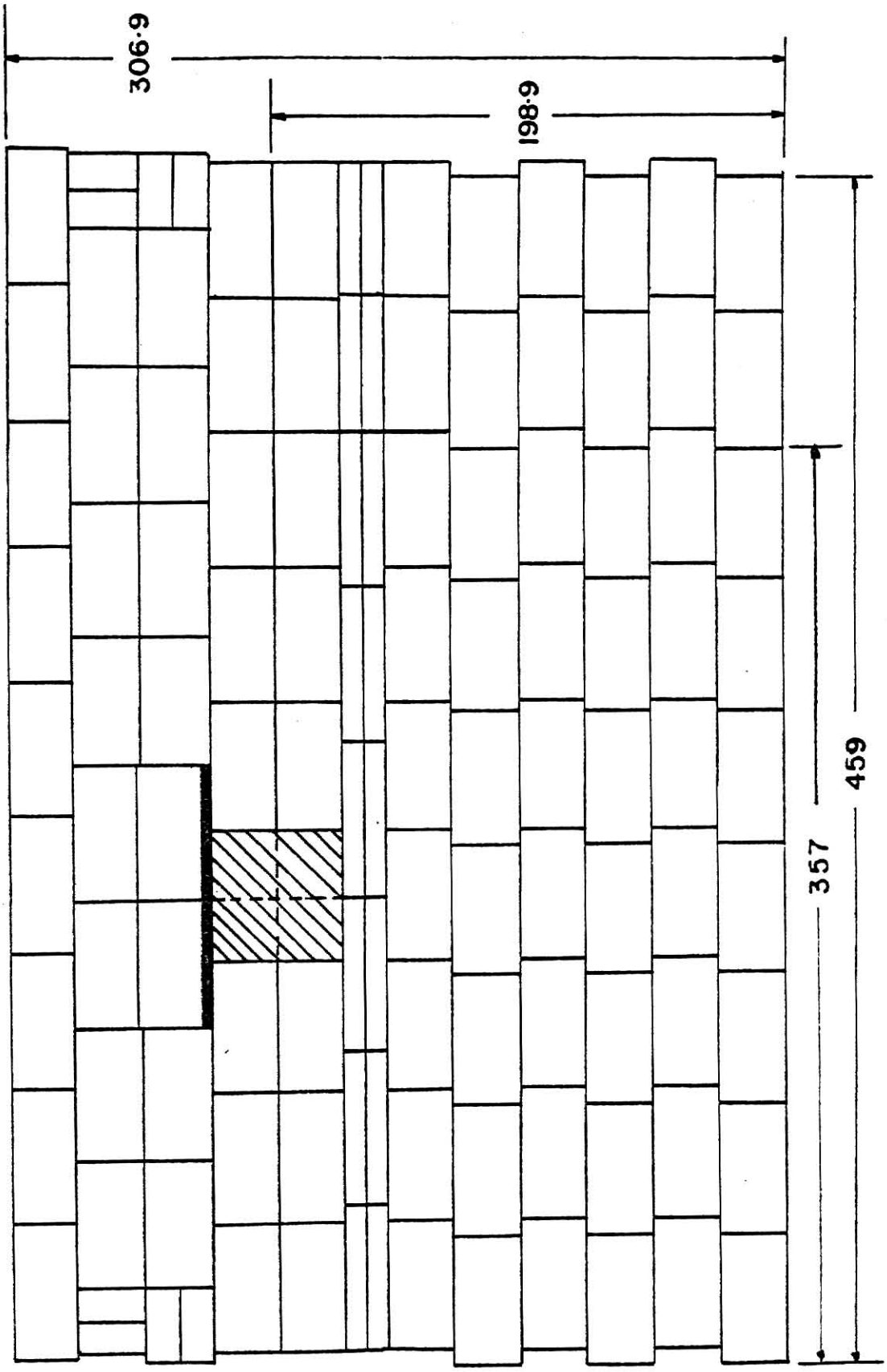

Fig. 3.2 Front view of the 50.8-cm thick duct-bearing concrete wall.
(all dimensions in centimeters)

displaced along the horizontal centerline of the solid wall. The additional wall length, on the source traverse side, shielded the detector traverse area from the gamma-ray source. As shown in Fig. 3.3, the solid shielding wall was between the detector traverse area for all values of source positions.

The 1.016-m thick wall (Phase II) was constructed by placing another thickness of concrete wall blocks in front of the 50.8-cm wall. Its stacking pattern was similar to the one used for the thinner wall; however, blocks were displaced slightly to cover the cracks between individual blocks in the first layer, and the second layer was only 3.57 m long since it did not contain the wall extension.

Experimental measurements, made in Phase III, were for a 1.524-m thick wall. This wall was also constructed by placing an additional layer of wall blocks directly in front of the 1.016-m thick wall.

As discussed previously, the major portions of the shield wall were constructed from solid concrete blocks. These blocks, discussed in this section, 50.8 x 50.8 x 24.5 cm. Block specifications were established during the planning stages of this project. A prime criterion in the design of these blocks was the ability to stack them to obtain the three required shield wall thicknesses (0.508, 1.016, and 1.524 m). Additional criteria were quality control, negligible gamma streaming between blocks, fabrication time to complete the requisite number of blocks, design flexibility, ease of handling, transportability to the shielding site, stability of the free standing walls, and removal from the experimental area following project completion.

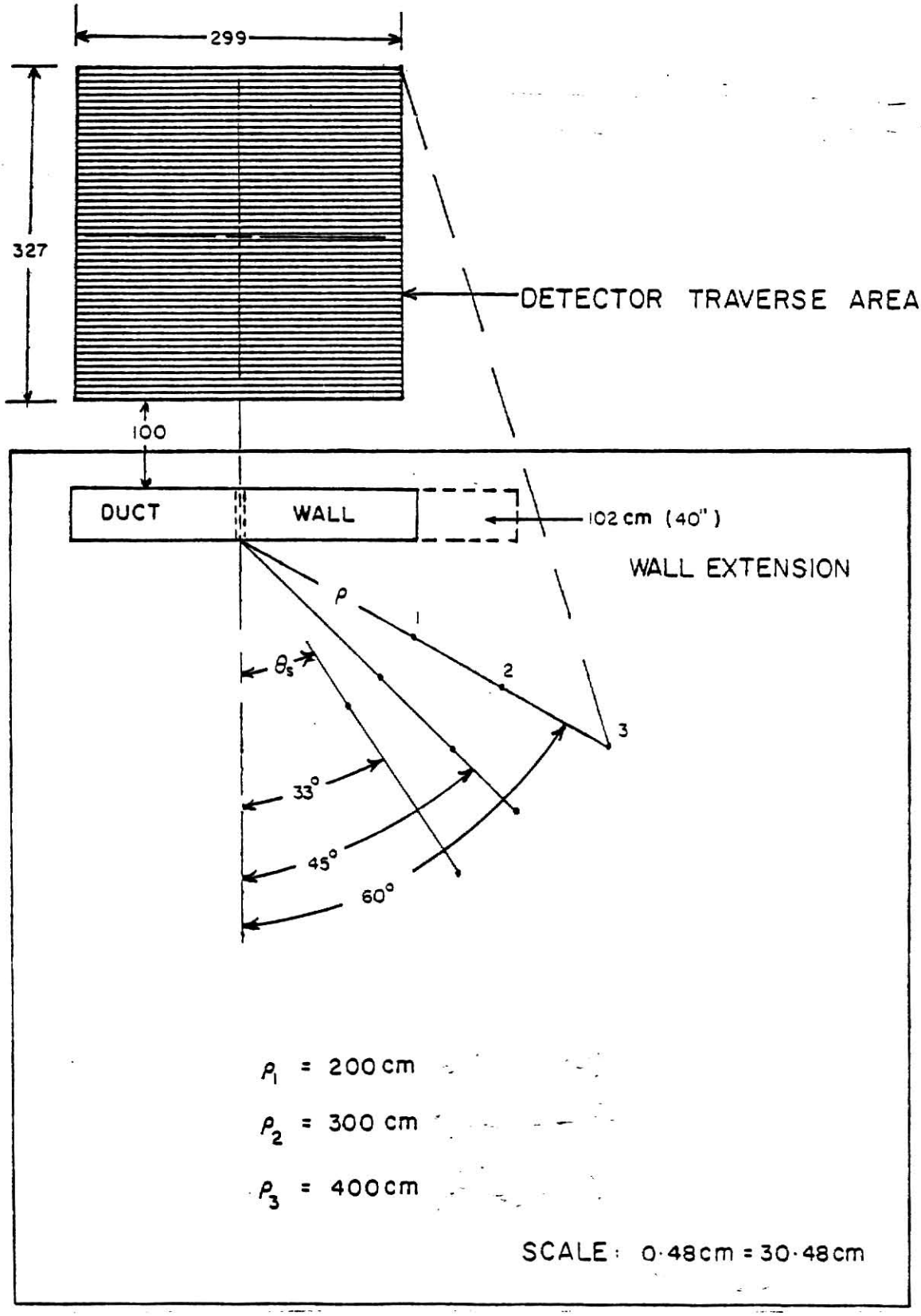

Fig. 3.3 Experimental arrangement used for the benchmark measurements made in the 50.8-cm. thick wall.

Each wall block was of essentially the same composition. A "seven sack/30" mix was specified for each batch of concrete delivered by a local concrete company. This mix contained seven sacks of cement (300 kg) per cubic yard of sand and aggregate (30 weight percent heavy aggregate and 70 percent sand). The mean and standard deviation of the specific gravity for the wall blocks was measured to be 2.22 $\pm$ 2.1%. This value was calculated from size and weight measurements made using smaller concrete blocks which were poured at the same time each set of 16 wall blocks were being poured. Following pouring, a lifting insert was embedded into the exposed surface of each block. Figure 3.4 shows several of the finished wall blocks. The small hole, visible at the top of each block, is the location of the lifting insert. A metal eyebolt, which could be screwed into this threaded opening was used to lift the blocks with the aid of a forklift.

Cylindrical ducts having a wide range of length/diameter ratios were mocked up using sets of concrete duct blocks. The concrete for these blocks had an average specific gravity of 2.22 $\pm$ 2.1%. Hence, these blocks contained only ordinary concrete and had the diameter penetrations required to establish the duct configurations listed in Tables 2.3 - 2.6.

Duct blocks with the dimensions listed in Table 3.1 were fabricated using wooden forms. Cardboard tubes, designed specifically for concrete forming, were used to produce the 41.9-cm and 21.1-cm diameter duct openings. Steel pipe served as the duct forming material for the smaller diameter ducts. Solid blocks, for background measurements, and for fill blocks were also fabricated.

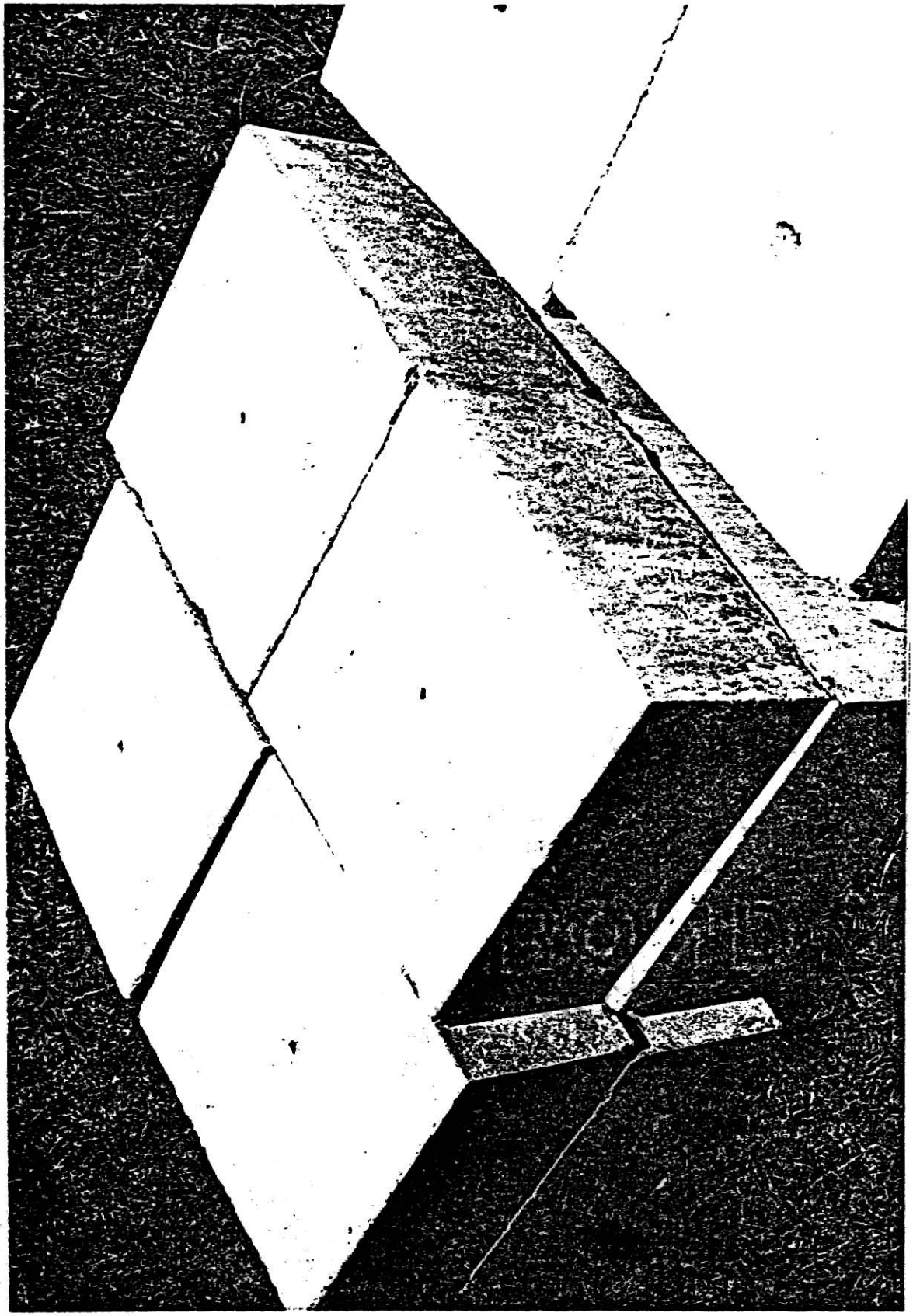

Fig. 3.4 Concrete shielding-wall blocks.

Table 3.1. Dimensions of concete blocks used to construct the duct openings in the concrete shielding walls. The specific gravity of these blocks was 2.22 ± 2.1%.

Block Type	Length		Width		Thickness	
	cm	in	cm	in	cm	in
Solid wall duct blocks						
Solid wall blocks	30.5	12	30.5	12	12.7	5
Fill blocks	40.4	15.9	10.2	4.0	25.4	10
41.9-cm (16.5-in) diameter duct						
Duct block pairs	50.2	19.75	50.2	19.75	12.7	5
Fill blocks	-	-	-	-	-	-
21.1-cm (8.3-in) diameter duct						
Duct block	30.5	12	30.5	12	12.7	5
Fill blocks	40.4	15.9	10.2	4.0	25.4	10
10.3-cm (4.06-in) diameter duct						
Duct block	30.5	12	30.5	12	12.7	5
Fill blocks	40.4	15.9	10.2	4.0	25.4	10
4.76-cm (1.88-in) diameter duct						
Duct block	30.5	12	30.5	12	12.7	5
Fill blocks	40.4	15.9	10.2	4.0	25.4	10
30.5-cm (12-in) square duct						
Fill blocks	40.4	15.9	10.2	4.0	25.4	10
15.2-cm (6-in) High x 30.5-cm (12-in) wide rectangular duct						
Duct blocks	61.0	24.0	30.5	12.0	7.62	3
	41.0	16.0	30.5	12.0	7.62	3
Fill blocks	40.4	15.9	10.2	4.0	25.4	10

Duct blocks were placed into the duct-block opening (refer to Fig. 3.2) of all three shielding walls in patterns similar to those shown in Figs. 3.5 and 3.6 for the 0.508-m thick wall. As is shown in these figures, the blocks were oriented in a manner which minimized gamma-ray streaming through the cracks between individual blocks. Additional duct blocks, with the same dimensions and insertion patterns, were used for the thicker wall configurations. Furthermore, 10.3-cm duct configurations were constructed by replacing the 21.1-cm diameter duct blocks with blocks of the same dimensions having the appropriate smaller diameter openings. The 41.9-cm diameter duct was the only duct insert not requiring solid fill blocks.

Annuli were constructed by inserting either water-filled or concrete-filled iron pipes through the center of the straight circular ducts. Small amounts of styrofoam were used to suspend these inserts in the center of the duct. Table 2.4 lists the annuli configurations investigated, and the dimensions of the duct annuli are presented in Table 3.2. The one steel-lined duct experiment consisted of inserting 0.953-cm inside the 10.3-cm diameter duct opening. Analysis of the annuli and iron lined ducts will not be addressed within this paper.

Table 3.2 Dimensions of Annuli used with the concrete shielding walls.

Outside Diameter		Inside Diameter		Remarks
cm	in	cm	in	
41.9	16.5	32.39	12.75	Water filled 12-in ID iron pipe
41.9	16.5	27.62	10.88	Water filled 10.06-in ID iron pipe
21.1	8.3	10.16	4.0	Concrete filled 3.5-in ID iron pipe
21.1	8.3	6.03	2.38	Concrete filled 2.13-in ID iron pipe

Figure 3.7 shows the collection of duct blocks and annuli inserts used throughout the experiment.

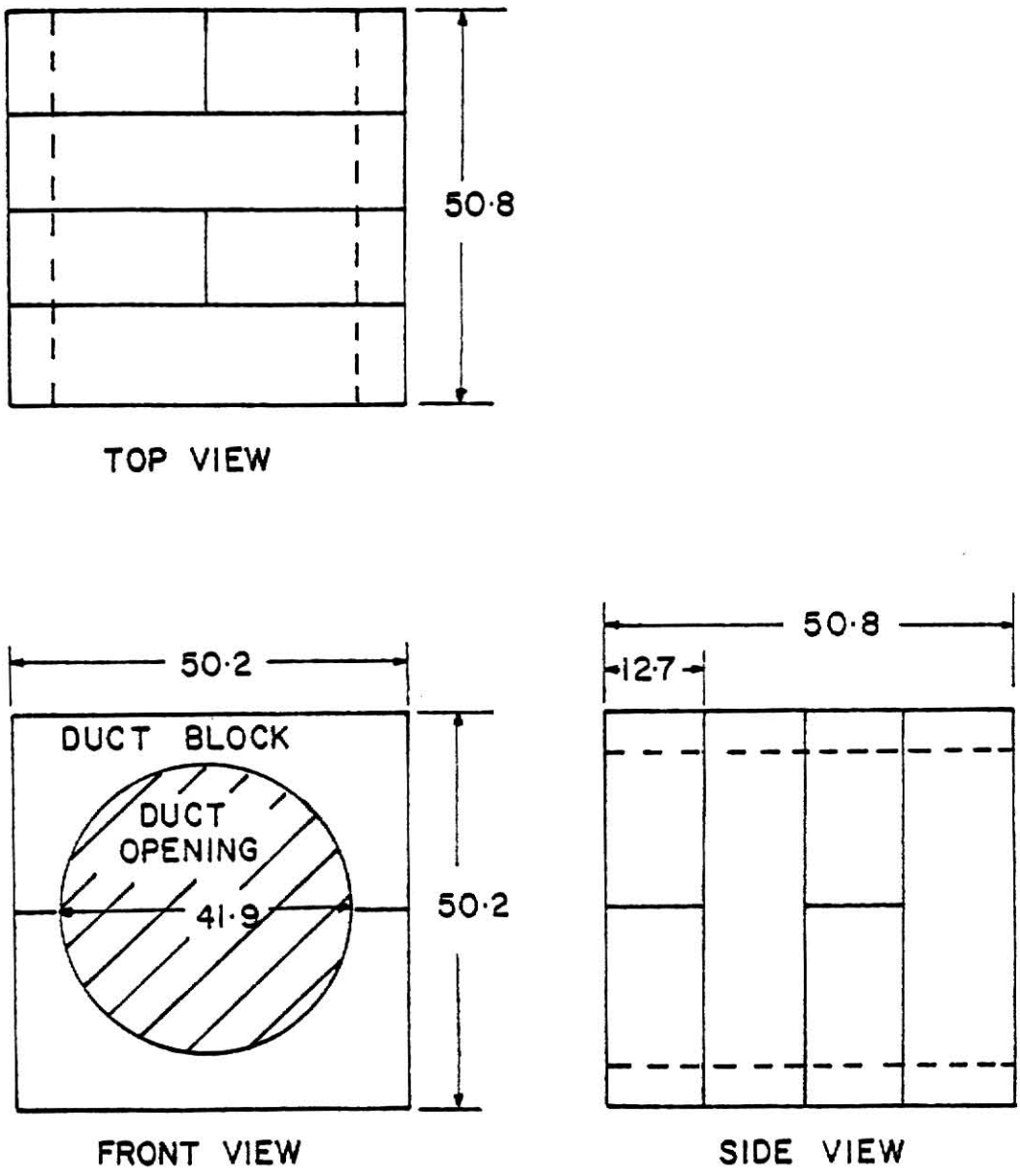

Fig. 3.5 Duct blocks used to mockup the 41.9-cm diameter duct in the 50.8-cm. thick wall.

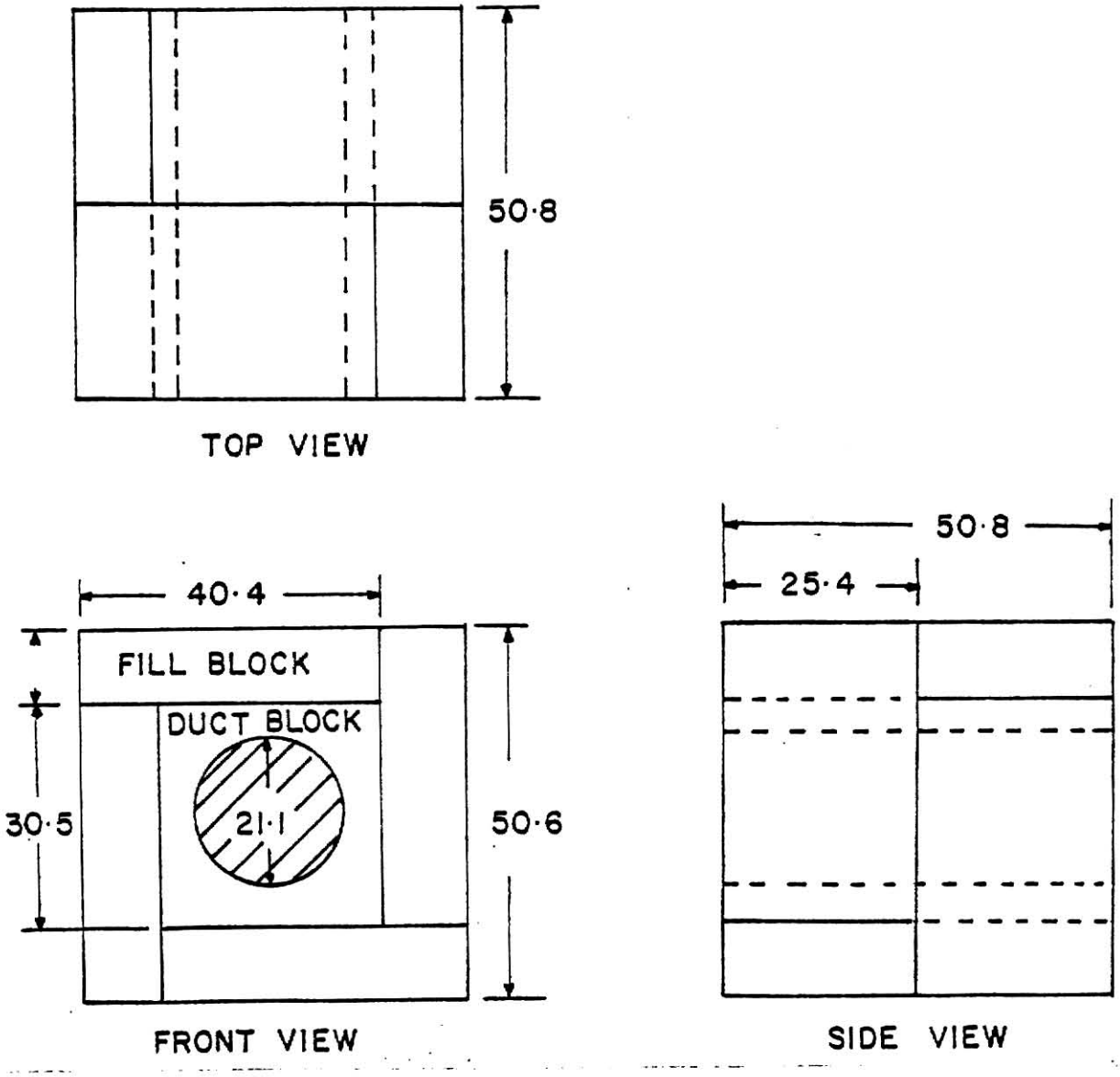

Fig. 3.6 Duct and fill blocks for the 21.1-cm diameter duct mockup in the 50.8-cm thick wall.

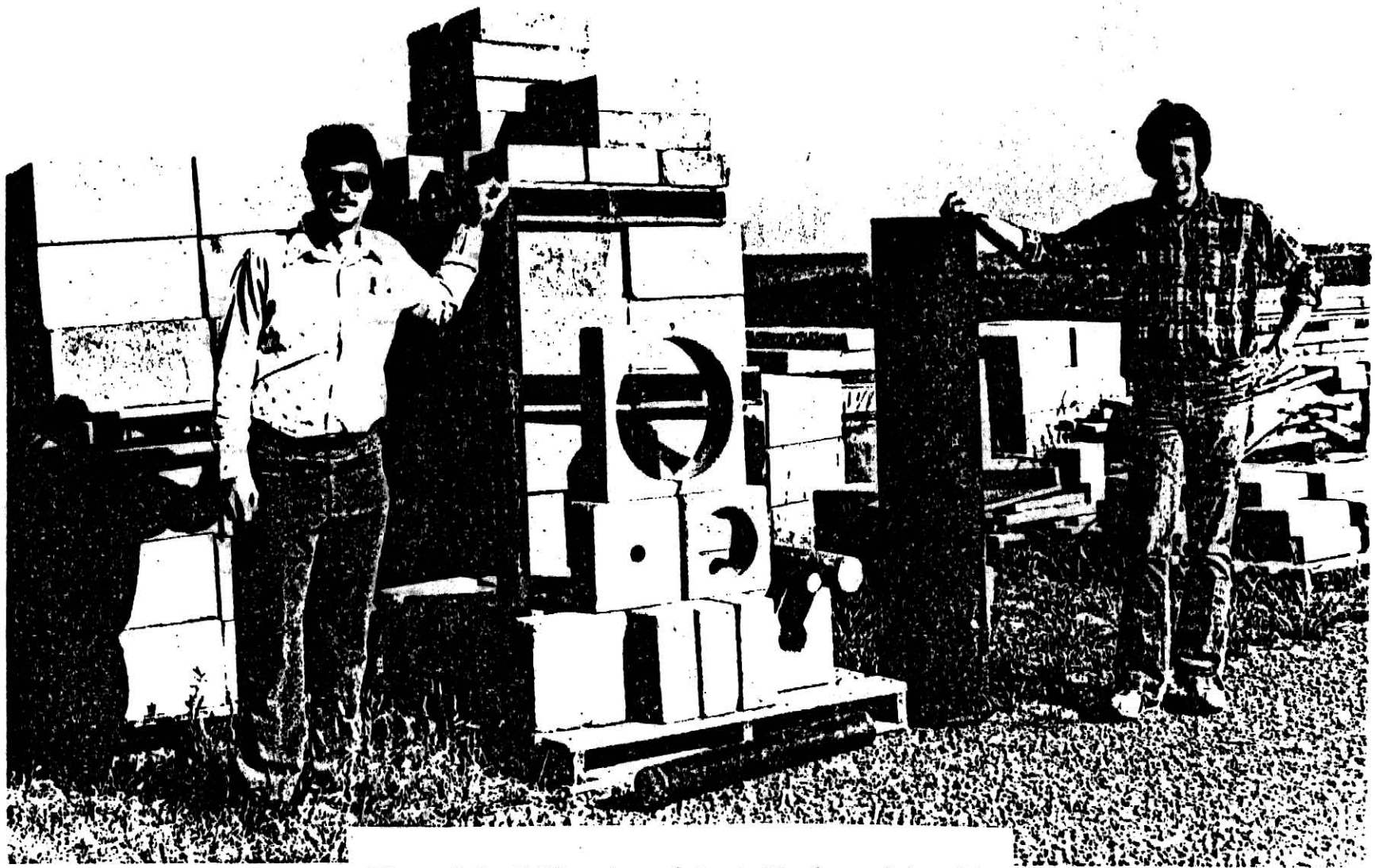

Fig. 3.7 Collection of Duct Blocks and Annuli

Two ^{60}Co sources were used in the gamma-ray streaming measurements. The less intense source, identified as the nominally 0.5-Ci source, is contained in a Technical Operations, Inc. Model 402 Gamma-Ray Projector. The more intense source, identified as the nominally 10-Ci source, is contained in a J. S. Shepherd and Associates Model 78-18 Irradiator.

The projector consists of a source storage shield, a source cable control unit, and a 6.4 m source tube. The source tube is a flexible metallic hose through which is mechanically projected the gamma-ray source on the end of a flexible cable. Electrical switches activate signals indicating whether the source is in its shielded storage position or in its fully exposed position.

The cobalt-60 gamma-ray source of nominal strength 10 Ci, is housed in a lead-shielded irradiator unit (J. L. Shepherd and Associates, Model 78-18). In operation the source was driven pneumatically from its shielded housing vertically to a position centered 1 in (2.54 cm) above the top of the housing and 78 in (1.98 m) above the wheeled base of the irradiator. The source is located 2 in (5.08 cm) radially from the centerline of the storage cask. The source and housing define a maximum collimation aperture illustrated in Fig. 3.8.

Five ^{60}Co sources were used in the calibration procedure. They are identified in Table 3.3. Uncertainties are expressed as estimated standard deviations. Source calibration was achieved by cross-calibration of the relative source strengths of the source to be calibrated and the next smaller source.

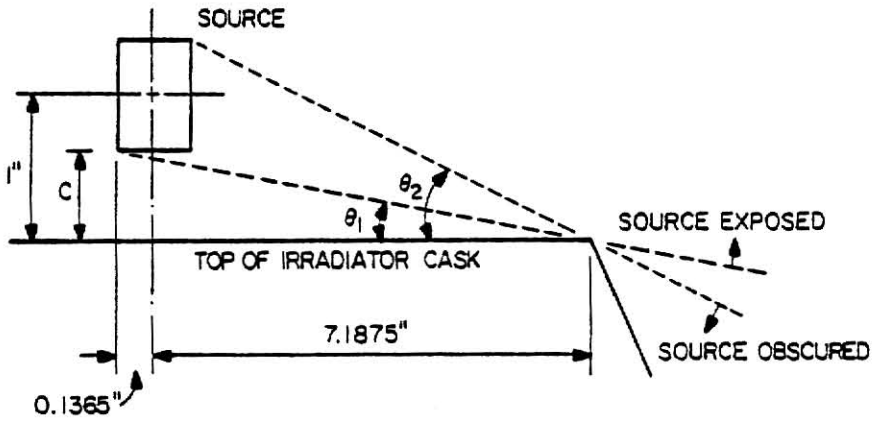

Source	C (cm)	θ_1 (deg)	θ_2 (deg)
10 Ci	2.22	6.813	9.068
250 Ci	1.59	4.878	11.034

Fig. 3.8 Source Position with respect to Lip of Steel Clad Lead Source Housing (not to scale).

Table 3.3 ^{60}Co source Identification and Intercalibration Data.

Source	Identification
A	Calibration Source, 94.7 μCi ± 3.1%, June 1, 1977
B	Intermediate Source, Serial No. 027-16
C	Intermediate Source, Serial No. 027-5
D	Gamma-Ray Projector Source, Nominally 0.5 Ci
E	Shepherd Source, Nominally 10 Ci

Source A is the principal calibration source, with calibration traceable to the U.S. National Bureau of Standards. Based on the above relative source strengths, and a ^{60}Co half life of 5.26 years, the source strengths, effective 1 June 1979, were computed and presented in Table 3.4.

Table 3.4 Cobalt-60 Source Strengths, Effective 1 June 1979.

Source	Strength (Ci)
A	$7.28 \times 10^{-6} \pm 3.1\%$
B	$6.24 \times 10^{-4} \pm 3.5\%$
C	$4.45 \times 10^{-2} \pm 3.8\%$
D	$4.74 \times 10^{-1} \pm 4.5\%$
E	$8.12 \pm 4.8\%$

Orientation of the irradiator unit with respect to the test wall for the streaming experiments is illustrated in Fig. 3.9. Because of the constraint presented by the 1-in vertical clearance between the center of the source and the top of the source housing, it was reasoned that the collimator need not provide more than a 1-in vertical clearance above the source centerline nor more than 1-in clearance on either side of the sources.

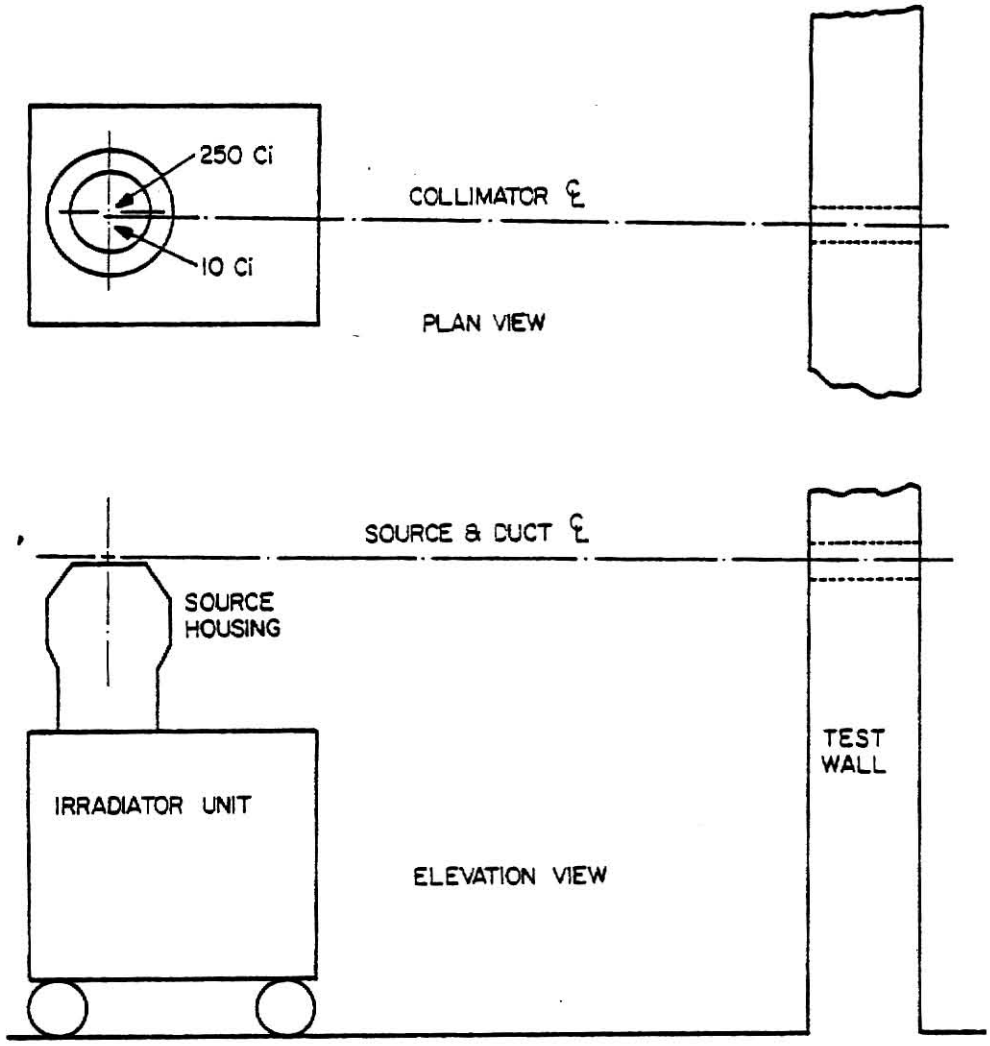

Fig. 3.9 Irradiator Position Relative to Test Wall

Placement of the collimator with respect to the source and irradiator housing is illustrated in Fig. 3.10.

The following factors affected design of the associated shadow shield. Firstly, it should be fabricated from readily available materials (lead bricks). Secondly, it should be of such size and mass to allow mounting on the irradiator support table (to the right of the source housing in Fig. 3.9) and within the confines of any weather housing used to protect the irradiator. Thirdly, it should provide the same or smaller aperture as the collimator. Such a shadow shield is illustrated in Fig. 3.11, shown in relation to the collimator.

A mockup of a collimator and shadow shield was constructed in Ward Hall at Kansas State University. Comparisons of pulse height distributions for the final collimator design with a ^{60}Co source showed the spectrum to be essentially identical to that of a "pure" ^{60}Co reference spectrum. Therefore, it was concluded that the collimator and shadow shield would result in negligible energy spectrum perturbation and would only serve to minimize skyshine contributions in the measurement area.

A collimator and a shadow shield of the same dimensions as those described above, were installed atop the J. L. Shepherd Irradiation Unit. When the 0.5-Ci source was used, it was supported in a wooden frame and positioned in the collimator at the same position to which the 10-Ci source was elevated during its use. The irradiator, with collimator and shadow-shield in place, is illustrated in Figs. 3.12 and 3.13.

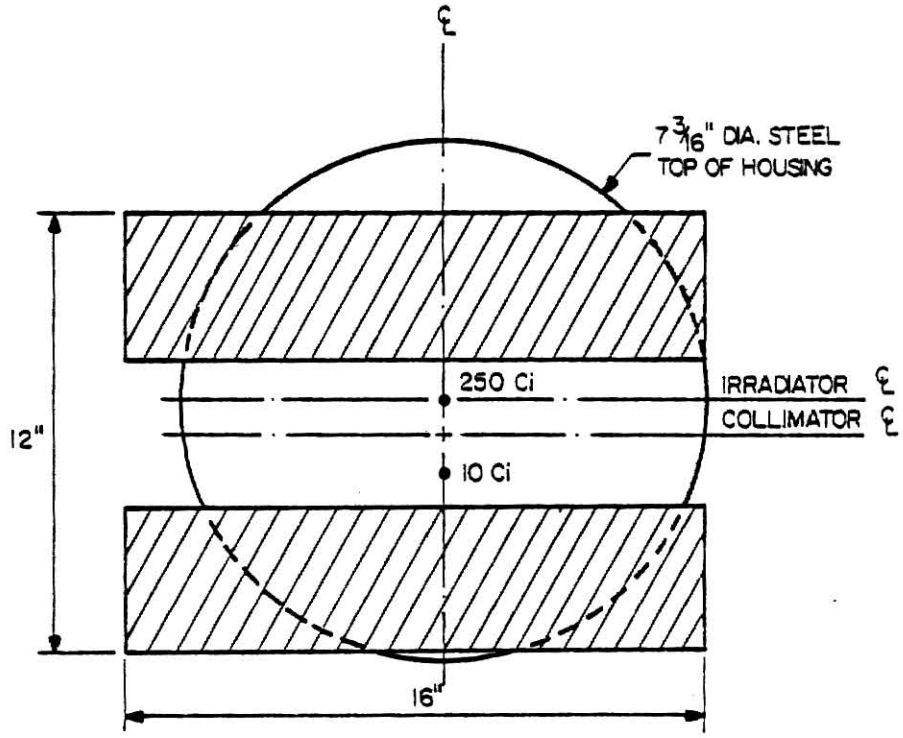

Fig. 3.10 Horizontal Sectional View through Sources and Collimator above Irradiator.

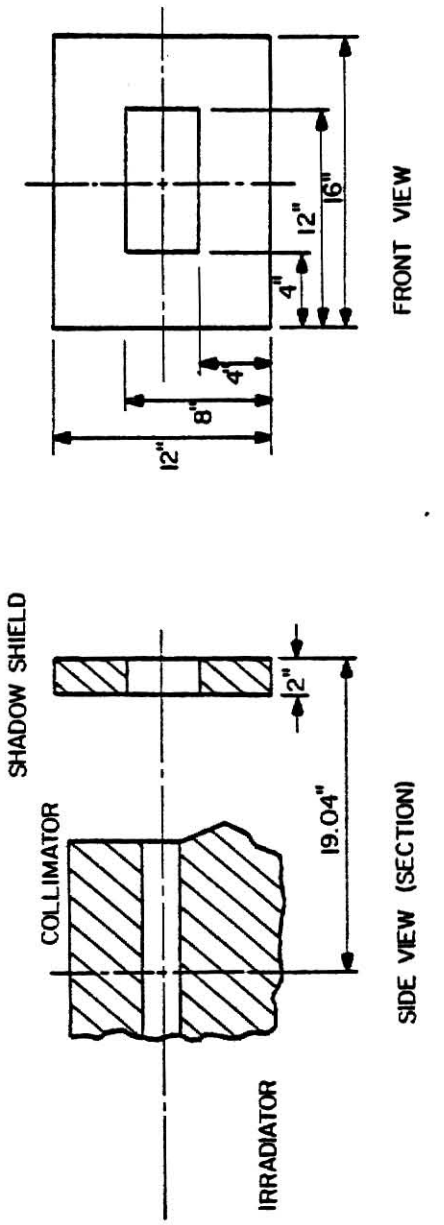

Fig. 3.11 Shadow Shield Position Relative to Source and Collimator

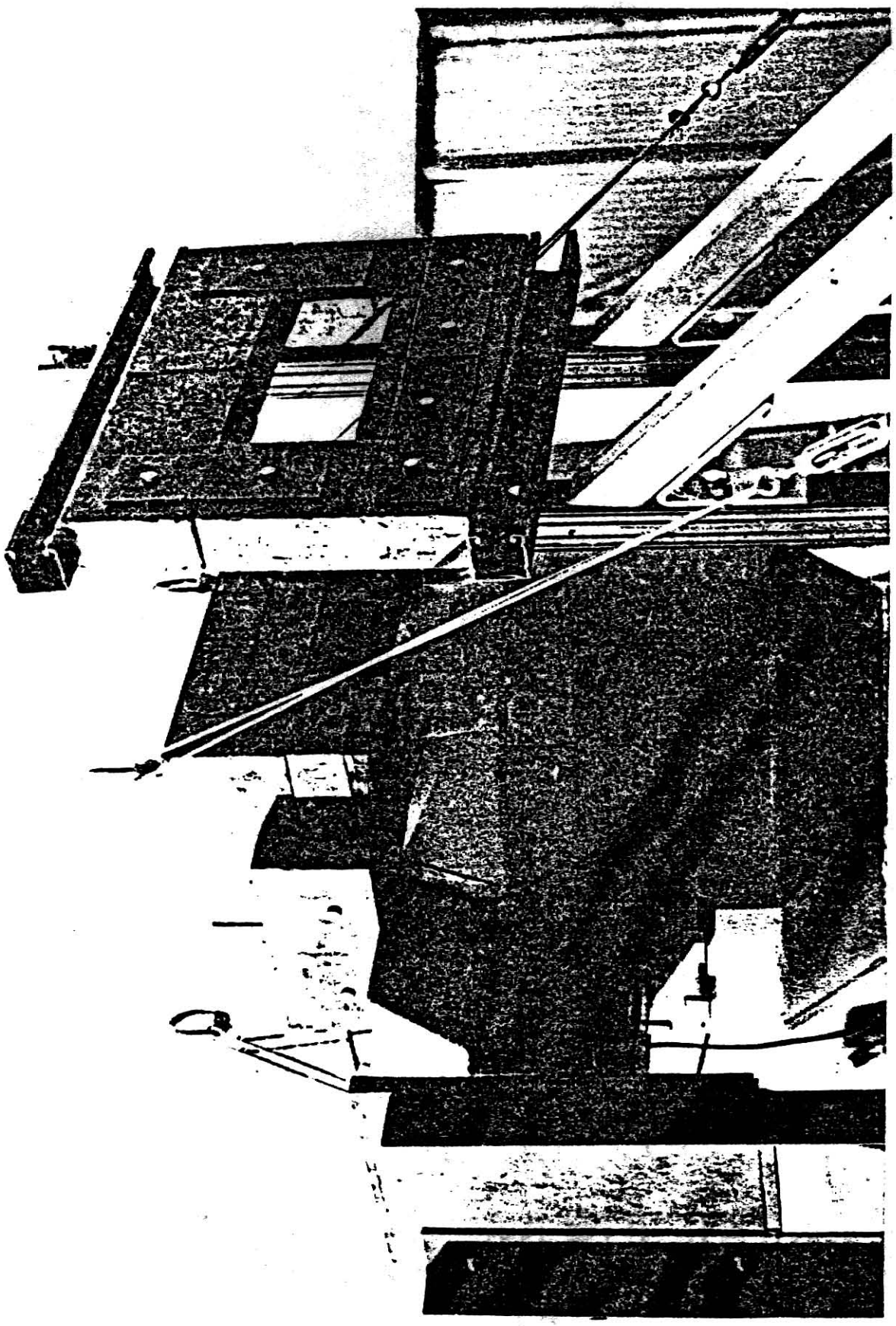

Fig. 3.12 Gamma-ray source housing, collimator, and shadow shield.

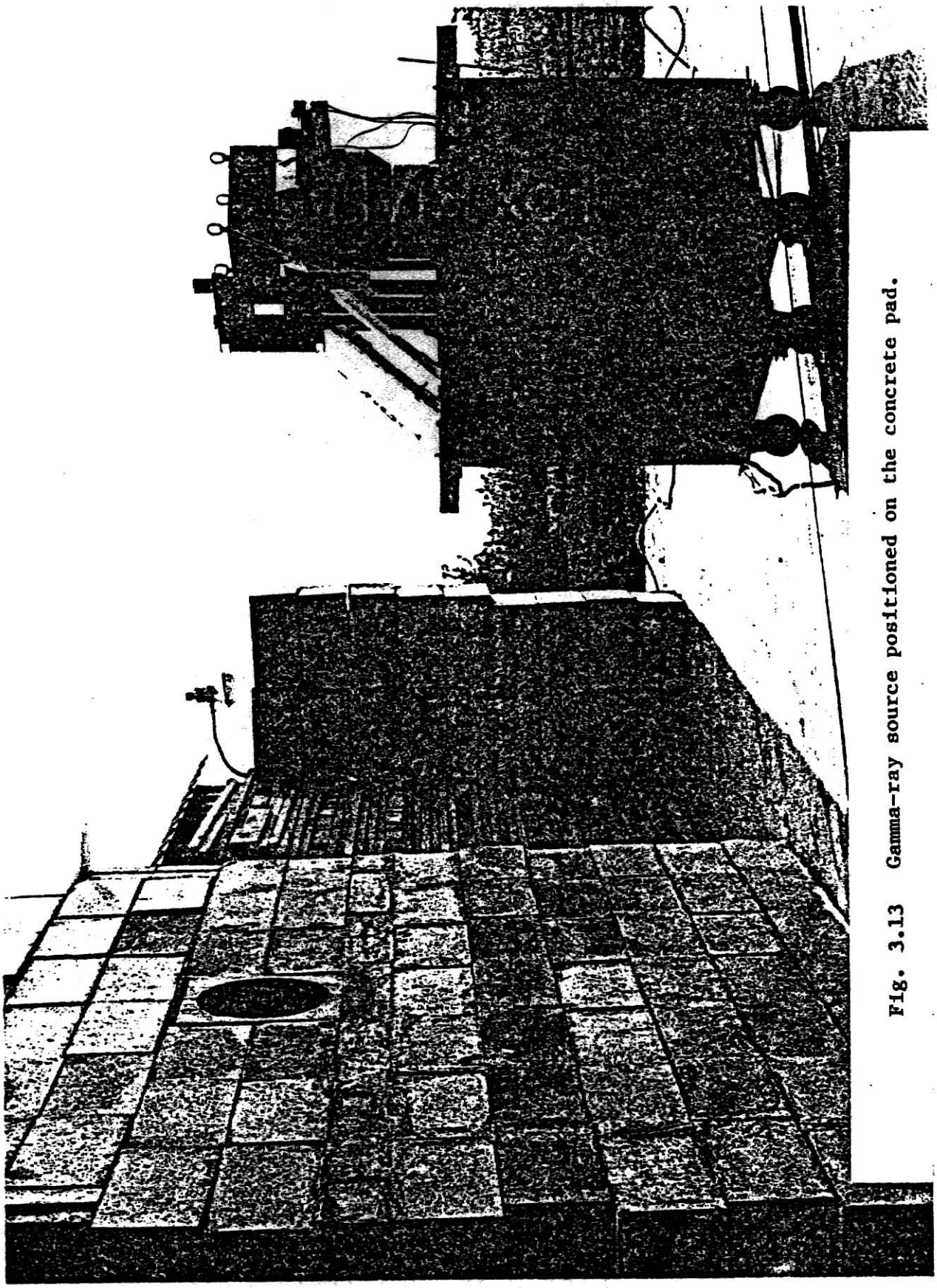

Fig. 3.13 Gamma-ray source positioned on the concrete pad.

For a given wall configuration and source position, exposure rates were measured using one of three procedures -- x traverse (along d with c and y fixed), c traverses (along c with d and y fixed), and isodose (along lines of equal dose in one c-d plane). Nearly 500 traverse and isodose exposure rate profiles were made during the experimental phase of this project. Acquisition of this large quantity of data was achievable because the ionization chamber was mounted to a remotely controlled traverse system. Moreover, the source could be rapidly moved to a new position and the time required to change duct configurations for a given wall thickness was minimized by using a small duct-block opening in the experimental wall.

In addition to the standard x and z traverses and isodose measurements performed with straight and annular ducts, two special configurations were measured. These configurations, the reflecting room and reflecting wall were performed to measure the effect of scattering within a room or from a wall respectively. Analyses of these experiments are not attempted as they are outside of the scope of the techniques presented.

One reflecting room experiment was performed to measure the duct scattered components arising directly from a bare ^{60}Co gamma-ray source and from the associated scattering sources within the room. Dimensions of the room and the experimental arrangement are provided in Figs. 3.14 and 3.15. Based upon the results of previous measurements made without the room, this study was completed using the 101.6-cm thick wall containing a 21.1-cm diameter straight circular duct. Within the constraints of the materials available, the room was nominally cubical. It was constructed adjacent to the duct-bearing shielding wall using concrete blocks and slabs as shown in Fig. 3.16. The ceiling and floor of

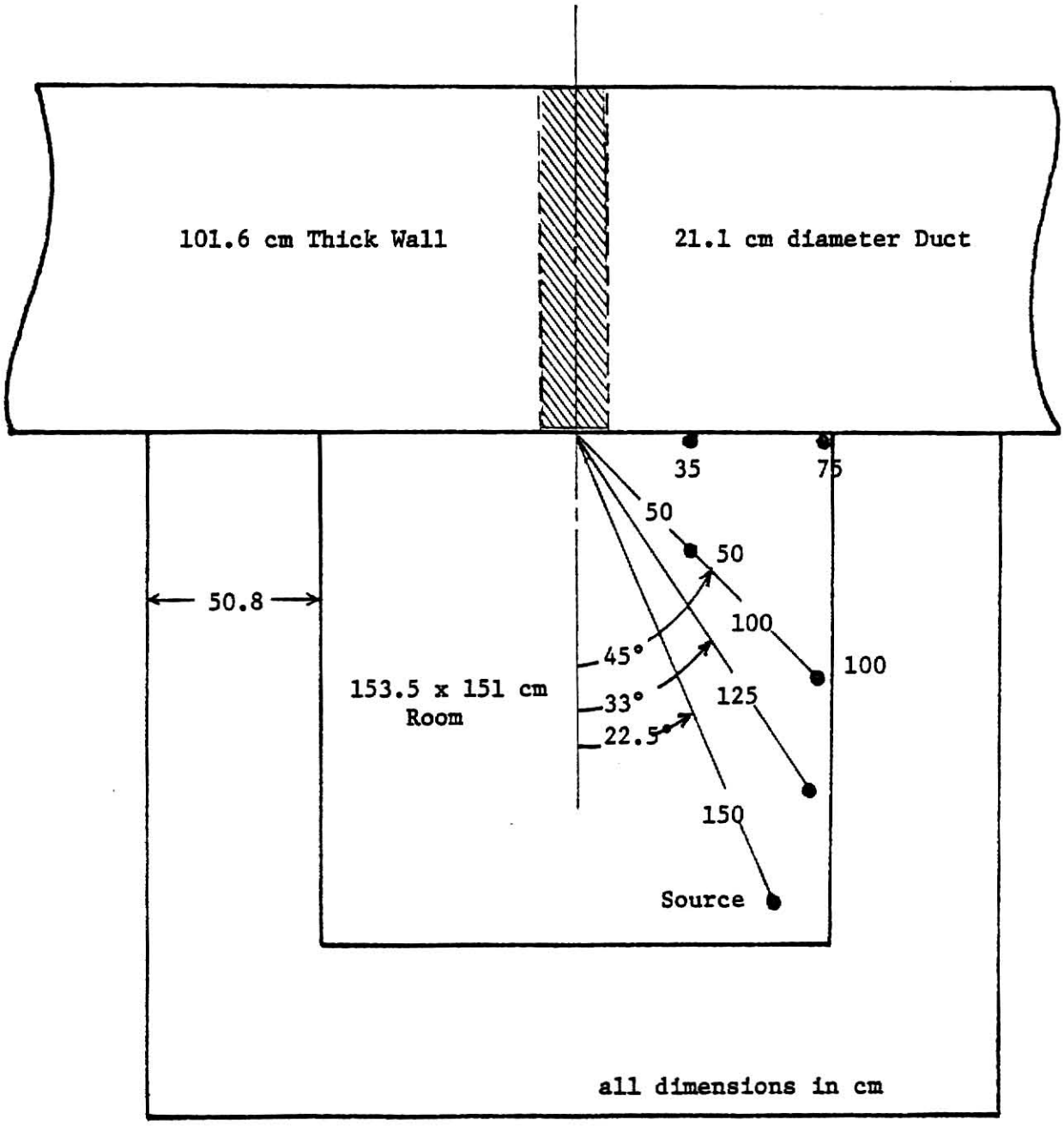

Fig. 3.14 Reflecting room configuration

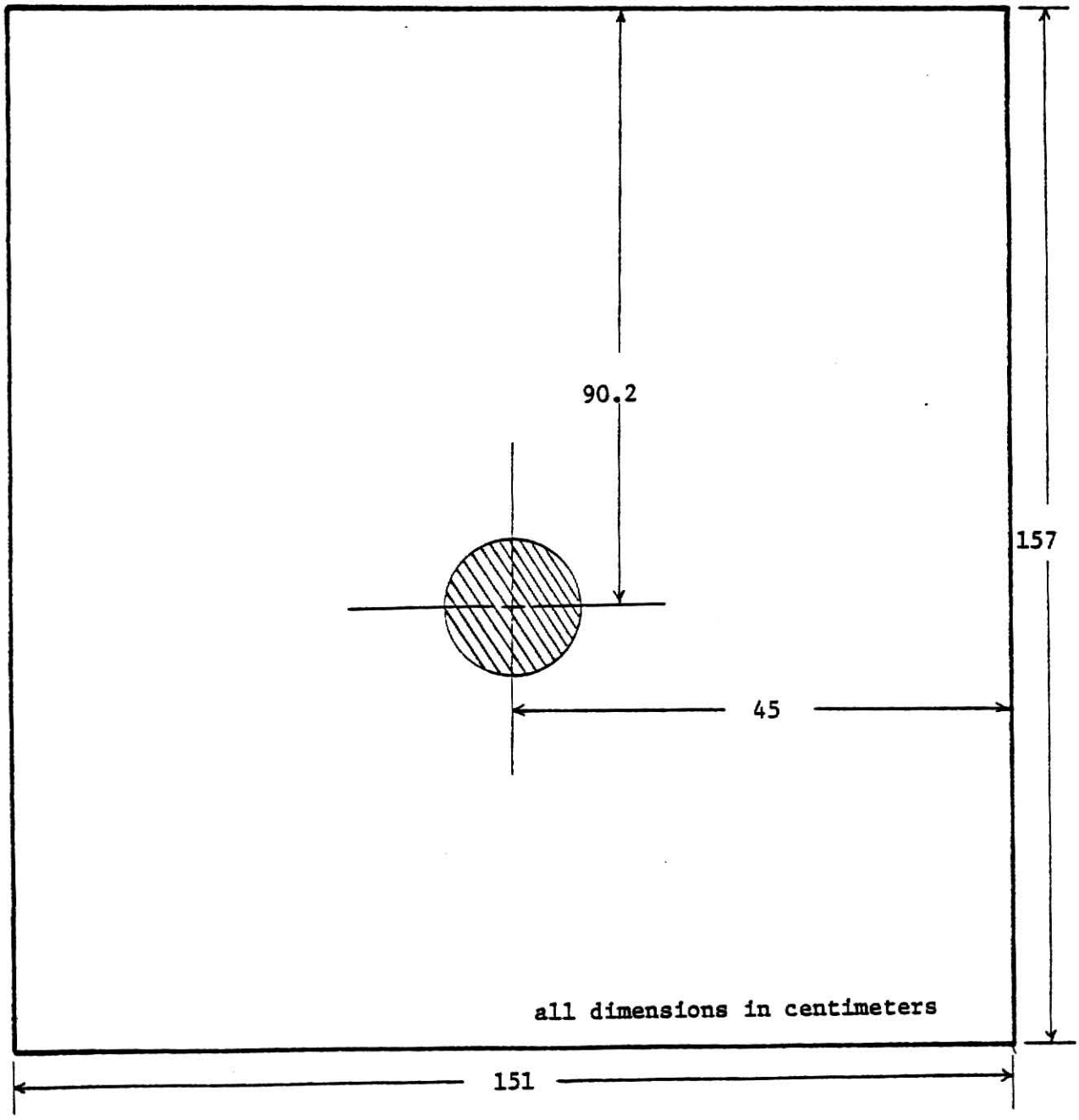

Fig. 3.15 Front view of the shielding wall area used for the reflecting room experiment.

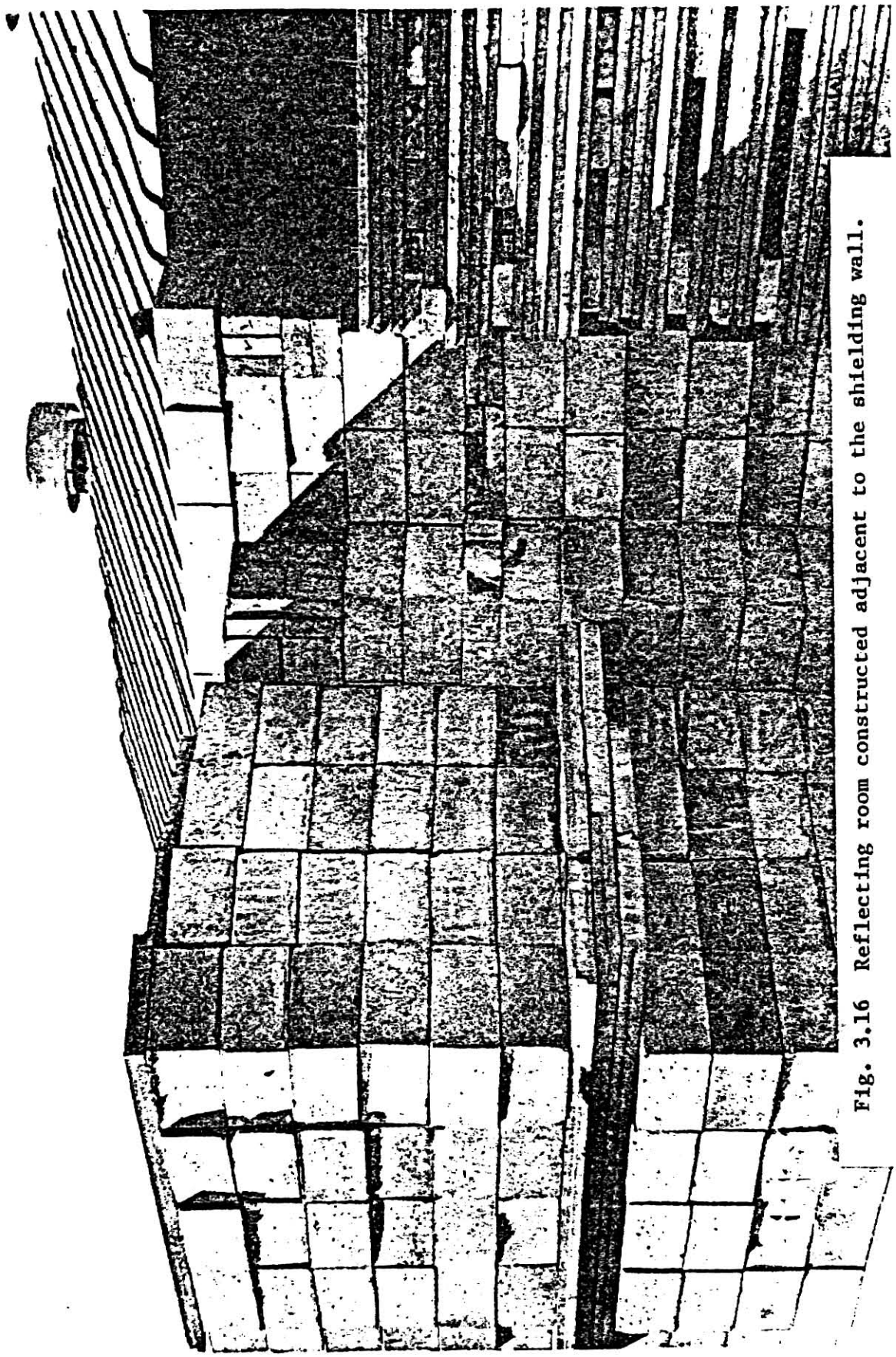

Fig. 3.16 Reflecting room constructed adjacent to the shielding wall.

the room had a minimum concrete thickness of 23 cm. Room walls were constructed from the standard 50.8-cm thick, solid-concrete, shielding-wall blocks.

The nominal 0.5-Ci ^{60}Co gamma ray projector source was used for all scattering room measurements. Its holder was attached to a mounting support such that, when the source was extended, the active volume was at the desired position within the test room. The room dimensions were established from the design constraint that the exposure rate from gamma rays scattering through the duct would be within the range of the detection system (< 500 μR/hr). Room access, for repositioning the gamma-ray source holder, was gained by removing several concrete blocks at one side of the structure.

As specified in Table 3.5, all measurements were made with the source at the duct centerline except for the single angle of 45°.

Table 3.5. Summary of Reflecting Room Measurements made using the Nominal 0.5 Ci Source and the 101.6-cm Thick Wall with a 21.1-cm Diameter Duct.

Experimental Parameters			
θ_s (degrees)	ρ (cm)	y (cm)	c (cm)
22.5[a]	150	0	150
22.5[a]	150	0	250
33[a]	125	0	150
33[a]	125	0	250
33	125	-38	150
33	125	-38	250
45	50	0	150
45	50	0	250
45[b]	100	0	150
45[b]	100	0	250
45[a]	100	0	150
45[a]	100	0	250
90	35	0	150
90	35	0	250
90	75	0	150
90	75	0	250

[a] Measurements repeated without the scattering room

[b] Source elevated 15 in above duct centerline

Measurements were also made of the duct-penetrated radiation arising from source photons first reflecting off a back wall and then streaming through the duct. This experiment was performed using the 101.6-cm thick shielding wall with a 10.3-cm diameter straight circular duct. As shown in Fig. 3.17, a 101.6 x 101.6 x 50.8-cm thick reflecting wall was positioned 457 cm from the front face and parallel to the shielding wall. The reflecting wall was centered on the axis of the open duct. These dimensions were chosen so that only the reflecting wall could be seen from the detector side of the duct wall through the duct. Thus the component of the duct penetrating radiation caused by photons streaming directly through the duct after being scattered from the reflecting wall was maximized.

The reflecting wall was constructed using the standard 50.8-cm thick solid wall blocks. It was stacked on a wooden pallet and positioned using the forklift.

Gamma rays from the nominal 10 ci ^{60}Co source provided the radiation for illiminating the reflecting wall. It was positioned 513 cm from the reflecting wall at an angle of 30 degrees. Source elevation was at the duct centerline.

Exposure rate traverse data were measured at the duct centerline elevation (y = 0) for c - 100, 150, and 250 cm. Background measurements were also made with the reflecting wall removed.

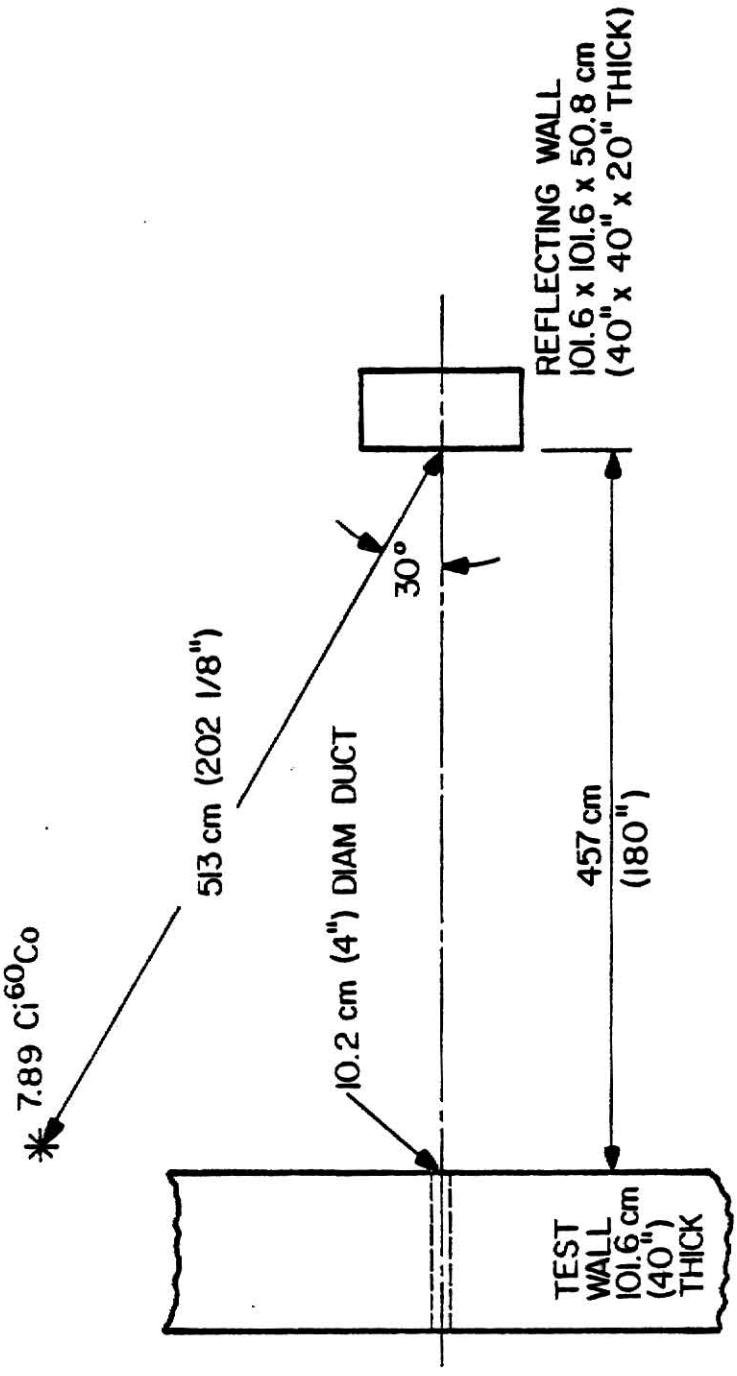

Fig. 3.17 Reflecting Wall Geometry

4.0 DISCUSSION OF INSTRUMENTATION

For this duct streaming experiment, it was anticipated that measurements would have to be made of transmitted radiation fields approaching background levels. Accordingly, a very sensitive high pressure ionization detector (HPIC) was used as the gamma photon detector in this study.

The specific detector used was a Reuter-Stokes RSS-111 Area Monitor System, serial number 1-3575, calibrated by the manufacturer on 24 March 1977. This system employs a spherical ion chamber 25.4 cm in diameter made of 0.30 cm thick stainless steel. The spherical chamber is filled with high-purity argon at a pressure of 25 atmospheres (2.5 MPa) at $0^{\circ}C$. The center electrode of the ion chamber is an aluminum sphere, 5.1 cm in diameter. The ion chamber is contained in a cubical weather housing made of 0.24 in thick type 1100 aluminum alloy. The detector response for photons between 0.3 to 2.0 MeV is relatively flat (see Fig. 4.1), and thus the energy averaged weight factor, $\overline{F}$, for these photons should be close to unity.

The HPIC system was calibrated by the manufacturer with ^{60}Co gamma rays to read directly in units of μR/h. According to AEC Health and Safety Laboratory (HASL), the presence of the aluminum protective housing should affect the detector response to gamma rays from ^{60}Co by only about 1%. With several sources calibrated by the U.S. National Bureau of Standards, the manufacturer's calibration, the approximate energy sensitivity, and directional isotropy of the HPIC detector was verified by KSU experimenters (6).

Spatial mapping of gamma-ray exposure rates, behind the duct-bearing walls, was accomplished using a detector traversing mechanism

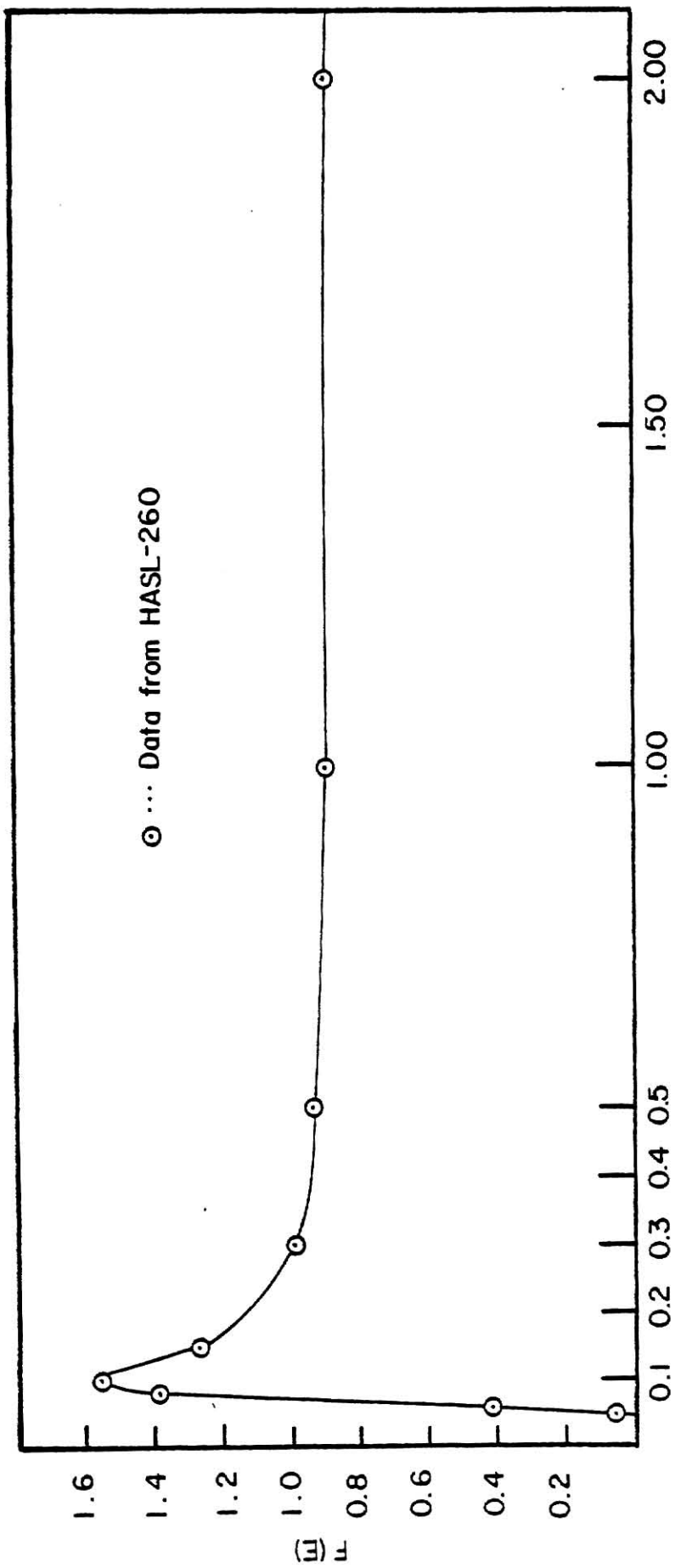

Fig. 4.1 Energy Sensitivity of the Reuter-Stokes High Pressure Ionization Chamber

designed and fabricated at Kansas State University. The traverse system was assembled inside the instrumentation building and positioned near the centerline of the duct opening. Figure 4.2 shows the traverse system which can be described as a three dimensional, rectilinear, remote controlled, motorized positioning device with nominal traversing distances of 3 x 3 m in the horizontal plane and 1 m in the vertical dimension.

The traverser consisted of a system of precision machined rods and circumferential linear bearings. Motorized drive units, attached to the horizontal plane bearings, provided the tractive force and remote control. Stationary plastic ladders were engaged by gears on the drive units to move the detector throughout the horizontal plane.

The design objective for the traverser was to arrange the rods and linear bearings in such a way as to allow the detector to be positioned at any desired point within the traverser volume. To accomplish this objective, the z dimension of the traverser was a parallel set of guide rods with two bearings on each rod (see Fig. 4.4). These bearings were mounted on the z-dimension motorized drive unit which in turn supported the detector. As shown in Fig. 4.3, the x-dimension drive unit which moved along the x-dimension guide rods had the terminations for the z-dimension rods, drive ladders, and one set of parallel linear bearings. Additionally, the x-dimension traverse assembly included a cabling assembly to assure parallel movement of each side. This arrangement provided the system with the desired horizontal plane x-z movement capability.

Once, this arrangement was chosen, the horizontal plane rods were sized for their load handling capabilities. The design constraint considered was how much the rods would deflect under load. The deflec-

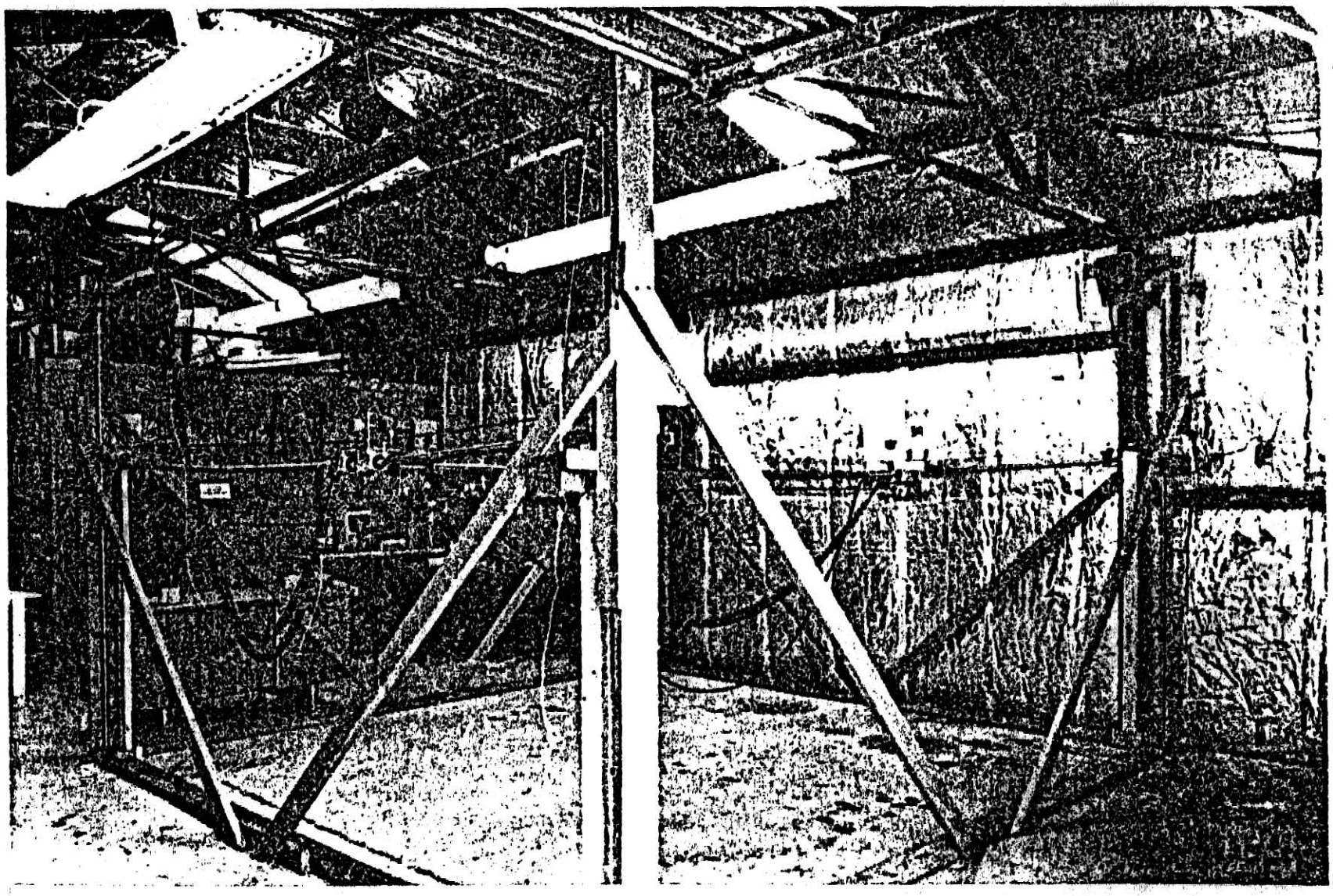

Fig. 4.2 Ion chamber traverse system located inside the instrumentation building.

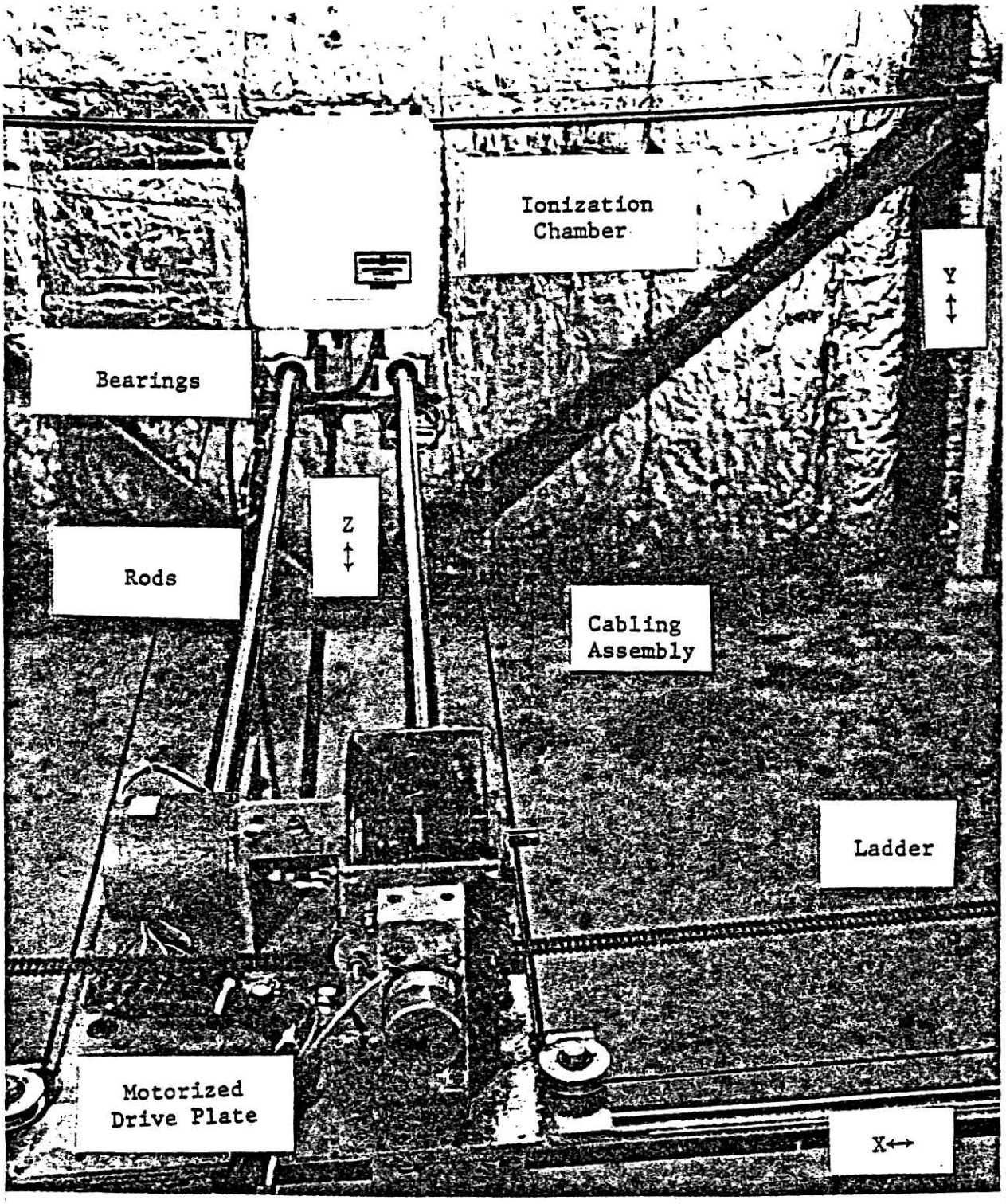

Fig. 4.3 Ion chamber mounted to the traverse system.

tion was calculated assuming that the ends of the x-traverser rods were fixed and that the load of the z-traverser dimension represented a point load at the midpoint of the x-dimension guide rod. Estimated deflection and measured deflections were in good agreement at 8.9 cm.

Vertical height adjustments of the x-z traversing assembly were made by manually sliding the counterbalanced assembly up or down on 2.54-cm diameter steel rods. Linear bearings on each x-guide rod were attached to a metal anchor plate located at each corner of the assembly. Once in position, the assembly remained stationary in the x-z plane since the corner anchor plates rested on wooden supports.

Finally, the entire system was supported by a wooden frame constructed of 2 x 4-in and 2 x 6-in lumber. This frame provided the necessary dimensional rigidity for the system. The four corner y-dimension rods were attached to the four corner uprights on the frame and pulleys were attached to the top of the uprights for the counterbalancing cables.

High quality metal guide rods and matched linear bearings were used to achieve the desired traverse motion for the ionization chamber. The x- and z-dimension traverser rods were 3.1750 $\pm$ 0.0005-cm diameter precision machined 1060 steel rods surface hardened to Rockwell 58-63 "C". Ionization chamber travel, parallel to the plane of the rods, was achieved using recirculating ball type bearings. These bearings were selected to provide the required low friction rolling load carrying capability. Static and dynamic friction in these bearing assemblies was low and decreased with wear-in. Dust seals prevented foreign matter from entering the bearings which could have damaged the precision machined surfaces. The z-dimension rod/bearing arrangement is shown in Fig. 4.4.

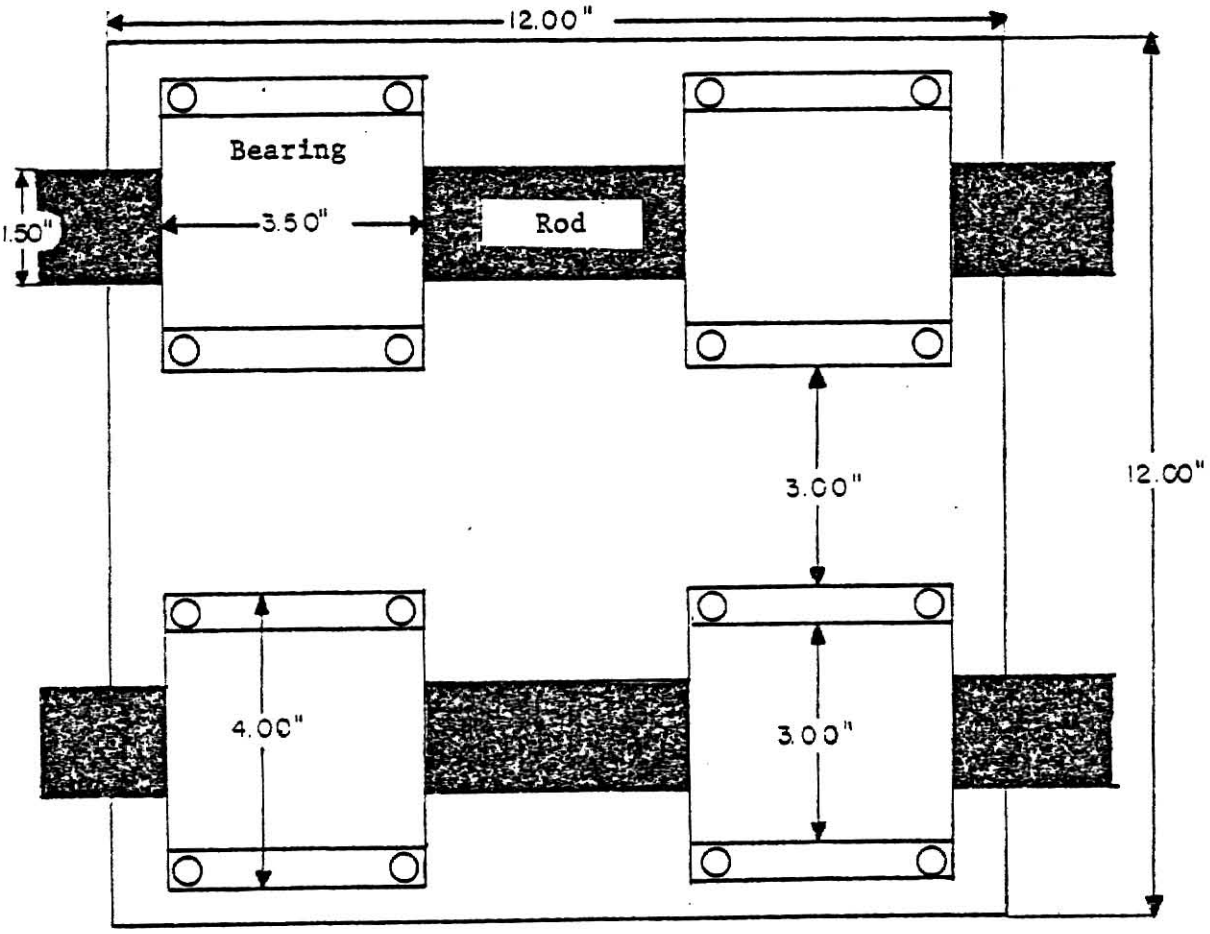

Fig. 4.4 Z traverse drive rods and bearings.

Remote control of the ionization chamber's position, within the traverse area required construction of two motorized drive units. Since the basic task performed by the x- and z-dimension drive units was the same, two similar drive units were constructed. However, bearing placement was different because the ionization chamber was mounted to the z-dimension drive unit. Photographs of the x- and z-dimension drive plates are shown in Figs. 4.5-4.7. The traverser was designed to have a maximum transit speed of 15 cm/s and a maximum scanning speed of 5 cm/s with 475 N gross linear thrust.

Several types of motors were considered for the drive system which would move the HPIC. It was clear that DC stepping motors were the best choice for this particular application. These motors can be varied in speed over a wide range, are quickly reversible, have a high stall torque, and are brushless.

A stepping motor is a DC motor with a multi-pole permanent magnet rotor and a four pole wound stator. Rotation is achieved by alternately exciting and de-exciting these four stator fields in sequence, so that the permanent magnet rotor will rotate in steps to follow the new magnetic field alignments. This characteristic gives the stepping motor a decided advantage over an AC motor in that its rotational speed can be easily varied simply by stepping the stator magnetic field at different rates. Moreover, the speed-torque characteristics of a stepping motor are such that maximum torque is achieved at zero rotor speed. This was the most desirable speed-torque characteristic for this system since with the traverser stopped, the motor had to overcome not only the inertia of the system but also the static friction within the system. Stepping motors also operate without brushes. This was an important consideration since the ionization cham-

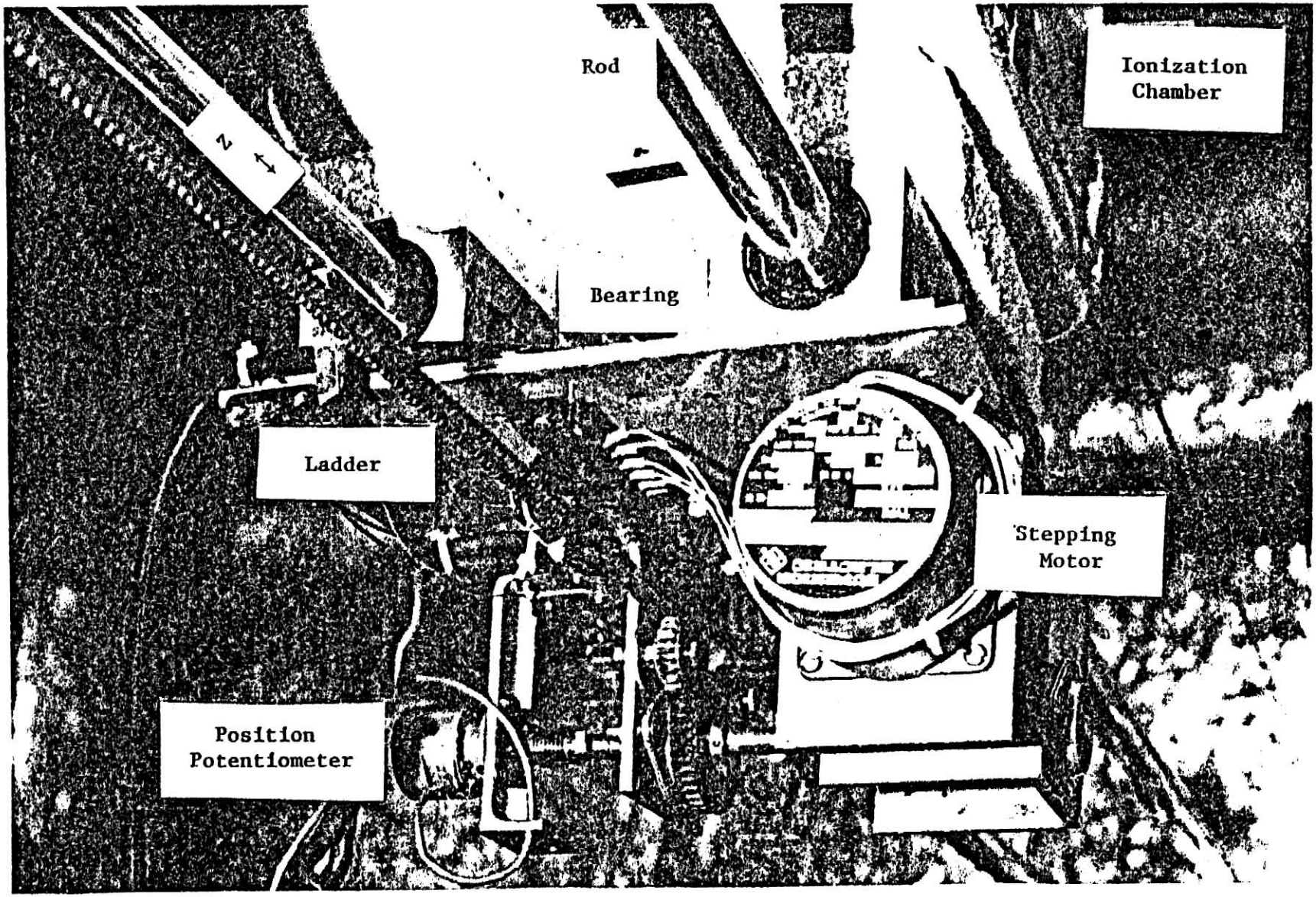

Fig. 4.5 Bottom view of z-dimension motorized drive plate and ionization chamber.

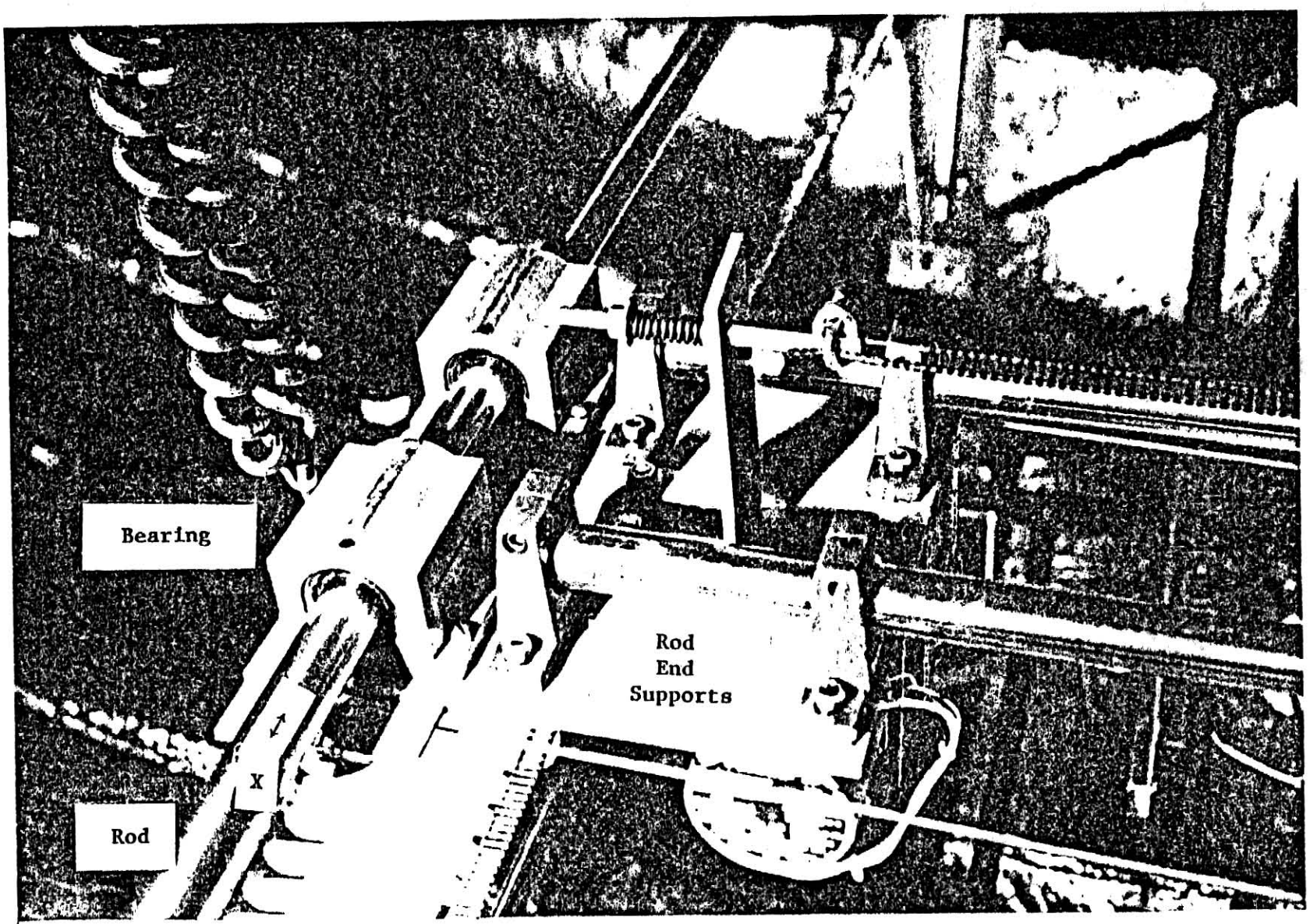

Fig. 4.6 Top view of x-dimension motorized drive plate, rods, bearings, and supports.

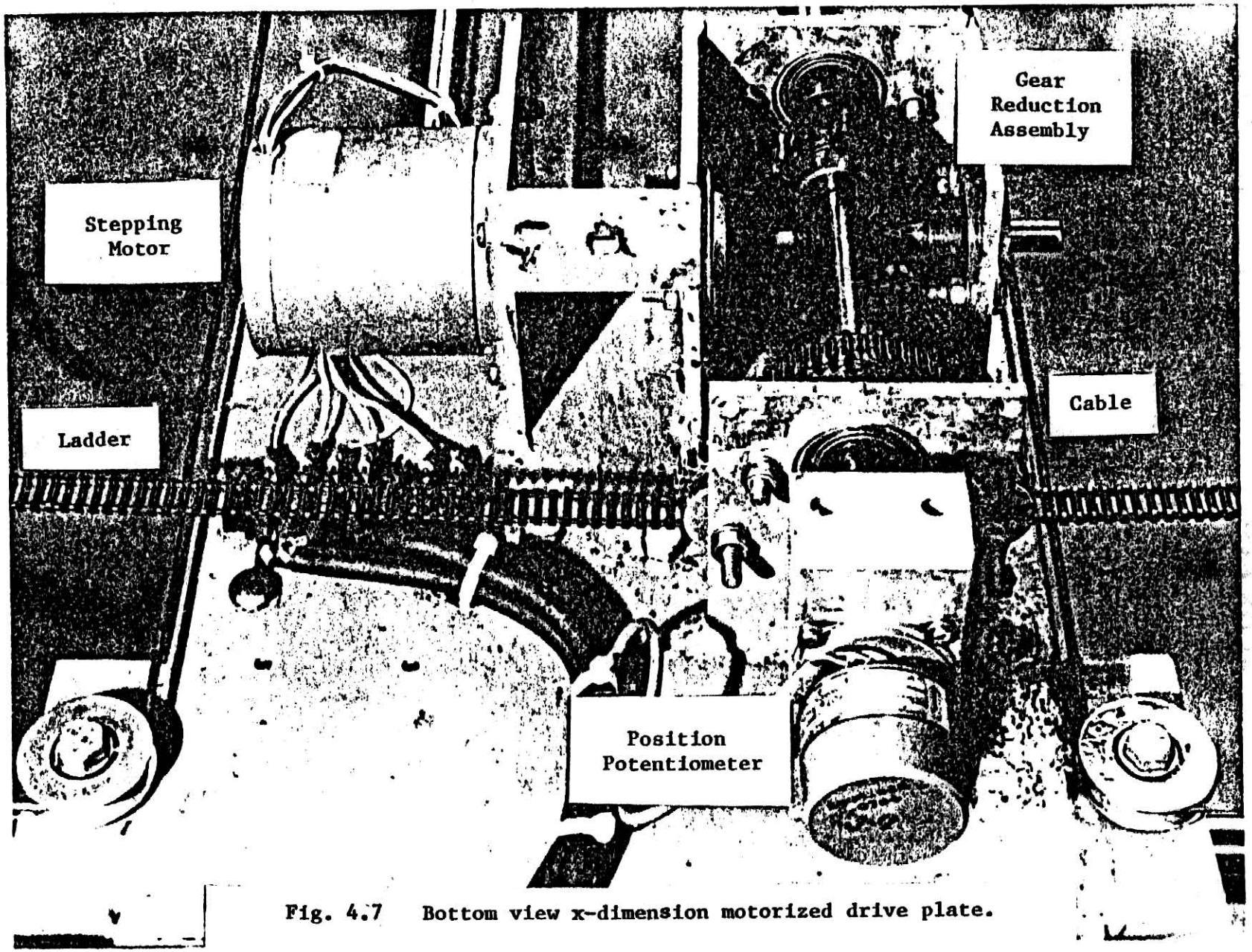

Fig. 4.7 Bottom view x-dimension motorized drive plate.

ber was mounted near the stepping motors and it was felt that the electrical noise from brushes might superimpose itself upon the ionization chamber's electronics and become an undesired source of electronic noise.

The maximum desired speed for the HPIC of 15 cm/s specified a particular reduction ratio for a reduction assembly attached to the motor drives. It was then possible to calculate the frictional losses within the system and to specify the acceleration rates (from which the inertial requirements of the drive mechanism could be estimated). From these factors, the torque required to move the system at the specified speed could be obtained. With such an analysis, a Superior Electric Model M092-FD09 motor coupled with the same manufacturer's model STM-103 translator module was chosen for the motor system.

Stepping motors require, as an integrated system, electronics to switch the stator windings in an orderly manner. A translator module and external control circuitry were designed to perform this function. The translator module purchased for this project was contained on a single prefabricated circuit board. It was used to switch the stator windings such that either a clockwise or counterclockwise rotation resulted. The traverser electronics translated all the signals from the control panel and automatic control circuitry and interfaced them to the translator module. A block diagram (Fig. 4.8) illustrates the conceptual layout of the traverser electronics.

In the manual mode, the oscillator in the translator module provided the pulse train for the stator sequencer and established acceleration and deceleration ramps to meet the operator's request for speed and direction change of the HPIC. This manual mode of operation was used to collect exposure rate data in a sequence of x traverses where

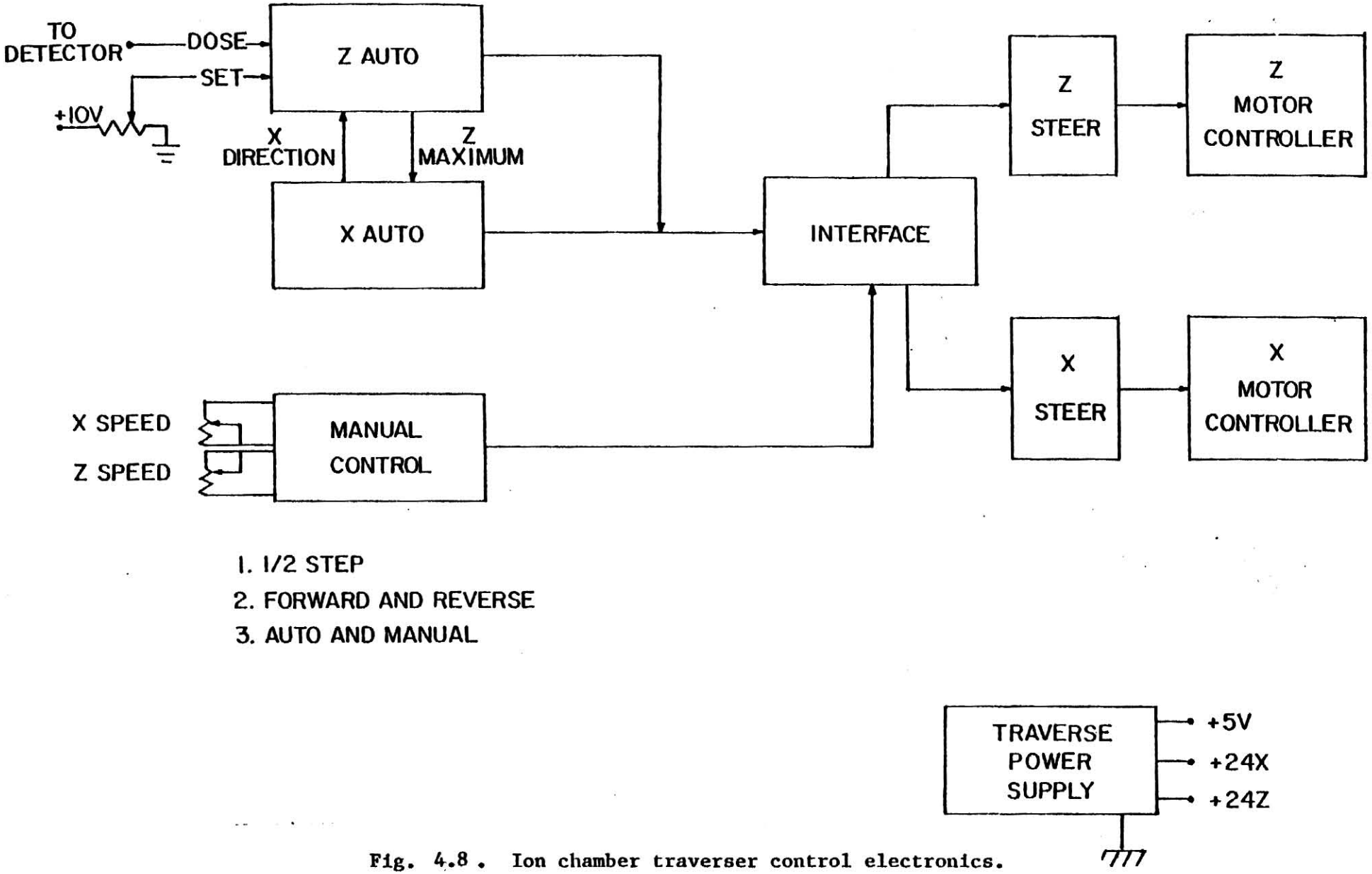

Fig. 4.8 . Ion chamber traverser control electronics.

the HPIC was moved in the x dimension at roughly 0.5 cm per second while the z and y coordinates of the HPIC were held fixed.

The interface module's function was to isolate the traverser electronics from the control system electronics. Signal isolation was important since the traverser performed high current switching in the stator sequencer, another possible noise source. Steer modules performed the actual direction selection by directing the selected pulse train to either the clockwise input or the counterclockwise input to the translator module. Traverser limit switches were also implemented in the steer module by disabling the pulse train from the translator module input for the motion of the HPIC in the direction of the activated limit switch.

The automatic mode was used to collect isodose data which provided qualitative data about the shape of the radiation field emerging from the duct. The design logic behind the isodose control system is illustrated in Fig. 4.9. To perform an isodose measurement, the isodose circuitry compared the actual exposure rate from the ion chamber to a constant set point. This comparison generated an error signal whose magnitude was used to control the speed of the HPIC in the z dimension using a voltage-to-frequency converter on the steer module. The sign of the error signal dictated the direction of motion in the z dimension. In the automatic mode, the ion chamber normally travelled at a maximum set speed in the x direction. However, when the magnitude of the error signal was very large, this x-dimension speed was linearly decreased towards zero speed. If zero speed was reached, the direction of travel in the x dimension was reversed and the speed ramped up to the maximum in the new x direction. This feature allowed the mapping of re-entrant contours.

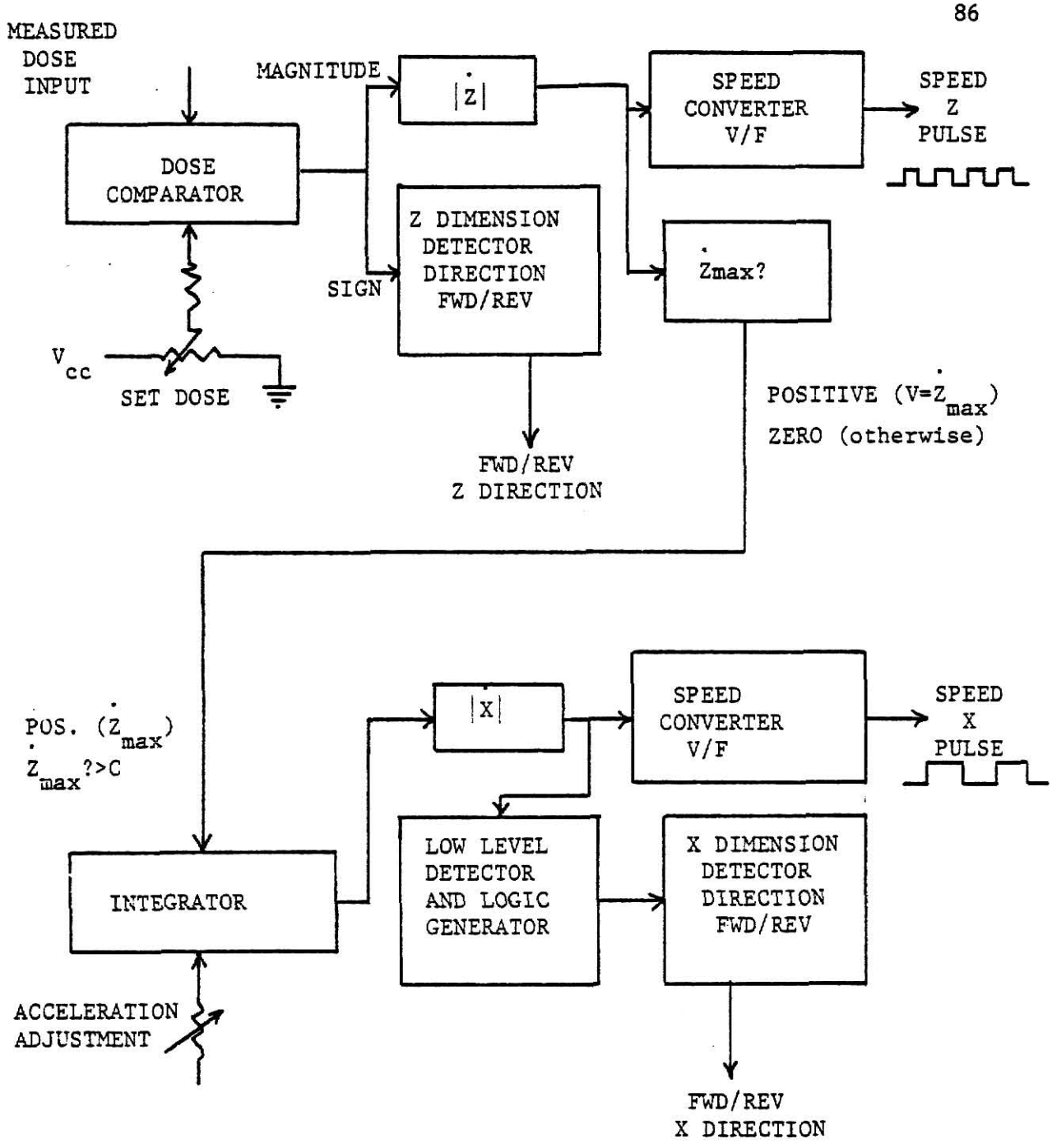

Fig. 4.9 Block diagram of X and Z contour-encoder control system

The position transmitter used in this system was a 20 turn potentiometer with 1% tolerance and 0.05% linearity. The shaft of this potentiometer was coupled directly to the shaft driving the ladder drive gear. Since the ladder drive system was linear and the potentiometer had a high linearity tolerance, the potentiometer wiper voltage was proportional to the position of the traverser throughout its span. Position reproducibility was typically 0.25 cm. Curve fits and linearity checks are presented in Figs. 4.10 and 4.11. Voltage across the position potentiometers was provided by a dedicated precision voltage source with full thermal compensation.

Each stepping motor was coupled to a reduction assembly through a flexible coupling. This coupling allowed for small alignment errors between the motor and the reduction assembly (see Fig. 4.12). The reduction assembly consisted of a 20:1 worm-gear reduction set supported by radial ball bearings with appropriate thrust loading capabilities. These gears were mounted on a 1.27-cm mild steel shaft with set screws. Fastened to the reduction shaft were the drive gear for the ladders and the position transmitter shaft. The reduction assemblies were fabricated at Kansas State University using 0.635-in aluminum plate in a welded construction to achieve maximum rigidity. Aluminum was chosen for its light weight, ease of machining, and availability. Limit switches were mounted on the base plate of the reduction assembly to assure that the HPIC did not exceed the system's physical travel limits.

It was important that the drive system for the traverser be linear, strong, and provide reproducibility. This objective was achieved, in this application, by using Winfred M. Berg type 16GCF stainless steel cable reinforced plastic ladders. Each ladder was mated with specially

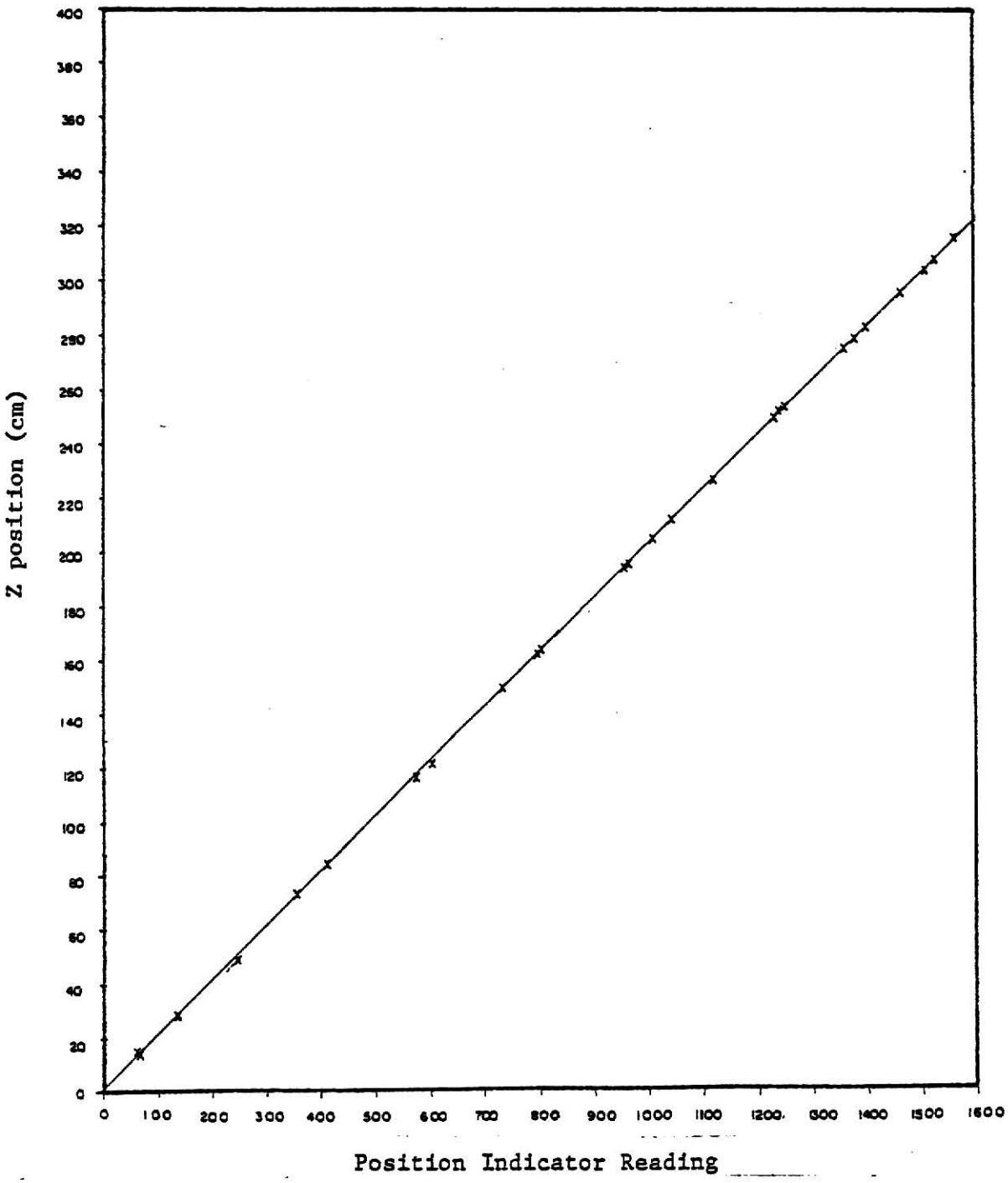

Fig. 4.10 Linear relationship between the Z dimension position indicator reading (arbitrary units) and the actual ion chamber position.

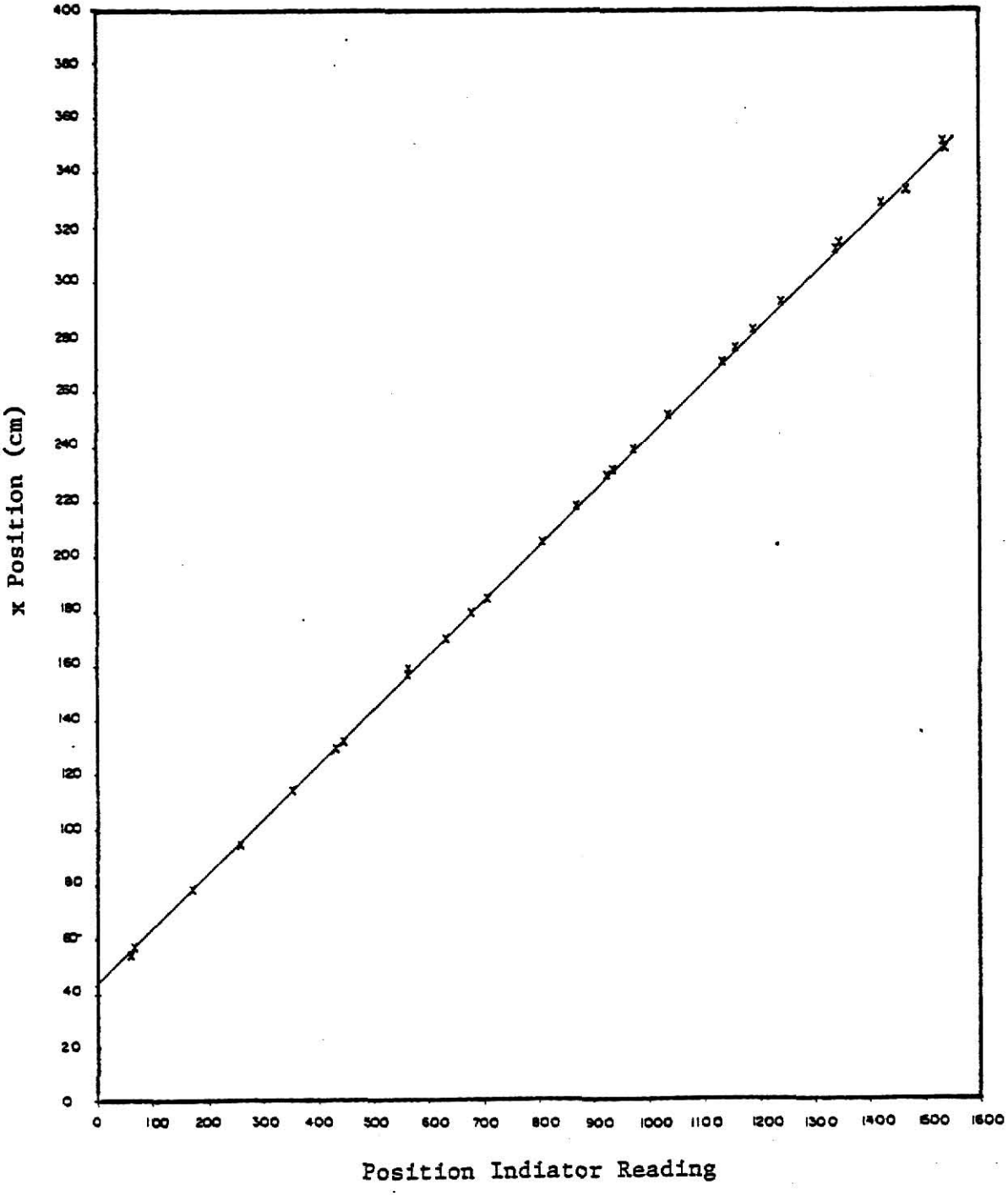

Fig. 4.11 Linear relationship between the x dimension position indicator reading (arbitrary units) and the actual ion chamber position.

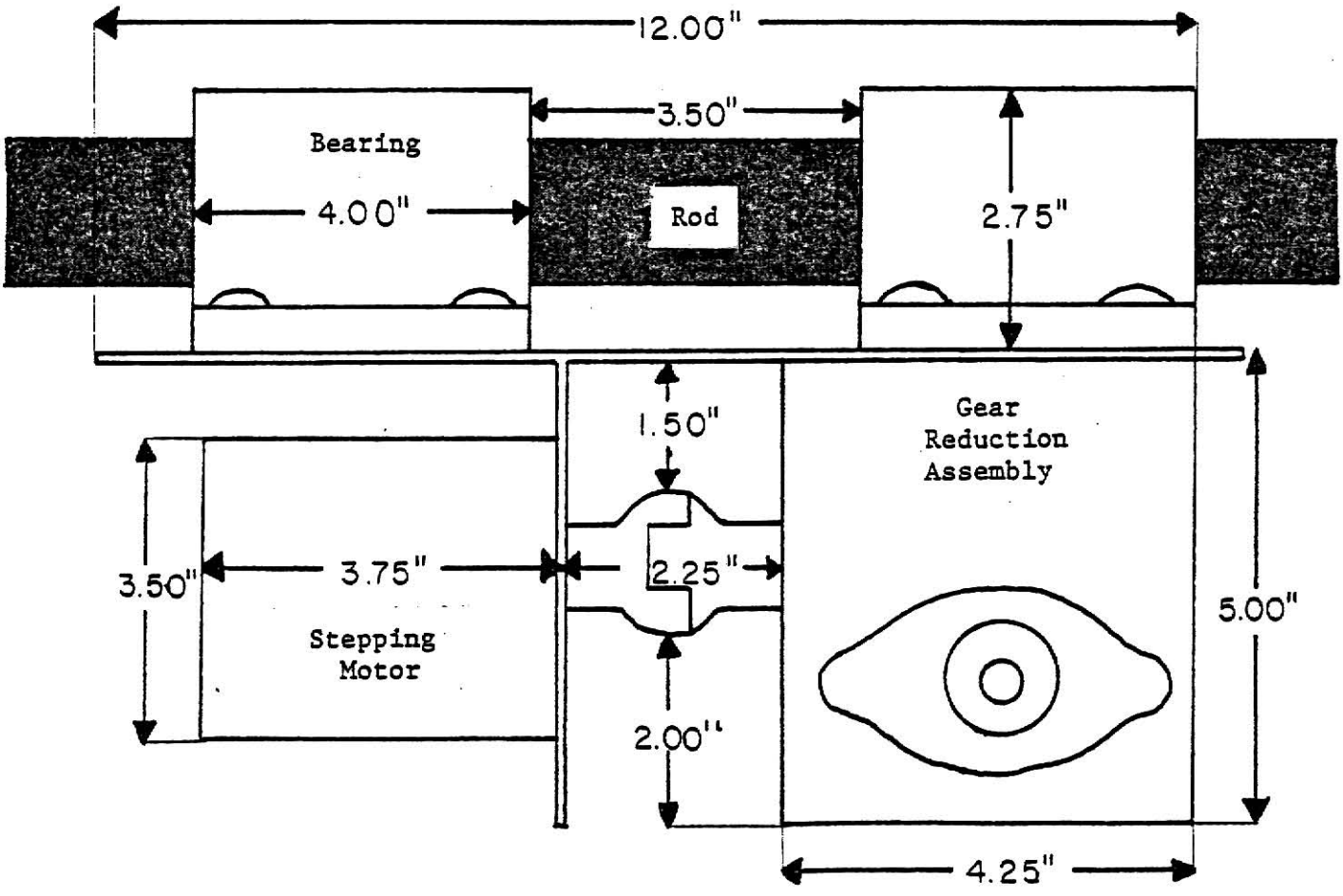

Fig. 4.12 Side view of traverse drive assembly.

machined spur gears which were mounted on the reduction output shaft. Idler gears were used to insure that the drive ladders completely engaged the driving gear throughout its rotation. The drive ladders were attached to spring loaded terminations at the end of the guide rods. These drive ladders performed admirably and are in a large part responsible for position reproducibility that exceeded the design criterion.

Exposure rate and ionization chamber position data were accumulated using a data collection system designed and constructed by members of the Nuclear Engineering Department at Kansas State University. This system, shown in Fig. 4.13, was situated in the instrument room of the facility's instrumentation building. The analog output of the high pressure ionization chamber's electrometer was channeled to the input of this system and to the x-y recorder. Detector position signals were fed directly to the data acquisition system from the detector traverse instrumentation.

Operational mode (traverse or isodose), detector movement, and data collection were all controlled by an operator from the system console. As is shown in Fig. 4.14, the console contained two basic sections--detector positioning and data acquisition. In the manual operation mode, the upper 3½ digit LED panel could be made to display (by proper selection of the "address" switches) one of the following experimental data: the x, y, or z position of the HPIC, a number proportional to the exposure rate, or a configuration identification number. The single digit LED "address" panel at the top of the console indicates which of these experimental data is being displayed. The value related to the exposure rate measured by the HPIC is continually displayed on the lower 3½ digit LED panel.

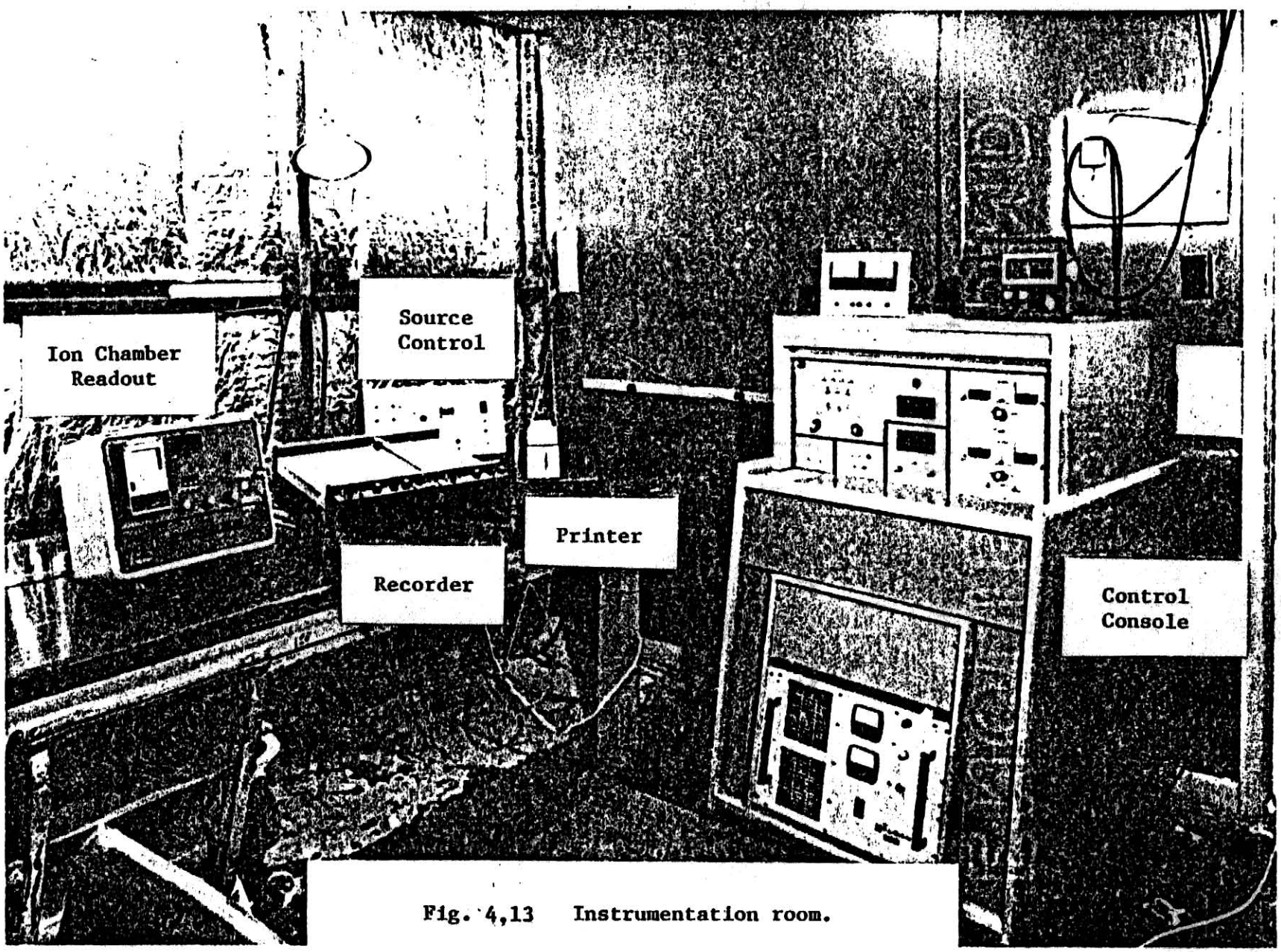

Fig. 4,13 Instrumentation room.

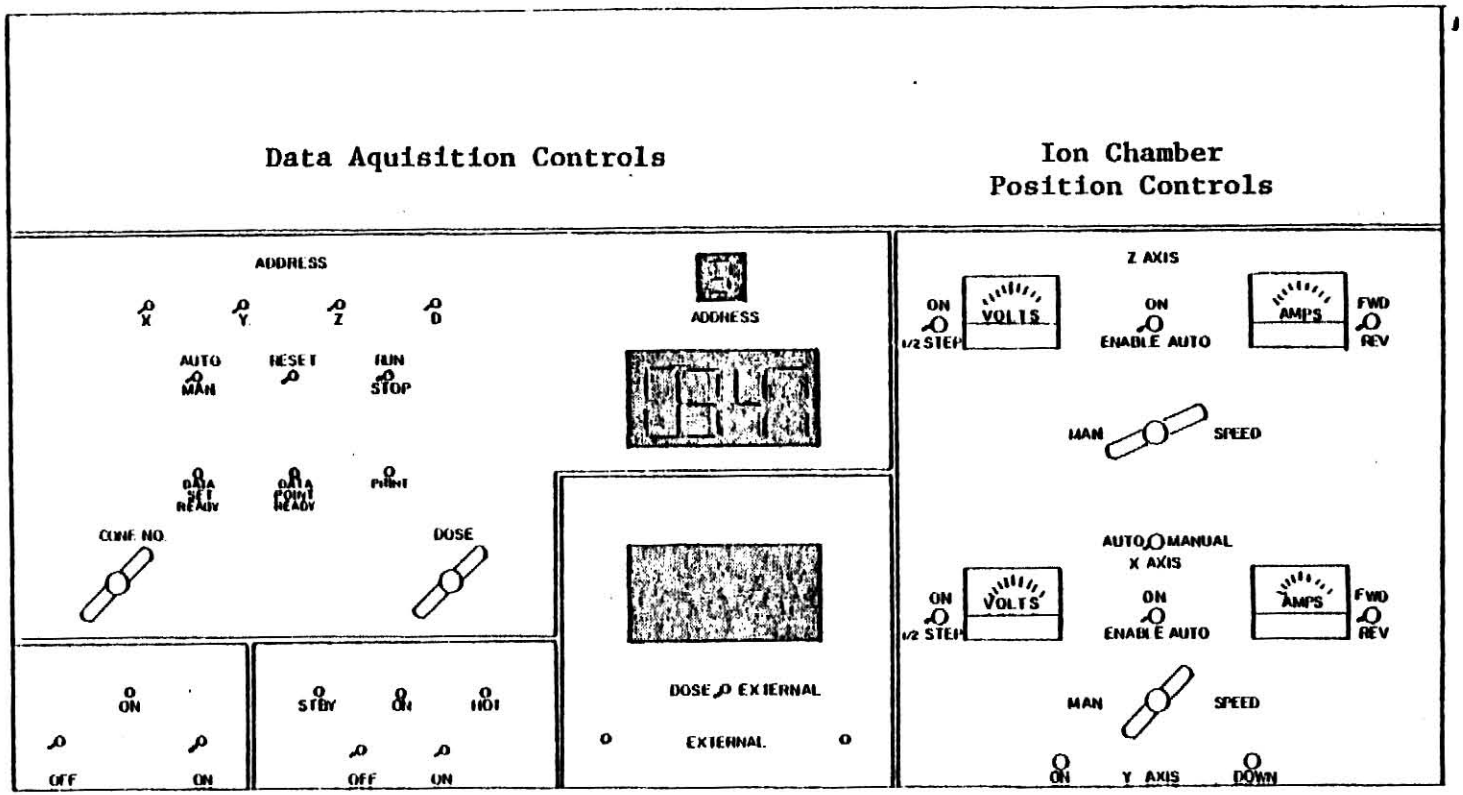

Fig. 4.14 Front panel of control console (see Fig. 4.13)

Input to the consol was data in the form of analog signals. Each of these analog signals were "frozen" at the same time by sample and hold modules. This feature removed any uncertainty in the time dependency of the individual values for x, y, z, and exposure rate contained in a given data set when the system was functioning in the automatic traverse mode. As is indicated in the data acquisition system block diagram, Fig. 4.15, these "frozen" analog signals were applied to an analog multiplexer (MUX) and the proper signal directed to the digital panel meter (DPM) according to the address signal supplied from the address generator. The multiplexer output was then converted to digital information in the DPM and printed. To uniquely identify the printed quantity, the leading digit was the address for that particular device. Address identification used was: 0 = configuration identification number; 1 = exposure rate; 2 = x position; 3 = z position; and 4 = y position.

The numerical values printed were only proportional to the actual physical values since the analog voltage signals were scaled to achieve a voltage range of 0 to 10 V. This scale was chosen to be compatible with the output level from the high pressure ionization chamber's electrometer. Input scaling of the DPM was simplified by using a common scaling network for all of the signals used at the output of the MUX. It should be mentioned that this was a very stable system and required only minor adjustments throughout the course of the project. Adjustments, when required, were made during the daily checkout of the system.

Several measures were taken to assure system stability. All power supplies were precision regulated and temperature compensated. The AC line input to the instrumentation system power supply was filtered, regulated, and conditioned. Additionally, the AC line to the instru-

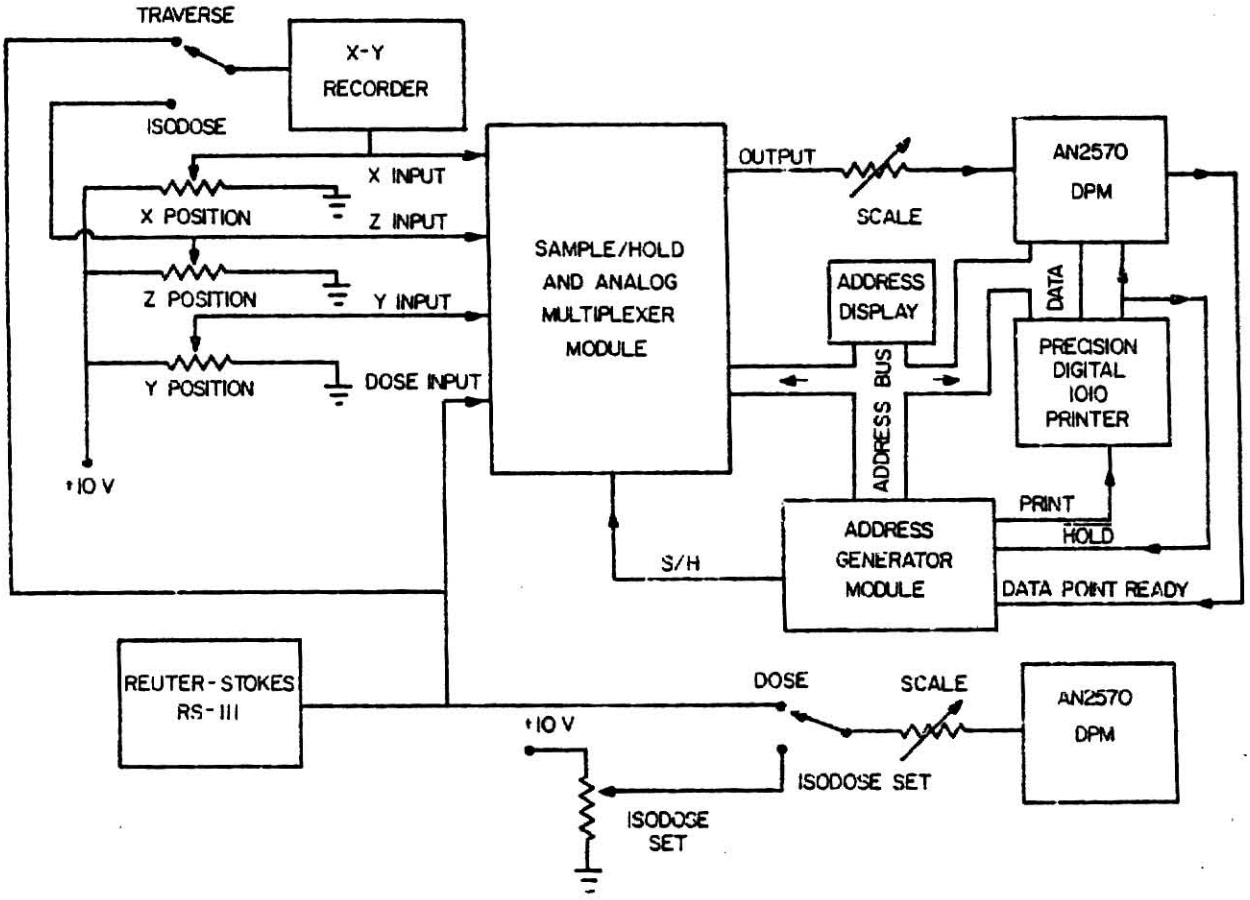

Fig. 4.15 Block diagram of data acquisition system. This portion of the system is driven by the address module through the S/H and address outputs.

ments was so designed that, in the event of a power surge, the system would shut down.

Data were displayed and converted using two Analogic AN2570 digital panel instruments (DPM). This 7 segment LED display unit operated with a full scale input range of $\pm$ 1.999 V giving a bipolar 3 digit ($\pm$ 1999) display. The printed output was derived from the latched BCD circuit (option added to the AN2570). An analog-to-digital converter (A/D), within this instrument was logically tied to the display through a binary coded decimal latched data bus. The A/D conversion was of the dual slope integrating type.

Digital logic control for the data acquisition system was provided by the address generator module. This module generated the address and sample/hold signals for the sample/hold module and synchronized the printer with the panel displays (AN2570 DPM). Two modes of address selection were provided. Manually selected data channels could be displayed and printed or all data channels could be displayed and printed sequentially. In the manual mode, the sample line was held in the sample state so that the selected data value could be obtained in real time. For automatic mode operation, the address generator supplied the sample command at the beginning of each data scan to hold the data at one point in time. As the system sequenced through the addresses, it provided a AN2570 DPM settling delay before issuing the print command. This delay was adjusted such that the AN2570 DPM usually completed 2 to 3 conversions on each data point. Thus it was assured that converted data were valid.

A Precision Digital Model 1010 data collector provided the desired hard copy printout of the information generated by the AN2570 digital panel meter. Data printing involved supplying the print command signal from the address generator and transmitting the BCD and hold-reading signals from the AN2570 DPM to the 1010 printer.

5.0 EXPERIMENTAL RESULTS

Presented in this chapter are: 1) the methods used to "reduce" or process the raw data into a consistent form, 2) samples of raw and reduced data for selected cases, and 3) analysis of experimental error.

The coordinate system identifying source and detector locations and angles of incidence is depicted in Fig. 5.1. Notation is as follows:

- S - source strength (Ci) effective June 1, 1979,
- t - time between date of measurement and June 1, 1979, i.e., decay time for source strength corrections,
- ρ - distance from source to center of duct at the entrance plane,
- θ - angle of incidence, measured between duct axis and ρ-axis,
- c - horizontal distance from detector to the duct exit plane,
- d - horizontal distance from the detector to the duct axis,
- y - vertical distance from detector to the duct axis,
- x,z - position potentiometer readings for the d and c distances, respectively,
- E - exposure rate instrument reading,
- $\dot{X}$ - exposure rate (μR/h).

Distances c and d are related to x and z by the formulas

$$c(cm) = 100 + (z - z_0)/4.956,$$

$$d(cm) = (x - 808.5)/4.919,$$

where z_0 is the potenticmeter reading at the reference (c = 100 cm) position; usually z_0 = 74 to 76. The quantities $\dot{X}$ and E are related by the formula

$$\dot{X} = 0.25\ (E - E_0),$$

where E_0 is a bias reading; usually E_0 = 8 to 10.

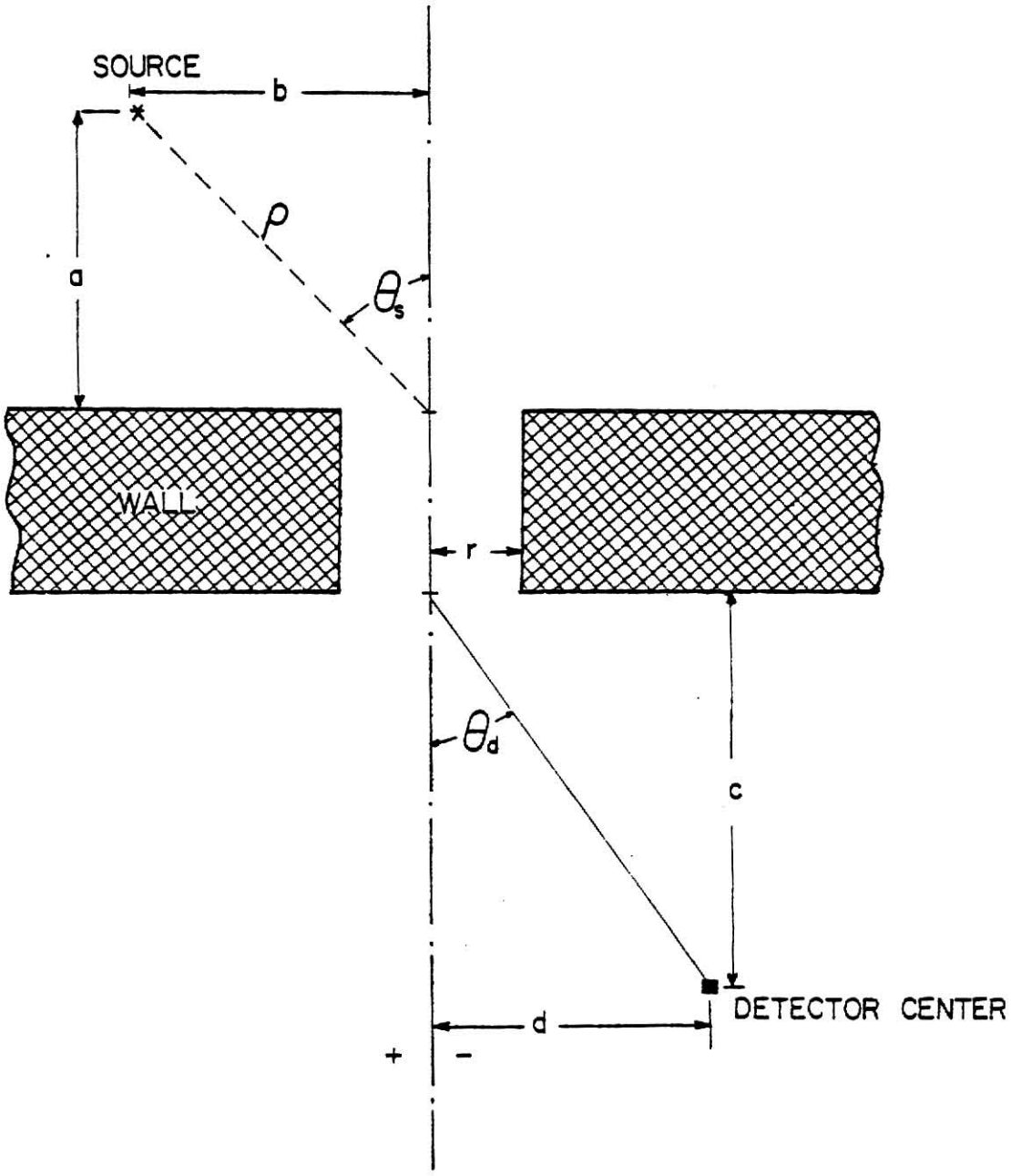

Fig. 5.1 Benchmark gamma-ray streaming geometry.

Reduced data are presented in the form $\rho^2\dot{X}/S$ ($m^2\mu R/Cih$), i.e., net exposure rates normalized to unit source strength and multiplied by ρ^2 to account for the inverse-square geometrical attenuation between source and duct entrance. The data are corrected for the background, or solid-wall, exposure rates, thus eliminating the effects of gamma rays scattered over or around the test wall.

A sample set of raw digital data, for the 100 cm thick wall with a 20 cm diameter duct, is presented in Table 5.1. Corresponding raw background data are presented in Table 5.2. The corresponding reduced data are presented in Table 5.3 and plotted in Figs. 5.2 to 5.5.

Table 5.1. Selected raw digital experimental x-z traverse data for the 100-cm thick wall using the ^{60}Co source of nominal strength 10 Ci. Data reported are values of E, the exposure-rate instrument readings.

Duct diam. (cm)	20	20	20	20	20	20	20	10	40	40/28*
θ (deg)	60	45	45	45	33	33	33	45	45	45
ρ (cm)	300	300	300	300	300	300	300	300	400	300
y (cm)	0	0	0	0	0	-38	-76	0	0	0
z	322	76	322	817	322	322	322	322	322	322
ID. No.	785	765	770	775	755	675	665	445	1355	1780
Date	12 Jul	12 Jul	12 Jul	12 Jul	12 Jul	12 Jul	12 Jul	18 Jul	19 Jul	23 Jul
x										
1545	195	147	168	171	148	149	143	157	301	167
1500	196	140	152	162	149	149	145	144	335	161
1400	197	151	134	162	153	149	140	135	467	166
1300	188	134	153	174	168	156	135	132	712	179
1200	172	142	166	223	224	179	142	128	1049	236
1100	182	172	238	310	433	237	147	132	1273	395
1000	285	444	502	326	962	386	153	160	1358	557
900	307	897	556	290	1054	583	166	202	1376	641
800	298	897	500	264	888	602	173	202	1344	777
700	331	958	570	298	917	524	175	142	1211	687
600	307	421	509	351	858	334	171	146	1336	616
500	186	195	236	327	369	243	167	152	1529	495
400	182	163	186	220	260	212	164	161	1339	301
300	189	160	178	187	334	208	174	161	756	229
200	203	169	179	180	325	210	185	191	467	221
100	217	175	191	186	283	211	195	193	485	214
76	225	179	196	186	271	214	197	-	470	217

*Annulus, 40 cm OD, 28 cm ID.

Table 5.2. Selected background (solid wall) digital experimental x-z traverse data for the 100-cm thick wall using the ^{60}Co source of nominal strength 10 Ci. Data reported are values of E, the exposure-rate instrument readings.

θ (deg)	60	45	45	45	45	33	33	33
ρ (cm)	300	300	300	400	300	300	300	300
y (cm)	0	0	0	0	0	0	-38	-76
z	322	76	322	322	817	322	322	322
ID No.	735	860	855	870	850	840	978	990
Date	9 Jul	10 Jul	10 Jul	10 Jul	10 Jul	10 Jul	10 Jul	11 Jul
x								
1545	193	156	165	176	170	133	139	140
1500	195	146	157	172	160	135	141	136
1400	200	142	149	167	147	129	134	130
1300	179	129	146	155	148	129	124	122
1200	164	121	137	152	148	128	129	116
1100	157	121	132	152	149	125	121	113
1000	153	122	136	150	147	134	122	113
900	149	121	136	153	146	131	125	112
800	157	121	138	153	145	133	125	117
700	154	125	140	159	148	134	129	121
600	161	131	143	165	158	140	139	129
500	169	132	146	169	164	145	142	131
400	178	143	161	180	153	151	152	141
300	189	154	173	195	173	165	168	148
200	204	166	187	207	182	180	180	167
100	222	183	202	226	192	197	194	175
76	221	187	206	237	190	198	195	182

Table 5.3. Reduced x-z traverse for the 100-cm thick wall using the ^{60}Co source of nominal strength 10 Ci.

Data reported are values of $\rho^2\dot{X}/S$ in units of $m^2\mu R/Cih$.

Duct Dia. (cm)	20	20	20	20	20	20	20	10	40	40/28*
θ (deg)	60	45	45	45	33	33	33	45	45	45
ρ (cm)	300	300	300	300	300	300	300	300	400	300
y (cm)	0	0	0	0	0	-38	-76	0	0	0
c (cm)	150	100	150	250	150	150	150	150	150	150
d (cm)										
120	-	-	-	-	6.7	4.2	2.8	-	150.4	4.8
100	2.5	1.4	-	7.3	11.0	9.0	3.7	-	279.4	9.3
80	2.3	5.9	-	21.1	27.0	14.1	7.3	-	450.0	28.3
59	7.0	14.4	29.8	45.3	86.7	32.7	9.6	0.0	562.3	74.3
39	37.2	90.6	103.0	50.4	233.1	74.3	11.3	6.8	606.0	119.0
19	44.5	218.4	118.2	40.5	260.0	128.9	15.2	18.6	613.5	142.7
-2	39.7	218.4	101.9	33.5	212.5	134.3	15.8	18.1	597.4	180.6
-22	49.8	235.5	121.0	42.2	220.4	111.2	15.2	0.6	527.8	154.4
-42	41.1	81.6	103.0	54.3	202.1	54.9	11.8	-	538.4	133.7
-63	4.8	17.7	25.3	45.9	64.1	28.4	10.1	-	537.4	98.6
-83	1.1	5.6	7.0	16.0	30.7	16.9	6.5	-	581.4	39.6
-103	-	1.7	1.4	3.9	-	11.3	7.3	-	281.4	15.8

*Annulus, 40 cm OD, 28 cm ID.

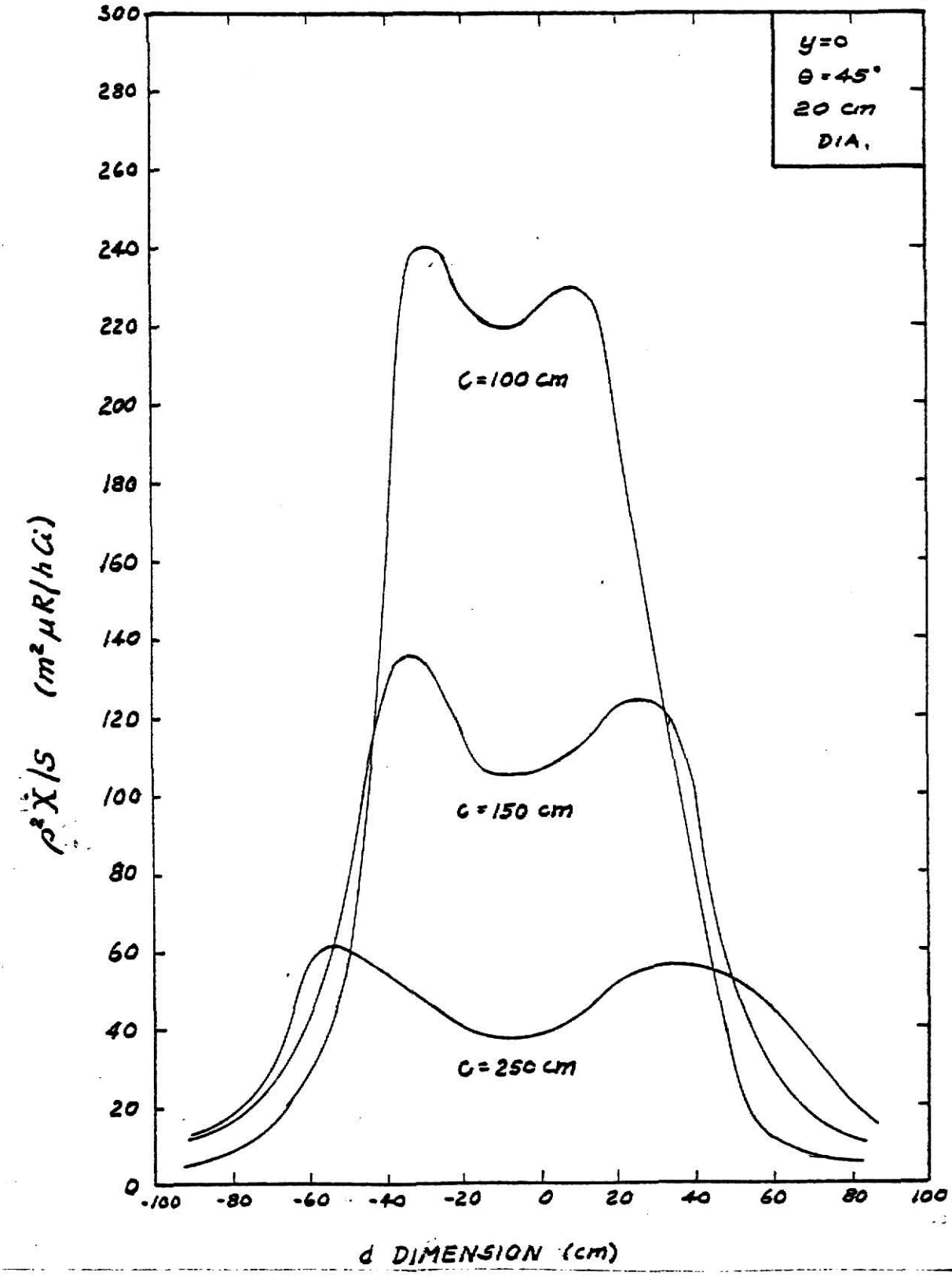

Fig. 5.2 Normalized exposure rate as a function of c and d for the 100-cm thick wall with a 20-cm diameter duct. Measured at a 45° angle of incidence, with y = 0.

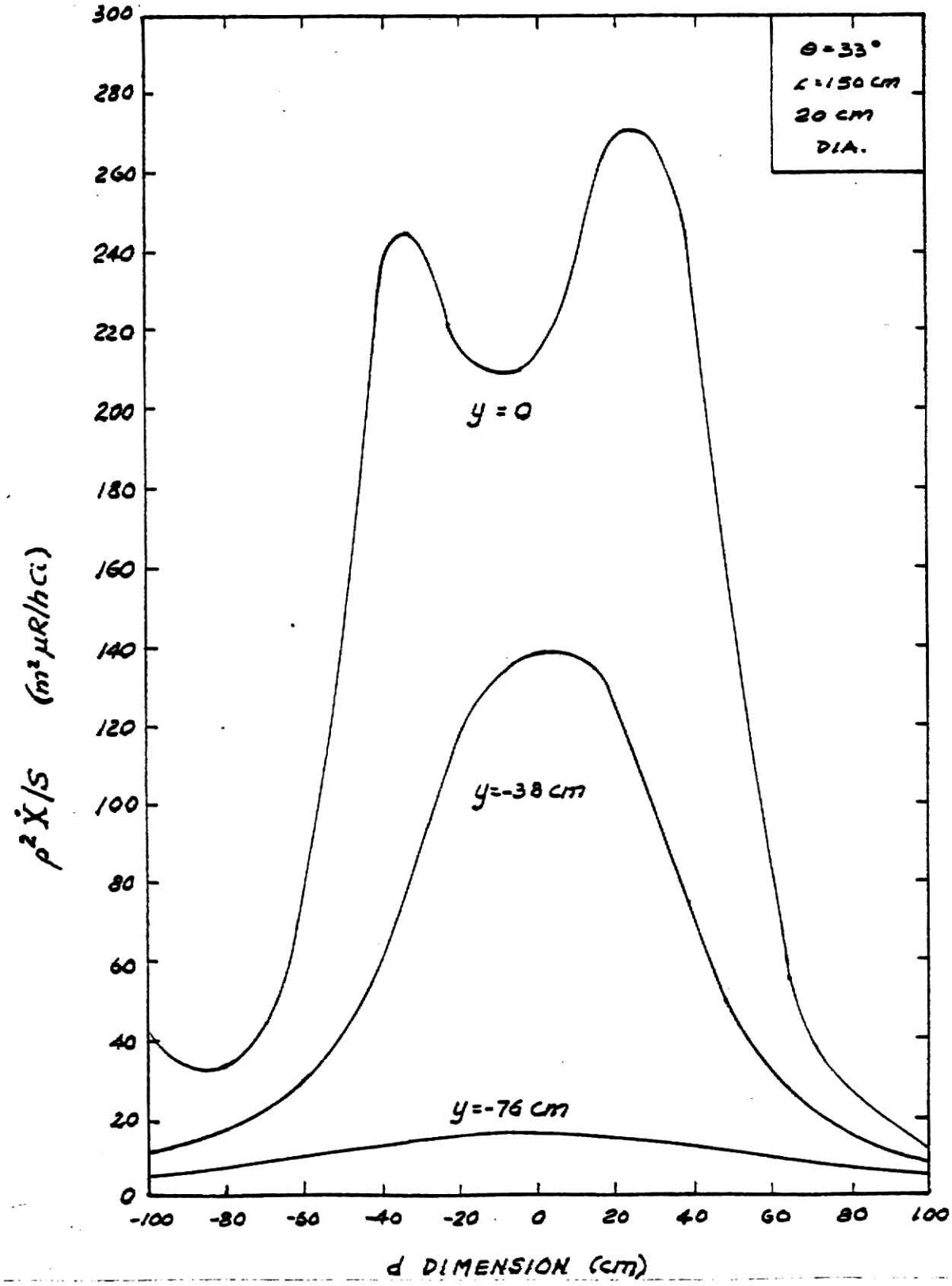

Fig. 5.3 Normalized exposure rate as a function of d and y for the 100-cm thick wall with a 20-cm diameter duct. Measured at c = 150 cm, with θ = 33°.

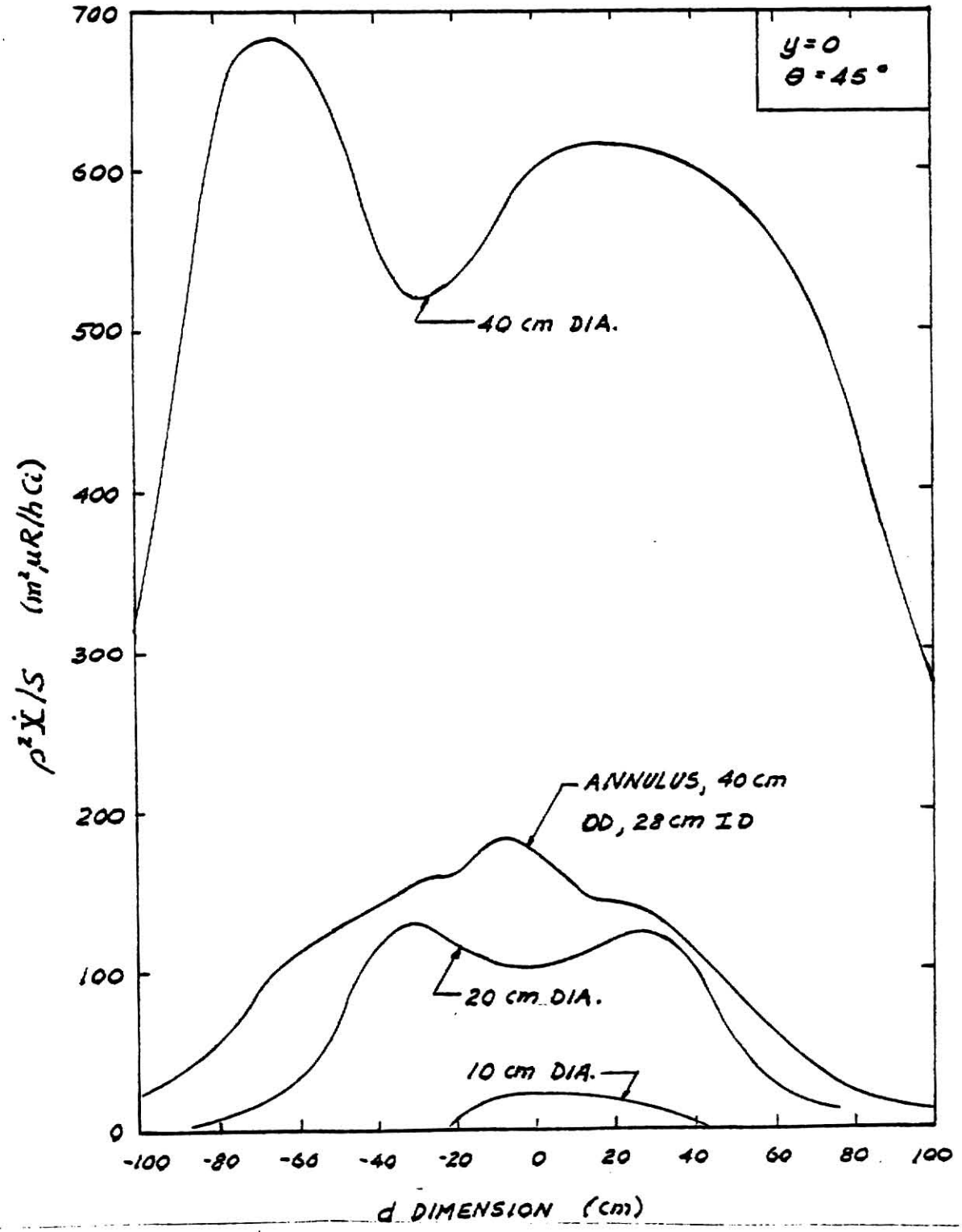

Fig. 5.4 Normalized exposure rate as a function of d and duct diameter. Measured at c = 150 cm, y = 0, and θ = 45°.

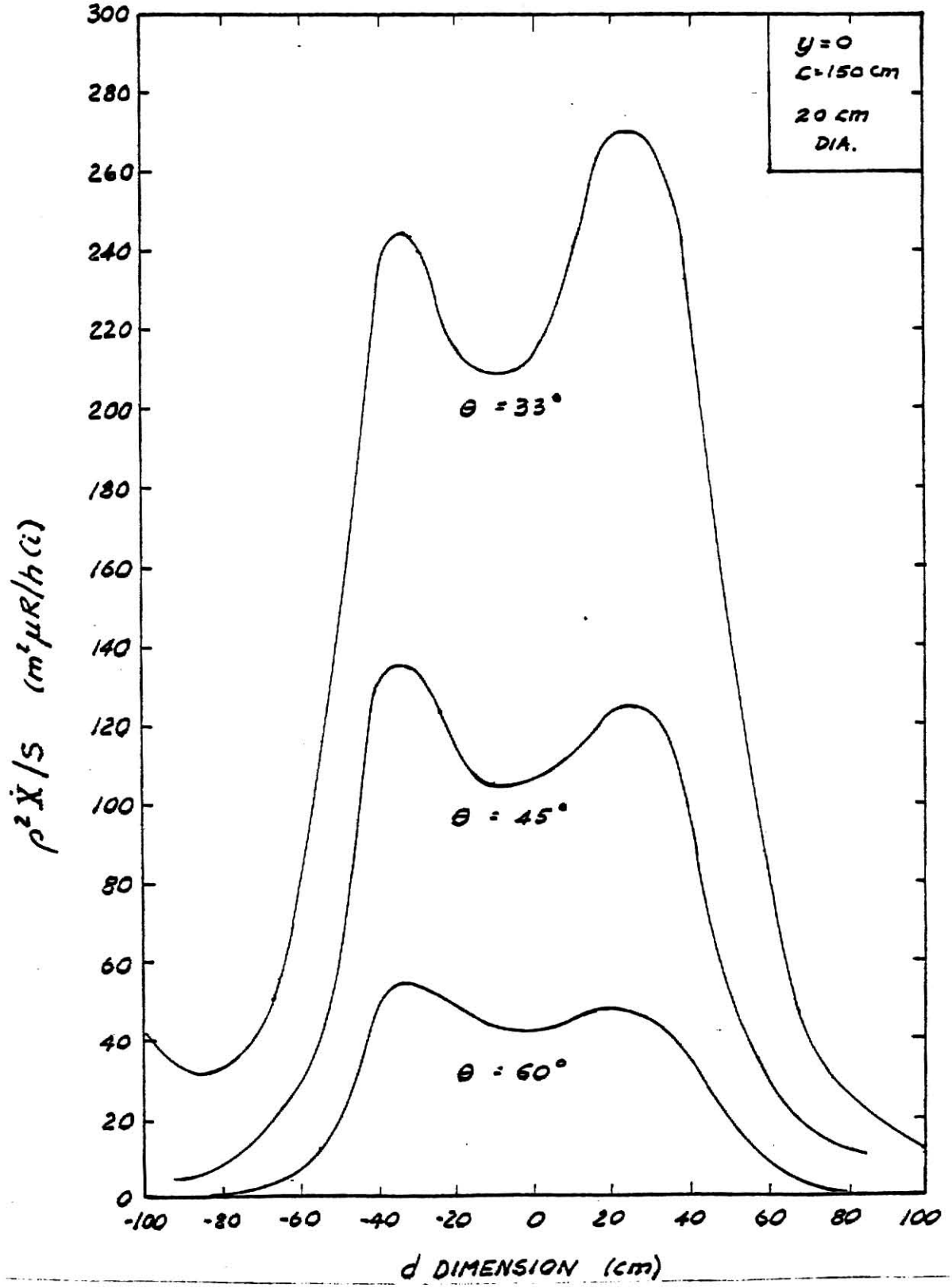

Fig. 5.5 Normalized exposure rate as a function of d and θ for the 100-cm thick wall with a 20-cm diameter duct. Measured at c=150 cm, with y=0.

A few measurements were also made of the exposure rate as a function of the distance c, or z-position, and the elevation y, all at the x-position of the duct axis, namely x = 808.5 or d = 0. These c traverse measurements were made only for the 20-cm diameter duct in the 100-cm thick wall. Raw data are presented in Tables 5.4 and 5.5. The matching reduced data are presented as Table 5.6 and illustrated as Figs. 5.6 and 5.7.

Isodose lines, in the x-z (or c-d) planes were also determined for selected values of ρ, θ, and y for various sized ducts in the 100-cm thick wall. Representative results are illustrated in Figs. 5.8 - 5.12. The normalized exposure rates, $\rho^2\dot{X}/S$ ($m^2\mu R/Cih$), are approxiamate values, based on the estimated background (solid-wall) exposure rates assumed to be constant throughout the measurement plane. The results are thus appropriate only for qualitative interpretation.

Table 5.4. Selected raw digital experimental C traverse data for the 100-cm thick wall with a 20-cm diameter duct using the ^{60}Co source of nominal strength 10 Ci. Data reported are values of E, the exposure-rate instrument readings.

Duct Dia. (cm)	20	20	20	20	20	20
θ (deg)	33	33	33	45	45	45
ρ (cm)	400	200	200	400	200	200
y (cm)	0	-38	-76	0	-38	-76
x	808	808	808	808	808	808
ID No.	273	263	253	123	233	243
Date	21 Aug	21 Aug	21 Aug	21 Aug	21 Aug	21 Aug
z						
76	980	1029	205	532	501	133
100	908	1048	213	500	519	133
200	704	1156	220	406	569	140
300	570	1178	226	351	596	145
400	481	1140	243	305	589	152
500	422	1060	251	285	551	160
600	366	971	261	258	508	166
700	328	865	280	245	464	176
800	304	772	306	228	426	191
900	277	698	333	218	387	202
1000	265	624	361	213	354	218
1100	250	566	376	203	324	232
1200	240	507	396	199	295	241
1300	229	460	398	198	276	239
1400	218	421	392	188	256	241
1500	205	387	376	185	239	230
1600	204	353	361	182	223	229
1698	195	331	346	180	214	222

Table 5.5. Selected background (solid wall) digital experimental ^{60}Co traverse data for the 100-cm thick wall using the ^{60}Co source of nominal strength 10 Ci. Data reported are values of E, the exposure-rate instrument readings.

θ (deg)	33	33	33	45	45	45
ρ (cm)	400	200	200	400	200	200
y (cm)	0	-38	-76	0	-38	-76
x	808	808	808	808	808	808
ID No.	373	363	353	323	333	343
Date	21 Aug	21 Aug	21 Aug	21 Aug	21 Aug	21 Aug
z						
76	135	99	93	141	94	80
100	137	100	92	143	91	88
200	145	104	95	143	97	91
300	149	107	98	146	105	92
400	151	111	101	154	101	95
500	155	110	100	162	102	98
600	157	112	102	159	107	100
700	158	112	102	161	105	101
800	160	116	106	160	112	102
900	162	113	105	161	112	100
1000	165	113	104	165	108	100
1100	169	113	99	160	108	100
1200	158	114	105	161	107	101
1300	157	115	103	164	110	103
1400	159	113	105	161	112	105
1500	154	112	103	164	107	101
1600	154	109	102	159	111	97
1698	155	109	104	161	105	102

Table 5.6. Reduced C traverse data for the 100-cm thick wall using the ^{60}Co source of nominal strength 10 Ci. Data reported are values of $\rho^2\dot{X}/S$ in units of $m^2\mu R/Cih$.

Duct dia (cm)	20	20	20	20	20	20
θ (deg)	33	33	33	45	45	45
ρ (cm)	400	200	200	400	200	200
y (cm)	0	-38	-76	0	-38	-76
d (cm)	0	0	0	0	0	0
c(cm)						
100	429	118	14.2	199	51.7	6.7
105	391	120	15.4	181	54.3	5.7
125	284	134	15.9	134	59.9	6.2
145	214	136	16.2	104	62.3	6.7
165	168	131	18.0	77	61.9	7.2
186	136	121	19.2	62	57.0	7.9
206	106	109	20.2	50	50.9	8.4
226	86	96	22.6	43	45.6	9.5
246	73	83	25.4	35	39.9	11.3
266	58	74	28.9	29	34.9	12.9
286	51	65	32.6	24	31.2	15.0
307	41	57	35.2	22	27.4	16.8
327	42	50	36.9	19	23.9	17.8
347	37	44	37.4	17	21.1	17.3
367	30	39	36.4	14	18.3	17.3
387	26	35	34.6	11	16.8	16.4
408	25	31	32.9	12	14.2	16.8
427	20	28	30.7	10	13.8	15.2

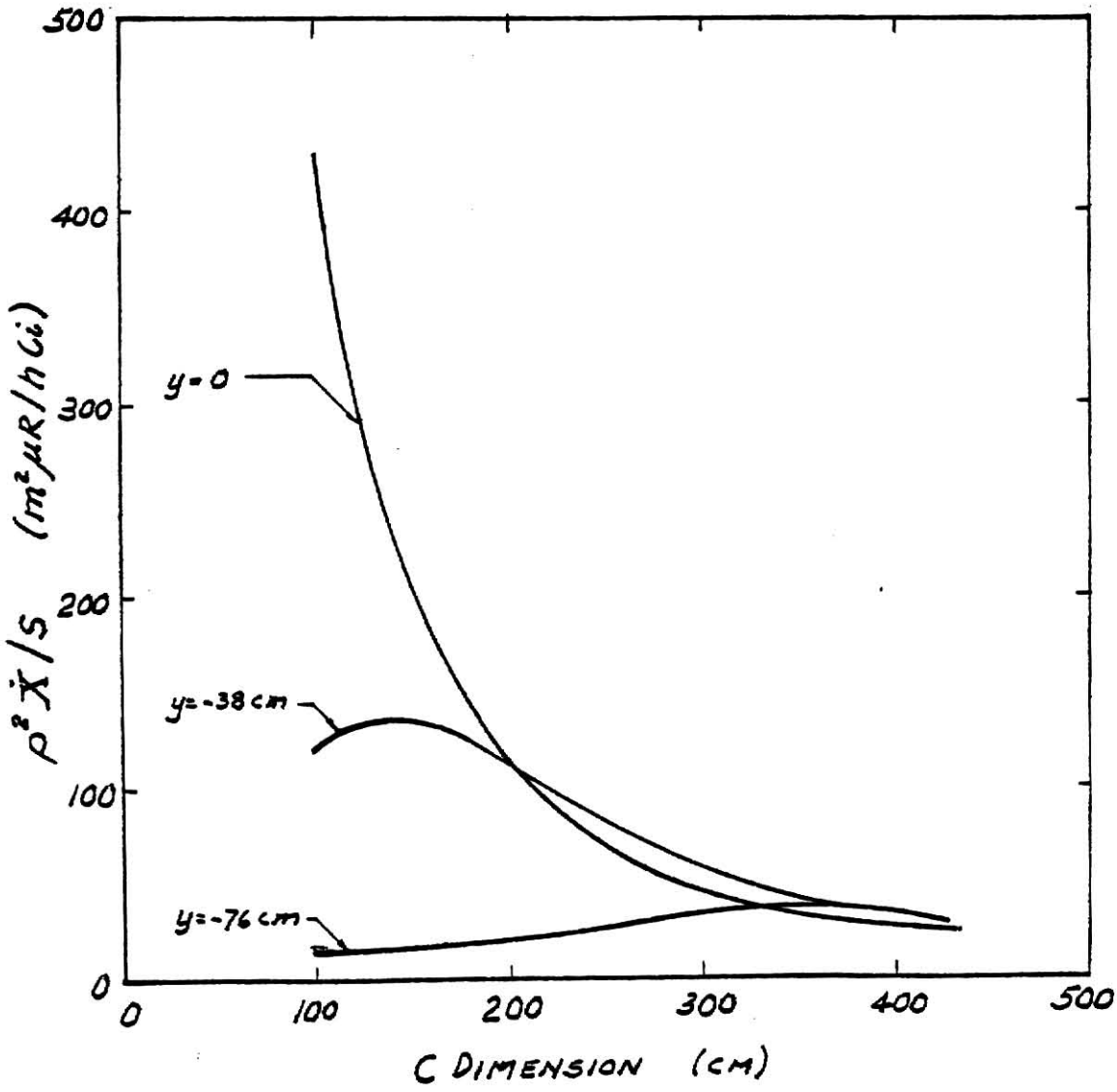

Fig. 5.6 Normalized exposure rate as a function of distance from a 100-cm thick wall of a 20-cm diameter and a 33° angle of incidence. (Measured at d = 0).

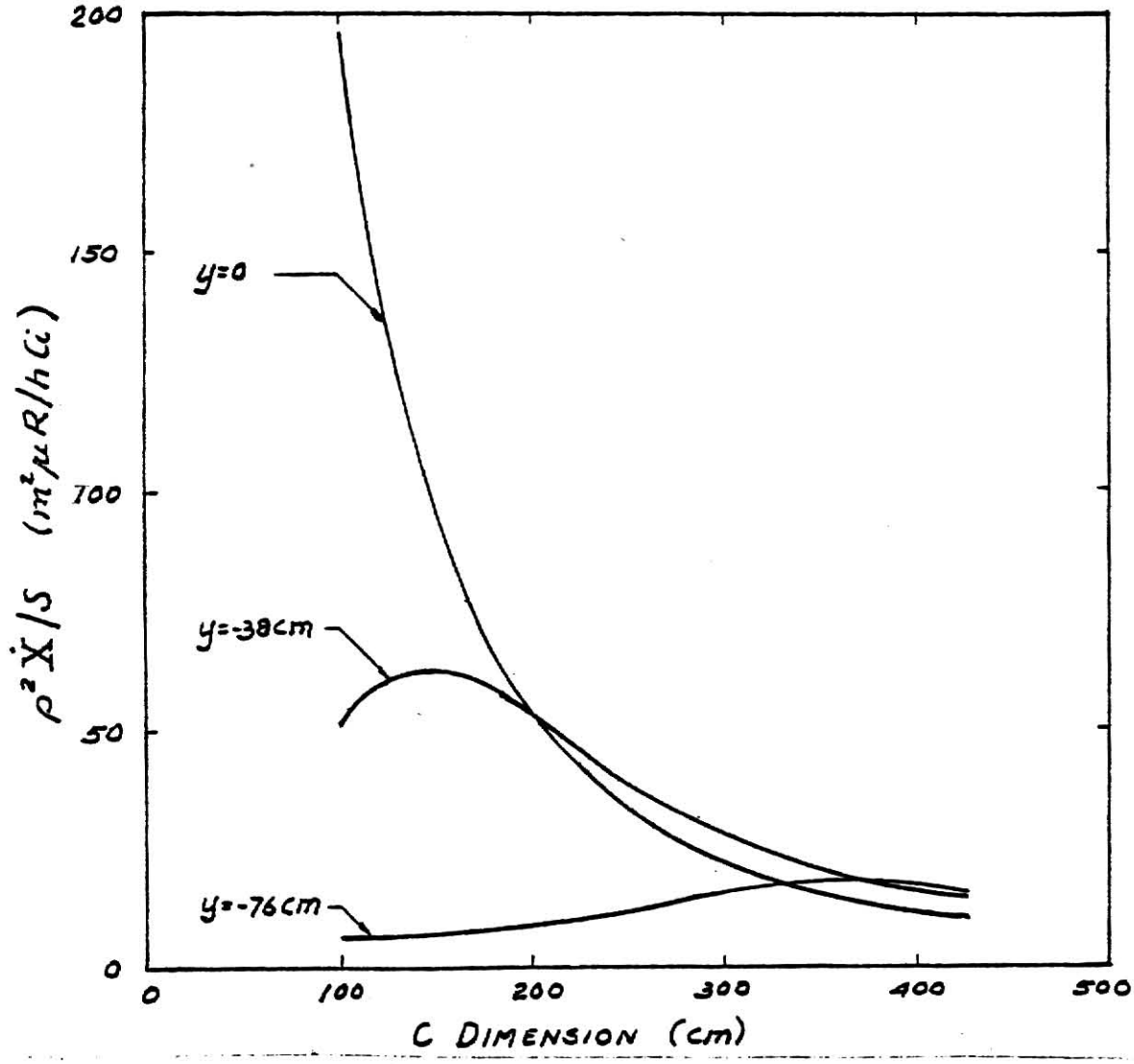

Fig. 5.7 Normalized exposure rate as a function of distance from a 100-cm thick wall with a 20-cm diameter duct and a 45° angle of incidence. (Measured at d = 0).

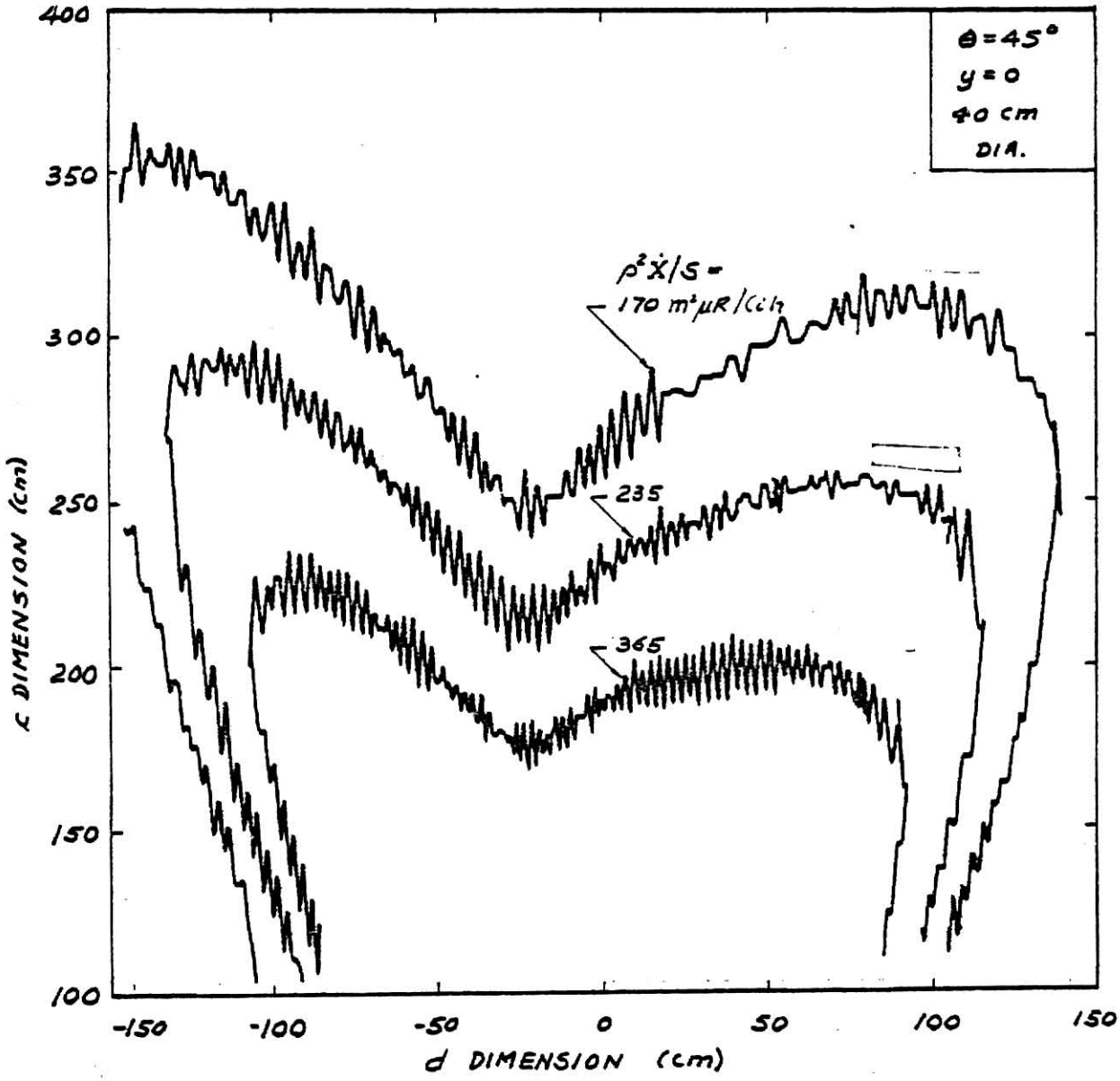

Fig. 5.8 Isodose plot for the 100-cm thick wall with a 40-cm diameter duct and an angle of incidence of 45°. Measured at y = 0 and ρ = 4m.

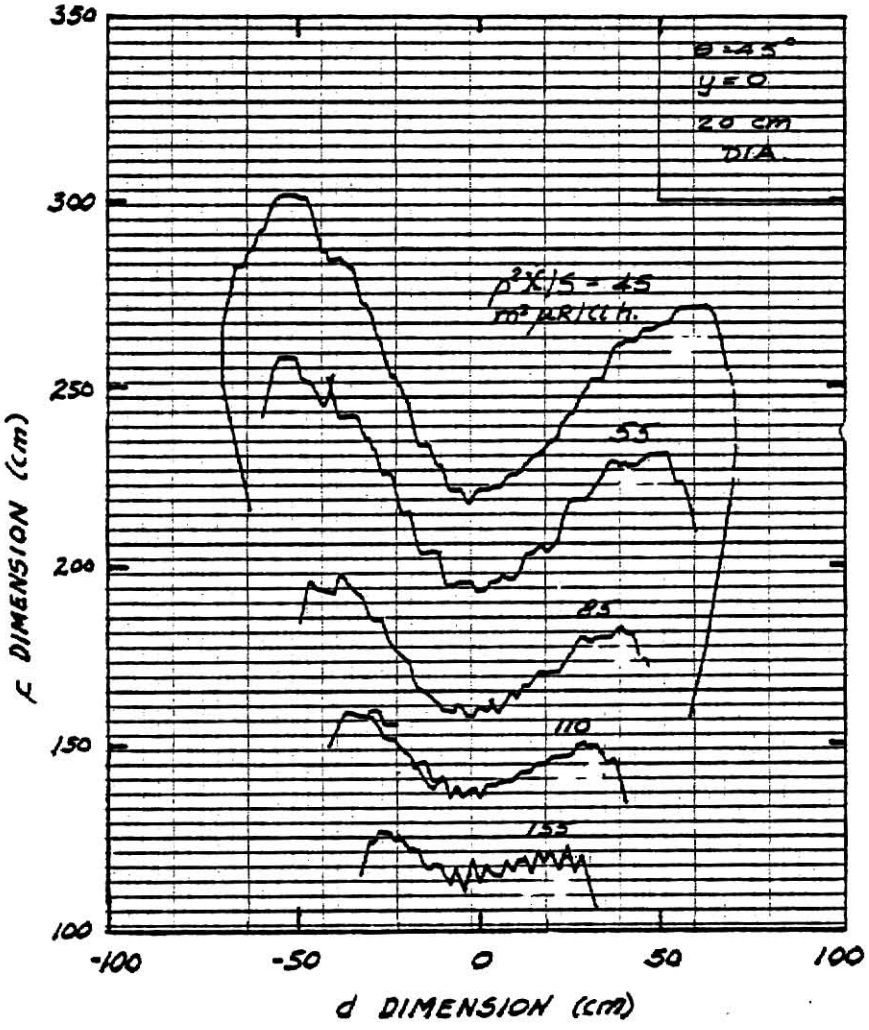

Fig. 5.9 Isodose plot for the 100-cm thick wall with a 20-cm diameter duct and an angle of incidence of 45°. Measured at y = 0 and ρ = 3m.

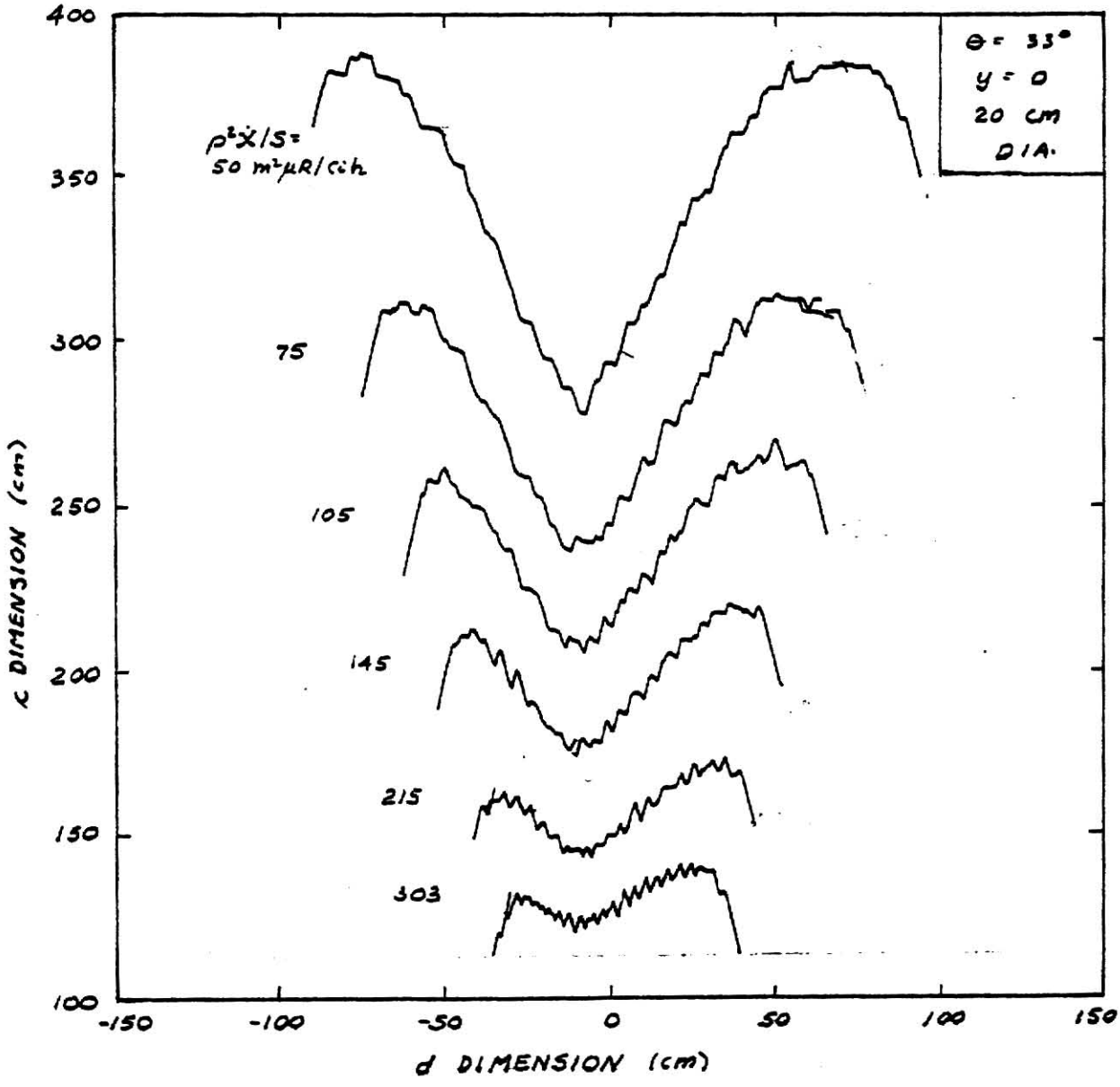

Fig. 5.10 Isodose plot for the 100-cm thick wall with a 20-cm diameter duct and an angle of incidence of 33°. Measured at y = 0 and ρ = 3m.

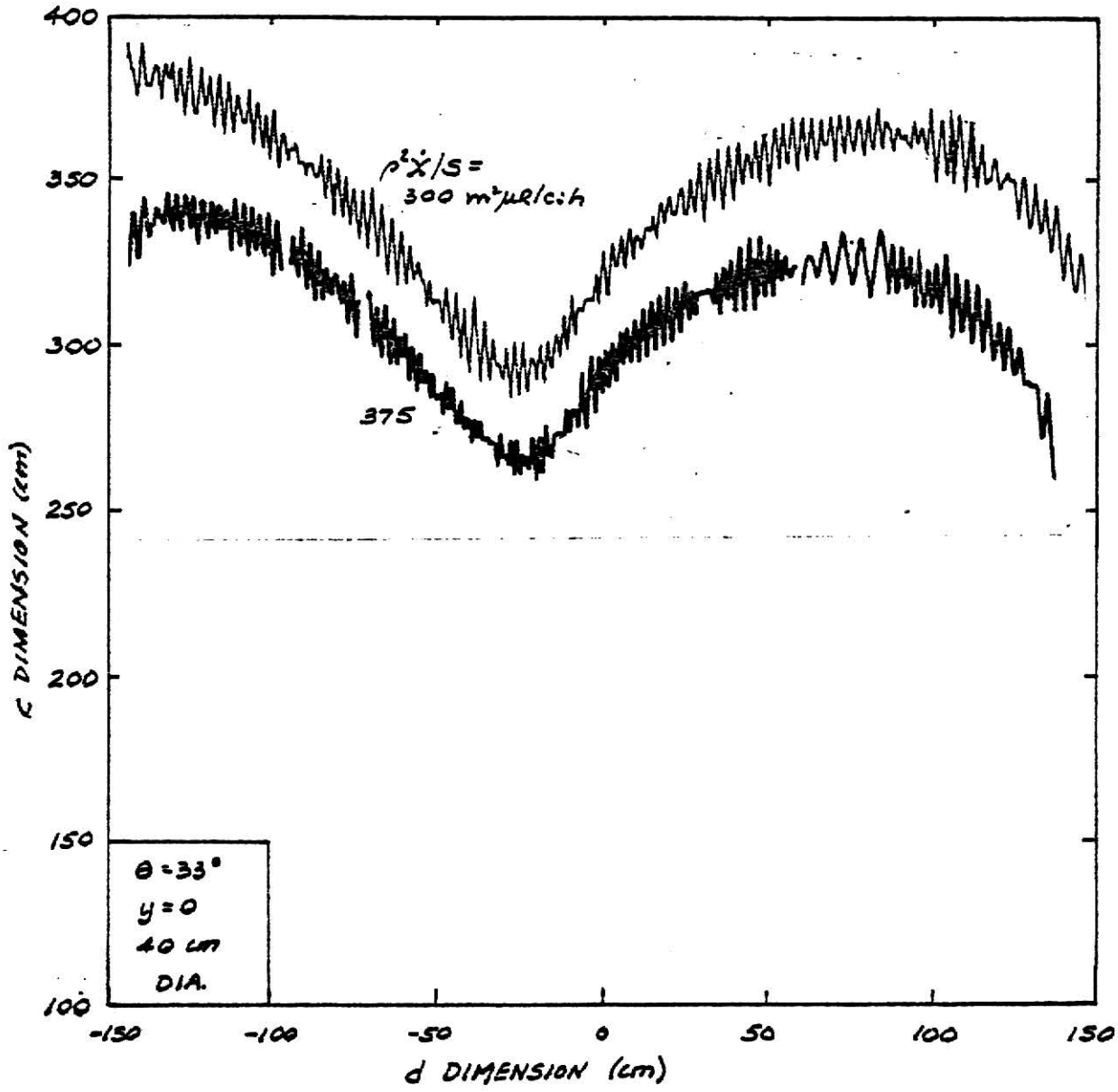

Fig. 5.11 Isodose plot for the 100-cm thick wall with a 40-cm diameter duct and an angle of incidence of 33°. Measured at y = 0 and ρ = 3m.

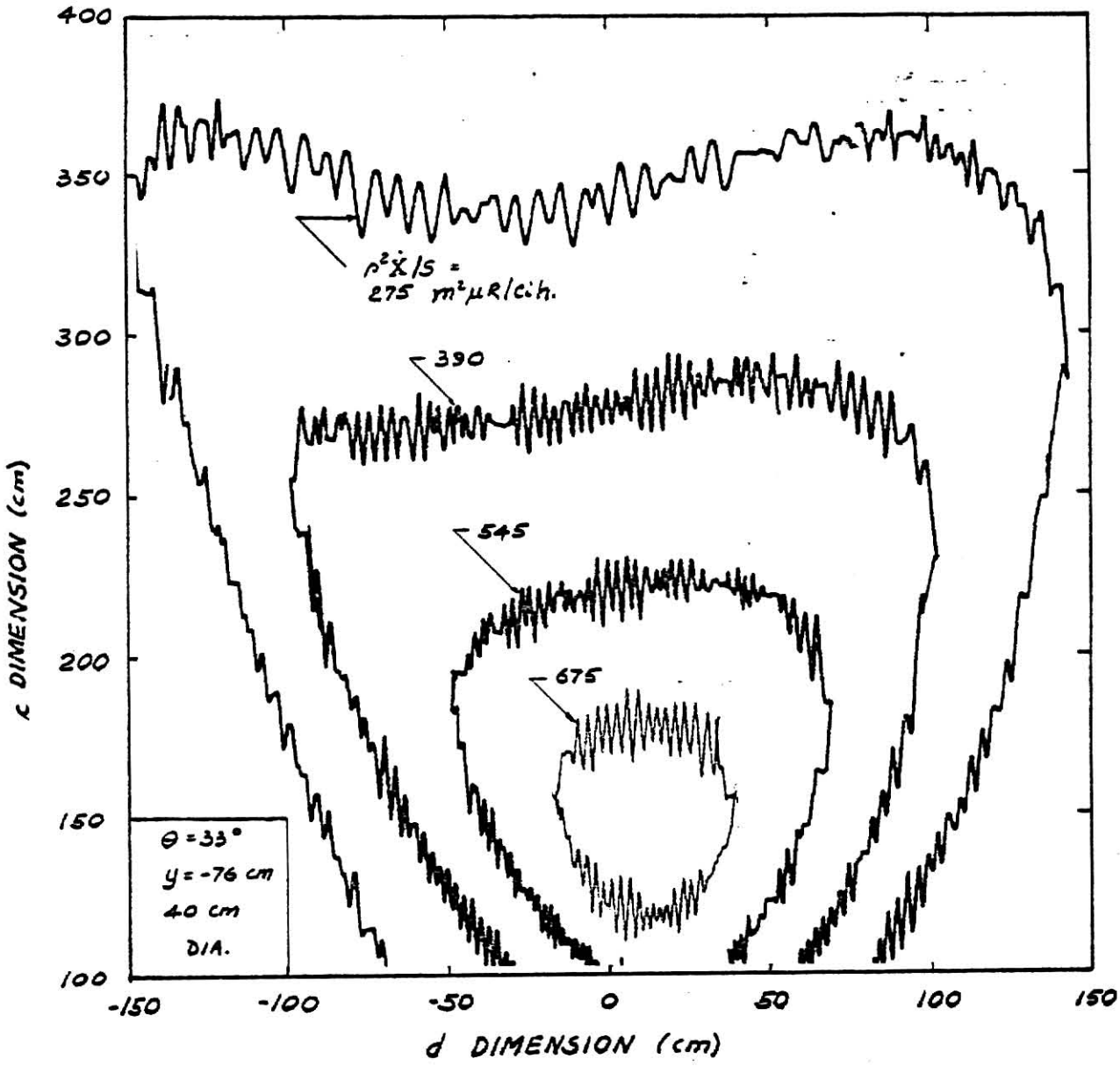

Fig. 5.12 Isodose plot for the 100-cm thick wall with a 40-cm diameter duct and an angle of incidence of 33°. Measured at y = -76 cm and ρ = 4m.

Because duct penetration data were collected over a period of many months, great care was taken in design and operation to insure long term stability in the measurement system. To aid in the verification of the constancy of the system response, a standard daily startup procedure was adopted for this experiment. An example of the checkoff sheet used in this startup procedure is shown in Table 5.7.

During this daily verification procedure the following items were examined and adjusted if necessary:

(i) internal voltages of the potentiometers in the data acquisition system used to record detector position and the detector signal,

(ii) the proper operation of the limit switches of the detector traversing mechanism and the position indication for the detector at these limit positions,

(iii) the response of the HPIC to a known calibrated Co-60 check source,

(iv) measured background radiation exposure rates at the four corners of the traversing area,

(v) miscellaneous maintenance and safety items.

From these daily checkout procedures, it was found the system was remarkably stable and little adjustment was ever needed. Moreover, it was found that the background radiation field at the experimental site was nearly constant throughout the course of the experiment at $9.0 \pm 1.5 \mu R/h$.

As is discussed earlier, a collimator/shadow shield assembly was constructed around the Co-60 sources to minimize air-scattering (skyshine) around the test wall. Nevertheless, the duct test section must be uniformly illuminated over a sufficient area so that the total duct penetration component may be obtained. The area of illumination on

Table 5.7 Startup Checklist Used for Daily Operation

Startup Procedure Date July 25, 1979

Check-out dosimeters	✓	Protective Rope Placement	✓
Oil Mechanism	✓	Source Carriage Placement	✓
Check Line Conditioner (115 V)	✓		
Check 10V power supply	✓		
Adjust Configuration Pot (1999)	✓		
Adjust Dose Set Pot (199)	✓		

Check Microswitches (X,Z) =	(0, 0)	✓
	(100, 0)	✓
	(100,100)	✓
	(0,100)	✓

Check Position Pot Readout	X-Pot	Z-Pot
(0, 0)	76	76
(100, 0)	1545	76
(100,100)	1544	1698
(0,100)	76	1698

Check Exposure Rate: Check Source at (100,0)
HPIC at (0,0) 102 μR/h

Check Background: Position		
	(0, 0)	8.1 ± 0.3 μR/h
	(100, 0)	9.6 ± 0.2 μR/h
	(100,100)	9.2 ± 0.3 μR/h
	(0,100)	8.6 ± 0.3 μR/h
	Average	8.9 ± 0.6 μR/h

Shutdown Procedure

Turn off electrometer	✓
Gather Protective Rope	✓
Lock-up Sources	✓
Check-in dosimeters	✓
Line Conditioner Off	✓
Air Conditioner Off	✓
Circuit Breakers Off	✓

the test wall was measured in this experiment by using a small GM probe to trace out the pnembra boundary on the test wall. Except for the larger ducts in the thicker walls with large source angles and small ρ values, it was possible to illuminate not only the entire hot duct mouth but also a sufficient area of the adjacent test wall so that the uncollided photon beam would fully illuminate the duct mouth. For those cases where such complete illumination was not possible, it was verified that the hot duct mouth was still always fully illuminated as well as the adjacent test wall surface up to several centimeters away from the duct.

In all duct configurations, both the duct measurements and the corresponding solid wall measurements were performed with the same area of the test wall illuminated. In this way, the difference between the two measurements would give only the duct penetration component (assuming the background exposure rate was the same for both measurements).

In this experiment the detection area on the cold side of the test wall was located inside a thin walled metal building. With such an arrangement measurements could be obtained in inclement weather and a controlled environment could be maintained for the sensitive detection system. The building wall adjacent to the cold side of the duct was modified to eliminate any structural beams near the exit radiation beam. Only a thin corrugated iron wall (0.17 cm thick) was left interposed between the cold side of the duct and the detection area.

To assess the importance of the iron wall on the experimental results, x-z traverses were made with and without a second piece of corrugated iron wall placed over the cold side of the duct mouth. These traverses were made for two different duct configurations.

In both cases the effect of the second piece of corrugated iron wall was to reduce the exposure rate profiles by about 4%. Thus the building wall may be inferred to cause the same percentage reduction in all the exposure rate profiles obtained in this project.

Although the measured exposure rates could have been corrected for the building wall attenuation, this correction was not performed in reducing the data since the wall attenuation tended to compensate for the expected over-response of the HPIC to the low energy, duct-scattered photons.

The geometric parameters which specify the source and detector position are indicated in Fig. 5.1. Accuracy of the pertinent dimensions relating the traverser area and detector position to the cold side of the duct wall (Fig. 5.13) are estimated to be within ± 1 cm. The potentiometer position indicators for the HPIC in the traverser area were found to drift only very slightly throughout the course of the experiment. The estimated position error in the x or z dimension obtained from the digital output of detection system is thought to be less than $\pm$ 0.5 cm.

The same uncertainty is expected for the y dimension since the same vertical block shims were used throughout the experiment to adjust the vertical height of the x-z traversing mechanism. Although the vertical height, y, of the detector was reproducible to within $\pm$ 0.5 cm, the exact vertical location of the HPIC varied within $\pm$ 4.45 cm depending on the x and z coordinates of the detector. This relatively large variation was a direct result of the "sag" in the x-z traverser mechanism such that when the detector was in the center of the traverse area the detector was 8.9 cm lower than when the detector was at either of the four corners. In Table 5.8 the measured vertical sag of the HPIC with respect to the y = 0 plane (containing the duct centerline) is presented

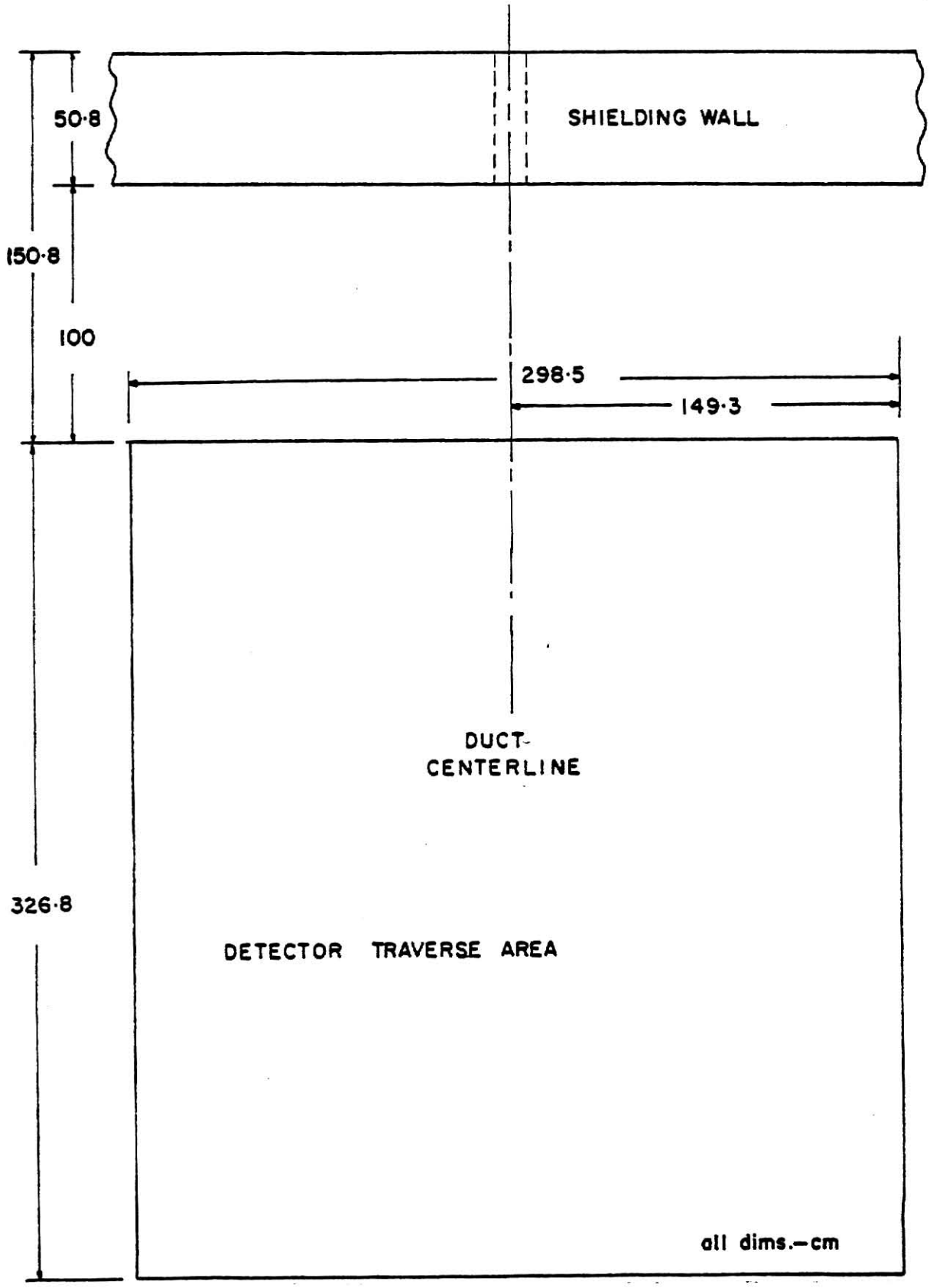

Fig. 5.13 Top view of detector traverse area and the 50.8-cm thick shielding wall.

for the detector in the center of the traverse area and along the periphery.

Table 5.8. Displacement of the center of the from the y = 0 plane for the detector at the center and along the periphery of the x-z traversing area.

c (cm)	d(cm) -150	0	150
0	+4.45	-2.22	+4.45
250	+1.43	-4.45	+1.43
500	+4.45	-2.22	+4.45

The source position on the hot side of the duct wall was determined by the two coordinates ρ and θ (see Fig. 5.2). The uncertainty in the measured values of ρ is $\pm$ 1 cm and in θ is $\pm 0.3^{o}$. The source cask was repositioned several times for the same nominal ρ and θ settings and the exposure rate profiles from x-z traverses were found to have no observable differences. Thus any positioning errors were significantly less than changes in θ or ρ necessary to affect the exposure rate profiles.

(ii) Exposure Rate Measurements

The exposure rate as determined with the Reuter-Stokes HPIC was observable in four manners in this experiment. The primary readout was a digital display built into the Reuter-Stokes Area Monitor System and whose indication was used to verify the manufacturer's calibration of the HPIC system (6). The three other exposure rate indicators were (i) a pressure sensitive paper strip chart recorder (also calibrated by the manufacturer) built into the HPIC system, (ii) an X-Y linear recorder which plotted exposure rate versus position ("x-z and c traverses"), and (iii) a digit readout

(both with printer and digital display) on the data acquisition system. The exposure rate as measured on the traverse profiles from the X-Y recorder was generally well within ± 2μR/h of the primary digital indication. Since the exposure rate signal for the X-Y recorder is taken directly from the Reuter-Stokes system without interposing amplification or digital conversion, the data obtained from x-z or c-traverses are thought to be the most accurate obtained in this experiment.

The digital printout of the exposure rate produced by the data acquisition system, E, was found to be well represented by

$$E = E_o + b\ (\dot{X})$$

where "E_o" represents an "offset" (typically between 8 and 12 units) and "b" is a voltage-to-exposure-rate conversion factor whose value was found to be 3.98 ± .02 ($mV \cdot \mu Rh^{-1}$). The linearity of this digital readout with the primary readout was excellent ($r^2 = 0.99998$). An example calibration is shown in Fig. 5.14. One major deviation from the linearity was noted. Above an exposure rate of 475μR/h, the exposure rate potentiometer reading saturated and remained constant (see Fig. 5.12). Thus exposure rate printouts above E = 1900 must be viewed as suspect.

To obtain the "reduced data" for a particular duct configuration, the difference between the exposure rate obtained with the duct in the wall and that from the corresponding solid wall was taken. With this difference the bias, E_o, in the potentiometer readings subtracts out and only the value of b is needed to convert the reduced exposure rate potentiometer reading.

Finally it should be mentioned that the sensitive HPIC had a significantly long time constant of about 10 sec. Thus as the detector moved through a varying radiation field, it was necessary to move sufficiently slowly so as to prevent the indicated exposure rate reading from lagging

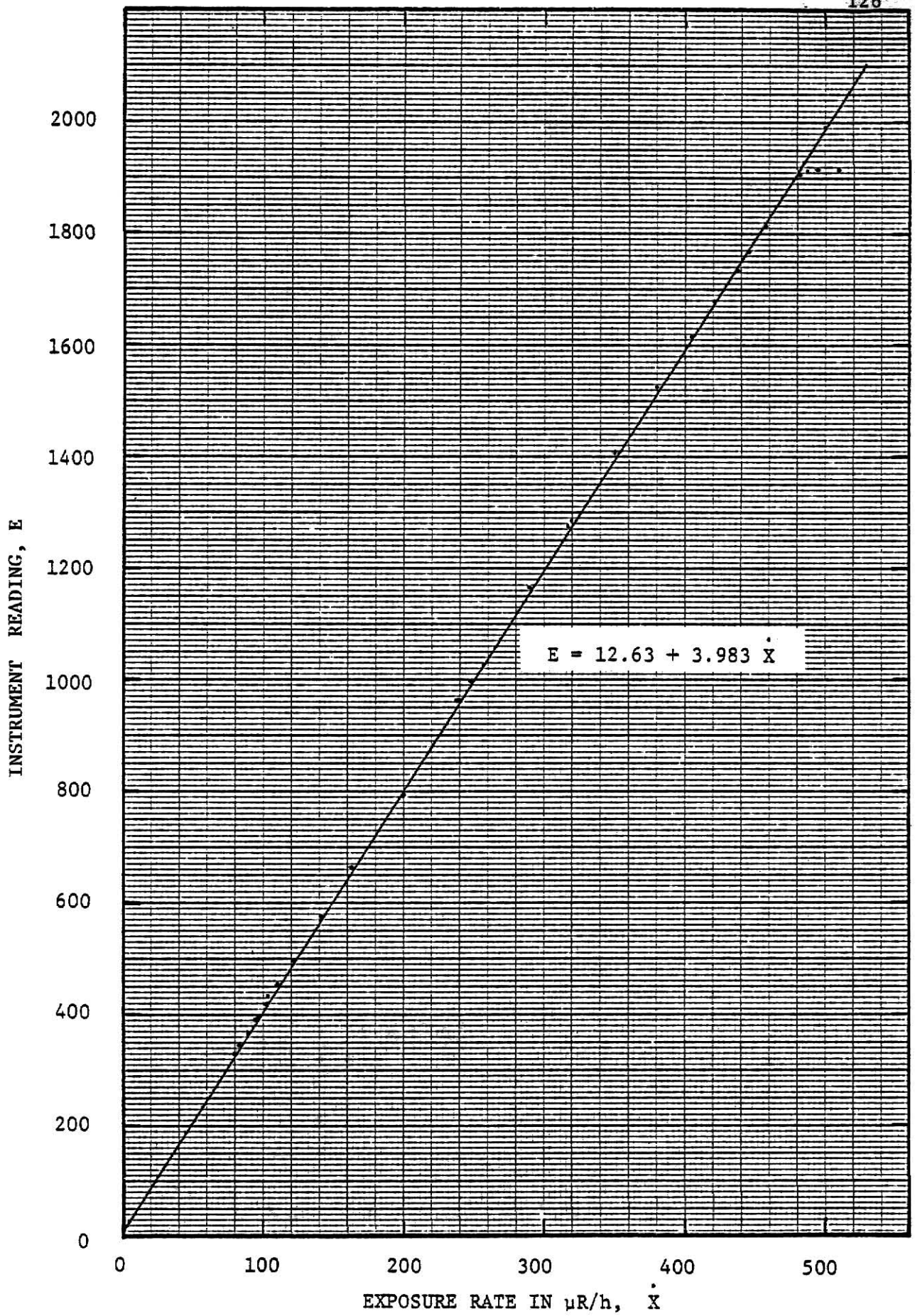

Fig. 5.14 Instrument reading for the exposure rate from the experimental data acquisition system versus the exposure rate as measured directly from the Reuter-Stokes Area Monitor. The straight line is a least squares fit to the data.

behind the actual value. In plotting the x-z traverses and c traverses, the detector was stopped at the traverse positions where data were to be recorded for a sufficient length of time to allow the detector response to reach equilibrium. On many of the x-z traverse plots, sharp rises or dips in the exposure rate profiles can be observed at the positions where the detector was stopped.

The long detector time constant can also be seen to affect the isodose profiles. From the isodose profiles it is seen that there is significant oscillatory variation in the z position (up to one-half of the detector diameter) caused by the tracking mechanism searching for the "target" exposure rate. With a proper choice of detector drive speeds to complement the detector time constant, these oscillations were minimized but not eliminated. For all the isodose profiles, the indicated exposure rate on the Reuter-Stokes strip chart was constant to within a few percent thus indicating the tracking mechanism was indeed functioning correctly.

(iii) Uncertainties in the Reduced Data

To obtain the exposure rate arising solely from the presence of the duct in the test wall (i.e., the duct penetration component) it was necessary to make two measurements: (a) the exposure rate with the duct in place, and, without changing the source-collimator configuration, (b) the exposure rate with the duct filled with concrete (i.e., a solid wall). The first measurement gives the sum of the duct penetration component (E_d), the skyshine or air scattered component (E_s), and the natural background E_b. The second measurements should then be only the sum of the skyshine and background components, if it is assumed that the filled duct negligibly affects the skyshine component and that the test

wall is so thick that any direct penetration component is totally negligible (easily calculated and compared to measured values).

The reduced exposure rate (normalized to unit source strength and corrected for the geometric attenuation of the source-to-duct distance, ρ) is thus given by

$$\frac{\rho^2 \dot{X}}{S} = \frac{1}{b} \frac{\rho^2}{S} \{E_d+E_s+E_b-E'_s-E'_b\}$$

where E is an exposure rate instrument reading (unprimed quantities for the ducted wall, and primed quantities for the solid wall). The source strength is denoted by S, and b an instrument-to-exposure-rate conversion factor (see (ii) above). For the reduced data presented in this study it was assumed that $(E_s + E_b) = (E'_s + E'_b)$, and that the two measured exoosure rates, $(E_d + E_s + E_b)$ and $(E'_s + E'_b)$, were both estimated to contain random errors of about $\pm$ 2μR/h ($\pm$ 8 units of the instrument system). The correction factor $1/b$ was taken to be 0.25 $\pm$ 5%.

The uncertainty in ρ is typically less than 0.5%; however, the strengths of the two sources used in this experiment are known only to within 4.8% for the 8.12-Ci source and to within 4.5% for the 0.474-Ci source (see Table 3.4). With these assumptions and error estimates, the "normalized reduced exposure rate" becomes

$$\frac{\rho^2 X}{S} = \{\frac{\rho^2}{4S} \pm 6.9\%\}\{(E_d+E_s+E_b) - (E'_s-E'_b) \pm 11.3\}$$

For large differences in the ducted and solid wall exposure rates, almost all the uncertainty in the normalized reduced exposure rate is due to the 6.9% uncertainty in (ρ^2/S). However for small differences the uncertainty in the exposure rate measurements can lead to very large percentage errors in the normalized reduced exposure rates as is shown in Table 5.9.

Table 5.9. Estimated percentage error in the normalized exposure rate ($\rho^2\dot{X}/S$) for various duct penetration exposure rates.

$\dot{X} = \frac{1}{b}(E_d+E_s+E_b-E'_s-E'_b)$ (μR/h)	% error in $\frac{\rho^2\dot{X}}{S}$
10	29.1
25	13.3
50	8.9
100	7.9
300	7.0
500	6.9

6.0 CALCULATIONS AND COMPARISONS

This chapter will present and discuss the results of the calculational models and compare and contrast these calculations with the corresponding experimental results. Unfortunately, before a direct comparison of the calculations and the experiment can be attempted, the calculated results must first be modified to replicate the conditions measured by the experiment as closely as possible.

The largest discrepency existing between the models and the experiment is the detector size. Exposure rate measurements were made using a 25.4 cm spherical high-pressure ion chamber. Model predictions are for a point detector and, therefore, direct comparisons with the experimental results will require volume weighting of the predicted exposure rates for these comparisons to be meaningful.

Response of the detector for a general unknown field is given by

$$D = \frac{\int d^3r\ D(r)\ V(r)\ F(r)}{\int d^3r\ V(r)\ F(r)} \qquad (6.1)$$

where

- D(r) is the 3-dimensional space dependent function describing the exposure rate,
- F(r) is the detector response function as a function of position within the detector,
- V(r) is the detector volume as a function of position within the detector.

For this model, the detector is assumed to be equally responsive throughout the volume of the detector, i.e., F(r) = constant. Additionally, the spatial dependence of the exposure rate field is

assumed to be one-dimensional in the d (or x) axis, i.e., constant vertically along the wall and away from the wall. Therefore, Eq. 6.1 can be written as

$$D = \frac{\int dx\ D(x)\ V(x)}{\int dx\ V(x)} \tag{6.2}$$

or discretely as

$$D = \frac{\sum_i V_i\ D_i}{\sum_i V_i} \tag{6.3}$$

where V_i is the volume about node i and D_i is the total exposure rate at node i.

A five point grid mesh was chosen to represent the exposure rate gradient in x and the appropriate weight factors were calculated such that the exposure rate at the center of the detector is given by:

$$D_0 = D_{-2}w_1 + D_{-1}w_2 + D_0w_3 + D_1w_4 + D_2w_5. \tag{6.4}$$

The weight factors, w_n, were calculated as follows

$$w_n = \frac{V_n}{V} \tag{6.5}$$

where

$$V_n = 2\pi[r^2(x_2 - x_1) - \tfrac{1}{3}(x_2^3 - x_1^3)], \tag{6.6}$$

V is the volume of the sphere, x_1, x_2 are the boundaries of the node and r is the detector radius. Substituting Eq. 6.6 into Eq. 6.5 gives Eq. 6.7 describing the weight factors explicitly

$$w_n = \frac{1}{6r^3}[r^2(x_2 - x_1) - \tfrac{1}{3}(x_2^3 - x_1^3)]. \tag{6.7}$$

Experimental data were measured using a spherical detector of 25.4 cm radius. The detector was represented discretely as evenly spaced chordal sections of a sphere with the section (nodal) boundaries at

$$x_1 = 0.0 \text{ cm}, \; x_2 = 2.5 \text{ cm for } w_3$$
$$x_1 = 2.5 \text{ cm}, \; x_2 = 7.5 \text{ cm for } w_2 \text{ and } w_4$$
$$x_1 = 7.5 \text{ cm}, \; x_2 = 12.7 \text{ cm for } w_1 \text{ and } w_5$$

relative to the sphere center. The weight factors, w_n, were evaluated at the nodal boundaries listed above using Eq. 6.7 and were found to be:

$$w_1 = w_5 = 0.1085$$
$$w_2 = w_4 = 0.2456$$
$$w_3 = 0.2914.$$

The sum of both calculated components (duct wall and lip scattering) were smoothed using this technique.

With a direct comparison of calculated results to experimental measurements now being possible, Figs. 6.1 and 6.2 graphically illustrate these comparisons over θ with r constant and over r with θ constant respectively. Additionally, Appendix A presents a complete set of calculated versus experimental results for the entire range of parameters in the 100 cm wall. Table 6.1 contains a tabulation of calculated to experimental $(\frac{C}{E})$ values for both the lip and duct wall scattering component models. These ratios were evaluated only at the peak exposure rate value of the respective component. Large errors

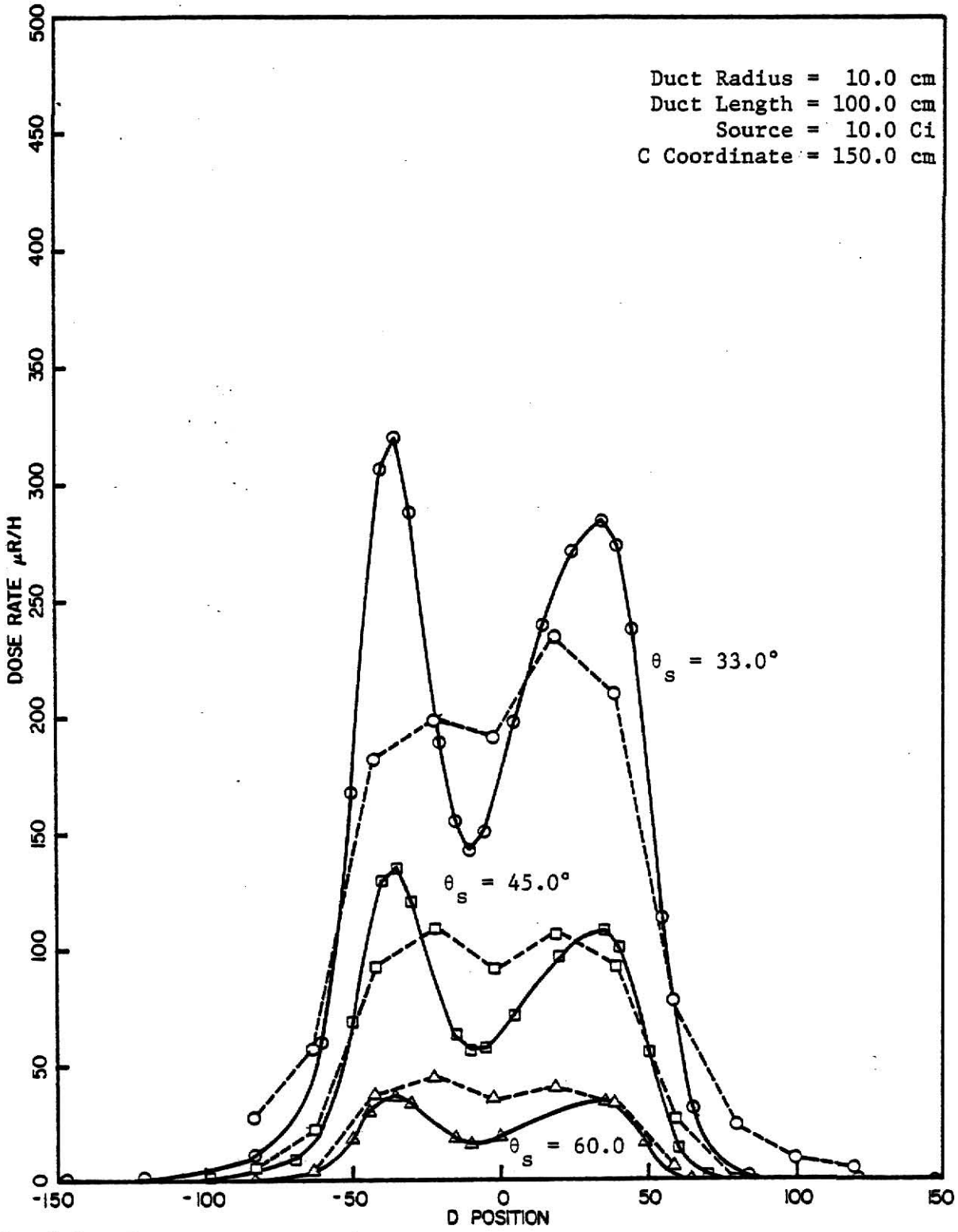

Fig. 6.1. Exposure rate profiles as a function of source angles for the 100-cm-thick wall (experimental points connected with dashed straight line segments for visual clarity).

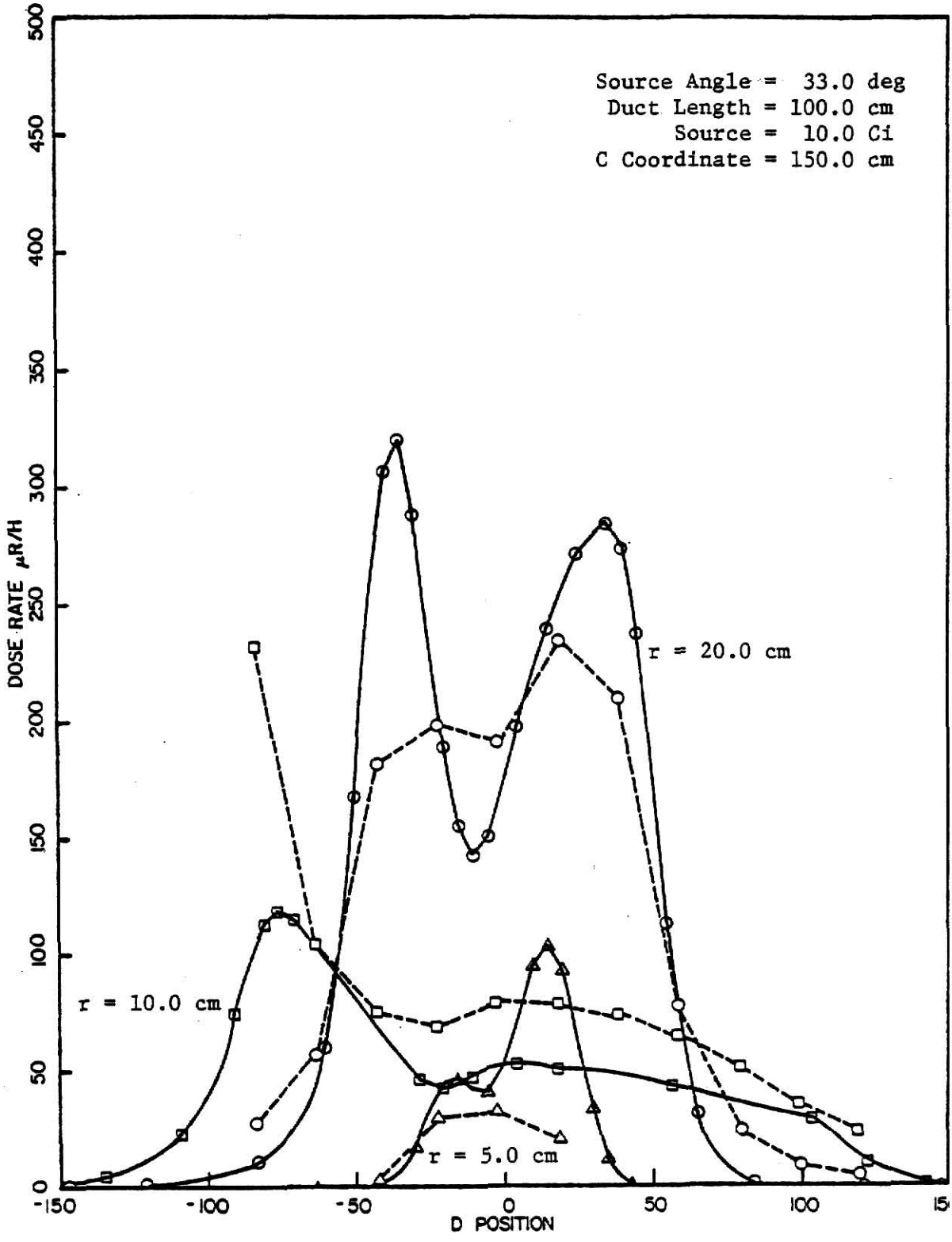

Fig. 6.2. Exposure rate profiles as a function of duct radius for the 100-cm-thick wall (experimental points connected with dashed straight line segments for visual clarity).

TABLE 6.1

Peak $(\frac{C}{E})$'s for Wall Length, L = 100.0 cm

Source Angle, θ_s (deg)	"C" Coordinate (cm)	$(\frac{C}{E})_L$	$(\frac{C}{E})_D$
	DUCT RADIUS R = 20.0 cm		
33.0	100.0	0.893	0.624
33.0	150.0	-----	0.661
33.0	250.0	0.697	0.681
45.0	100.0	0.515	0.548
45.0	150.0	1.320	0.518
45.0	250.0	1.765	0.629
60.0	100.0	1.146	0.562
60.0	150.0	1.259	0.467
60.0	250.0	1.060	0.477
	DUCT RADIUS R = 10.0 cm		
22.5	100.0	1.085	1.050
22.5	150.0	1.254	1.263
22.5	250.0	1.250	1.303
33.0	100.0	1.228	1.044
33.0	150.0	1.023	1.099
33.0	250.0	1.321	1.254
45.0	100.0	0.846	0.852
45.0	150.0	0.785	1.087
45.0	250.0	1.460	1.053
60.0	100.0	0.667	0.718
60.0	150.0	0.966	0.888
60.0	250.0	0.783	0.989
	DUCT RADIUS R = 5.0 cm		
22.5	100.0	1.356	1.579
22.5	150.0	2.096	3.143
22.5	250.0	1.724	3.243
33.0	100.0	1.000	1.566
33.0	150.0	1.323	1.563
33.0	250.0	1.500	3.667
45.0	100.0	0.712	1.345
45.0	150.0	1.000	1.111
45.0	250.0	1.294	2.625

do exist in the tabulated values of $(\frac{C}{E})$ for the 5.0 cm duct simply because of the spacing of the experimental points. This spacing was coarse enough that experimental points did not exist for all component peaks. In these cases a representative point near the peak was used to calculate the respective $(\frac{C}{E})$ ratio.

Notice in Fig. 6.1 that the agreement between the calculated and experimental values is within 20%. This result is to be expected, at least on the duct wall scatter component, since measured peak exposure rates in these data sets were used to fit the lip penetration correction. However, when referring to Fig. 6.2, good agreement is also observed between calculated and experimental values for these configurations. These results lend credence to the validity of the models.

Figures 6.3 and 6.4 present the comparisons made between calculation and experiment for the 150 cm wall. Figure 6.3 compares exposure rate profiles with r constant and variable θ. Figure 6.4 compares exposure rate profiles with θ constant and variable r. Appendix B also presents the complete set of calculated versus experiment for the entire range of parameters in the 150 cm wall. Table 6.2 presents the $(\frac{C}{E})$ ratios for the 150 cm wall. These ratios were evaluated in the same manner as for the 100 cm wall with large uncertainties at small duct radii. Notice that the calculated and experimental results are still in good agreement for a 50% longer duct and therefore, higher duct aspect ratio.

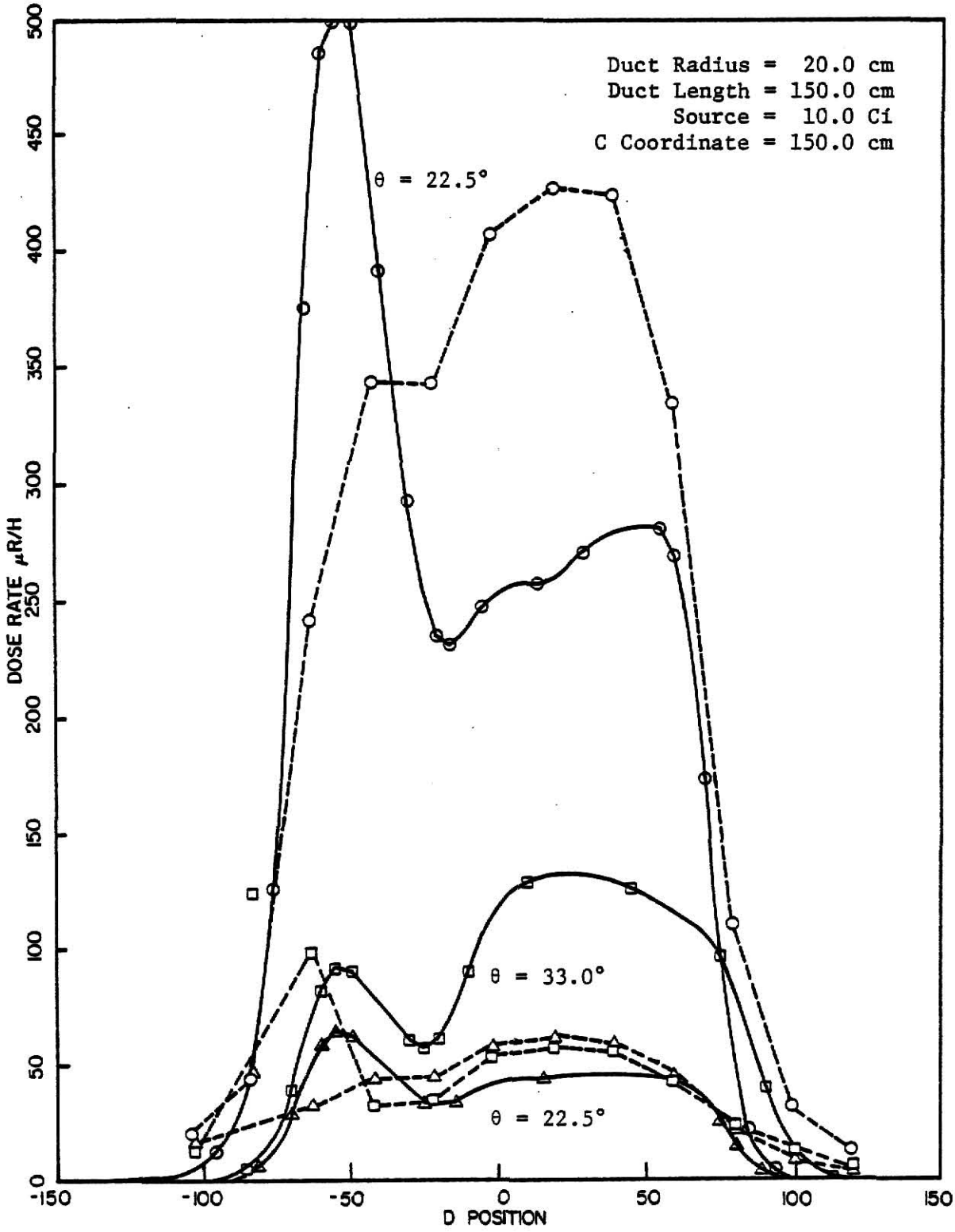

Fig. 6.3. Exposure rate profiles as a function of source angle for the 150-cm-thick wall (experimental points connected with dashed straight line segments for visual clarity).

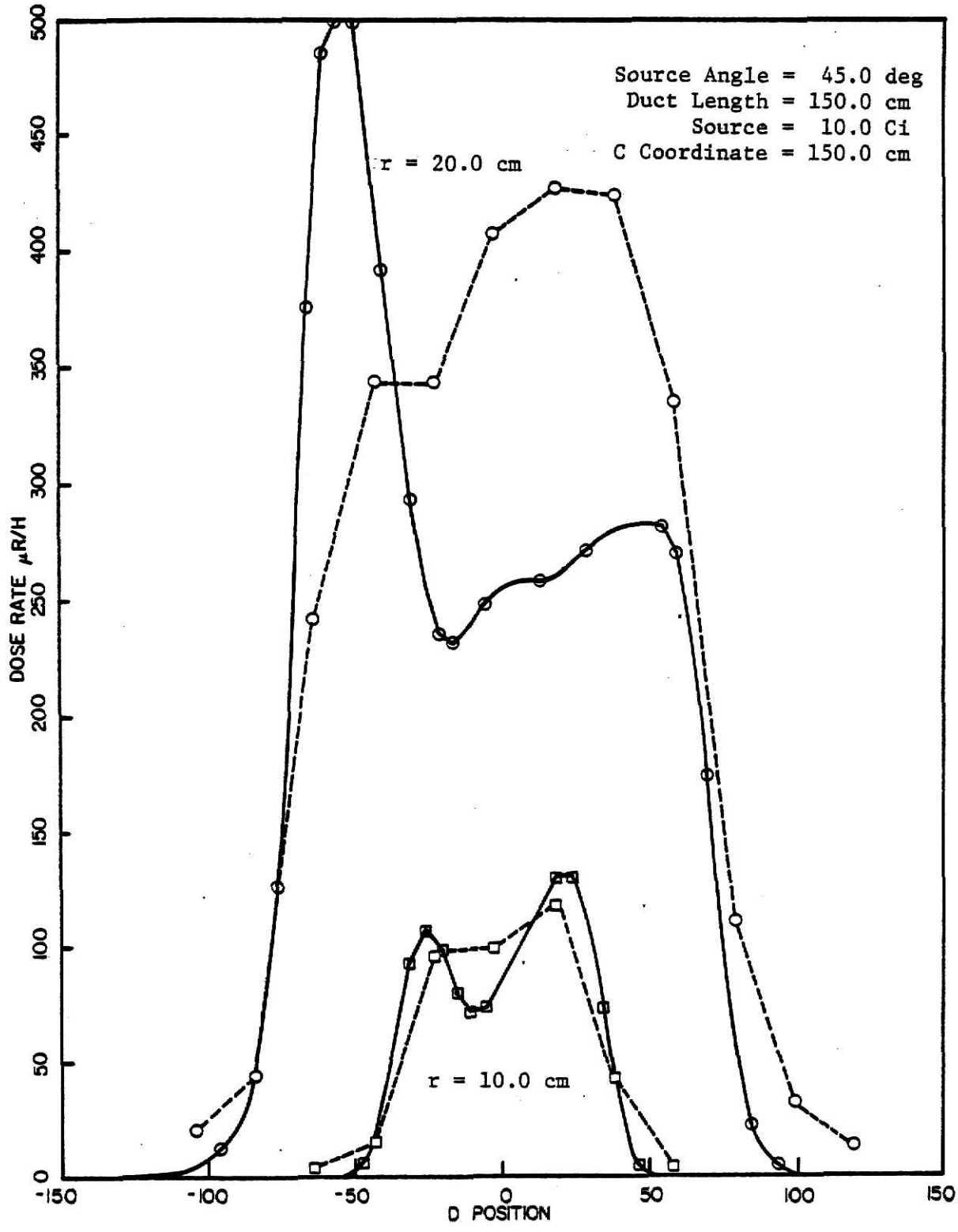

Fig. 6.4. Exposure rate profiles as a function of duct radius for the 150-cm-thick wall (experimental points connected with dashed straight line segments for visual clarity).

TABLE 6.2.

Peak $\left(\frac{C}{E}\right)$'s for Wall Length, L = 150.0 cm

SOURCE ANGLE, θ_s (deg.)	"C" Coordinate (cm)	$\left(\frac{C}{E}\right)_L$	$\left(\frac{C}{E}\right)_D$
	DUCT RADIUS, R = 20.0 cm		
22.5	150.0	----	2.254
22.5	300.0	1.813	0.940
33.0	150.0	1.191	0.790
33.0	300.0	1.813	0.940
45.0	150.0	----	0.688
45.0	300.0	1.740	0.774
60.0	150.0	0.752	0.703
60.0	300.0	0.939	0.645
	DUCT RADIUS, R = 10.0 cm		
22.5	150.0	-----	-----
22.5	300.0	2.091	0.444
33.0	150.0	1.374	1.343
33.0	300.0	1.896	1.578
45.0	150.0	1.081	1.107
45.0	300.0	1.559	0.968
60.0	150.0	0.786	0.894
60.0	300.0	1.000	1.111
	DUCT RADIUS, R = 5.0 cm		
22.5	150.0	2.368	-----
22.5	300.0	2.512	4.330
33.0	150.0	-----	-----
33.0	300.0	2.368	4.069

As illustrated by the preceding figures and tables as well as Appendices A and B, agreement between the calculated and measured exposure rates are typically within a factor of two. It should be noted that the accuracy achieved tends to decline as the aspect ratio of the duct, $(\frac{L}{r})$ grows larger. This result is to be expected since, with increasing aspect ratio, the scattering phenomena within the duct becomes more complex (tending toward multiple scatters). Under these conditions, models assuming single scatters only are not adequate to describe these processes. The solution of these high aspect ratio problems are more in the realm of the transport/albedo codes. Also, the high aspect ratio experiments tended to have extremely severe spatial exposure rate gradients. The corrections allowing direct comparison of this model with the experiment assumed that these gradients were only one-dimensional. However, it is doubtful that these large gradients would vary only across the duct and therefore, should these gradients become too large, comparison of calculation and experiment become questionable.

Throughout this development, the contributions from photons directly penetrating the wall or duct region has not been addressed. For most configurations, there is no discernable evidence of any direct penetration contributions. However, for large ducts and shallow angles there are a few results reported in Appendices A and B where the experimental exposure rates in the range $d < -30$ cm show evidence of direct penetration. This contribution is because, at these shallow angles of illumination and large duct radii, there

is very little material between the source and the detector.

Finally, the models adequately predicted the general shape of the exposure rate distributions. Even where the peak values were off by a factor of two or more the general shape was accurately predicted.

7.0 CONCLUSIONS

The most important result of this research effort has been the compilation of a complete set of benchmark quality gamma-ray streaming data.(12) During the experimental phase, nearly 500 traverses and isodose contours were measured in twenty-five configurations of wall length and duct radius/type. The range of aspect ratios measured was from 1.25 to 15. Results from the experimental phase show that the scattering phenomena are dependent on the angular gamma flux density at the duct mouth. Therefore, normalization of data for distance from the wall and source strength (xS/ρ^2) is possible. With this being the case, distributed sources can be analyzed by multiple application of the models and superposition of the results. Further confidence in the experimental apparatus and procedures is gained from the fact that, upon several occasions, configurations were rerun with different measurement crews and precision of typically ±5% was observed.

Another important finding is that it is the first few centimeters of concrete that are most actively involved in the scattering process. This observation was verified in two results of this research. First, the lip penetration correction integral was found to be very insensitive to where the limit is placed on the angle away from the duct edge past the first 3-4 cm of wall illumination. This finding substantiates one of the basic assumptions of this experiment in that it verifies that a collimated beam illuminating the area 3-4 cm away from the duct edge appears to be, for all practical purposes, a bare source. Secondly, the wall scattering model assumes that the scattering occurs

at an infinitesimal depth into the wall and approximates an integral with that assumption. Surprisingly enough, the wall scattering model proves to be fairly accurate with that assumption made.

8.0 RECOMMENDATIONS

The most interesting recommendations for further research is that of modelling the annular ducts and the off-centerline measurements. Both of these suggestions will undoubtedly prove to be most formidable. Thhe author recommends, for the annuli, a modified source term reflecting the presence of an assumed black body (the annulus) with the general spatial distribution of the air filled duct of the same size. The off-centerline measurements conceivably could be treated in much the same manner as the centerline measurements only with different scattering points to reflect the different geometry of the problem and different relative angular incident gamma flux at the duct mouth.

A further recommendation is, that should the experimental phase be resumed, that a detector of a much smaller physical size and shorter time constant be given serious consideration. While the Reuter-Stokes HPIC performed admirably throughout the course of the experiment, inherent characteristics of a detector 25.4 cm in diameter make working in radiation fields with potentially high spatial gradients very difficult. Additionally, detector with a larger dynamic range would be extremely desirable.

Finally, a computer based data acquisition and control system would prove to be extremely desirable as long as sufficient flexibility in hardware and software are provided for. Thhe proposed system should be capable of performing not only routine data collection, but also of complete traverser control as well as data reduction, storage, and transmission.

9.0 ACKNOWLEDGEMENTS

The author wish to acknowledge the technical and financial support of C. E. Clifford of Radiation Research Associates, Ft. Worth, Texas, and the Japanese industrial consortium represented by Century Research Center Corporation of Tokyo, Japan, for the sponsorship of this research.

Additionally, Drs. Simons, Faw and Shultis have provided technical guidance and support well beyond that required of them as professors and committee members during the course of this experiment. The author wishes to express to them the deepest appreciation for their efforts and support.

Finally, the author wishes to thank the crew of student experimenters that worked throughout the course of the project, especially those involved in double shift duty data gathering at the site. Truly, without the efforts and commitment of these people this research would not have been possible.

10.0 LITERATURE CITED

1. Shepherd, J. L., Glendale, California, private communication, 24 August, 1977.

2. Clifford, C. E., W. Y. Yoon, R. E. Faw, and J. K. Shultis, "Skyshine Benchmark Experiment," Vol. I Report RRA-77802-1, Radiation Research Associates, Fort Worth, Texas, February, 1978, p. 34.

3. Baran, J. A., "Reflection of Cobalt-60 Gamma Rays from Concrete," Ph.D. Dissertation, Kansas State University, 1968, p. 65.

4. Heath, R. L., "Scintillation Spectrometry Gamma-Ray Spectrum Catalogue," IDO-16880-2, August 1964.

5. De Campo, J. A., H. L. Beck, and P. D. Raft, "High pressure Argon Ion Chamber Systems for the Measurement of Environmental Exposure Rates," USAEC Report HASL-260, December, 1972.

6. "Testing of the Reuter-Stokes Area Monitor System," SKYSHINE Report No. 2, Dept. of Nuclear Engineering, Kansas State University, Manhattan, Kansas, November, 1977.

7. Nason, R., "Analysis of Skyshine Spectral Measurements," M.S. Thesis, Kansas State University, 1979.

8. Eisenhauer, C. M., and G. L. Simmons, "Point Isotropic Gamma-Ray Buildup Factors in Concrete," NS&E 56, pp. 263-70, 1975.

9. Clifford, C. E., G. G. Simons, R. E. Faw, and J. K. Shultis, "Benchmark Gamma Ray Streaming", Annual Progess Report, FY1978, Radiation Research Associates, Fort Worth, Texas, March, 1979.

10. Photon Cross Sections, Attenuation Coeficients, and Energy Absorption Coeficients From 10 keV to 100 GeV , (NSRDS-NBS 29), 1969.

11. Morgan, K. Z., and J. E. Turner, Principles of Radiation Protection , pp. 271-2, Wiley, 1967.

12. Simons, G. G., R. E. Faw, J. K. Shultis, and D. L. Stucker, Benchmark Gamma-Ray Streaming Experiments Final Report, Dept. of Nuclear Engineering, Kansas State University, Manhattan, Kansas, January, 1980.

APPENDIX A

The figures presented in this section are all of a standard format generated on the KSU ITEL System 370 computer. The legend in the upper right hand corner of each figure uniquely identifies that figure. Table A.1 presents a summary of the figures in this section as well as the page number for each figure. All figures in this section are for the 100.0 cm wall.

TABLE A.1

Duct Radius (cm)	Source Angle (deg)	Figure Numbers	Page
20.0	33.0[a]	A.1,2,3	147-49
20.0	45.0[a]	A.4,5,6	150-52
20.0	60.0[a]	A.7,8,9	153-55
10.0	22.5[a]	A.10,11,12	156-58
10.0	33.0[a]	A.13,14,15	159-61
10.0	45.0[a]	A.16,17,18	162-64
10.0	60.0[a]	A.19,20,21	165-67
10.0	60.0[b]	A.22,23,24	168-70
5.0	22.5[a]	A.25,26,27	171-73
5.0	33.0[a]	A.28,29,30	174-76
5.0	45.0[a]	A.31,32,33	177-79

a - rho equal to 300.0 cm
b - rho equal to 400.0 cm

THE FOLLOWING PAGES ARE BADLY SPECKLED DUE TO BEING POOR QUALITY PHOTOCOPIES.

THIS IS AS RECEIVED FROM CUSTOMER.

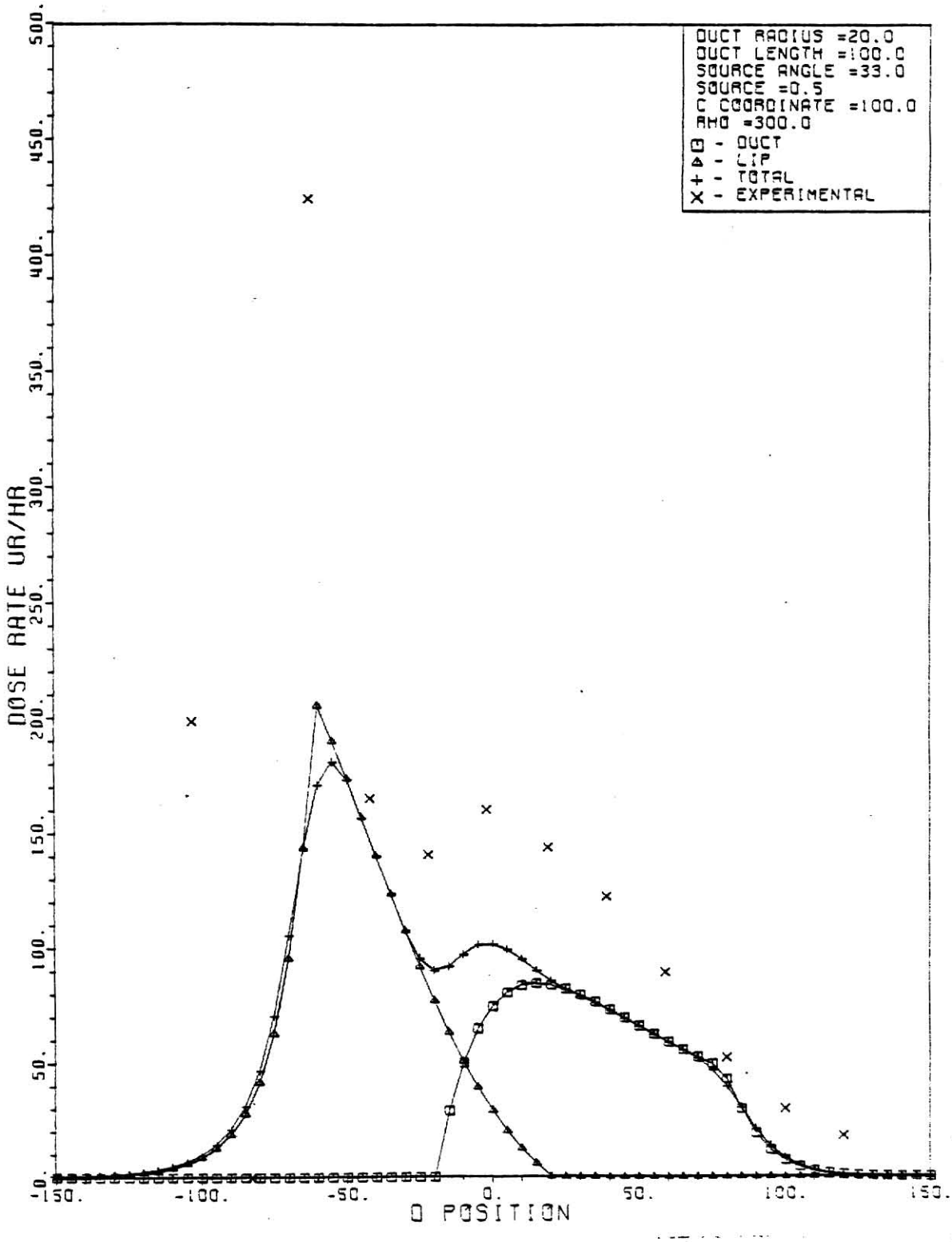
DUCT RADIUS =20.0
DUCT LENGTH =100.0
SOURCE ANGLE =33.0
SOURCE =0.5
C COORDINATE =100.0
RHO =300.0
⊡ - DUCT
△ - LIP
+ - TOTAL
X - EXPERIMENTAL
DOSE RATE UR/HR
0.
50.
100.
150.
200.
250.
300.
350.
400.
450.
500.
-150.
-100.
-50.
0.
50.
100.
150.
Θ POSITION

Fig. A.1.

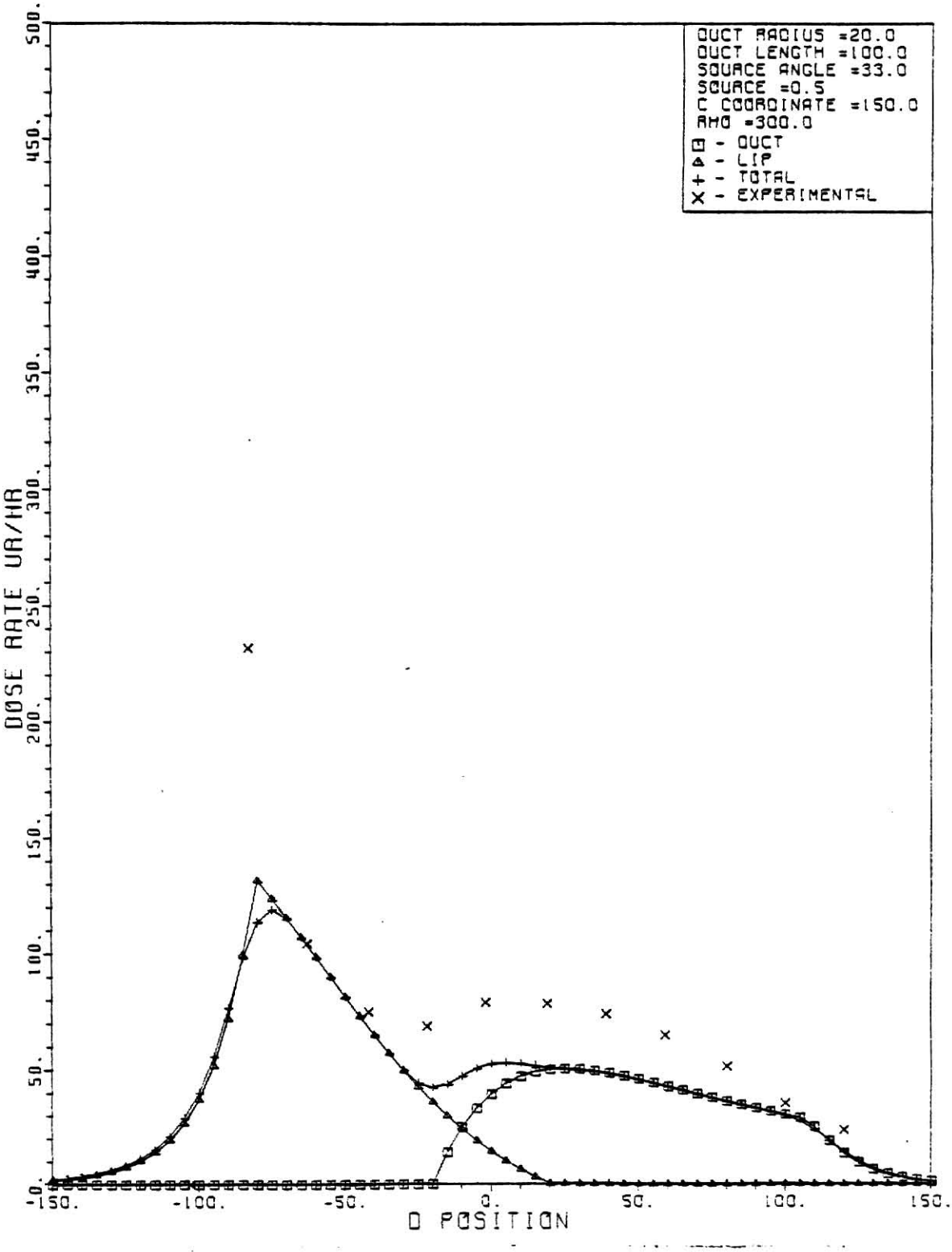
DUCT RADIUS =20.0
DUCT LENGTH =100.0
SOURCE ANGLE =33.0
SOURCE =0.5
C COORDINATE =150.0
AMO =300.0
⊡ - DUCT
△ - LIP
+ - TOTAL
× - EXPERIMENTAL
DOSE RATE UR/HR
0.
50.
100.
150.
200.
250.
300.
350.
400.
450.
500.
-150.
-100.
-50.
0.
50.
100.
150.
D POSITION

Fig. A.2.

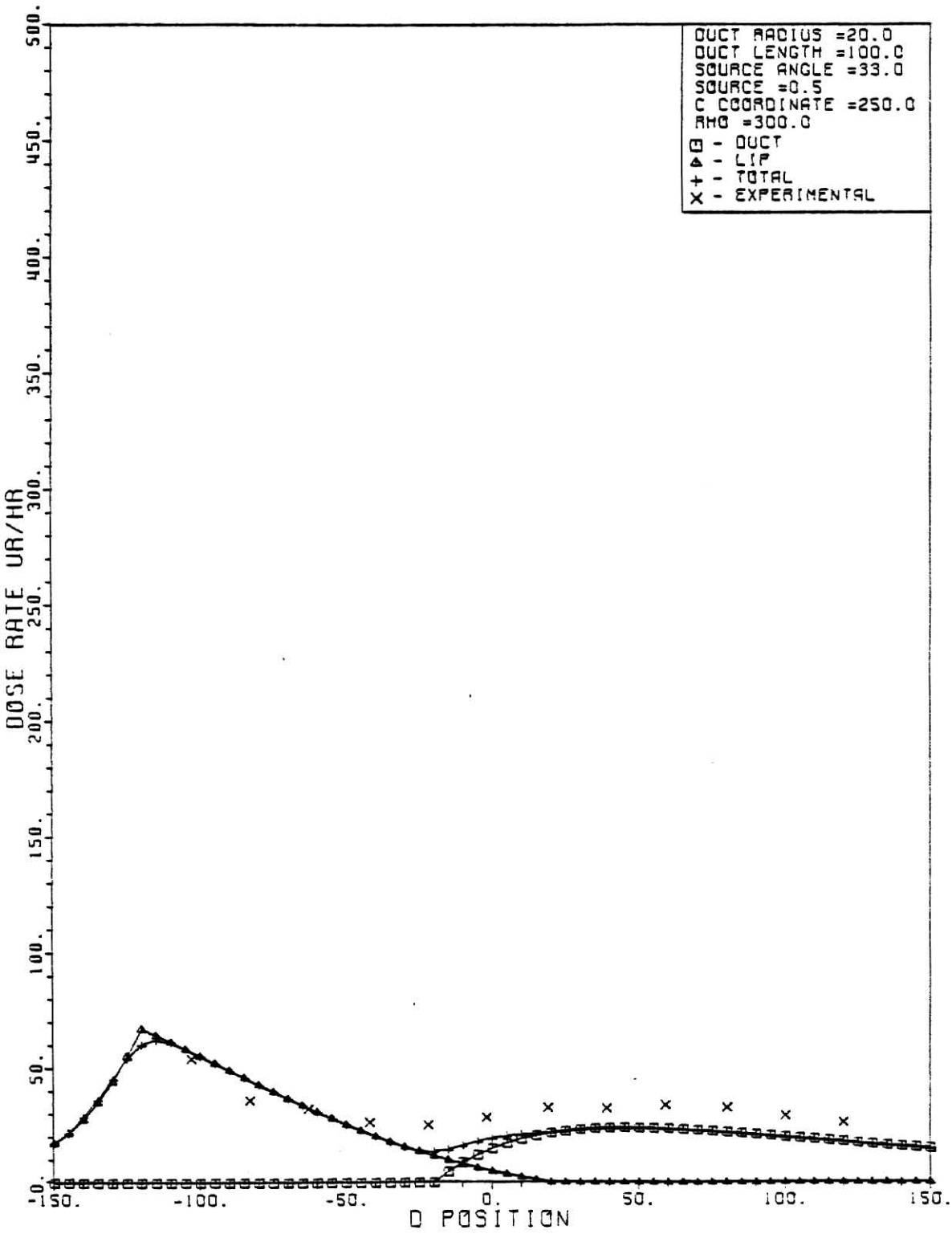
DUCT RADIUS =20.0
DUCT LENGTH =100.0
SOURCE ANGLE =33.0
SOURCE =0.5
C COORDINATE =250.0
RHO =300.0
⊡ - DUCT
▲ - LIP
+ - TOTAL
× - EXPERIMENTAL
DOSE RATE UR/HR
0.
50.
100.
150.
200.
250.
300.
350.
400.
450.
500.
-150.
-100.
-50.
0.
50.
100.
150.
D POSITION

Fig. A.3.

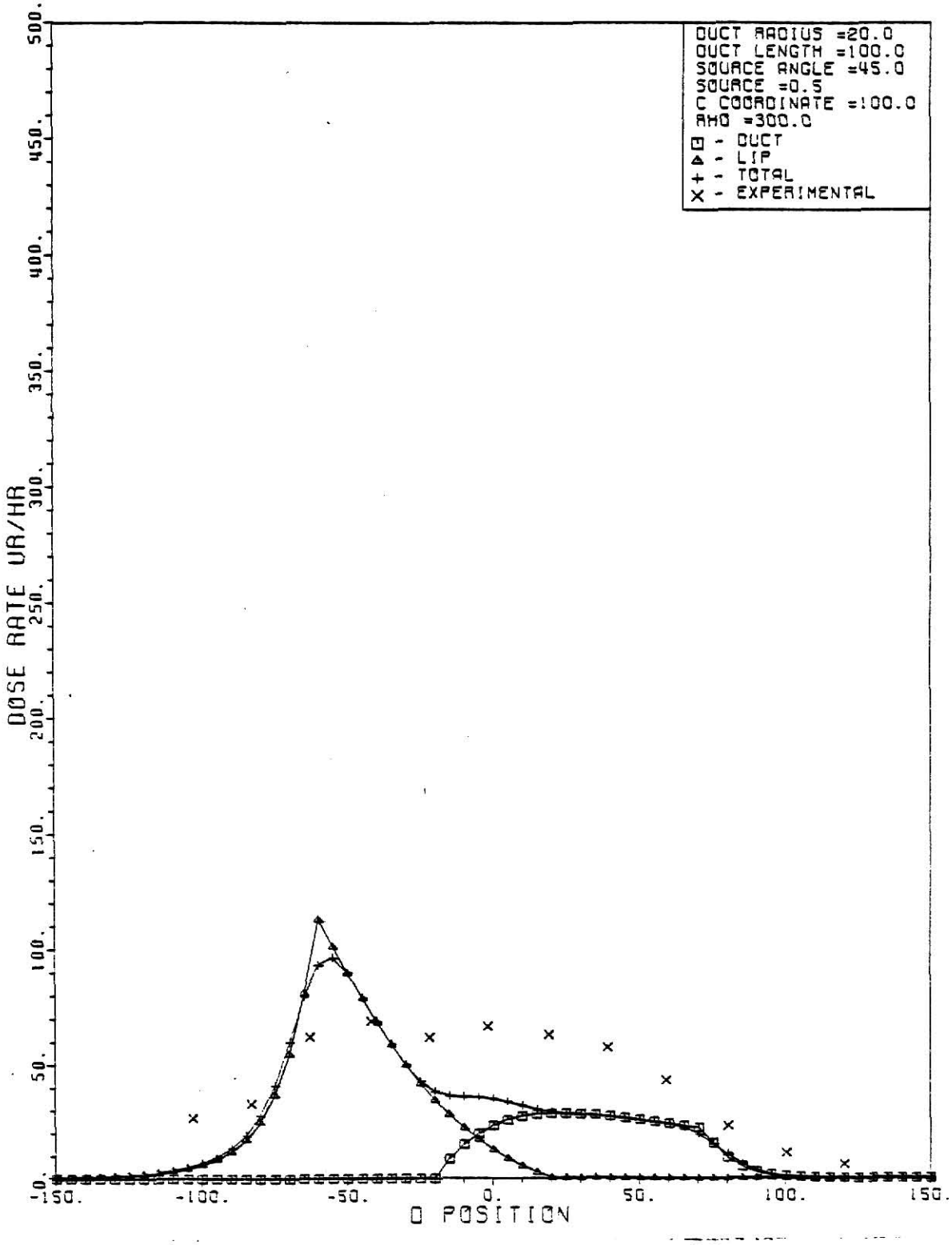
DUCT RADIUS =20.0
DUCT LENGTH =100.0
SOURCE ANGLE =45.0
SOURCE =0.5
C COORDINATE =100.0
RHO =300.0
□ - DUCT
△ - LIP
+ - TOTAL
× - EXPERIMENTAL
DOSE RATE UR/HR
0.
50.
100.
150.
200.
250.
300.
350.
400.
450.
500.
-150.
-100.
-50.
0.
50.
100.
150.
Θ POSITION

Fig. A.4.

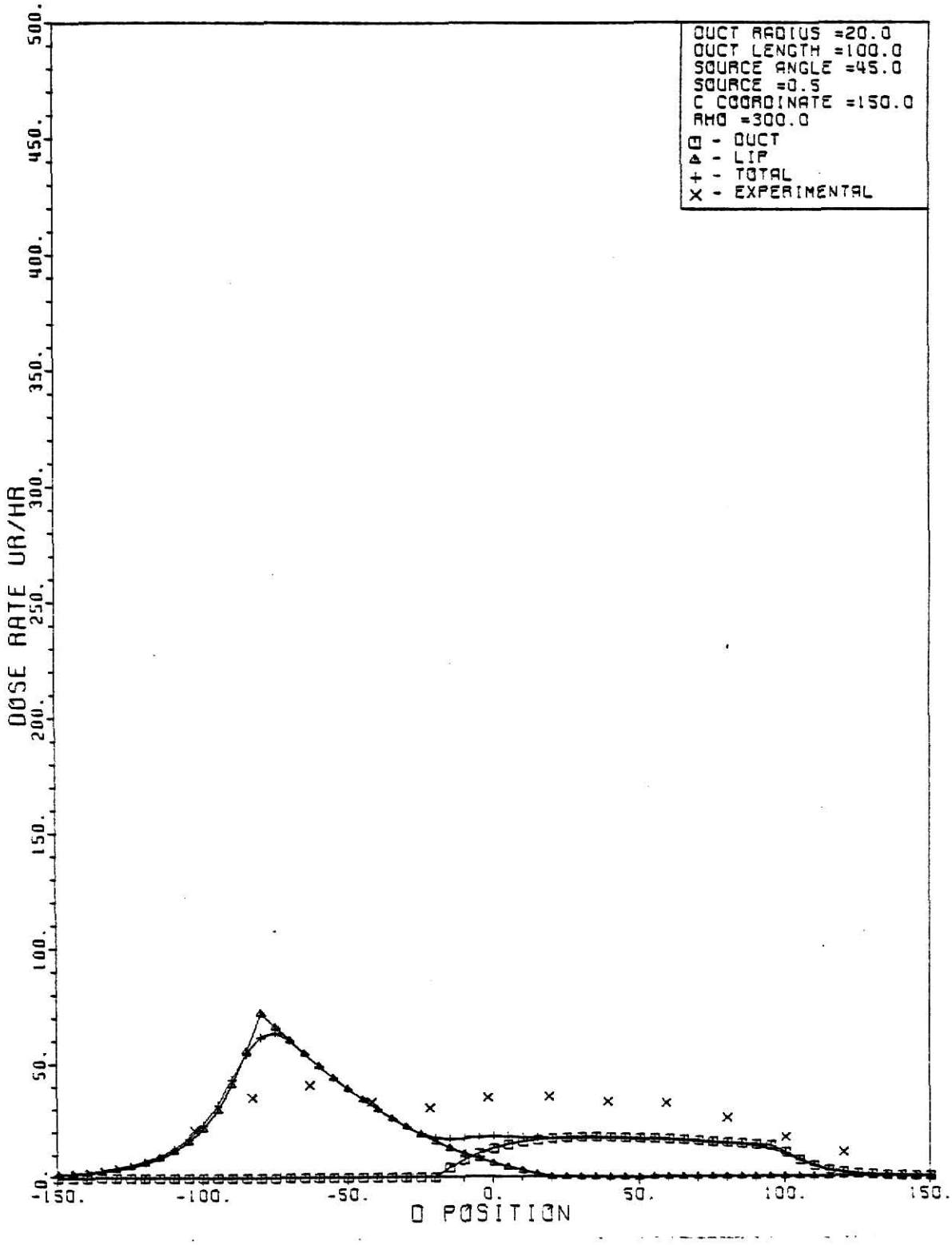
DUCT RADIUS =20.0
DUCT LENGTH =100.0
SOURCE ANGLE =45.0
SOURCE =0.5
C COORDINATE =150.0
RHO =300.0
□ - DUCT
Δ - LIP
+ - TOTAL
× - EXPERIMENTAL
DOSE RATE UR/HR
0.
50.
100.
150.
200.
250.
300.
350.
400.
450.
500.
-150.
-100.
-50.
0.
50.
100.
150.
D POSITION

Fig. A.5.

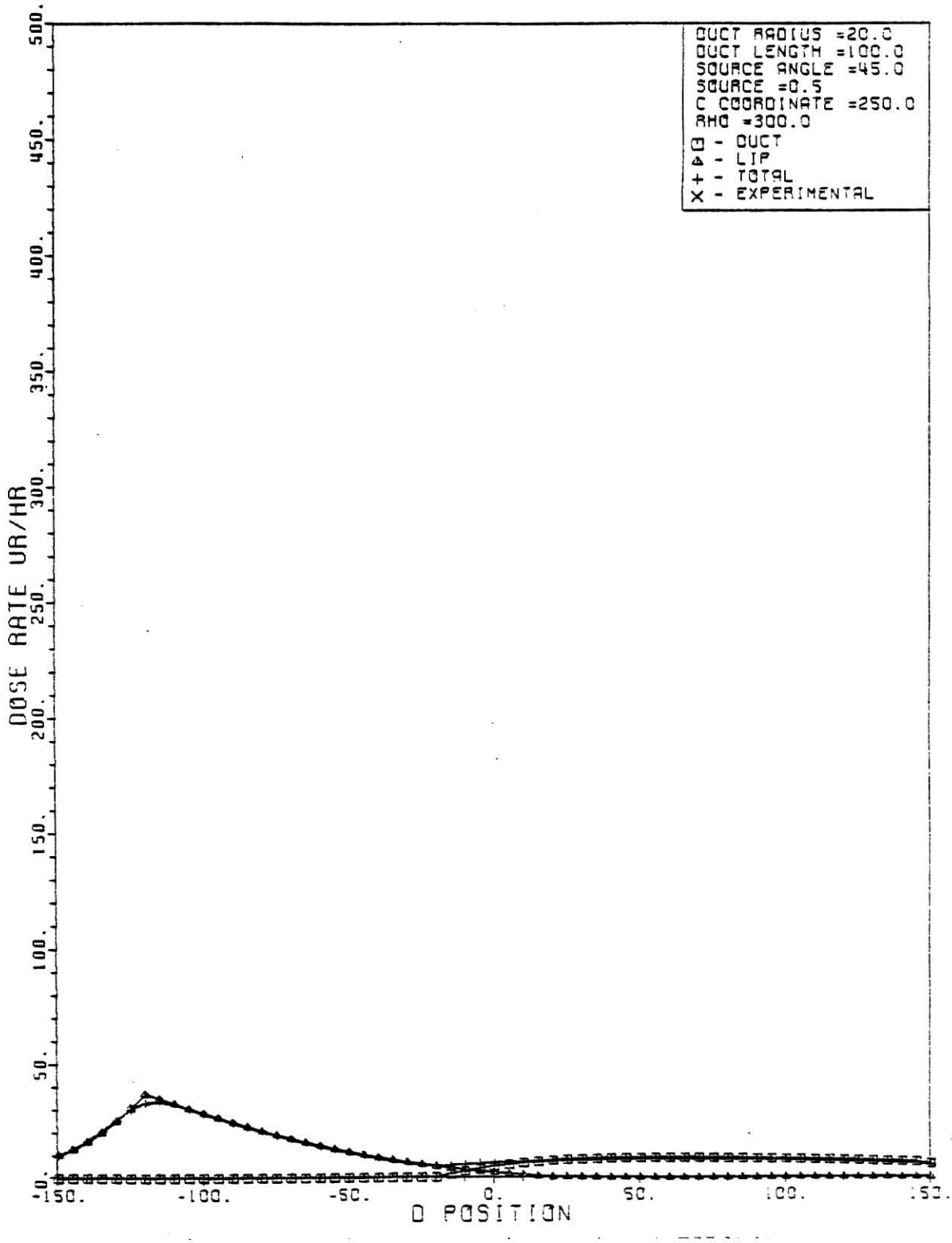
DUCT RADIUS =20.0
DUCT LENGTH =100.0
SOURCE ANGLE =45.0
SOURCE =0.5
C COORDINATE =250.0
RHO =300.0
□ - DUCT
Δ - LIP
+ - TOTAL
X - EXPERIMENTAL
DOSE RATE UR/HR
0.
50.
100.
150.
200.
250.
300.
350.
400.
450.
500.
-150.
-100.
-50.
0.
50.
100.
150.
D POSITION

Fig. A.6.

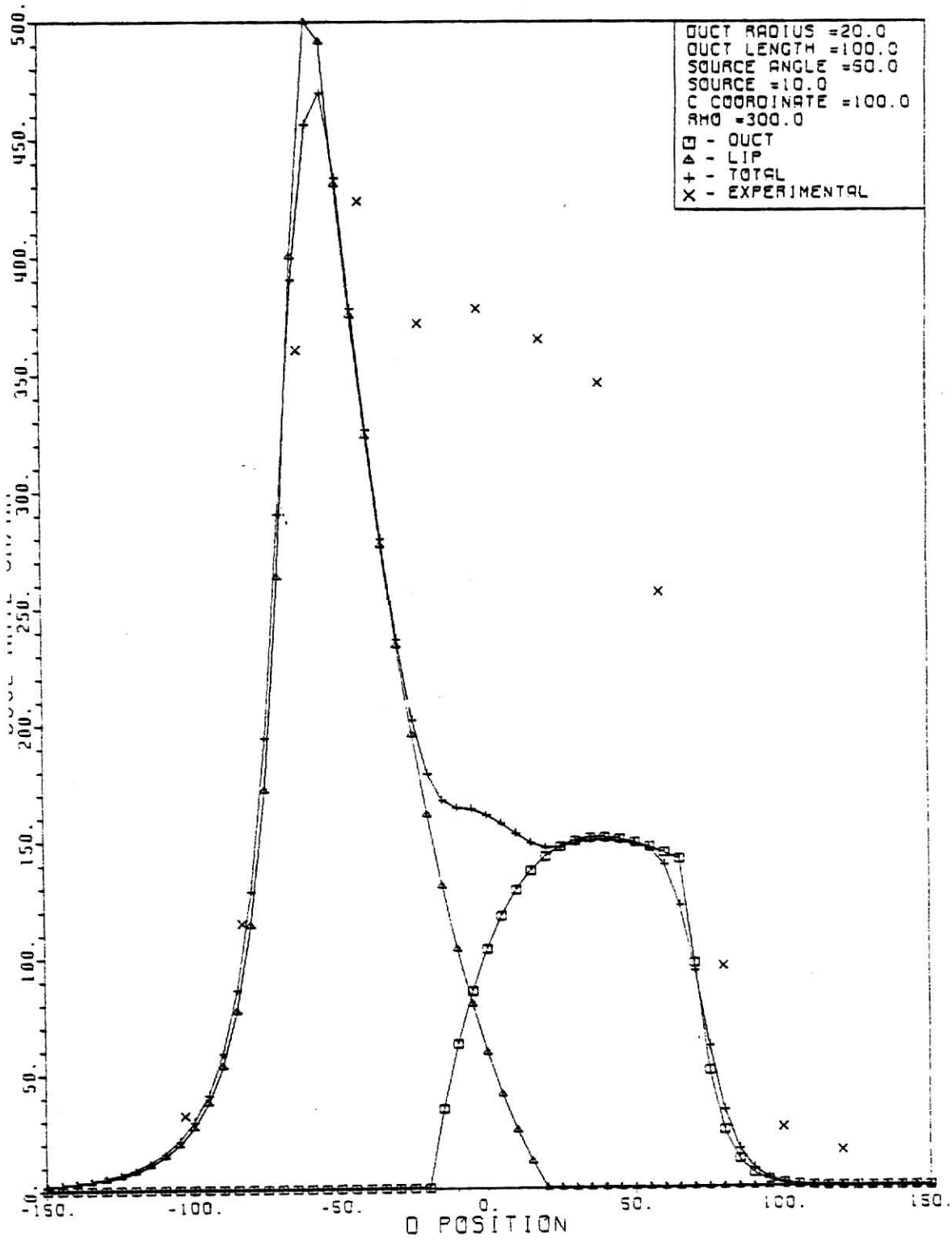
DUCT RADIUS =20.0
DUCT LENGTH =100.0
SOURCE ANGLE =60.0
SOURCE =10.0
C COORDINATE =100.0
RHO =300.0
⊡ - DUCT
▲ - LIP
+ - TOTAL
× - EXPERIMENTAL
500.
450.
400.
350.
300.
250.
200.
150.
100.
50.
0.
-150.
-100.
-50.
0.
50.
100.
150.
Θ POSITION

Fig. A.7.

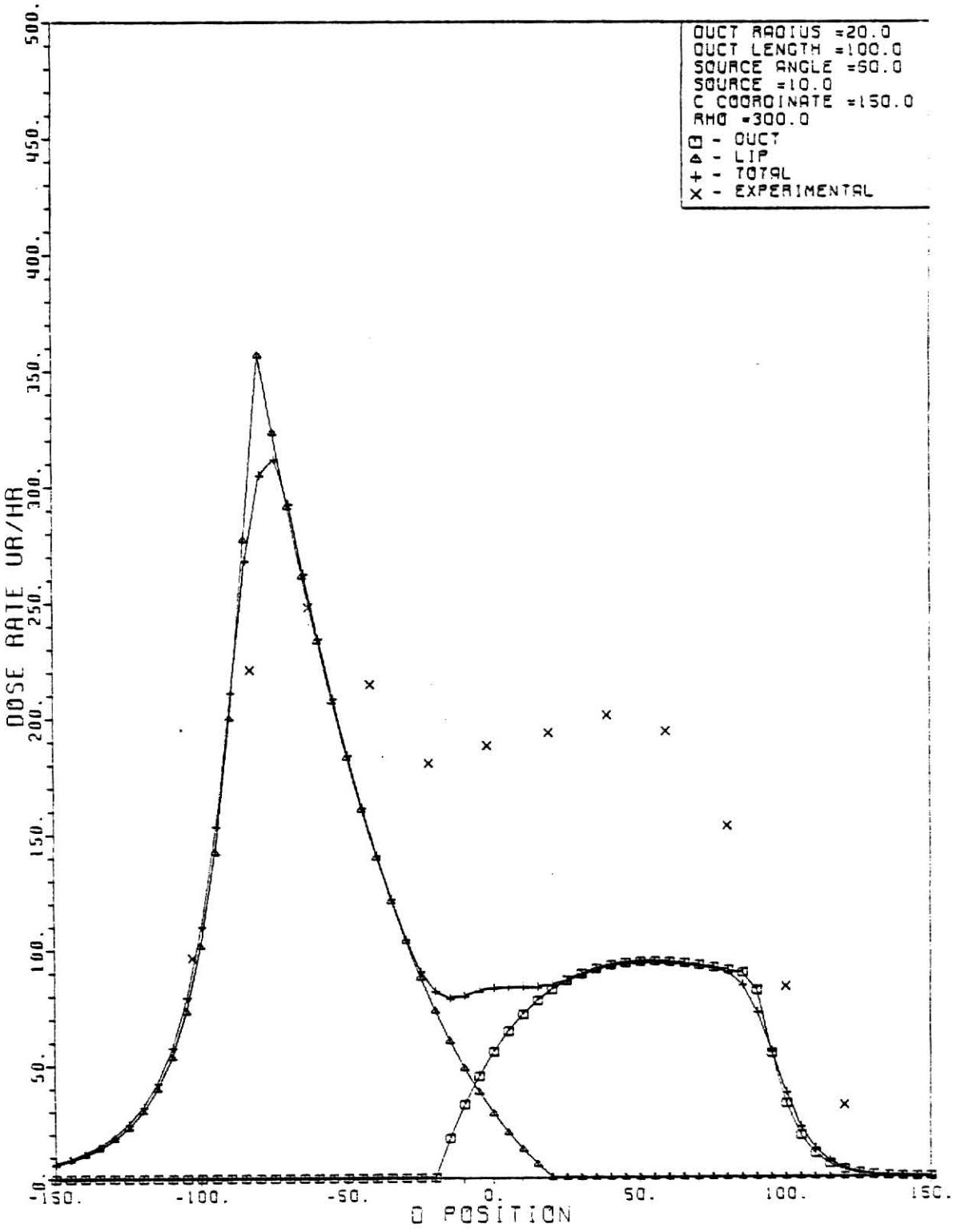
DUCT RADIUS =20.0
DUCT LENGTH =100.0
SOURCE ANGLE =60.0
SOURCE =10.0
C COORDINATE =150.0
RHO =300.0
□ - DUCT
△ - LIP
+ - TOTAL
× - EXPERIMENTAL
DOSE RATE UR/HR
0.
50.
100.
150.
200.
250.
300.
350.
400.
450.
500.
-150.
-100.
-50.
0.
50.
100.
150.
D POSITION

Fig. A.8.

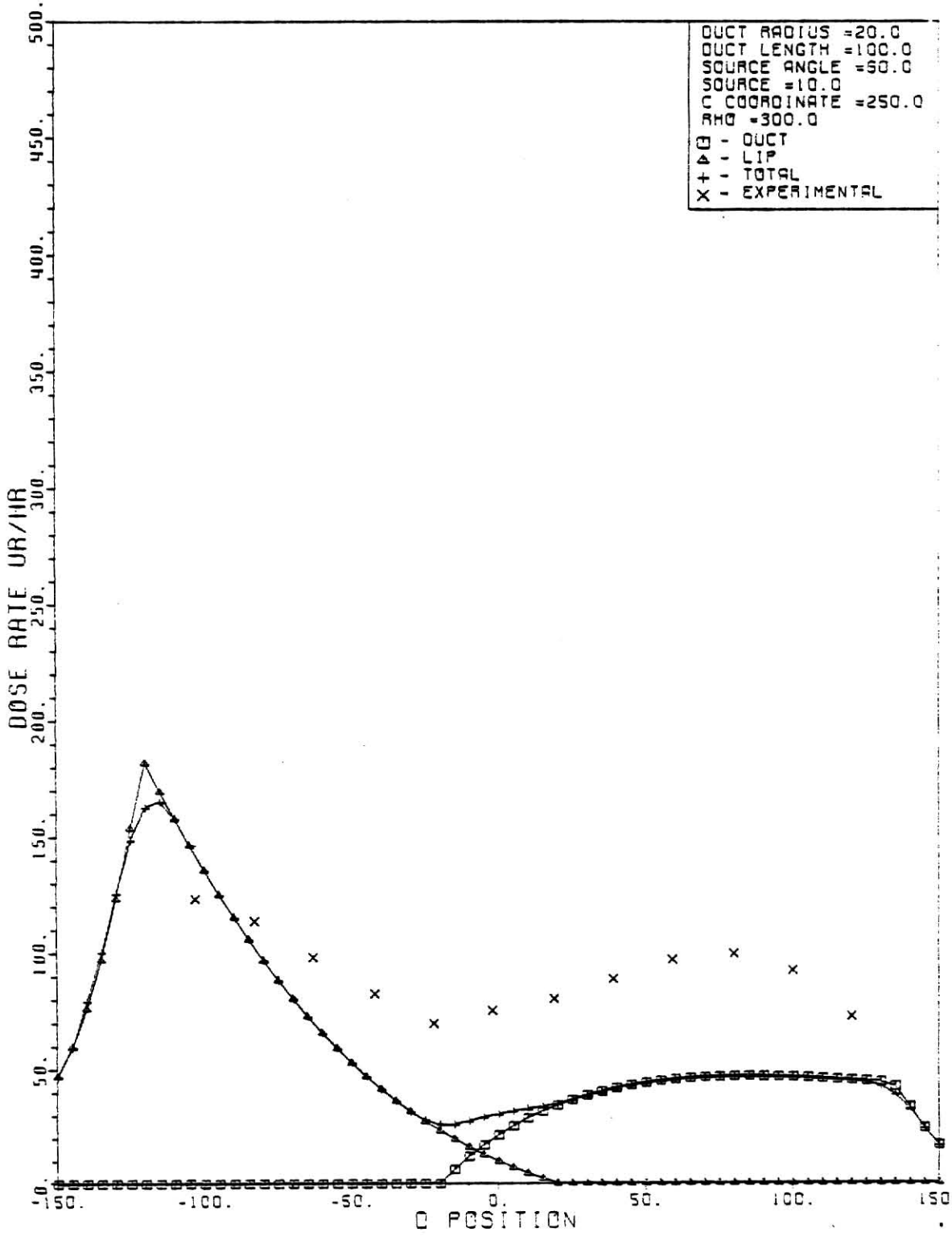
DUCT RADIUS =20.0
DUCT LENGTH =100.0
SOURCE ANGLE =60.0
SOURCE =10.0
C COORDINATE =250.0
RHO =300.0
□ - DUCT
△ - LIP
+ - TOTAL
× - EXPERIMENTAL
DOSE RATE UR/HR
0.
50.
100.
150.
200.
250.
300.
350.
400.
450.
500.
-150.
-100.
-50.
0.
50.
100.
150.
Q POSITION

Fig. A.9.

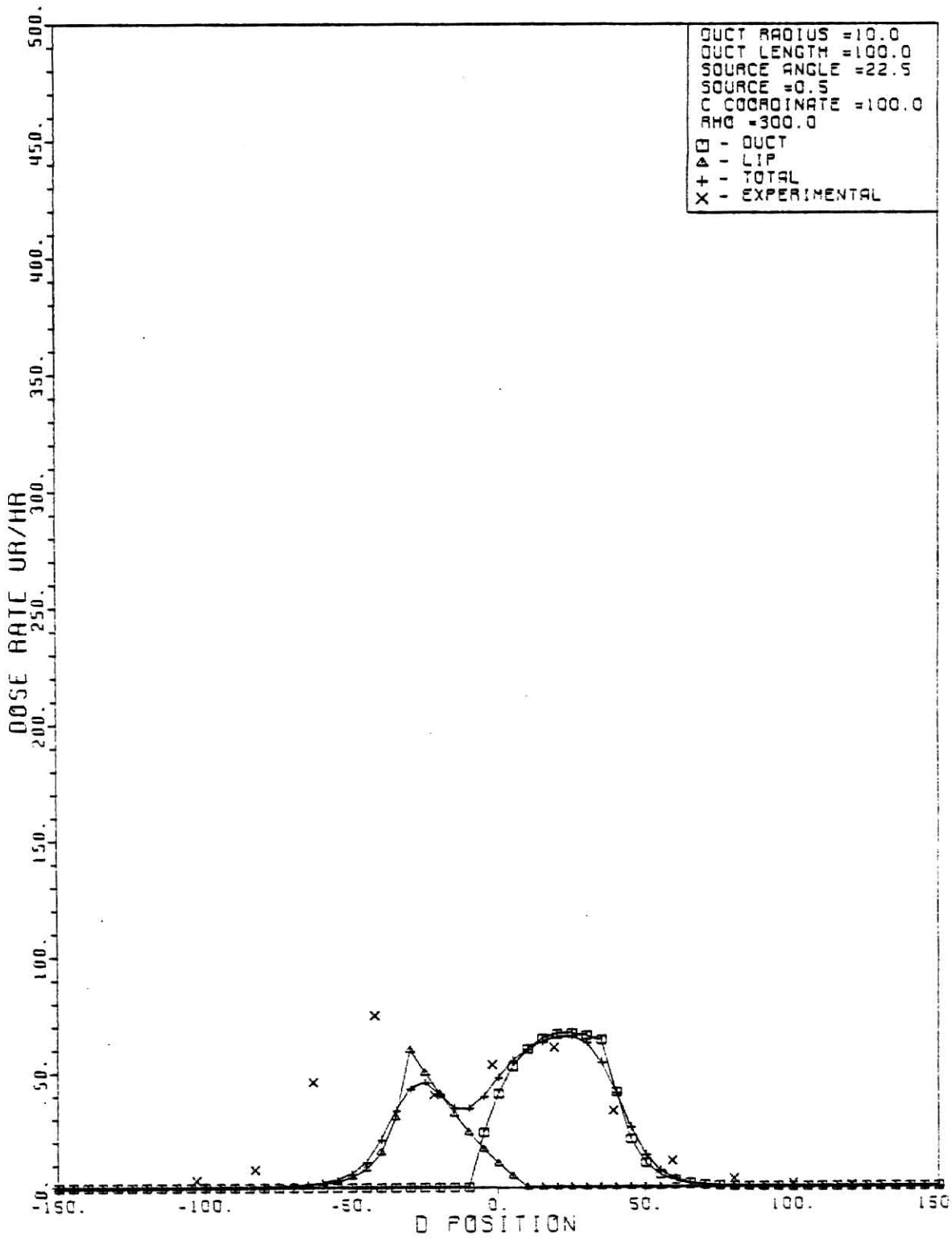
DUCT RADIUS =10.0
DUCT LENGTH =100.0
SOURCE ANGLE =22.5
SOURCE =0.5
C COORDINATE =100.0
RHO =300.0
□ - DUCT
△ - LIP
+ - TOTAL
× - EXPERIMENTAL
DOSE RATE UR/HR
0.
50.
100.
150.
200.
250.
300.
350.
400.
450.
500.
-150.
-100.
-50.
0.
50.
100.
150.
D POSITION

Fig. A.10.

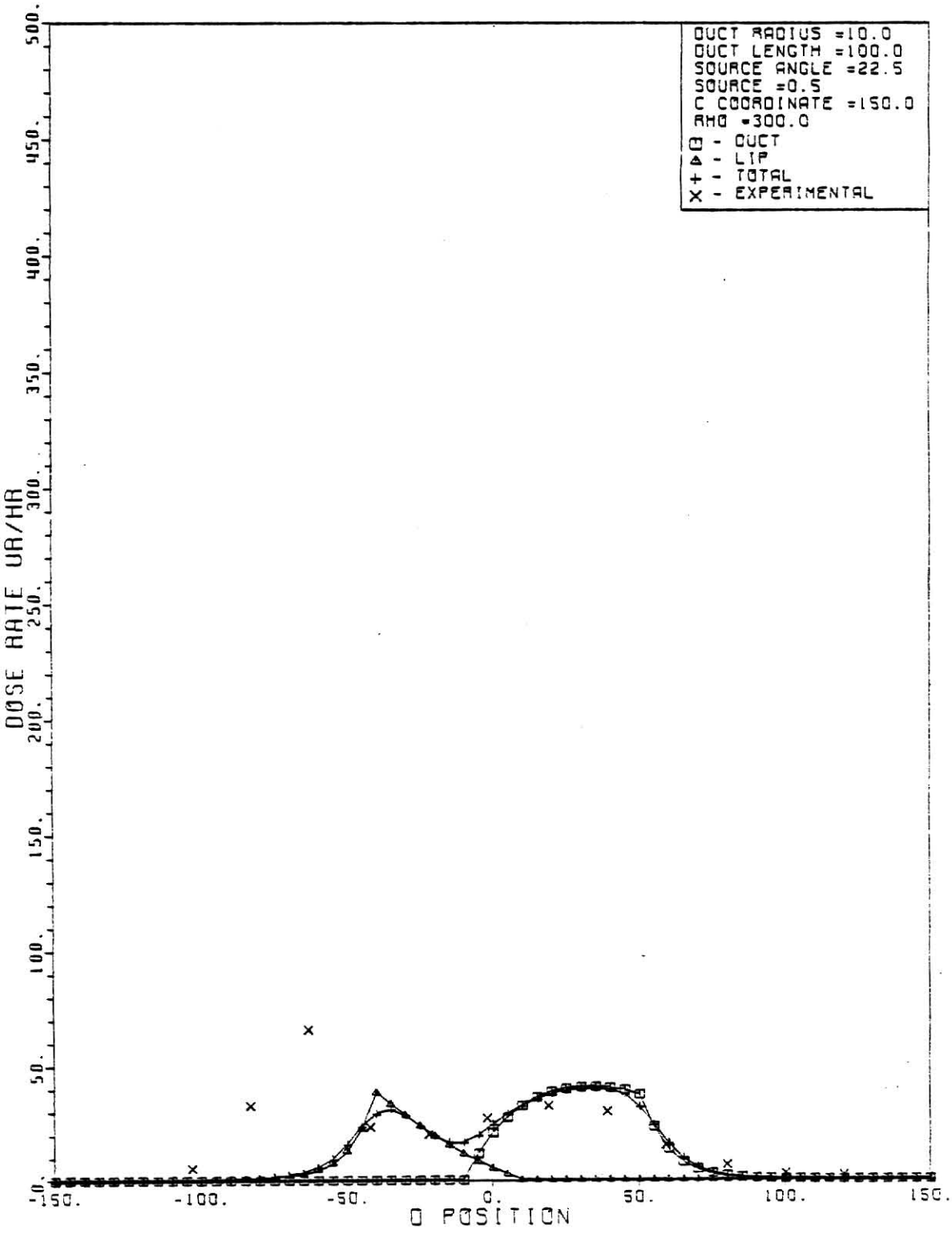
DUCT RADIUS =10.0
DUCT LENGTH =100.0
SOURCE ANGLE =22.5
SOURCE =0.5
C COORDINATE =150.0
RHO =300.0
□ - DUCT
Δ - LIP
+ - TOTAL
× - EXPERIMENTAL
DOSE RATE UR/HR
0.
50.
100.
150.
200.
250.
300.
350.
400.
450.
500.
-150.
-100.
-50.
0.
50.
100.
150.
Θ POSITION

Fig. A.11.

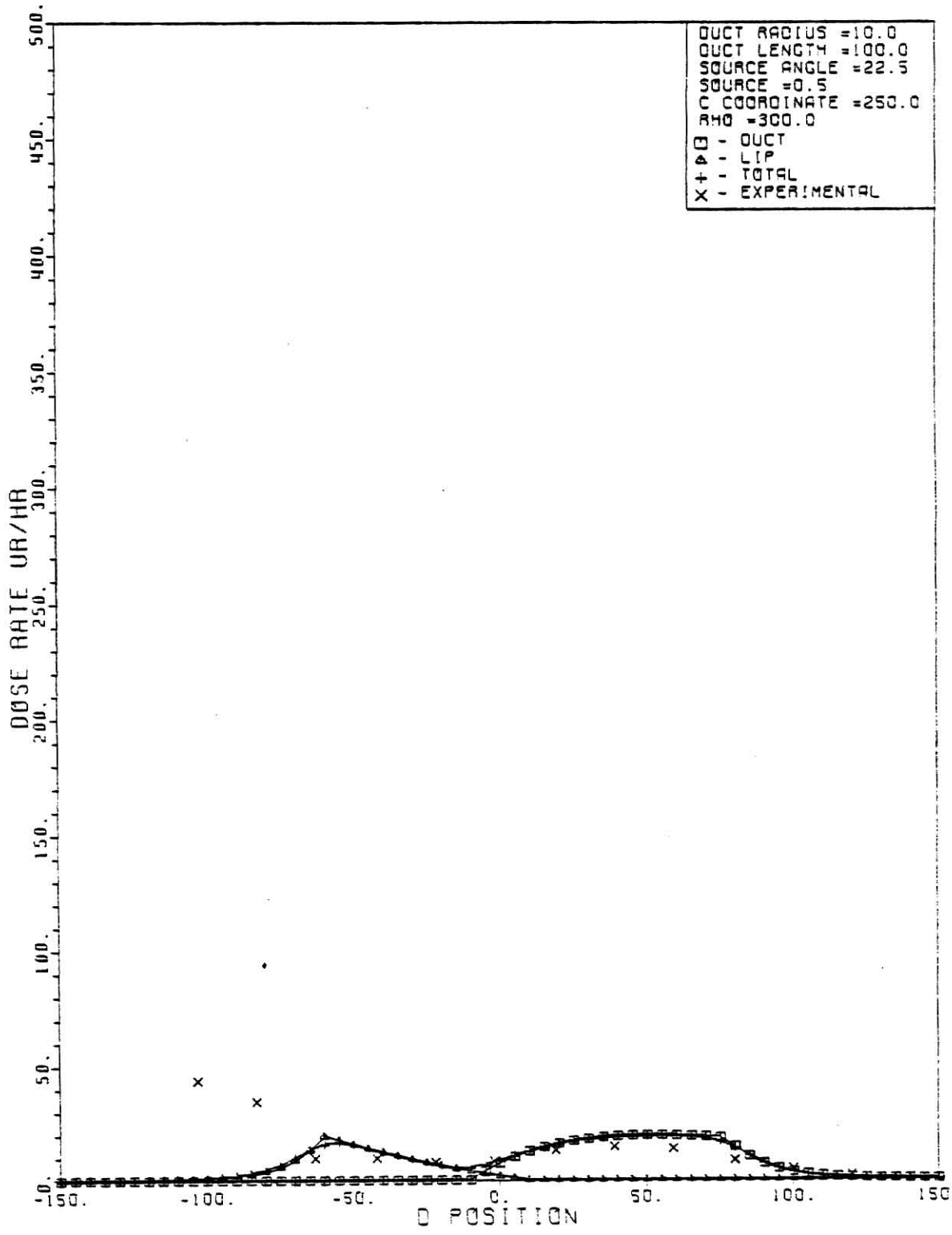
DUCT RADIUS =10.0
DUCT LENGTH =100.0
SOURCE ANGLE =22.5
SOURCE =0.5
C COORDINATE =250.0
RHO =300.0
□ - DUCT
◆ - LIP
+ - TOTAL
× - EXPERIMENTAL
DOSE RATE UR/HR
0.
50.
100.
150.
200.
250.
300.
350.
400.
450.
500.
-150.
-100.
-50.
0.
50.
100.
150
D POSITION

Fig. A.12.

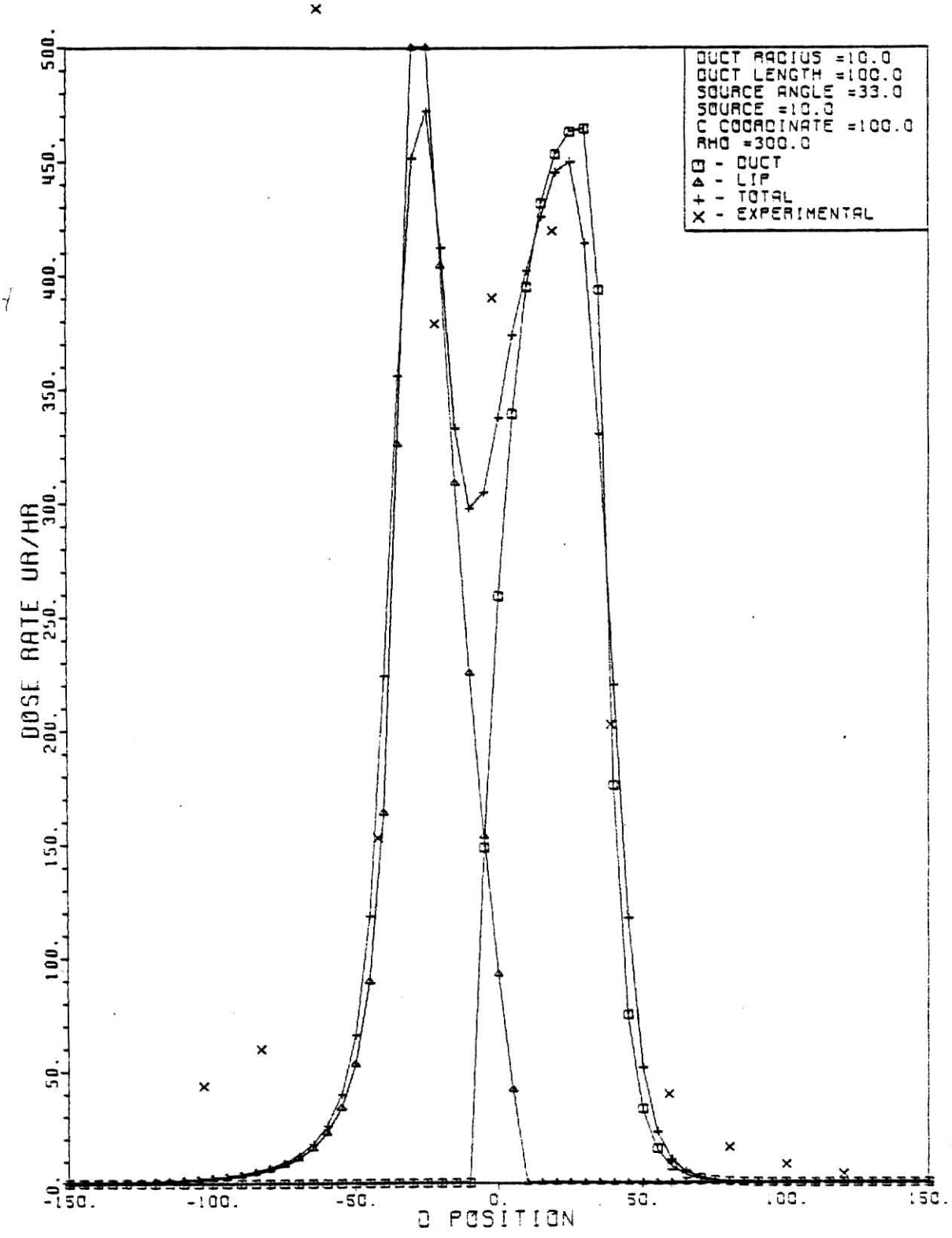
DUCT RADIUS =10.0
DUCT LENGTH =100.0
SOURCE ANGLE =33.0
SOURCE =10.0
C COORDINATE =100.0
RHO =300.0
□ - DUCT
△ - LIP
+ - TOTAL
× - EXPERIMENTAL
DOSE RATE UR/HR
D POSITION
-150.
-100.
-50.
0.
50.
100.
150.
-0.
50.
100.
150.
200.
250.
300.
350.
400.
450.
500.

Fig. A.13.

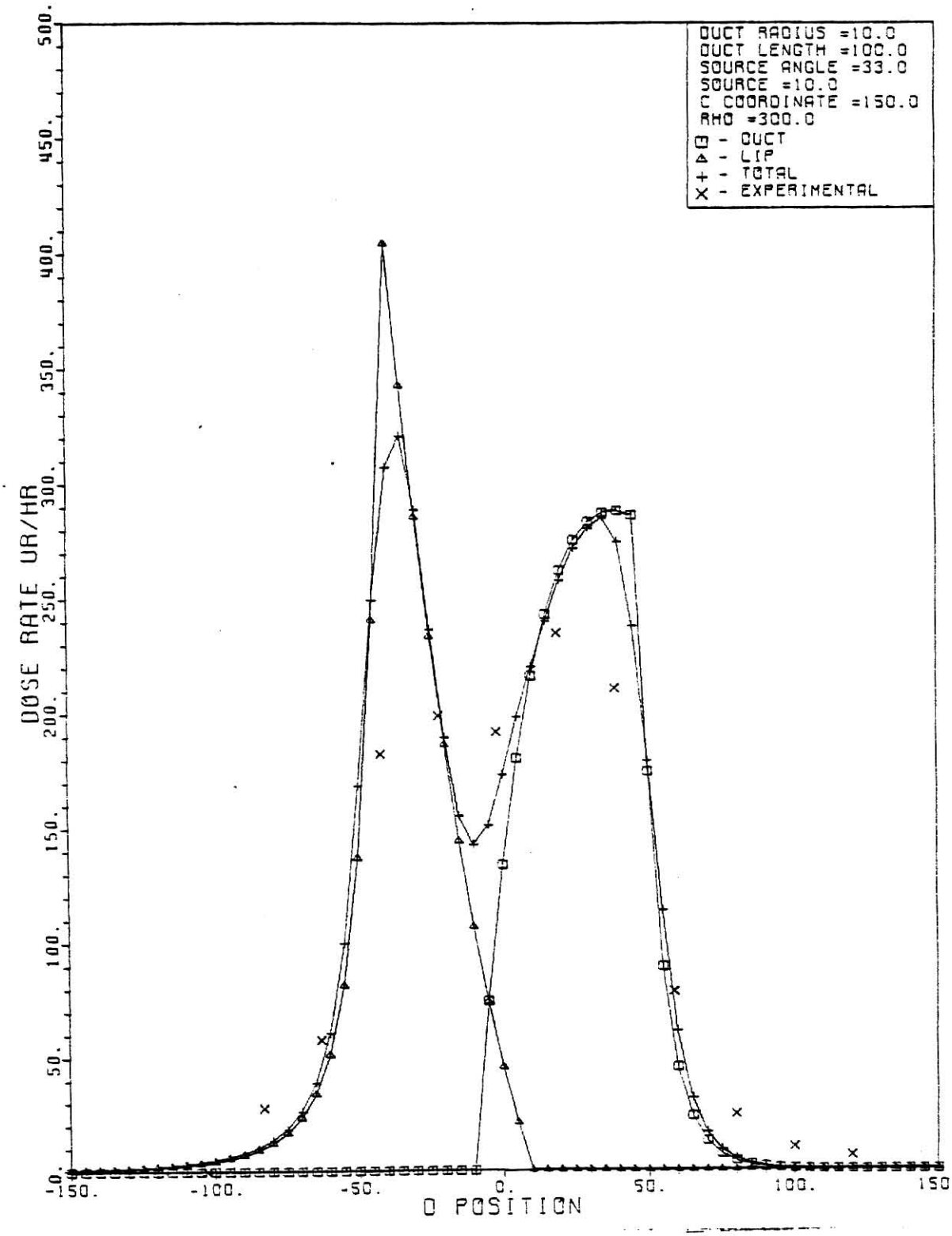
DUCT RADIUS =10.0
DUCT LENGTH =100.0
SOURCE ANGLE =33.0
SOURCE =10.0
C COORDINATE =150.0
RHO =300.0
□ - DUCT
△ - LIP
+ - TOTAL
X - EXPERIMENTAL
DOSE RATE UR/HR
500.
450.
400.
350.
300.
250.
200.
150.
100.
50.
-0.
-150.
-100.
-50.
0.
50.
100.
150
O POSITION

Fig. A.14.

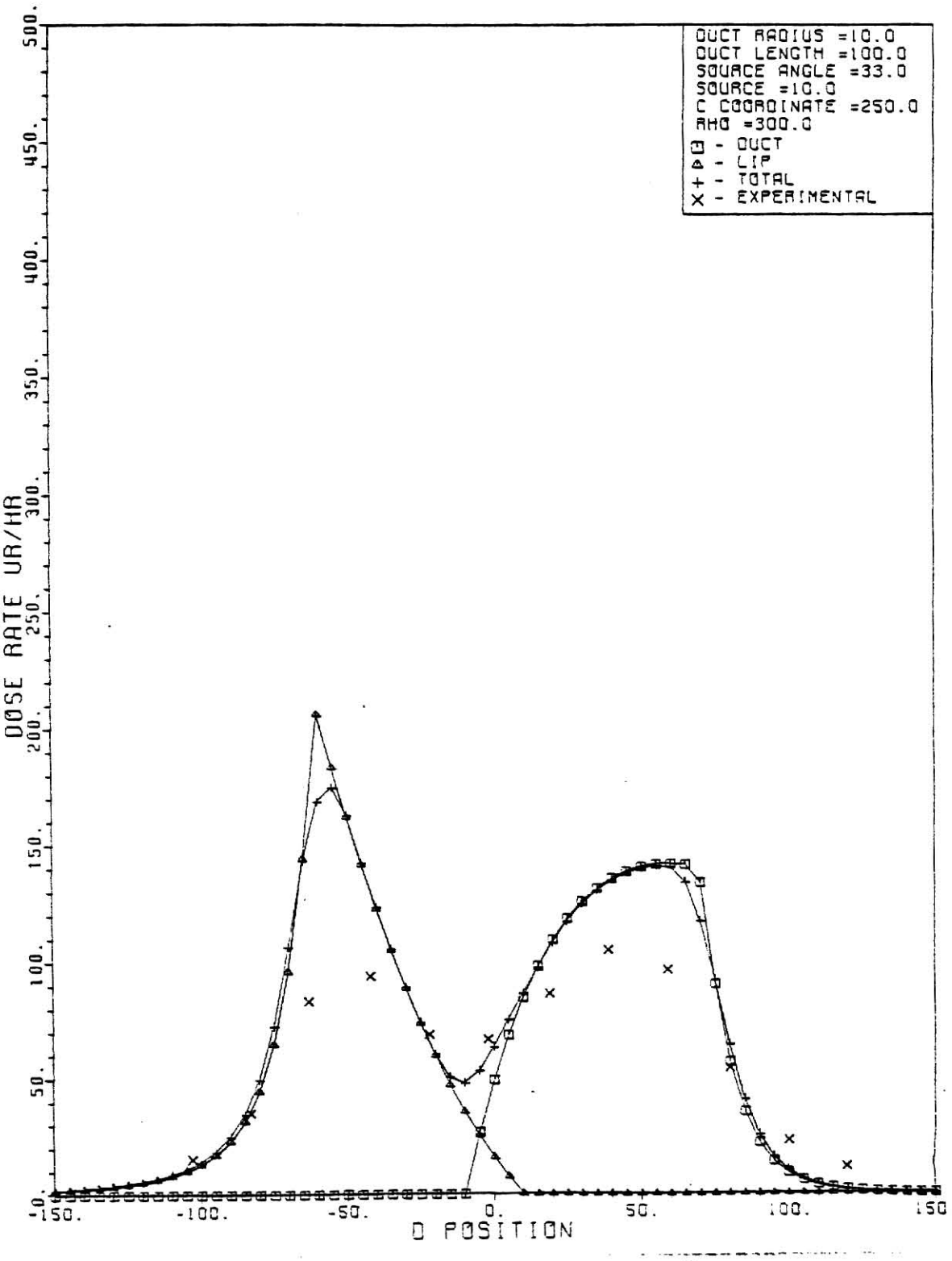
DUCT RADIUS =10.0
DUCT LENGTH =100.0
SOURCE ANGLE =33.0
SOURCE =10.0
C COORDINATE =250.0
RHO =300.0
□ - DUCT
Δ - LIP
+ - TOTAL
× - EXPERIMENTAL
DOSE RATE UR/HR
0.
50.
100.
150.
200.
250.
300.
350.
400.
450.
500.
-150.
-100.
-50.
0.
50.
100.
150.
D POSITION

Fig. A.15.

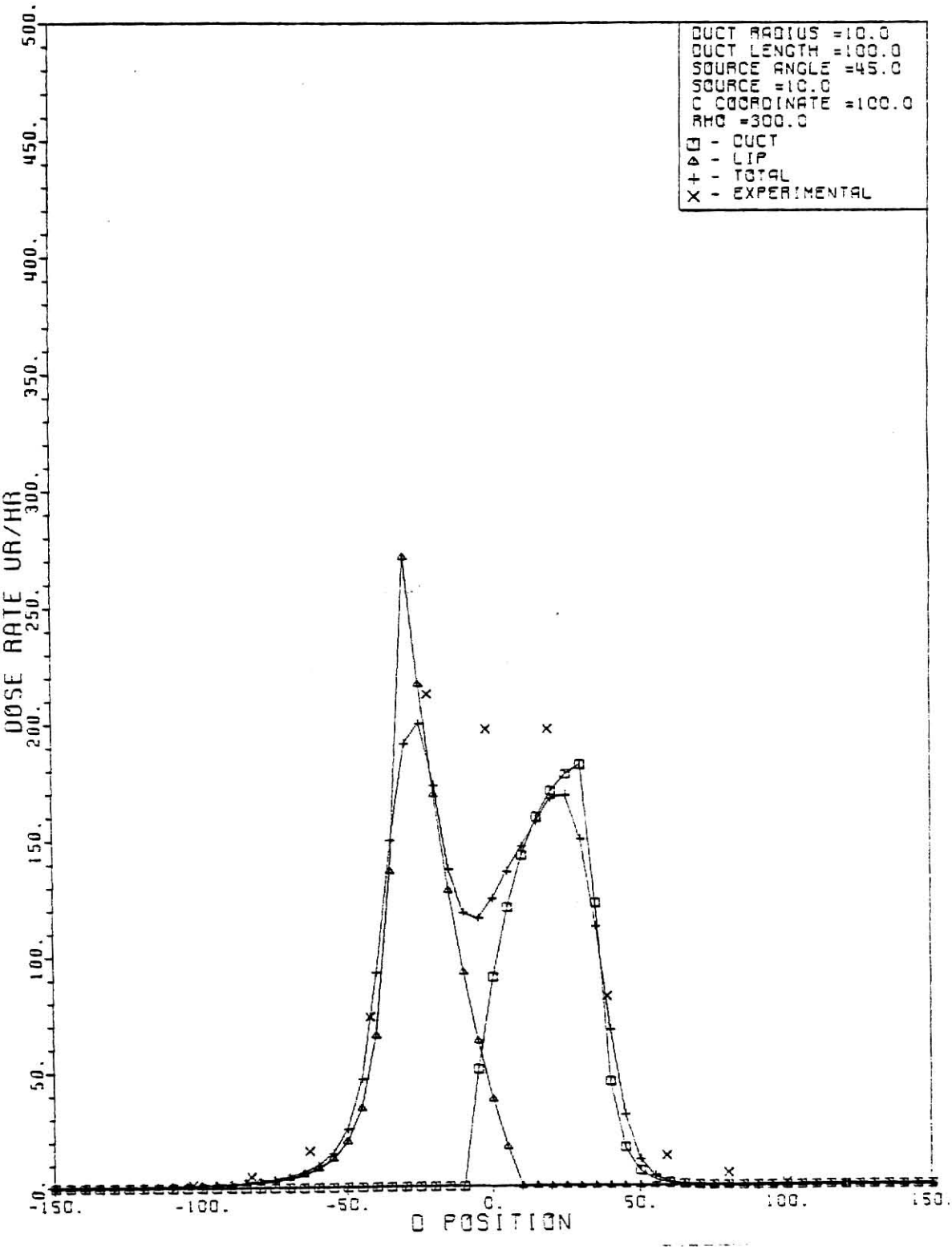
DUCT RADIUS =10.0
DUCT LENGTH =100.0
SOURCE ANGLE =45.0
SOURCE =10.0
C COORDINATE =100.0
RHO =300.0
□ - DUCT
△ - LIP
+ - TOTAL
× - EXPERIMENTAL
DOSE RATE UR/HR
0.
50.
100.
150.
200.
250.
300.
350.
400.
450.
500.
-150.
-100.
-50.
0.
50.
100.
150.
O POSITION

Fig. A.16.

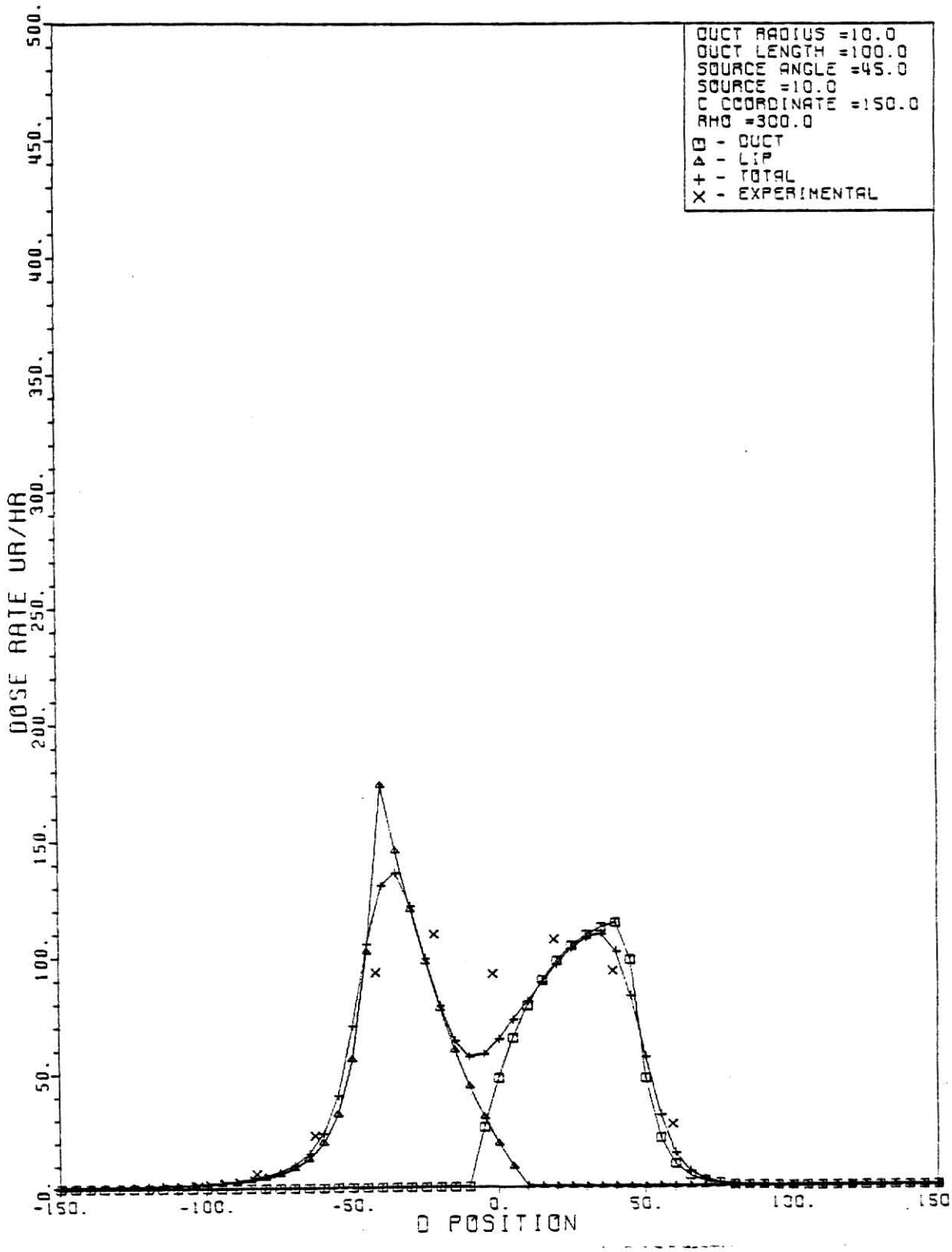
DUCT RADIUS =10.0
DUCT LENGTH =100.0
SOURCE ANGLE =45.0
SOURCE =10.0
C COORDINATE =150.0
RHO =300.0
□ - DUCT
△ - LIP
+ - TOTAL
X - EXPERIMENTAL
DOSE RATE UR/HR
0.
50.
100.
150.
200.
250.
300.
350.
400.
450.
500.
-150.
-100.
-50.
0.
50.
100.
150
D POSITION

Fig. A.17.

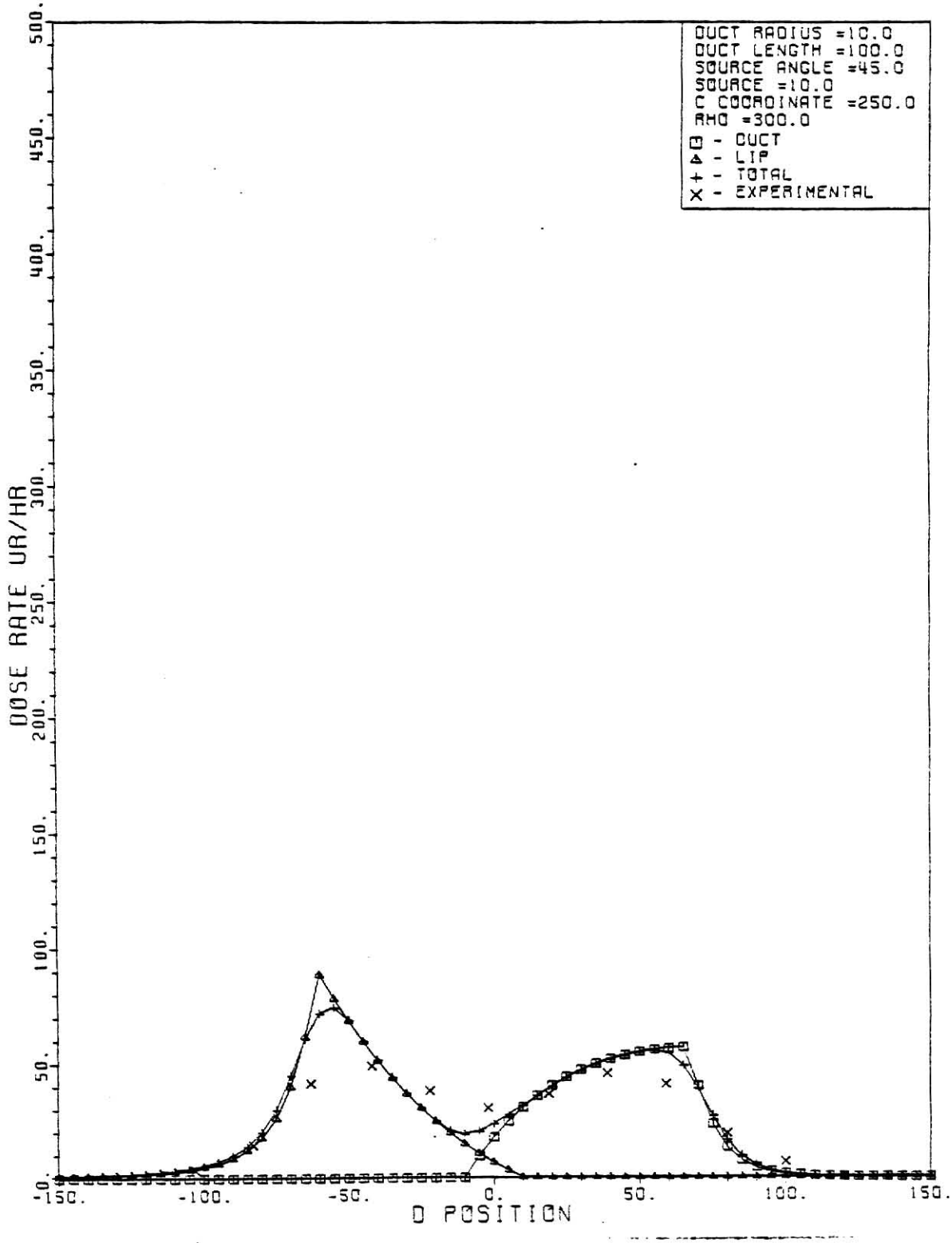
DUCT RADIUS =10.0
DUCT LENGTH =100.0
SOURCE ANGLE =45.0
SOURCE =10.0
C COORDINATE =250.0
RHO =300.0
□ - DUCT
△ - LIP
+ - TOTAL
× - EXPERIMENTAL
DOSE RATE UR/HR
0.
50.
100.
150.
200.
250.
300.
350.
400.
450.
500.
-150.
-100.
-50.
0.
50.
100.
150.
D POSITION

Fig. A.18.

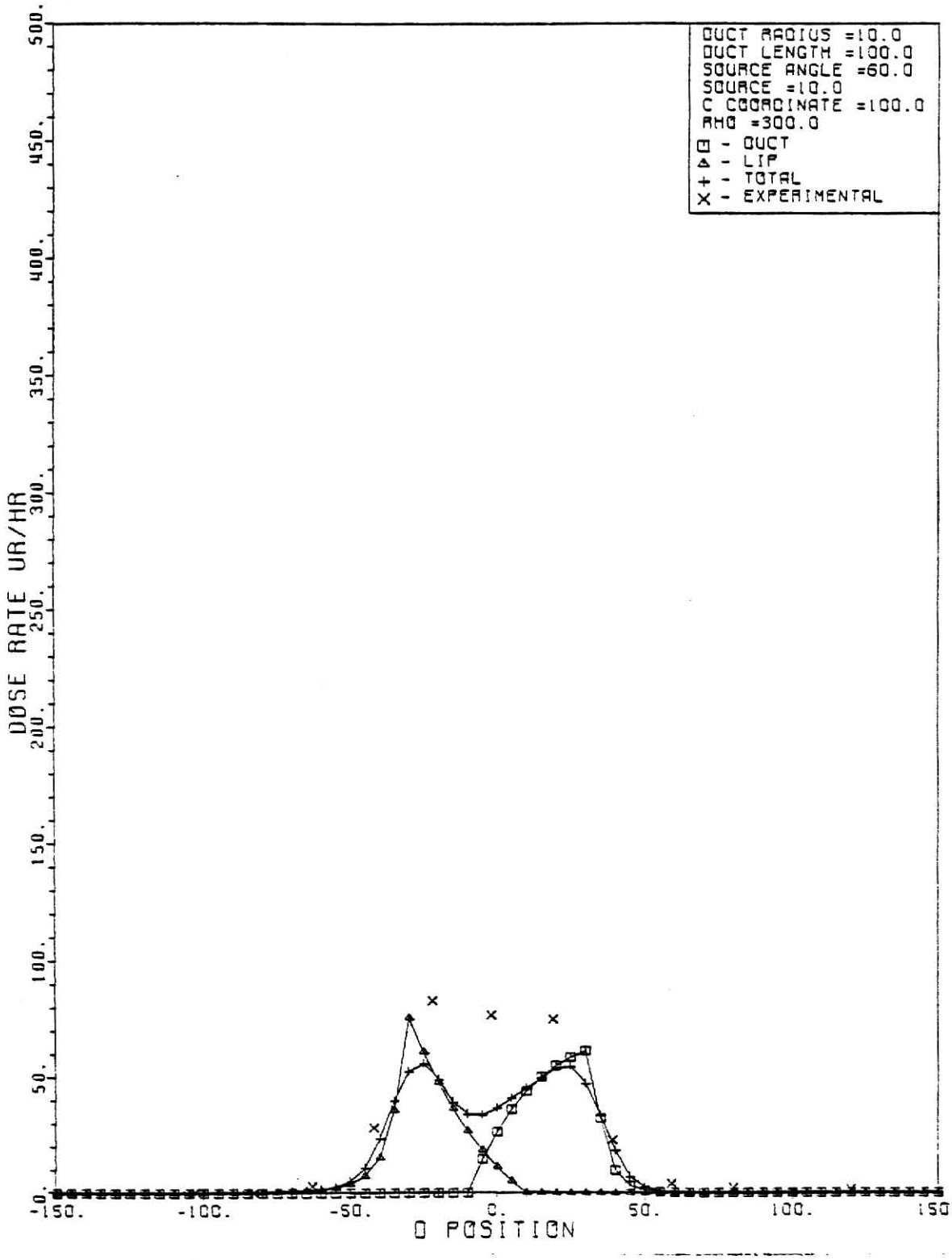
DUCT RADIUS =10.0
DUCT LENGTH =100.0
SOURCE ANGLE =60.0
SOURCE =10.0
C COORDINATE =100.0
RHO =300.0
□ - DUCT
△ - LIP
+ - TOTAL
× - EXPERIMENTAL
DOSE RATE UR/HR
0.
50.
100.
150.
200.
250.
300.
350.
400.
450.
500.
-150.
-100.
-50.
0.
50.
100.
150
Θ POSITION

Fig. A.19.

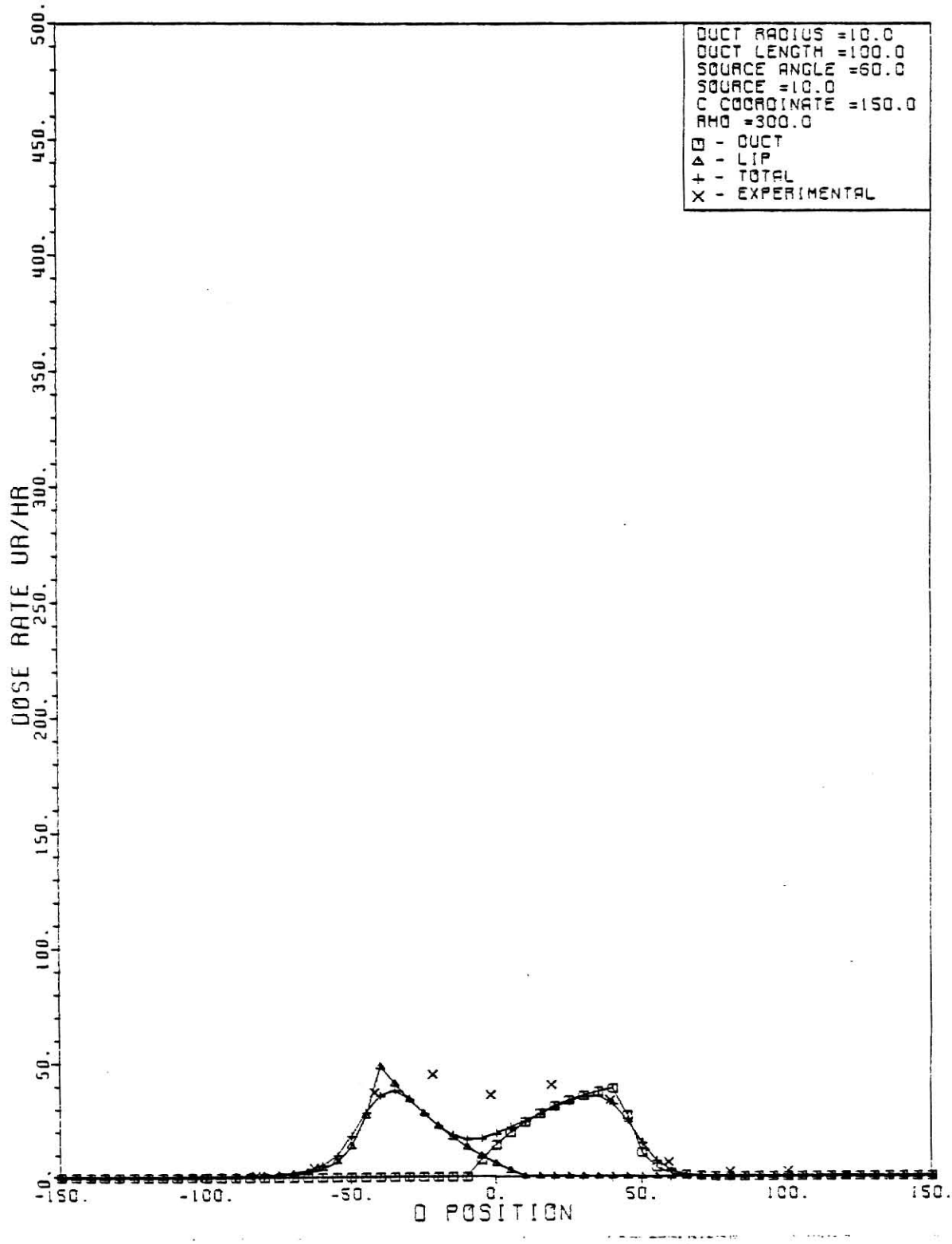
DUCT RADIUS =10.0
DUCT LENGTH =100.0
SOURCE ANGLE =60.0
SOURCE =10.0
C COORDINATE =150.0
RHO =300.0
□ - DUCT
△ - LIP
+ - TOTAL
× - EXPERIMENTAL
DOSE RATE UR/HR
0.
50.
100.
150.
200.
250.
300.
350.
400.
450.
500.
-150.
-100.
-50.
0.
50.
100.
150.
D POSITION

Fig. A.20.

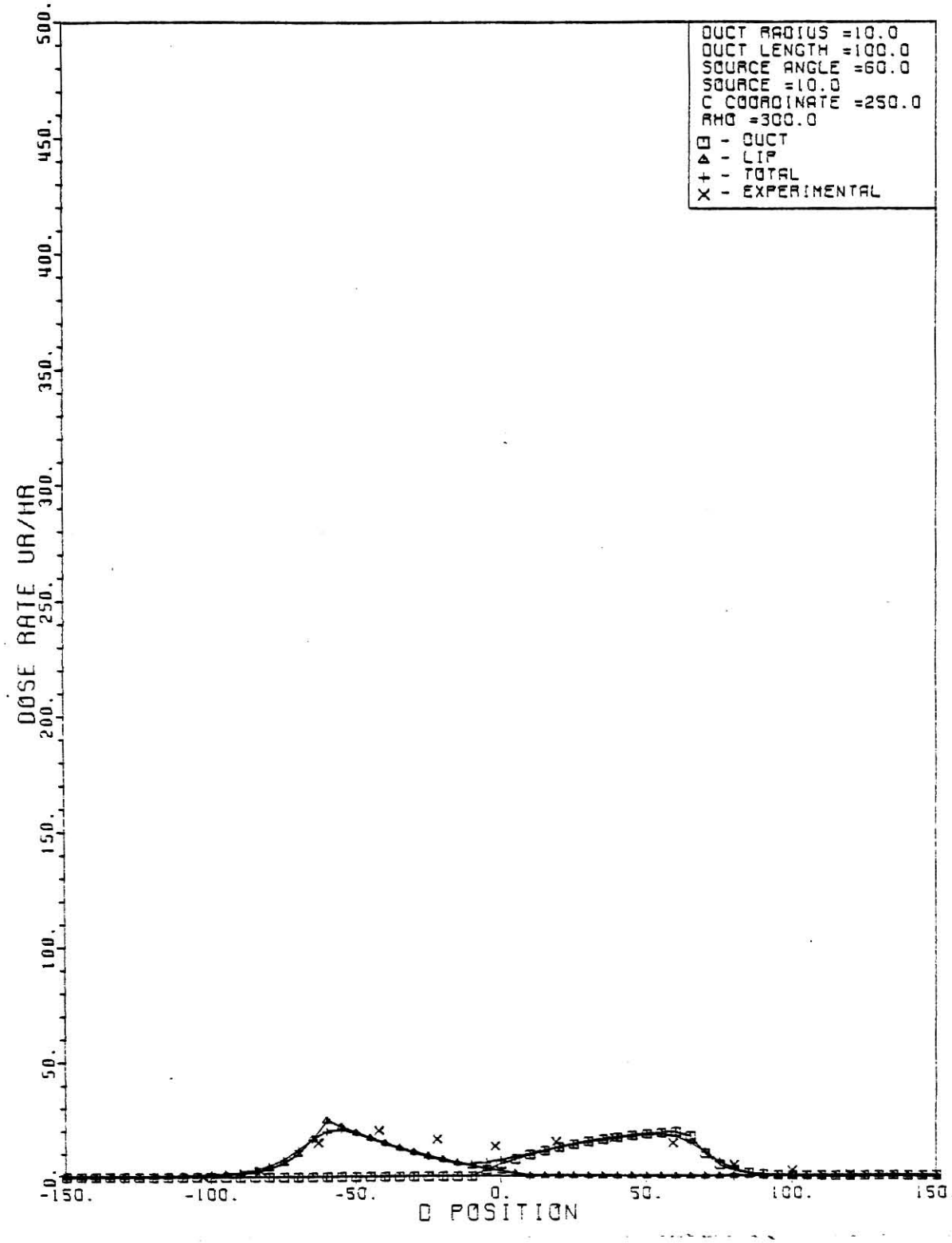
DUCT RADIUS =10.0
DUCT LENGTH =100.0
SOURCE ANGLE =60.0
SOURCE =10.0
C COORDINATE =250.0
RHO =300.0
□ - DUCT
△ - LIP
+ - TOTAL
X - EXPERIMENTAL
DOSE RATE UR/HR
0.
50.
100.
150.
200.
250.
300.
350.
400.
450.
500.
-150.
-100.
-50.
0.
50.
100.
150.
D POSITION

Fig. A.21.

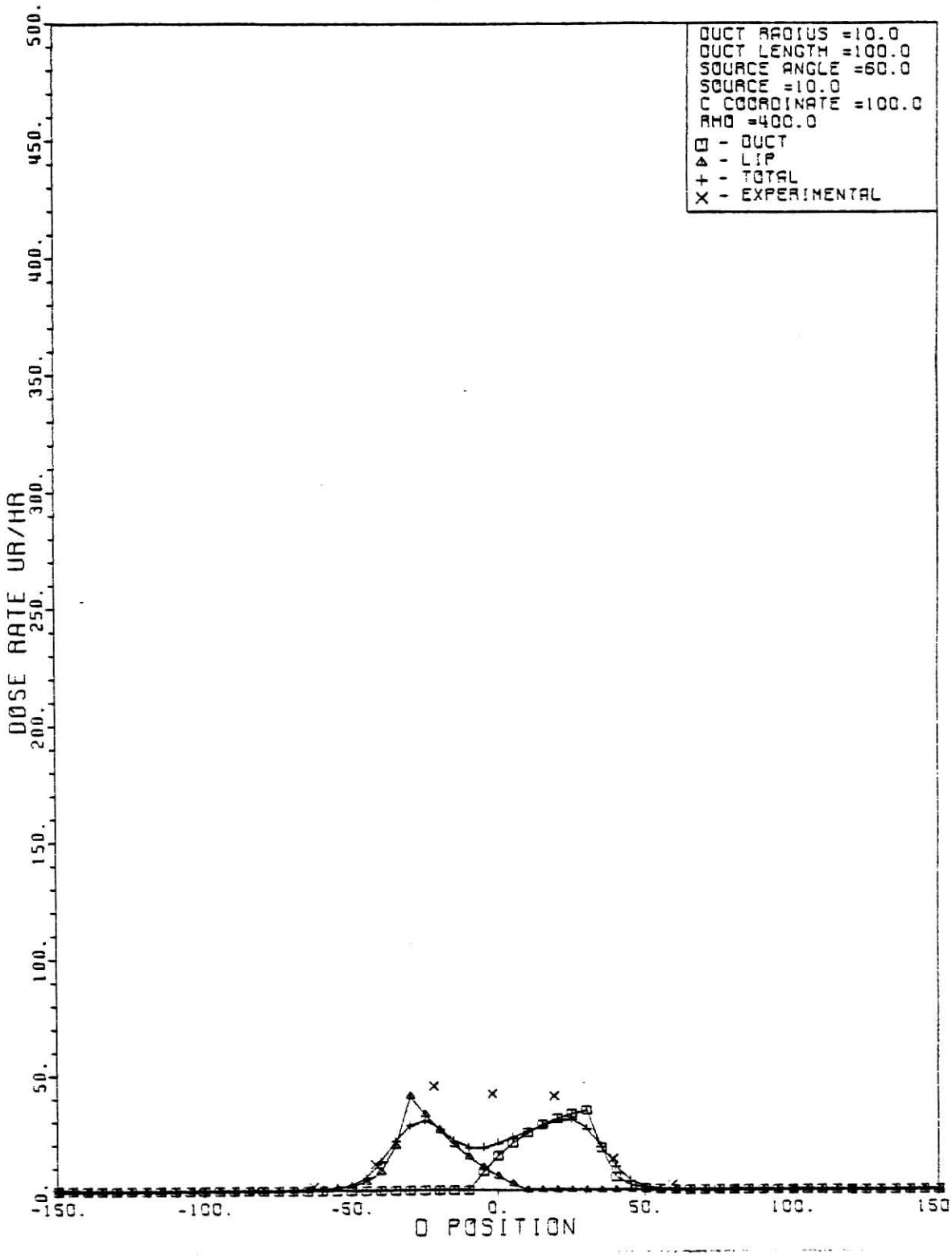
DUCT RADIUS =10.0
DUCT LENGTH =100.0
SOURCE ANGLE =60.0
SOURCE =10.0
C COORDINATE =100.0
RHO =400.0
□ - DUCT
△ - LIP
+ - TOTAL
X - EXPERIMENTAL
DOSE RATE UR/HR
0.
50.
100.
150.
200.
250.
300.
350.
400.
450.
500.
-150.
-100.
-50.
0.
50.
100.
150
O POSITION

Fig. A.22.

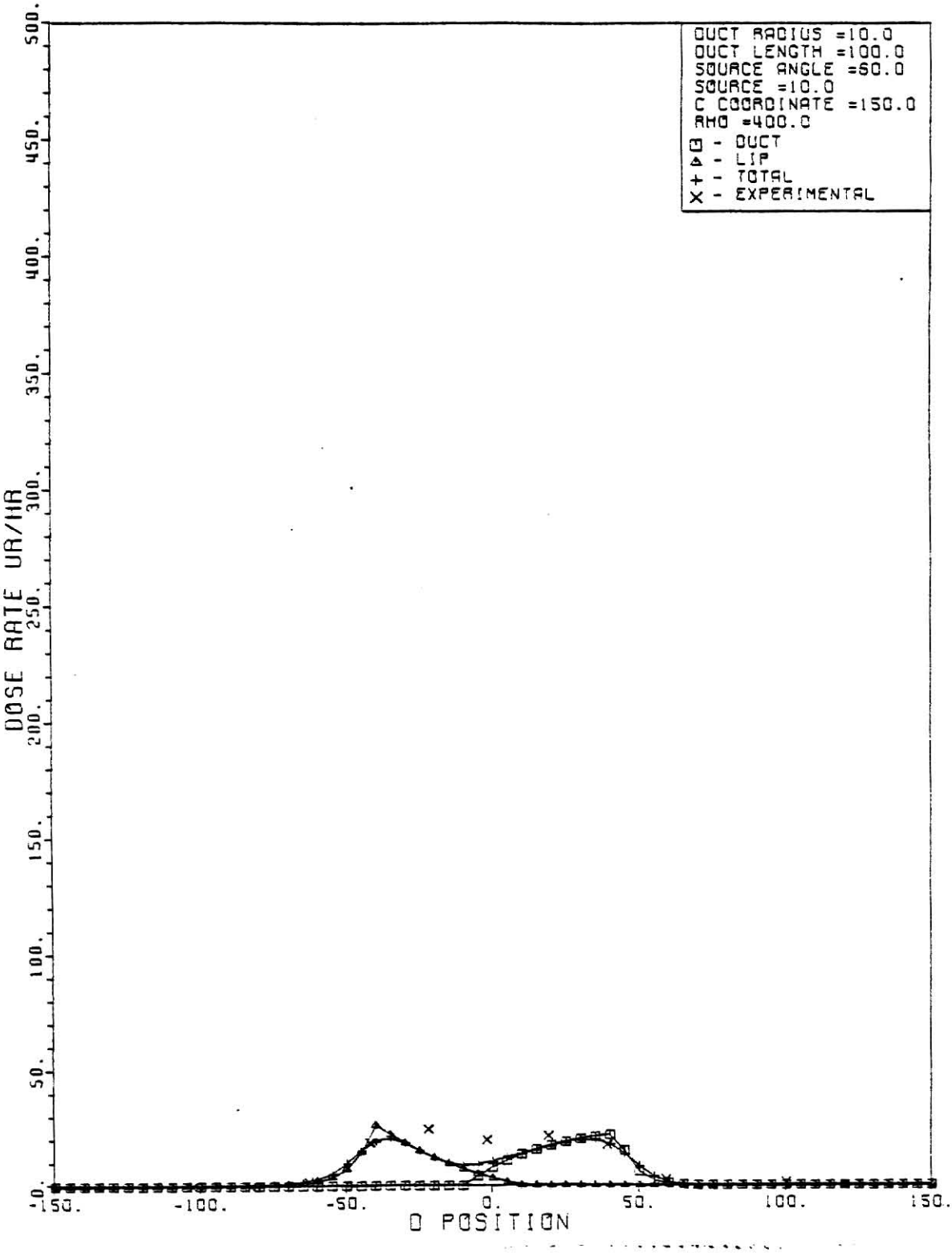
DUCT RADIUS =10.0
DUCT LENGTH =100.0
SOURCE ANGLE =60.0
SOURCE =10.0
C COORDINATE =150.0
RHO =400.0
□ - DUCT
△ - LIP
+ - TOTAL
X - EXPERIMENTAL
DOSE RATE UR/HR
0.
50.
100.
150.
200.
250.
300.
350.
400.
450.
500.
-150.
-100.
-50.
0.
50.
100.
150.
D POSITION

Fig. A.23.

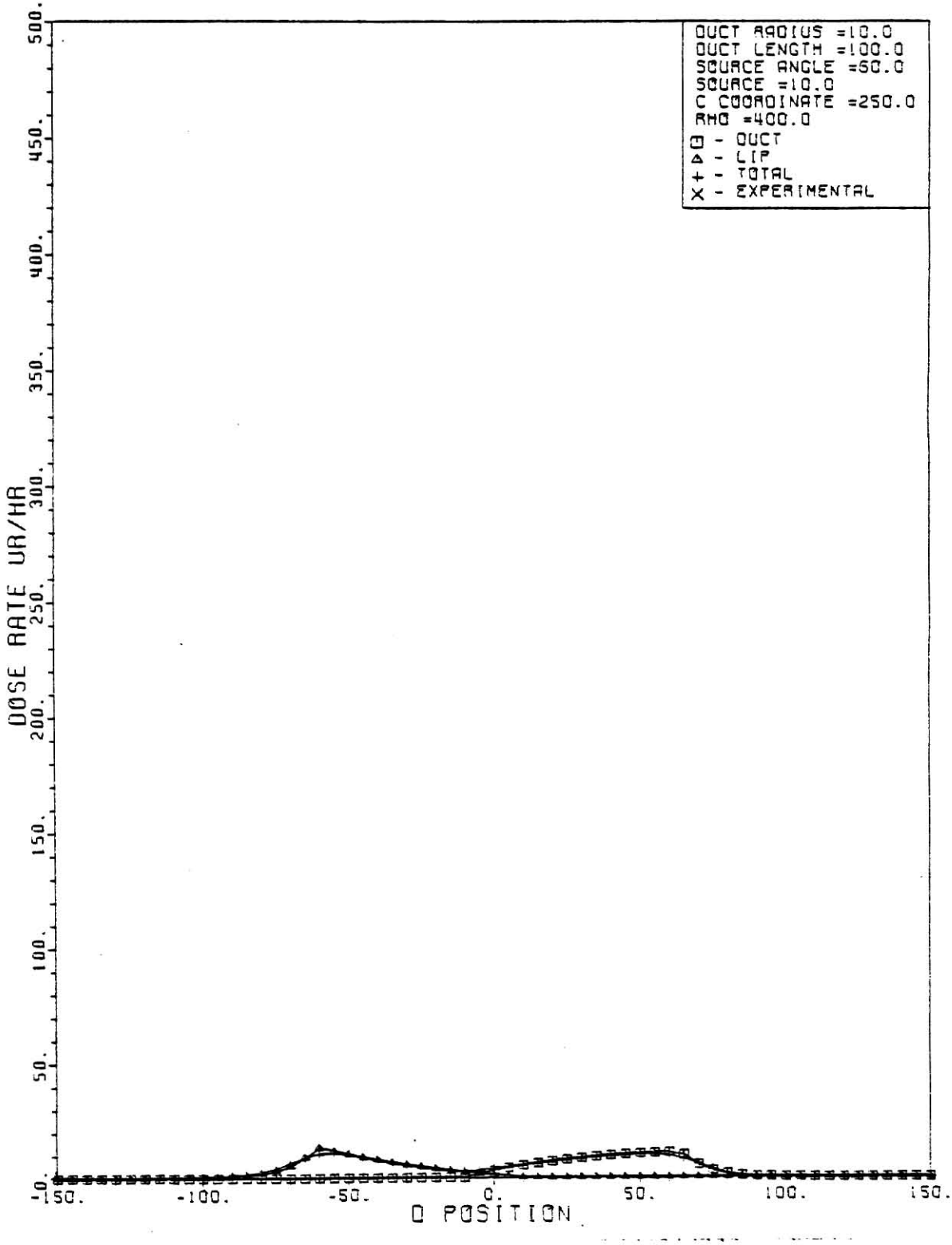
DUCT RADIUS =10.0
DUCT LENGTH =100.0
SOURCE ANGLE =60.0
SOURCE =10.0
C COORDINATE =250.0
RHO =400.0
□ - DUCT
△ - LIP
+ - TOTAL
X - EXPERIMENTAL
DOSE RATE UR/HR
0.
50.
100.
150.
200.
250.
300.
350.
400.
450.
500.
-150.
-100.
-50.
0.
50.
100.
150.
Q POSITION

Fig. A.24.

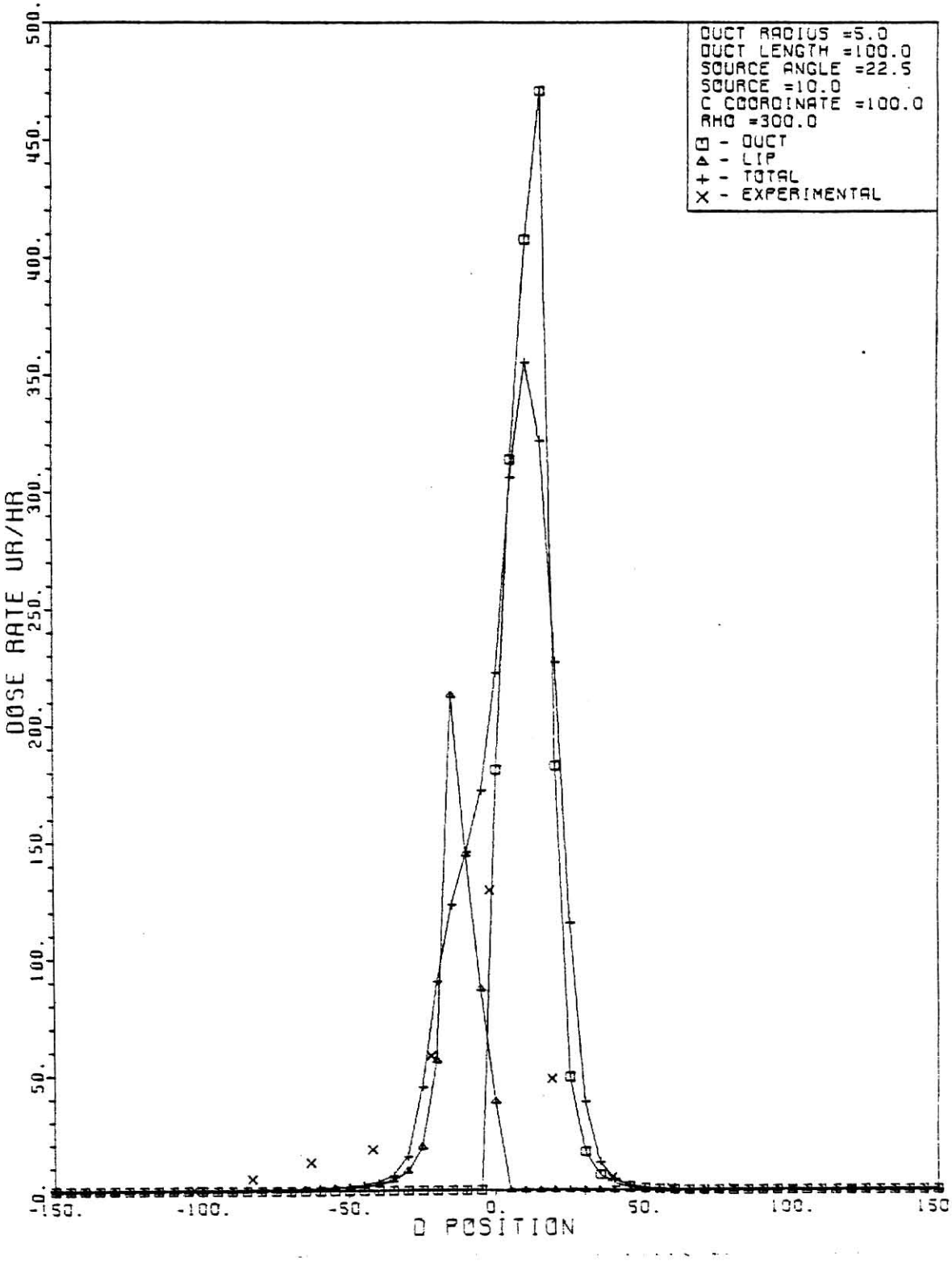
DUCT RADIUS =5.0
DUCT LENGTH =100.0
SOURCE ANGLE =22.5
SOURCE =10.0
C COORDINATE =100.0
RHO =300.0
□ - DUCT
Δ - LIP
+ - TOTAL
× - EXPERIMENTAL
DOSE RATE UR/HR
D POSITION
500.
450.
400.
350.
300.
250.
200.
150.
100.
50.
10.
-150.
-100.
-50.
0.
50.
100.
150

Fig. A.25.

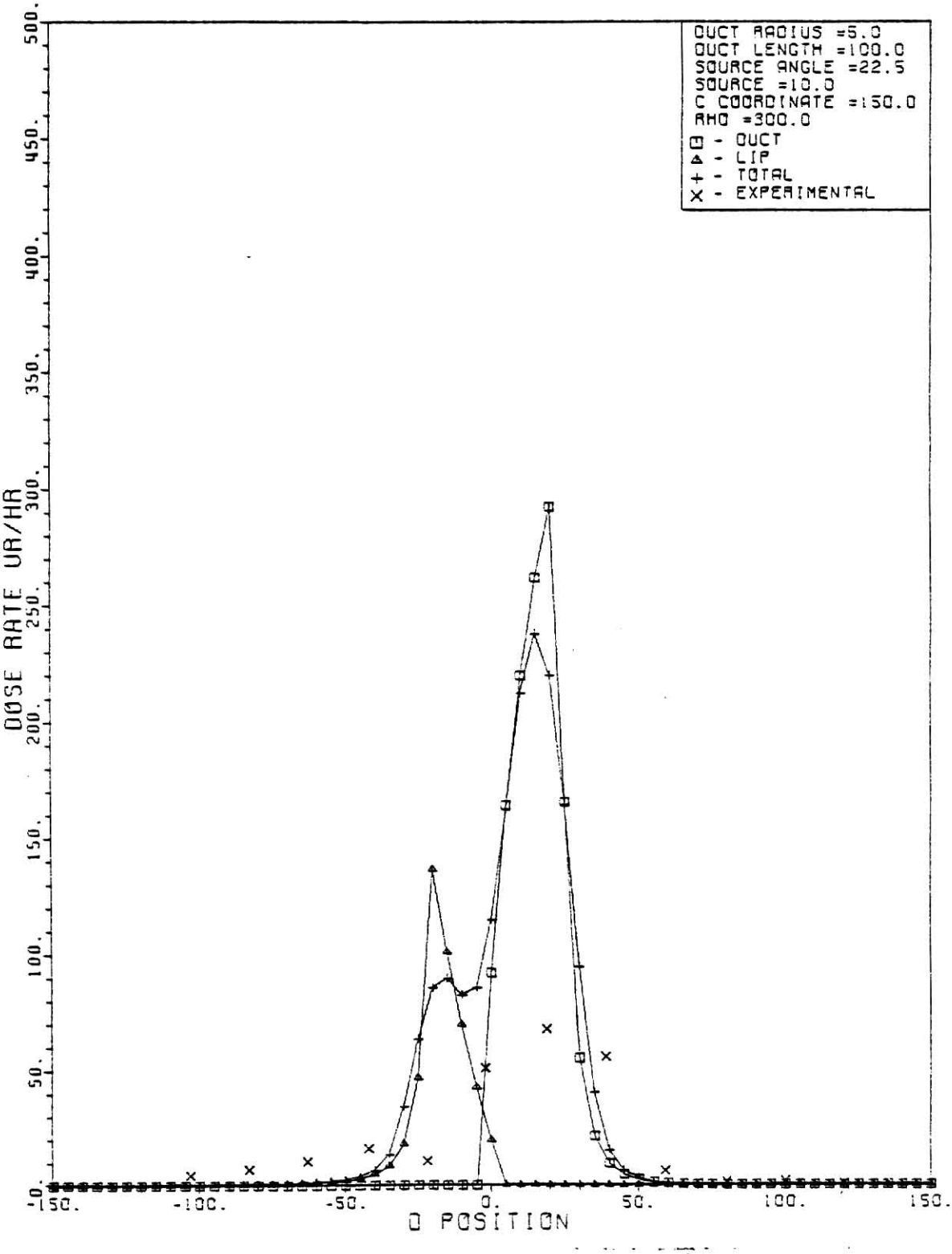
DUCT RADIUS =5.0
DUCT LENGTH =100.0
SOURCE ANGLE =22.5
SOURCE =10.0
C COORDINATE =150.0
RHO =300.0
□ - DUCT
△ - LIP
+ - TOTAL
× - EXPERIMENTAL
DOSE RATE UR/HR
0.
50.
100.
150.
200.
250.
300.
350.
400.
450.
500.
-150.
-100.
-50.
0.
50.
100.
150.
Q POSITION

Fig. A.26.

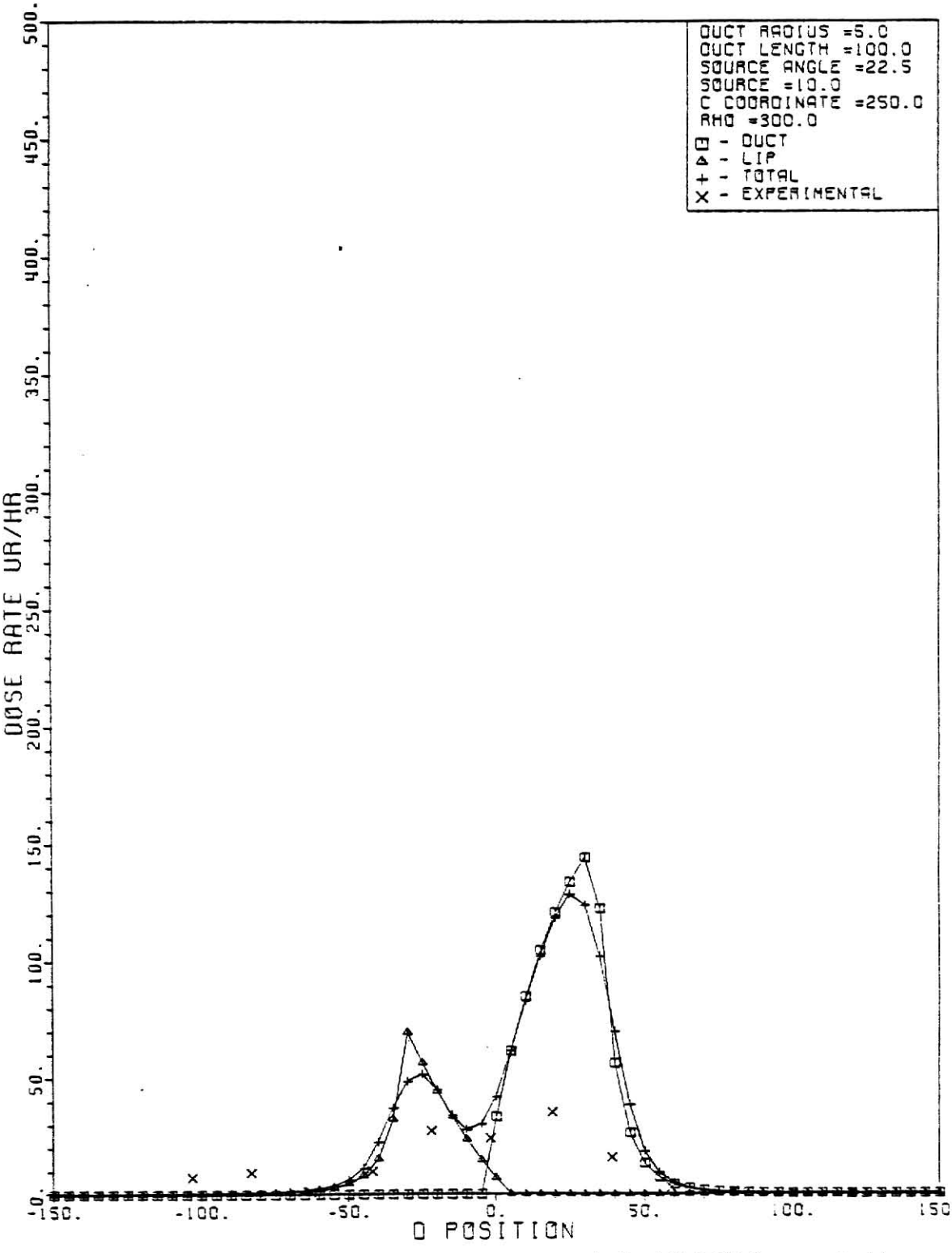
DUCT RADIUS =5.0
DUCT LENGTH =100.0
SOURCE ANGLE =22.5
SOURCE =10.0
C COORDINATE =250.0
RHO =300.0
□ - DUCT
△ - LIP
+ - TOTAL
× - EXPERIMENTAL
DOSE RATE UR/HR
0.
50.
100.
150.
200.
250.
300.
350.
400.
450.
500.
-150.
-100.
-50.
0.
50.
100.
150
Q POSITION

Fig. A.27.

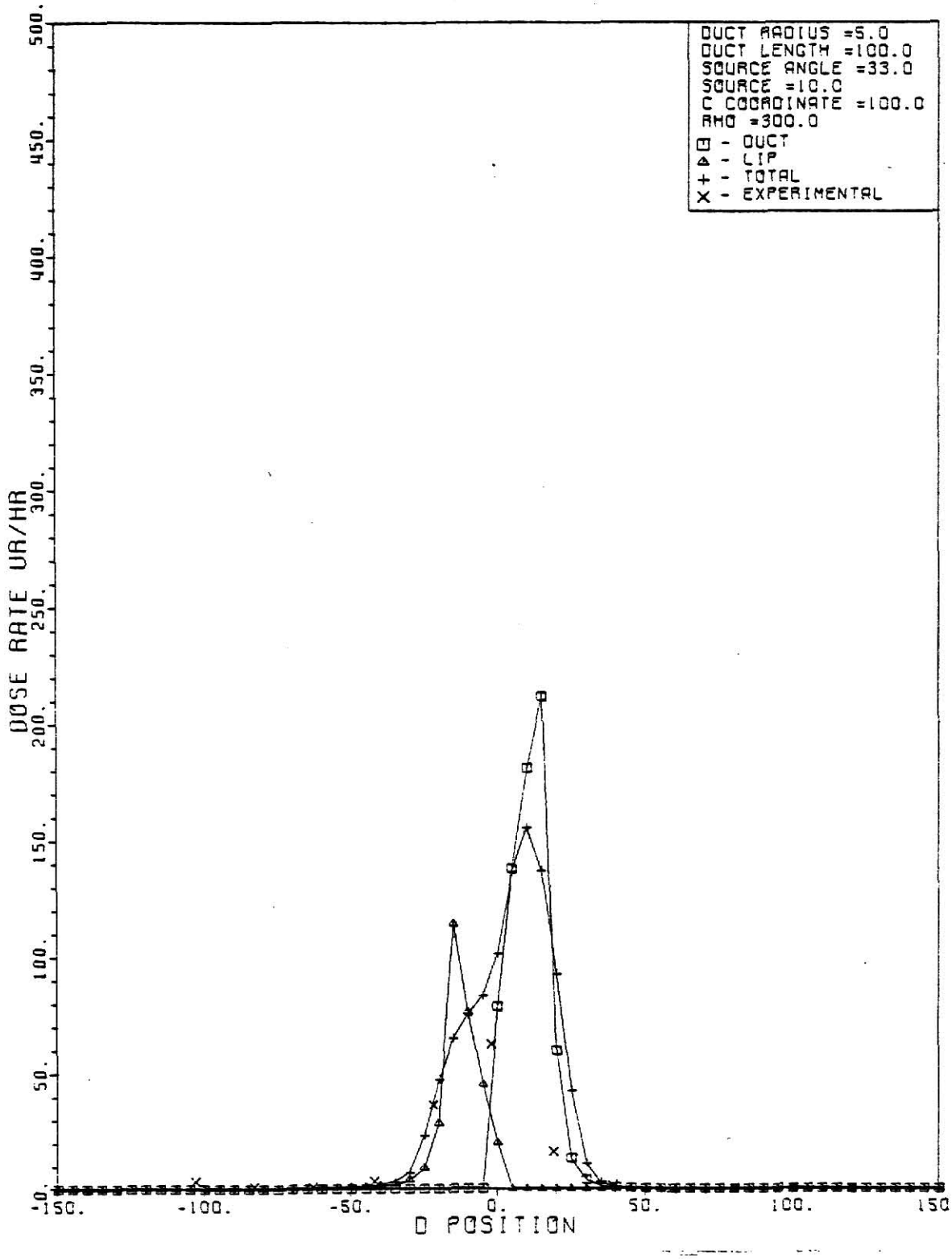
DUCT RADIUS =5.0
DUCT LENGTH =100.0
SOURCE ANGLE =33.0
SOURCE =10.0
C COORDINATE =100.0
RHO =300.0
□ - DUCT
△ - LIP
+ - TOTAL
X - EXPERIMENTAL
DOSE RATE UR/HR
0.
50.
100.
150.
200.
250.
300.
350.
400.
450.
500.
-150.
-100.
-50.
0.
50.
100.
150
D POSITION

Fig. A.28.

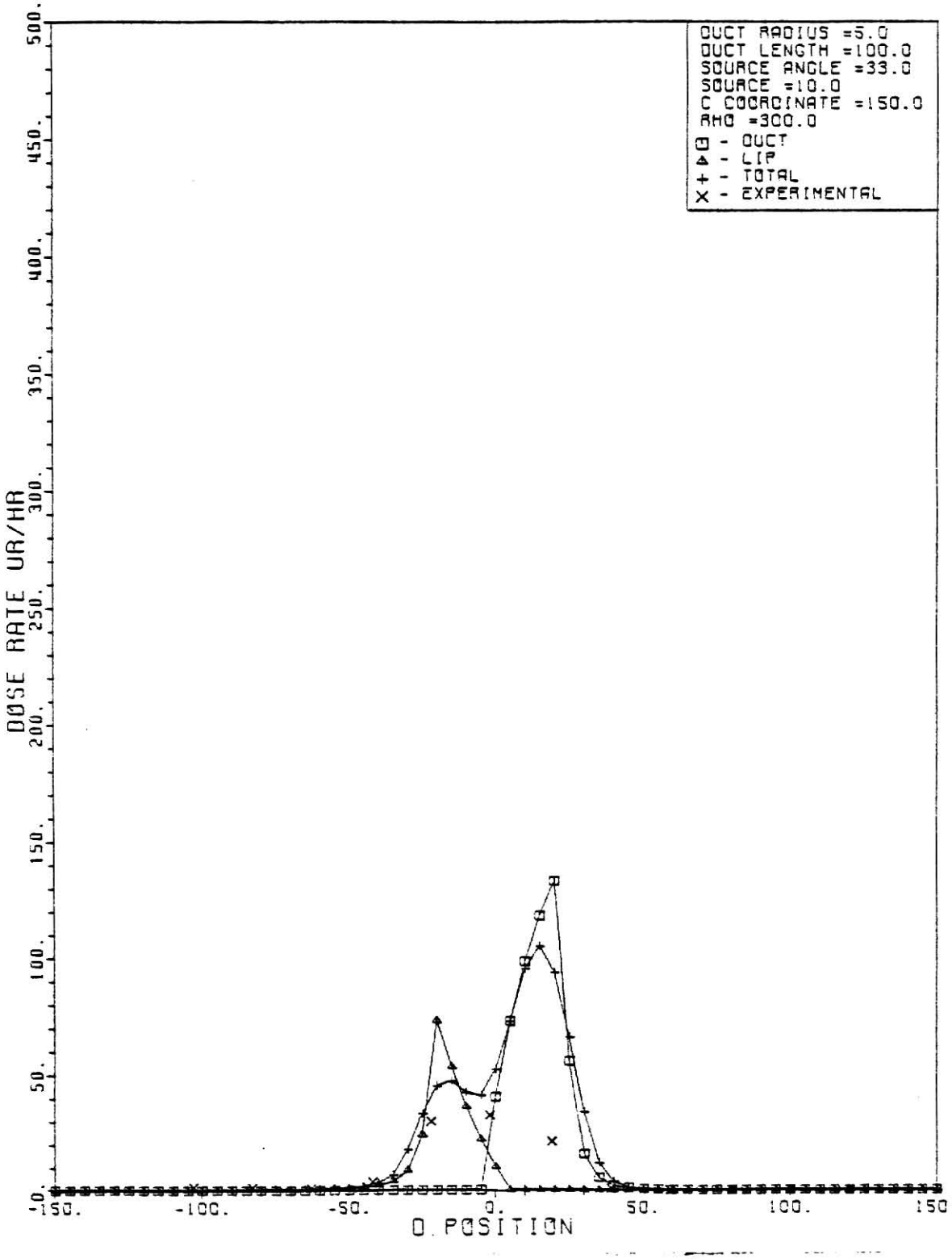
DUCT RADIUS =5.0
DUCT LENGTH =100.0
SOURCE ANGLE =33.0
SOURCE =10.0
C COORDINATE =150.0
RHO =300.0
□ - DUCT
△ - LIP
+ - TOTAL
X - EXPERIMENTAL
DOSE RATE UR/HR
0.
50.
100.
150.
200.
250.
300.
350.
400.
450.
500.
-150.
-100.
-50.
0.
50.
100.
150.
D POSITION

Fig. A.29.

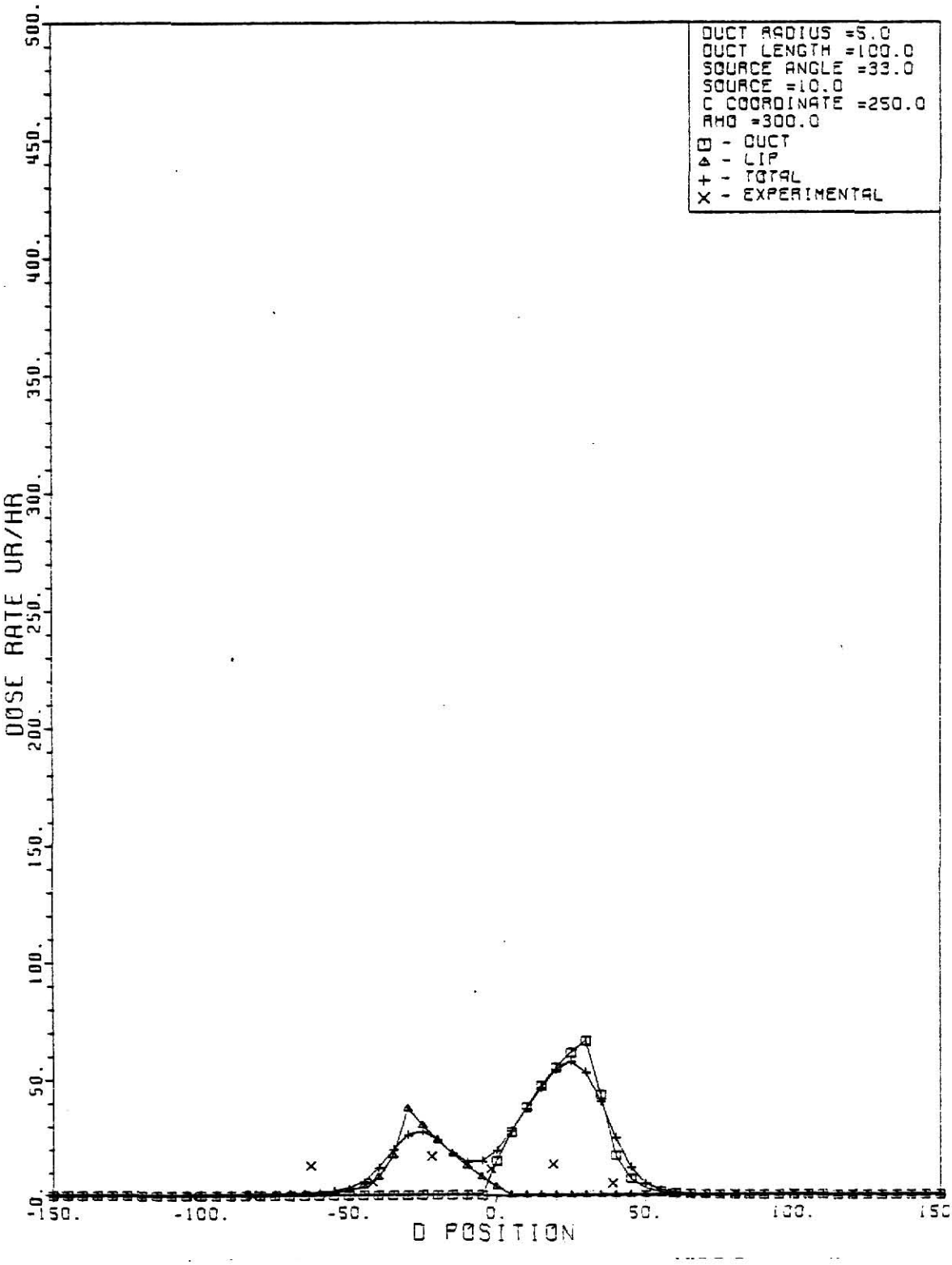
DUCT RADIUS =5.0
DUCT LENGTH =100.0
SOURCE ANGLE =33.0
SOURCE =10.0
C COORDINATE =250.0
RHO =300.0
□ - DUCT
△ - LIP
+ - TOTAL
X - EXPERIMENTAL
DOSE RATE UR/HR
0.
50.
100.
150.
200.
250.
300.
350.
400.
450.
500.
-150.
-100.
-50.
0.
50.
100.
150
D POSITION

Fig. A.30.

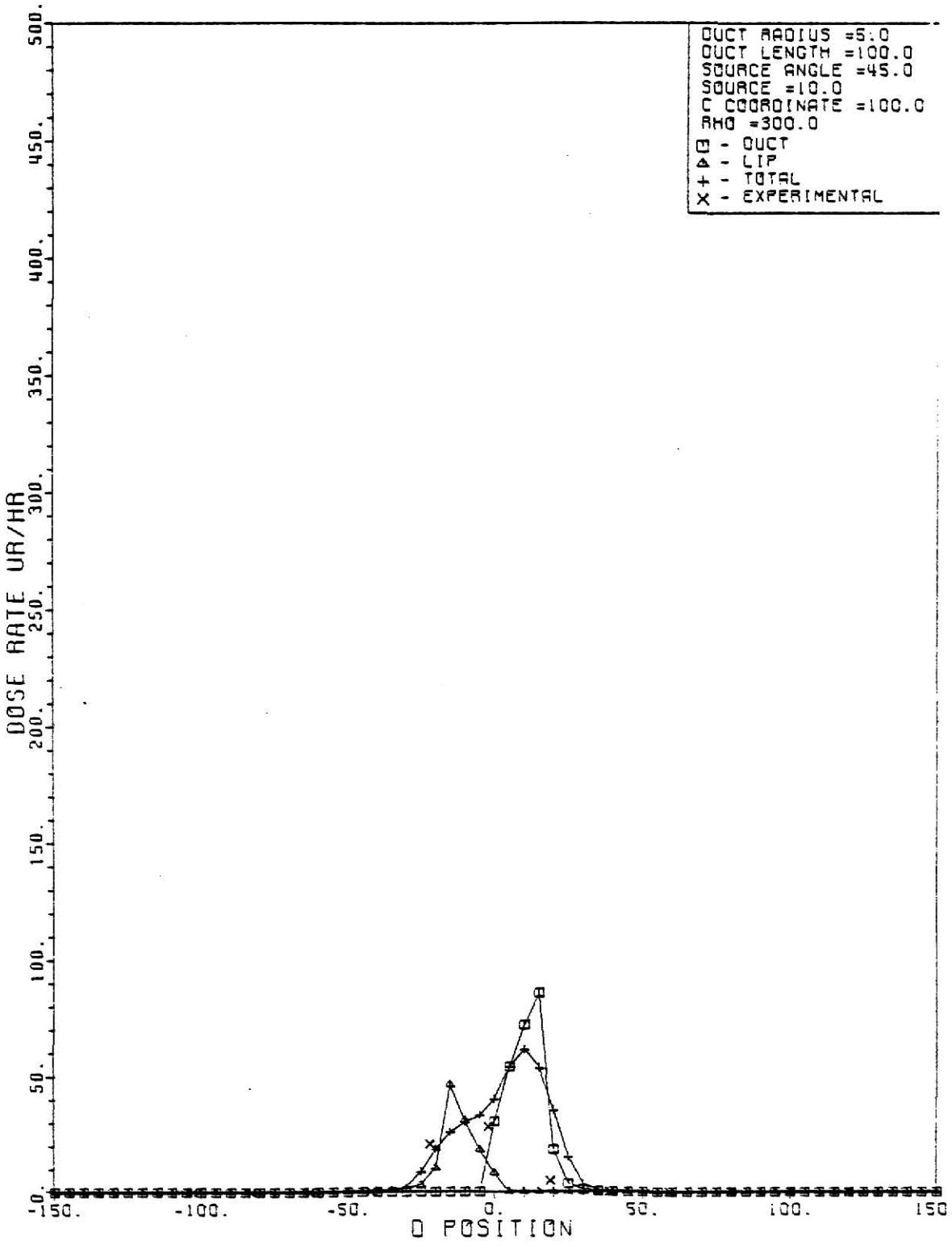
DUCT RADIUS =5.0
DUCT LENGTH =100.0
SOURCE ANGLE =45.0
SOURCE =10.0
C COORDINATE =100.0
RHO =300.0
□ - DUCT
Δ - LIP
+ - TOTAL
X - EXPERIMENTAL
DOSE RATE UR/HR
0.
50.
100.
150.
200.
250.
300.
350.
400.
450.
500.
-150.
-100.
-50.
0.
50.
100.
150.
Θ POSITION

Fig. A.31.

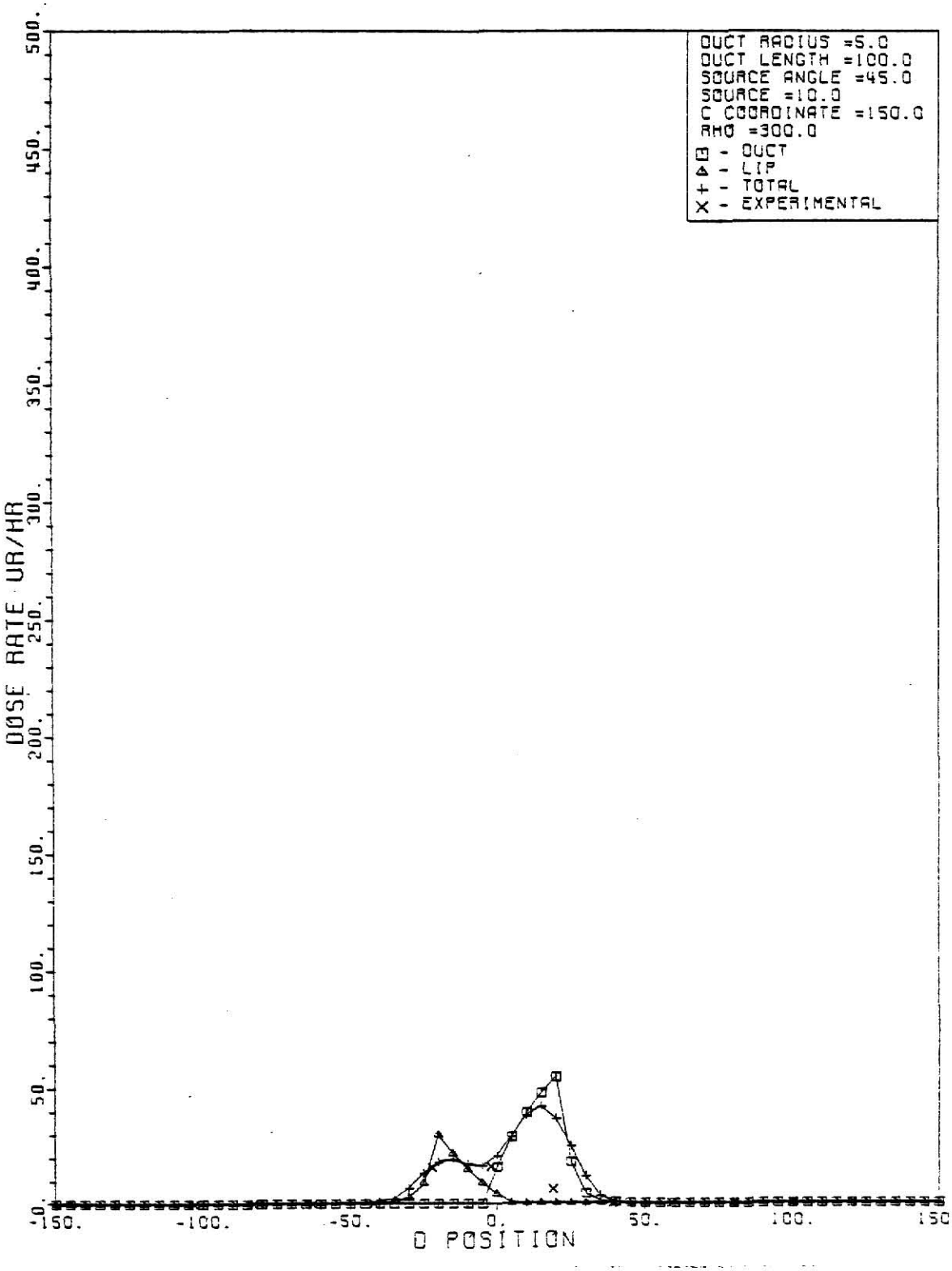
DUCT RADIUS =5.0
DUCT LENGTH =100.0
SOURCE ANGLE =45.0
SOURCE =10.0
C COORDINATE =150.0
RHO =300.0
□ - DUCT
△ - LIP
+ - TOTAL
X - EXPERIMENTAL
DOSE RATE UR/HR
0.
50.
100.
150.
200.
250.
300.
350.
400.
450.
500.
-150.
-100.
-50.
0.
50.
100.
150.
D POSITION

Fig. A.32.

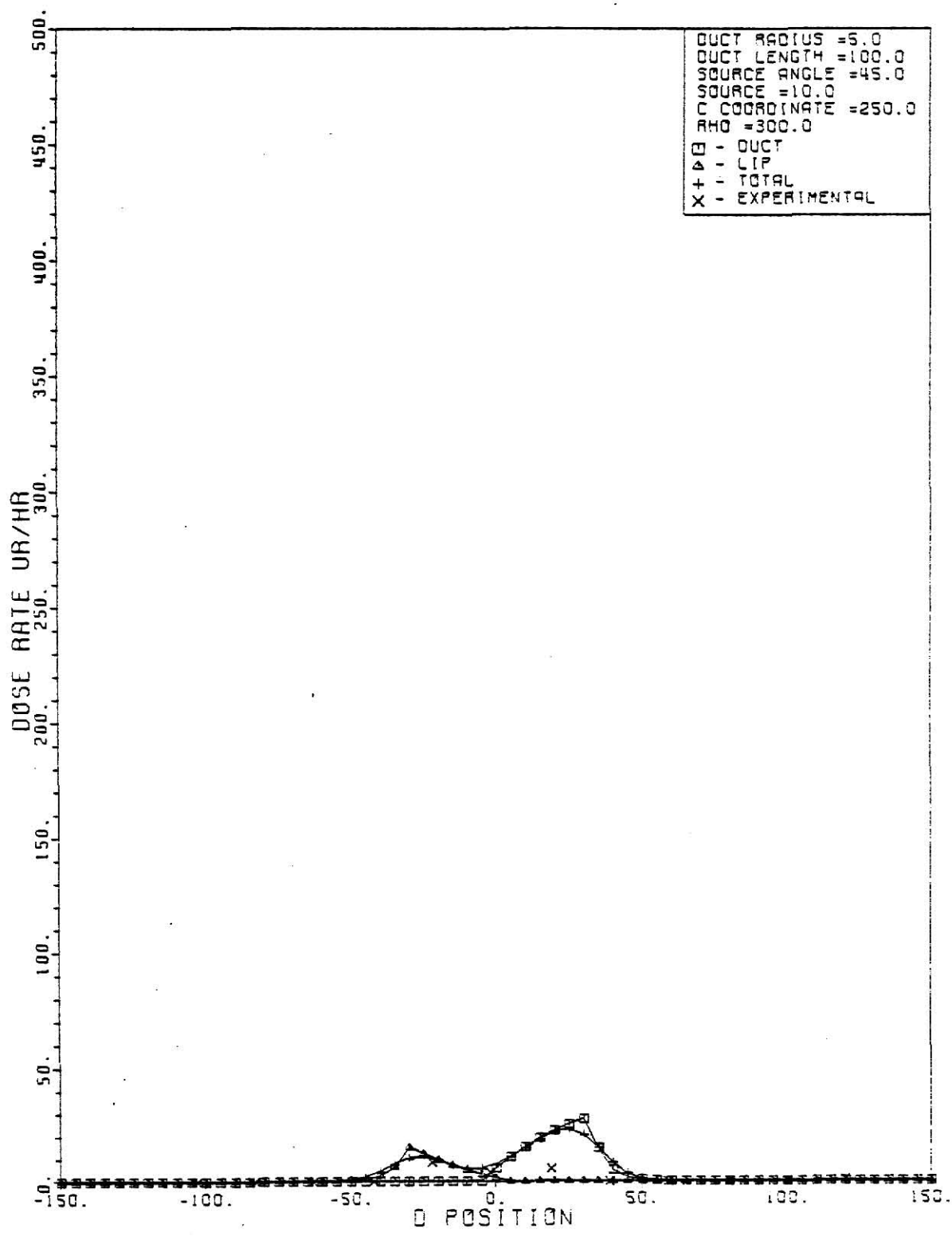
DUCT RADIUS =5.0
DUCT LENGTH =100.0
SOURCE ANGLE =45.0
SOURCE =10.0
C COORDINATE =250.0
RHO =300.0
□ - DUCT
Δ - LIP
+ - TOTAL
X - EXPERIMENTAL
DOSE RATE UR/HR
0.
50.
100.
150.
200.
250.
300.
350.
400.
450.
500.
-150.
-100.
-50.
0.
50.
100.
150.
D POSITION

Fig. A.33.

APPENDIX B

The figures presented in this section are identical to those of Appendix A only for the 150.0 cm wall. Table B.1 presents a summary of the figures in this section as well as the page number for each figure.

TABLE B.1

Duct Radius (cm)	Source Angle (deg)	Figure Numbers	Page
20.0	22.5	B.1,2	181-82
20.0	33.0	B.3,4	183-84
20.0	45.0	B.5,6	185-86
20.0	60.0	B.7,8	187-88
10.0	22.5	B.9,10	189-90
10.0	33.0	B.11,12	191-92
10.0	45.0	B.13,14	193-94
10.0	60.0	B.15,16	195-96
5.0	22.5	B.17,18	197-98
5.0	33.0	B.19,20	199-200

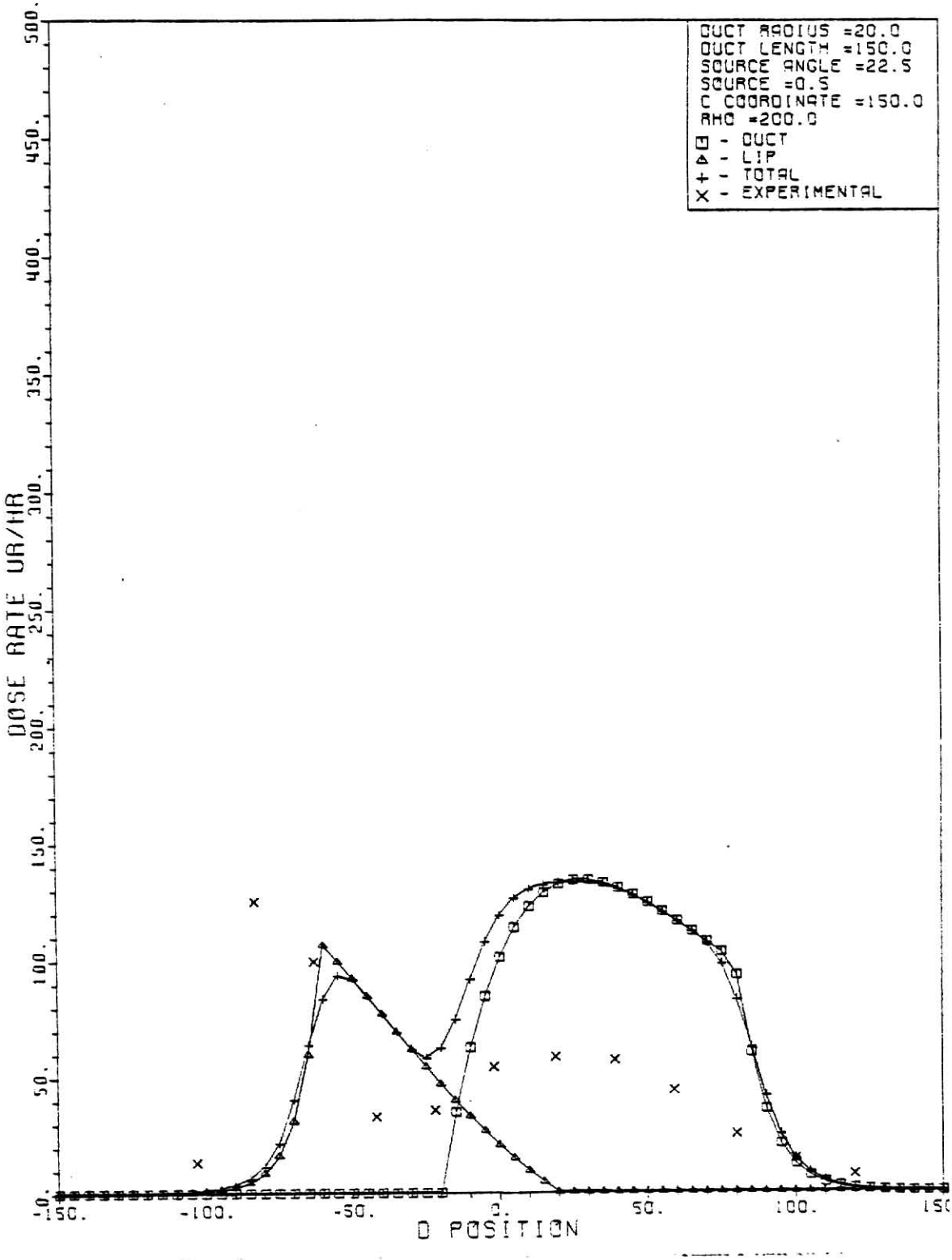
DUCT RADIUS =20.0
DUCT LENGTH =150.0
SOURCE ANGLE =22.5
SOURCE =0.5
C COORDINATE =150.0
RHO =200.0
□ - DUCT
△ - LIP
+ - TOTAL
× - EXPERIMENTAL
DOSE RATE UR/HR
500.
450.
400.
350.
300.
250.
200.
150.
100.
50.
0.
-150.
-100.
-50.
0.
50.
100.
D POSITION

Fig. B.1.

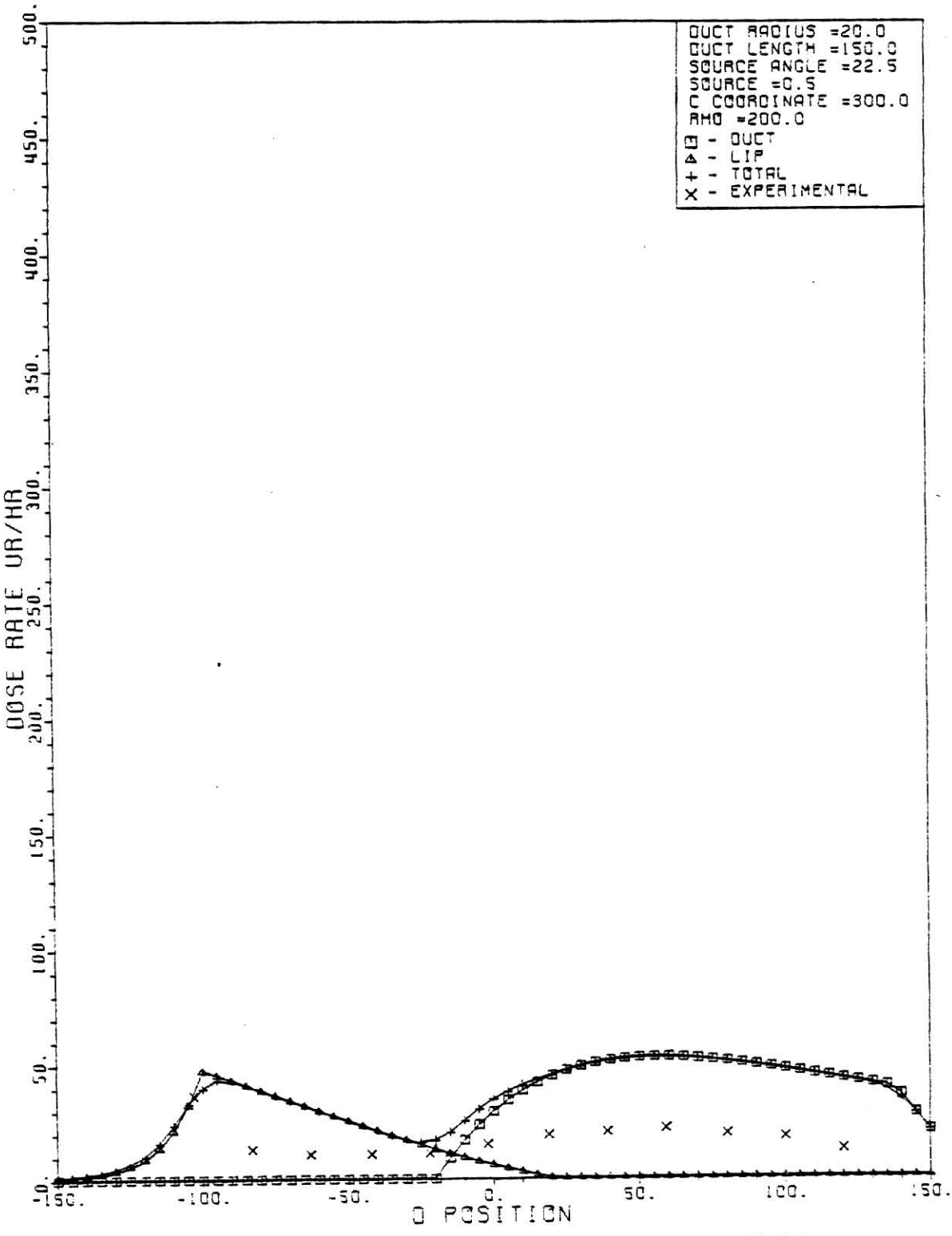
DUCT RADIUS =20.0
DUCT LENGTH =150.0
SOURCE ANGLE =22.5
SOURCE =0.5
C COORDINATE =300.0
RHO =200.0
□ - DUCT
△ - LIP
+ - TOTAL
× - EXPERIMENTAL
DOSE RATE UR/HR
500.
450.
400.
350.
300.
250.
200.
150.
100.
50.
0.
-150.
-100.
-50.
0.
50.
100.
150.
Q POSITION

Fig. B.2.

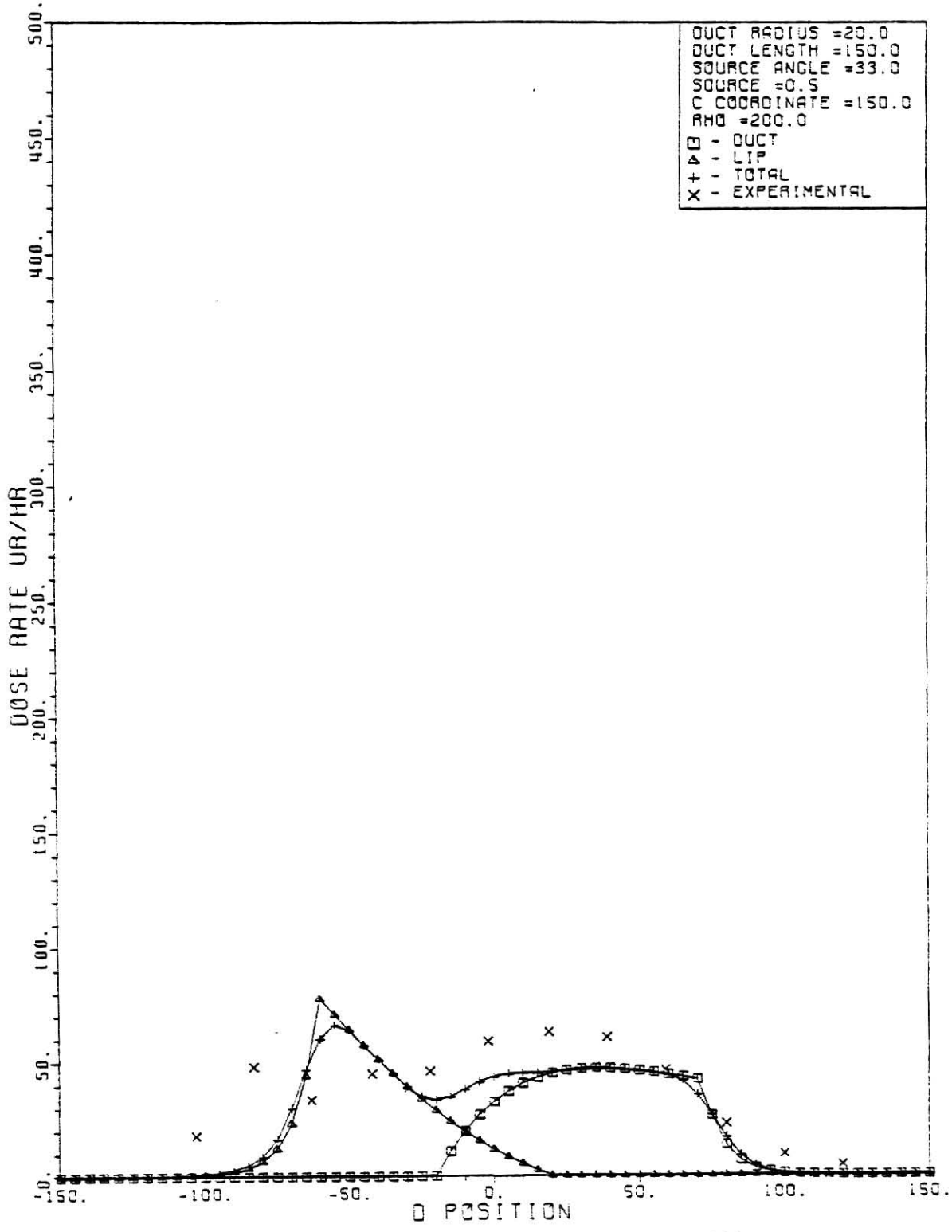
DUCT RADIUS =20.0
DUCT LENGTH =150.0
SOURCE ANGLE =33.0
SOURCE =0.5
C COORDINATE =150.0
RHO =200.0
□ - DUCT
△ - LIP
+ - TOTAL
× - EXPERIMENTAL
DOSE RATE UR/HR
0.
50.
100.
150.
200.
250.
300.
350.
400.
450.
500.
-150.
-100.
-50.
0.
50.
100.
150.
D POSITION

Fig. B.3.

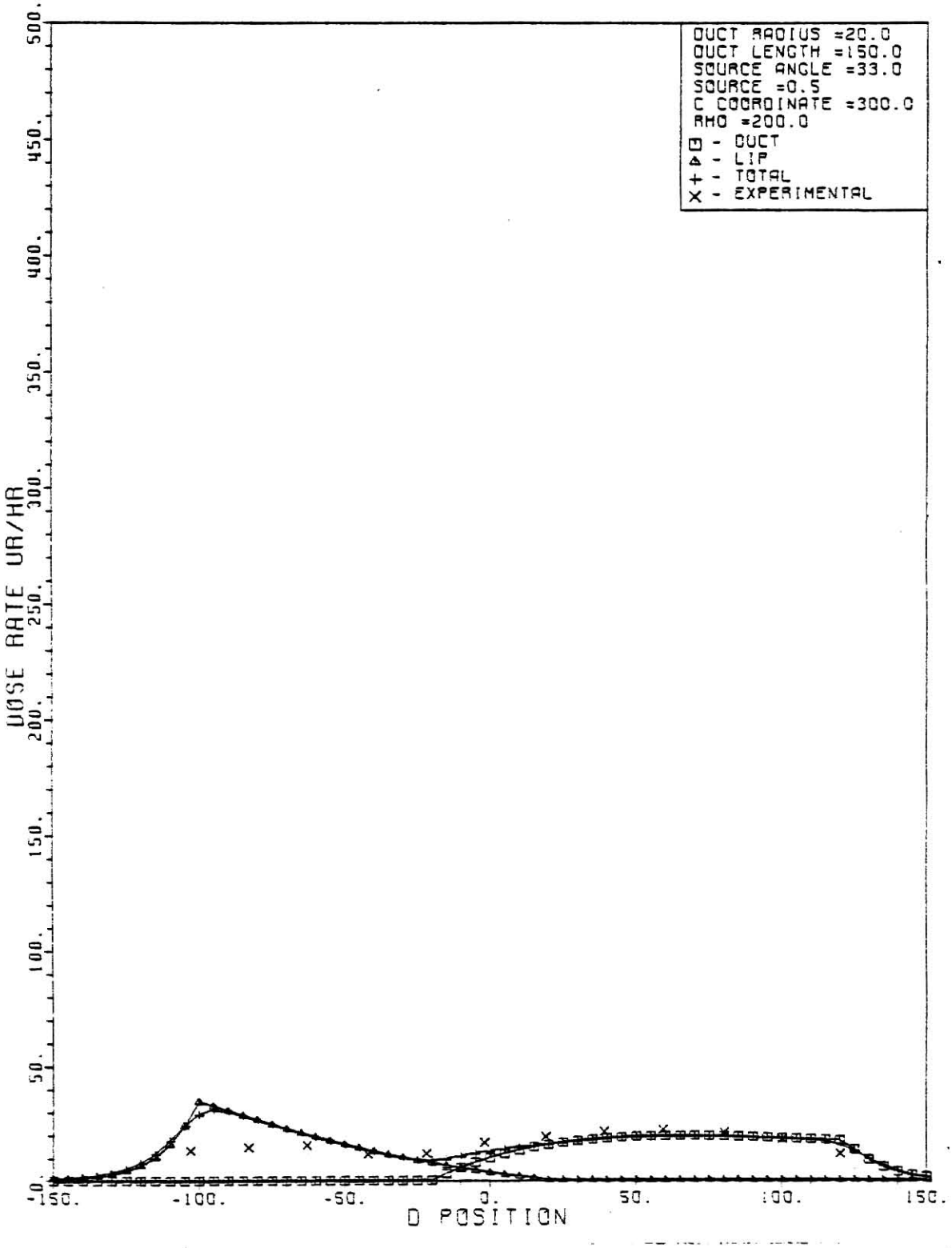
DUCT RADIUS =20.0
DUCT LENGTH =150.0
SOURCE ANGLE =33.0
SOURCE =0.5
C COORDINATE =300.0
RHO =200.0
□ - DUCT
△ - LIP
+ - TOTAL
× - EXPERIMENTAL
DOSE RATE UR/HR
0.
50.
100.
150.
200.
250.
300.
350.
400.
450.
500.
-150.
-100.
-50.
0.
50.
100.
150.
D POSITION

Fig. B.4.

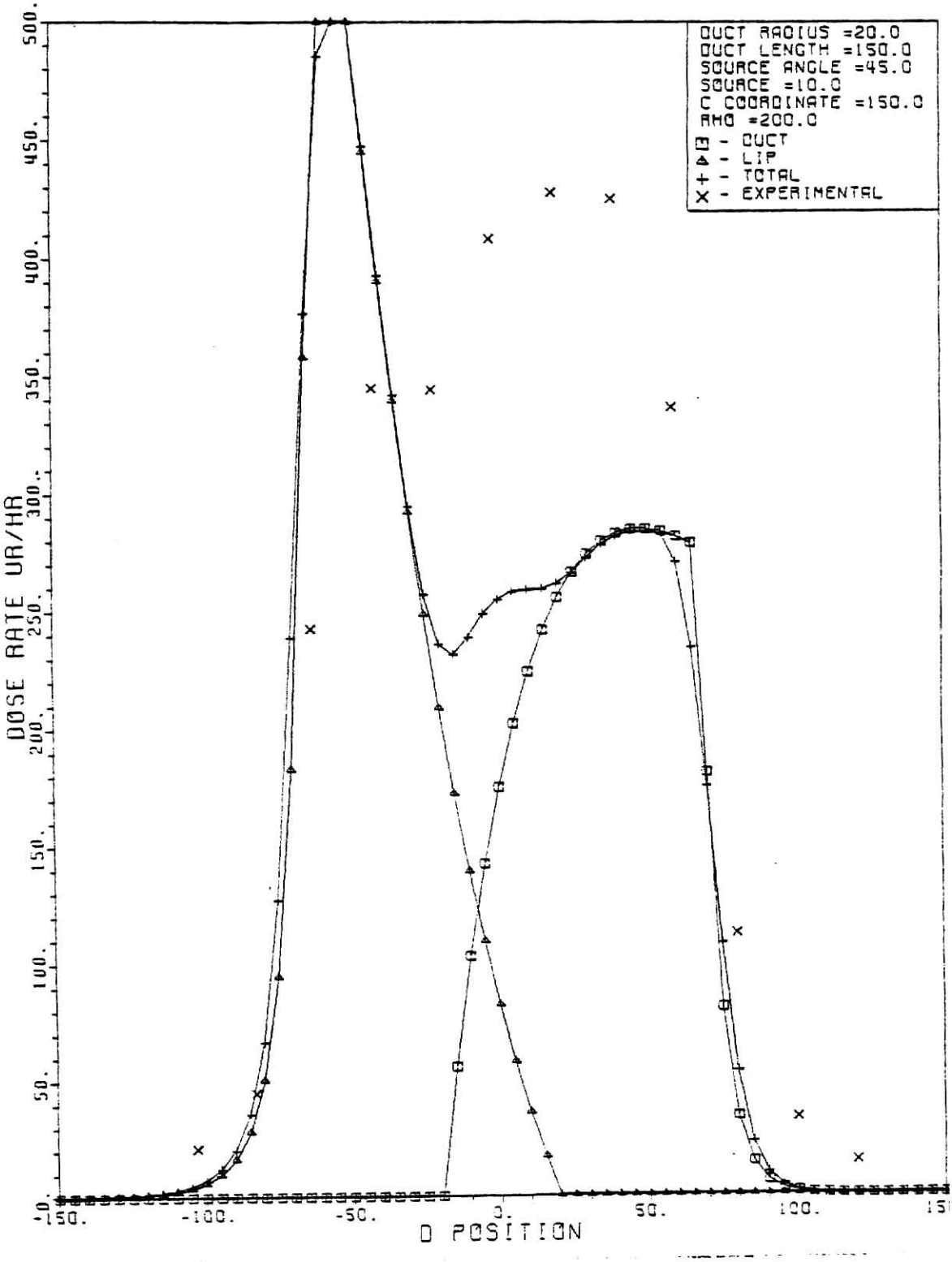
DUCT RADIUS =20.0
DUCT LENGTH =150.0
SOURCE ANGLE =45.0
SOURCE =10.0
C COORDINATE =150.0
RHO =200.0
⊡ - DUCT
Δ - LIP
+ - TOTAL
× - EXPERIMENTAL
DOSE RATE UR/HR
0.
50.
100.
150.
200.
250.
300.
350.
400.
450.
500.
-150.
-100.
-50.
0.
50.
100.
D POSITION

Fig. B.5.

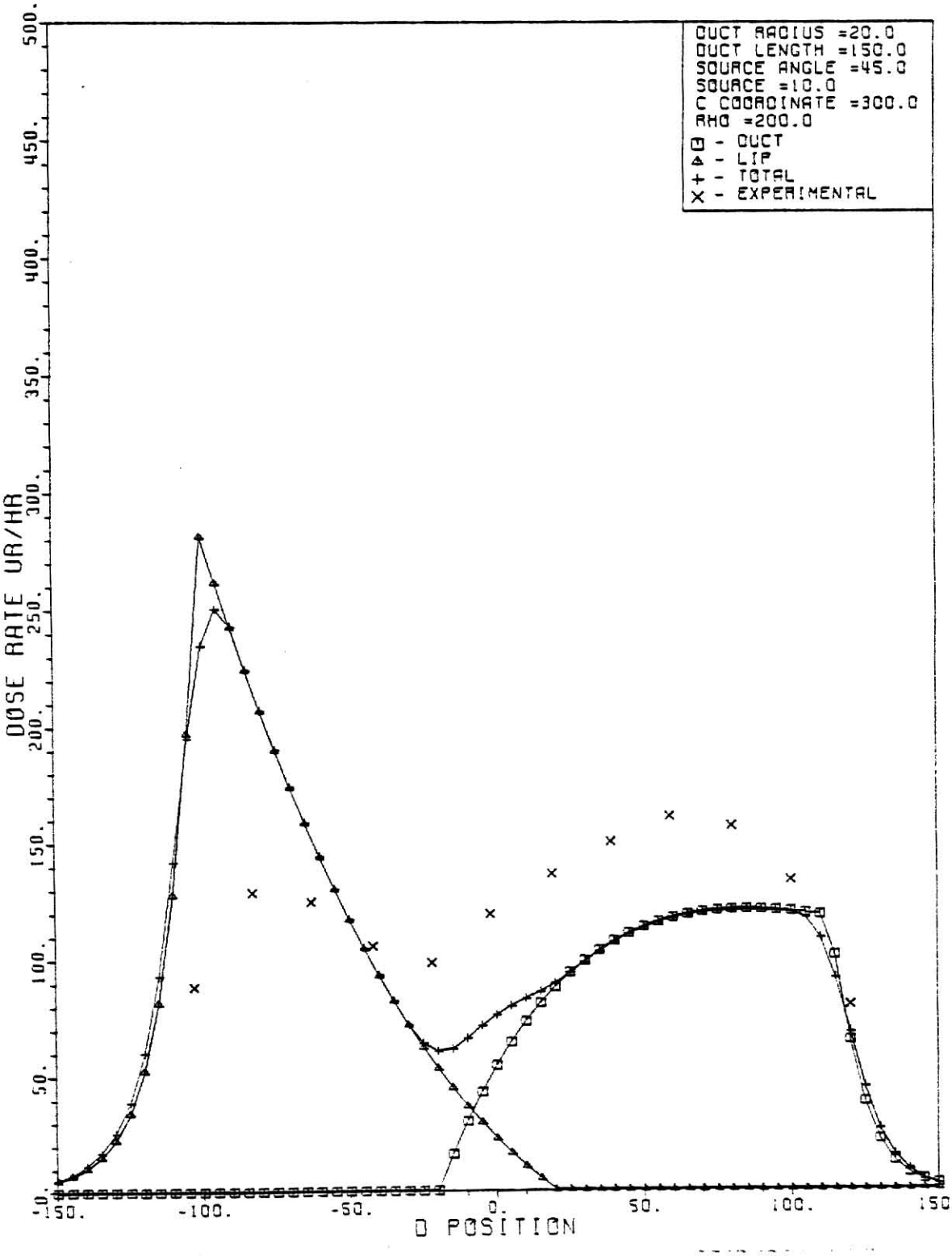
DUCT RADIUS =20.0
DUCT LENGTH =150.0
SOURCE ANGLE =45.0
SOURCE =10.0
C COORDINATE =300.0
RHO =200.0
□ - DUCT
△ - LIP
+ - TOTAL
× - EXPERIMENTAL
DOSE RATE UR/HR
500.
450.
400.
350.
300.
250.
200.
150.
100.
50.
10.
-150.
-100.
-50.
0.
50.
100.
150
D POSITION

Fig. B.6.

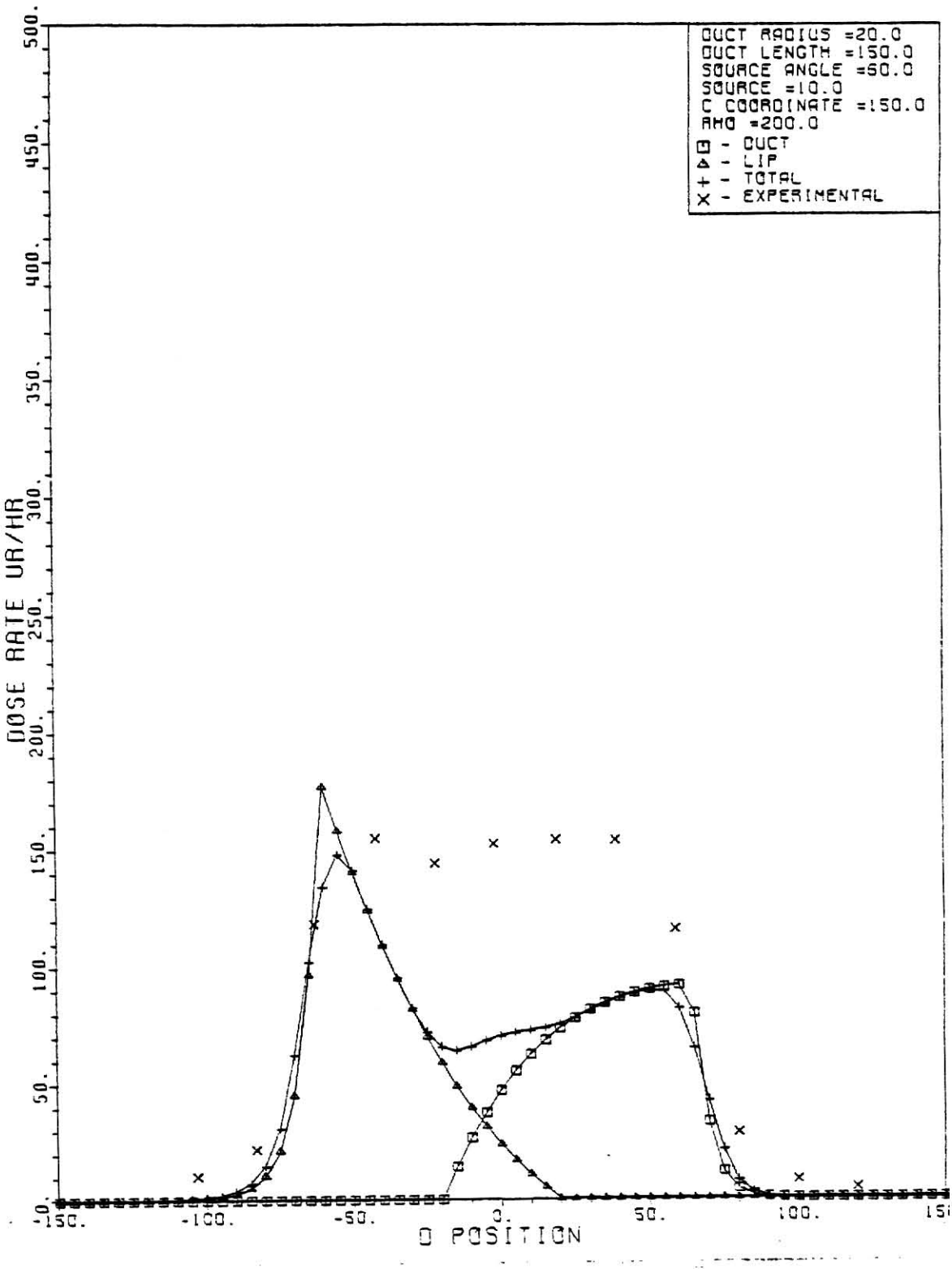
DUCT RADIUS =20.0
DUCT LENGTH =150.0
SOURCE ANGLE =60.0
SOURCE =10.0
C COORDINATE =150.0
RHO =200.0
□ - DUCT
Δ - LIP
+ - TOTAL
X - EXPERIMENTAL
DOSE RATE UR/HR
500.
450.
400.
350.
300.
250.
200.
150.
100.
50.
0.
-150.
-100.
-50.
0.
50.
100.
Θ POSITION

Fig. B.7.

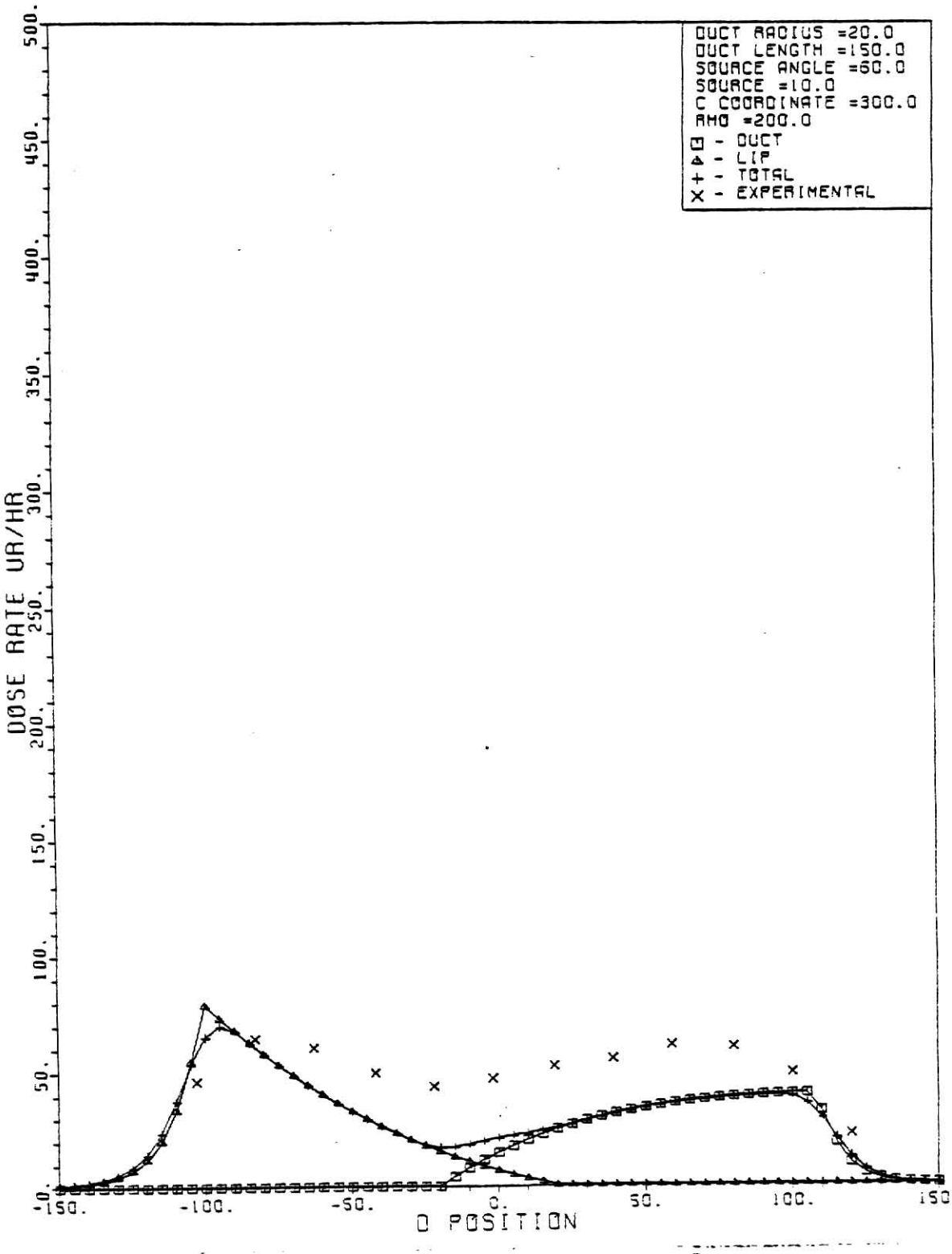
DUCT RADIUS =20.0
DUCT LENGTH =150.0
SOURCE ANGLE =60.0
SOURCE =10.0
C COORDINATE =300.0
RHO =200.0
□ - DUCT
△ - LIP
+ - TOTAL
× - EXPERIMENTAL
DOSE RATE UR/HR
0.
50.
100.
150.
200.
250.
300.
350.
400.
450.
500.
-150.
-100.
-50.
0.
50.
100.
150
D POSITION

Fig. B.8.

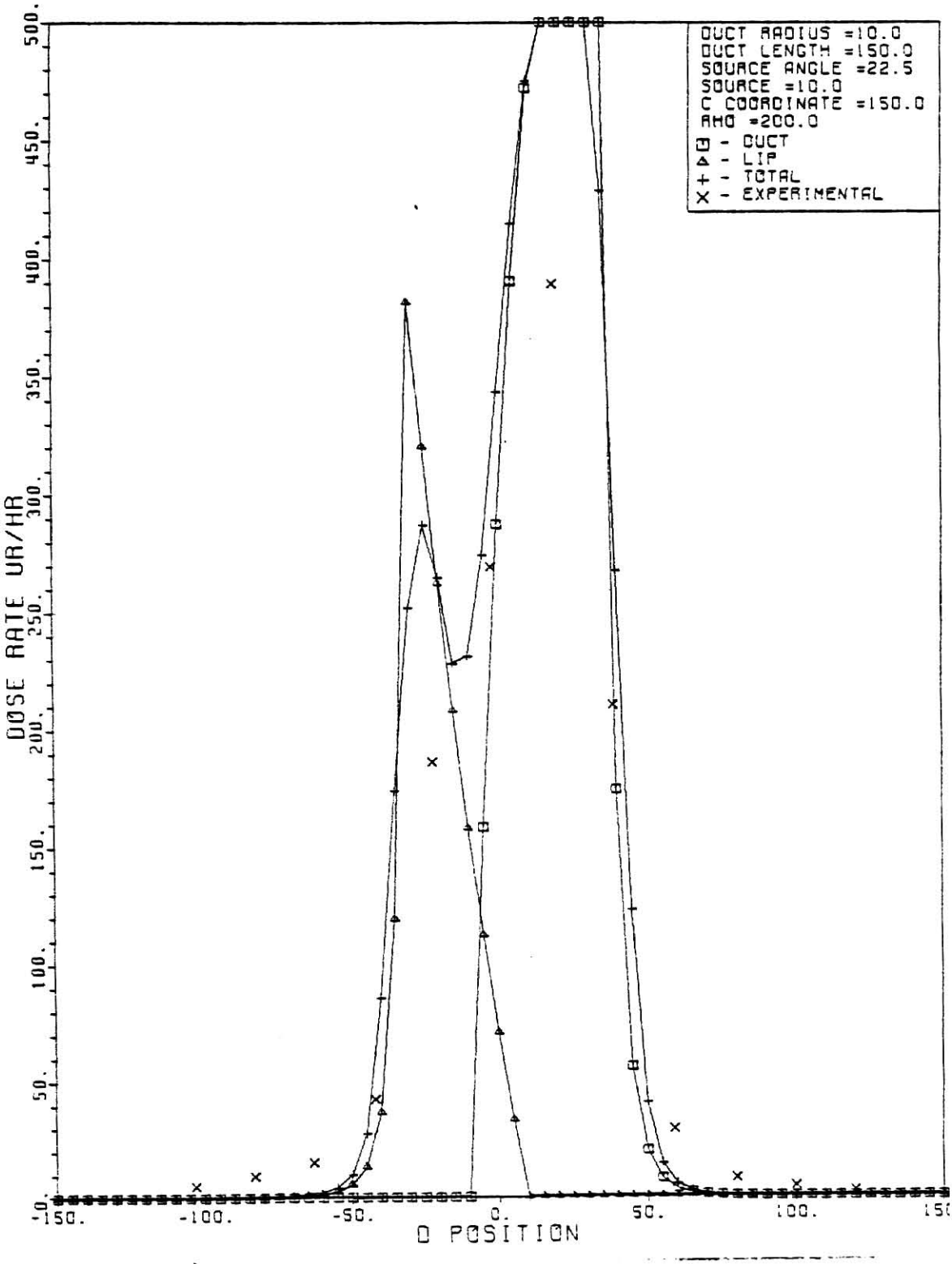
DUCT RADIUS =10.0
DUCT LENGTH =150.0
SOURCE ANGLE =22.5
SOURCE =10.0
C COORDINATE =150.0
RHO =200.0
⊡ - DUCT
△ - LIP
+ - TOTAL
× - EXPERIMENTAL
DOSE RATE UR/HR
0.
50.
100.
150.
200.
250.
300.
350.
400.
450.
500.
-150.
-100.
-50.
0.
50.
100.
150
O POSITION

Fig. B.9.

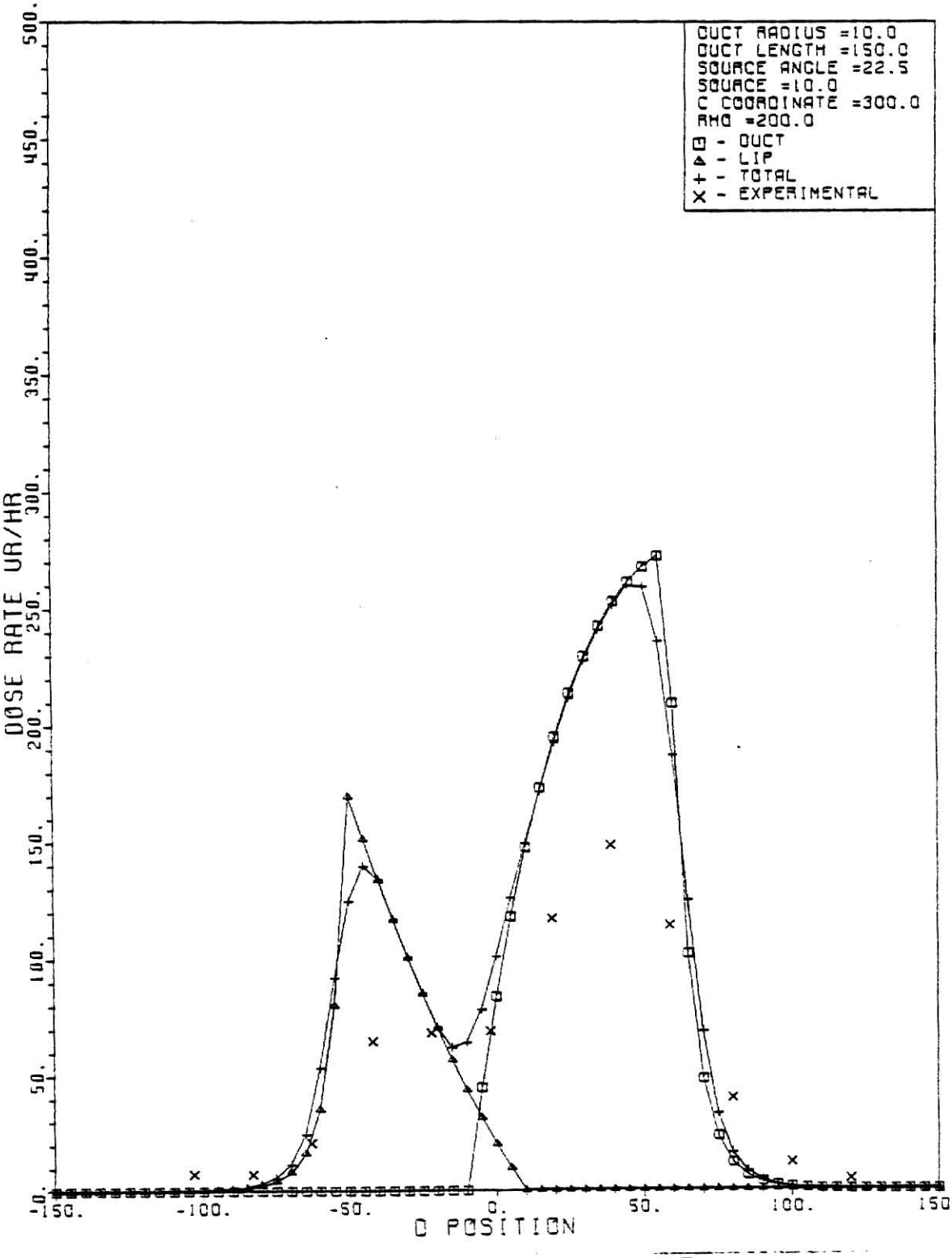
DUCT RADIUS =10.0
DUCT LENGTH =150.0
SOURCE ANGLE =22.5
SOURCE =10.0
C COORDINATE =300.0
RHO =200.0
□ - DUCT
▲ - LIP
+ - TOTAL
× - EXPERIMENTAL
DOSE RATE UR/HR
0.
50.
100.
150.
200.
250.
300.
350.
400.
450.
500.
-150.
-100.
-50.
0.
50.
100.
150
D POSITION

Fig. B.10.

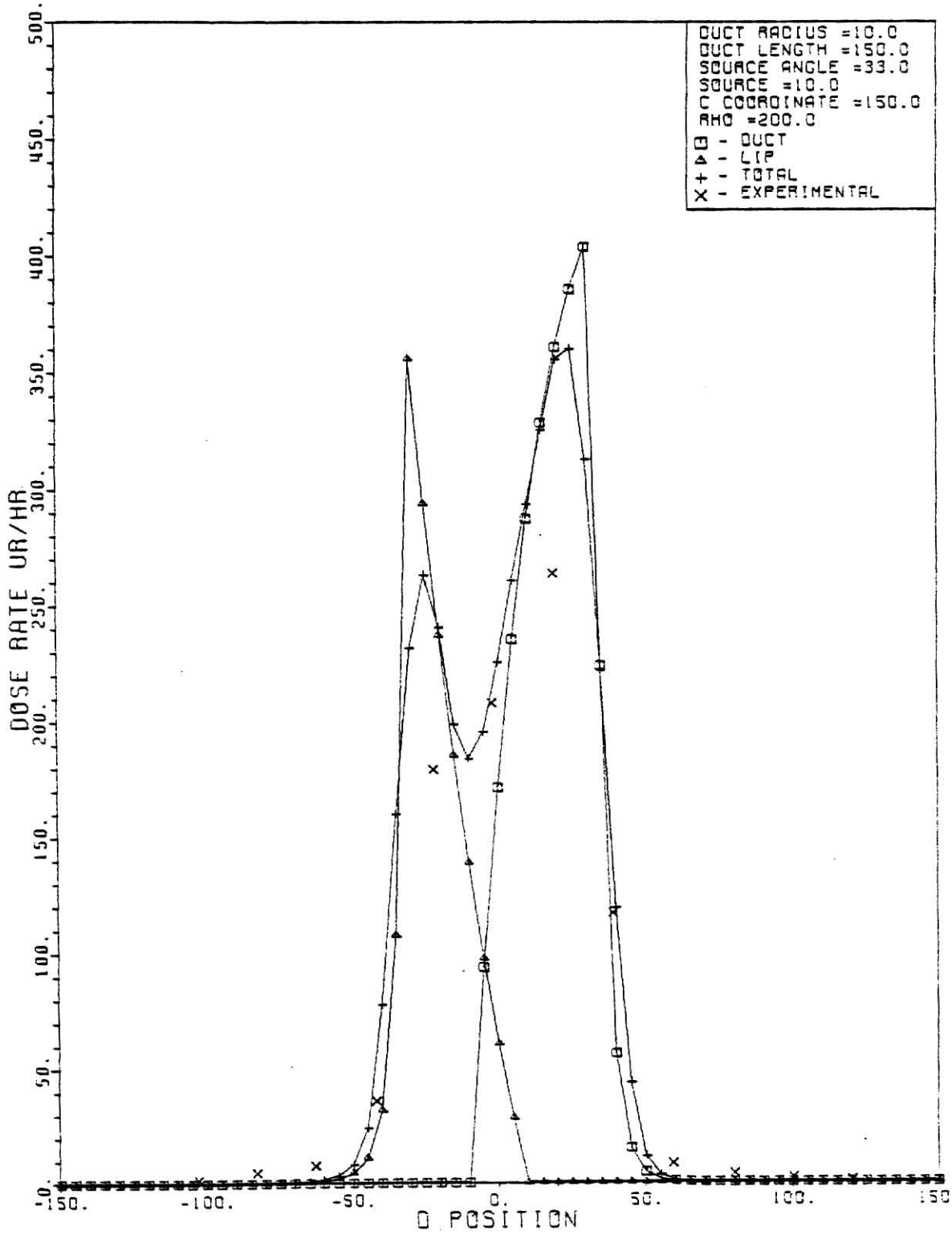
DUCT RADIUS =10.0
DUCT LENGTH =150.0
SOURCE ANGLE =33.0
SOURCE =10.0
C COORDINATE =150.0
RHO =200.0
□ - DUCT
△ - LIP
+ - TOTAL
× - EXPERIMENTAL
DOSE RATE UR/HR
0.
50.
100.
150.
200.
250.
300.
350.
400.
450.
500.
-150.
-100.
-50.
0.
50.
100.
150
Θ POSITION

Fig. B.11.

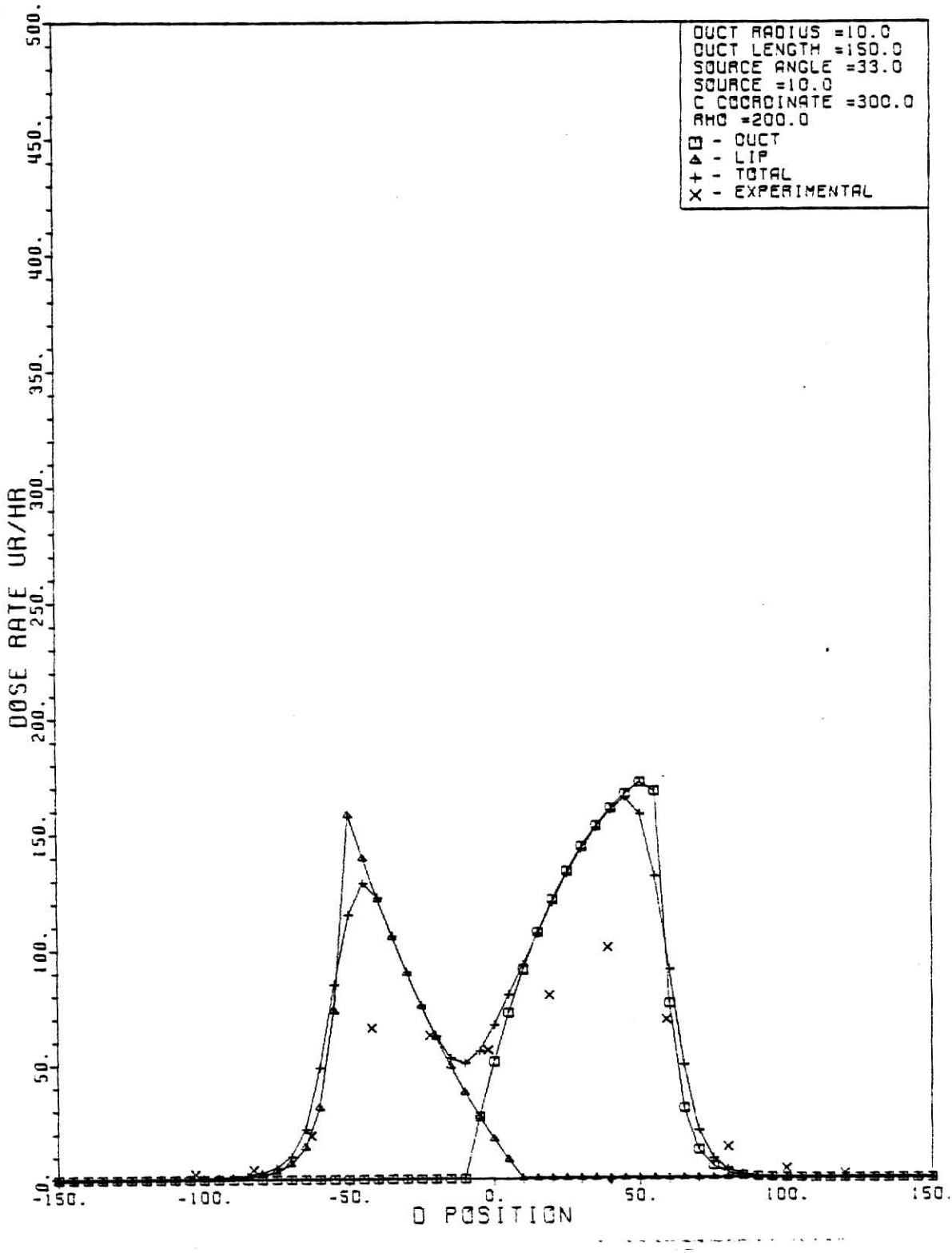
DUCT RADIUS =10.0
DUCT LENGTH =150.0
SOURCE ANGLE =33.0
SOURCE =10.0
C COORDINATE =300.0
RHO =200.0
⊡ - DUCT
△ - LIP
+ - TOTAL
× - EXPERIMENTAL
DOSE RATE UR/HR
0.
50.
100.
150.
200.
250.
300.
350.
400.
450.
500.
-150.
-100.
-50.
0.
50.
100.
150.
D POSITION

Fig. B.12.

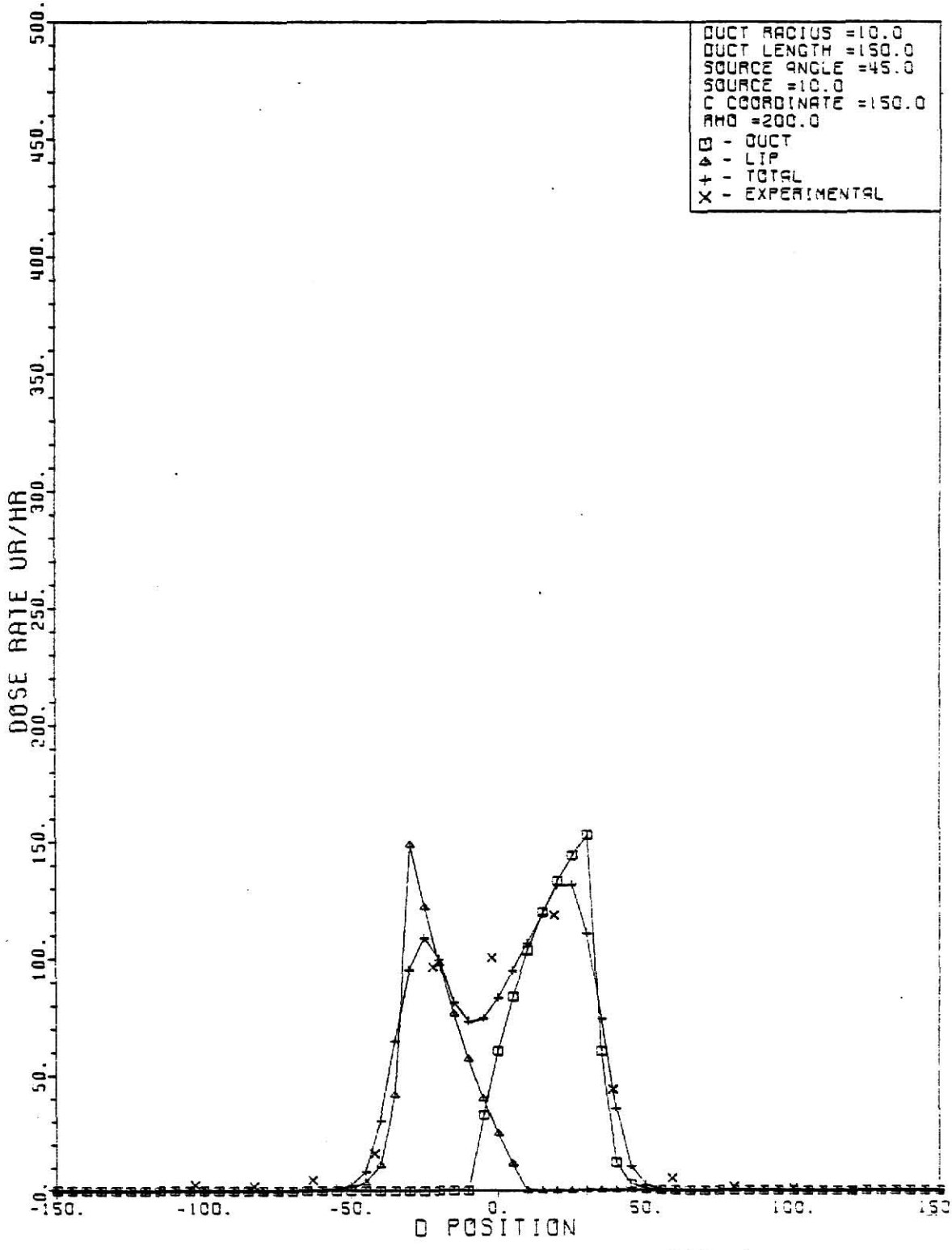
DUCT RADIUS =10.0
DUCT LENGTH =150.0
SOURCE ANGLE =45.0
SOURCE =10.0
Z COORDINATE =150.0
RHO =200.0
□ - DUCT
△ - LIP
+ - TOTAL
× - EXPERIMENTAL
DOSE RATE UR/HR
0.
50.
100.
150.
200.
250.
300.
350.
400.
450.
500.
-150.
-100.
-50.
0.
50.
100.
150.
D POSITION

Fig. B.13.

THIS BOOK WAS BOUND WITH TWO PAGES NUMBERED 194. PAGE 194, FIG. B.14. SHOULD BE NUMBERED PAGE 195.

THIS IS AS RECEIVED FROM CUSTOMER.

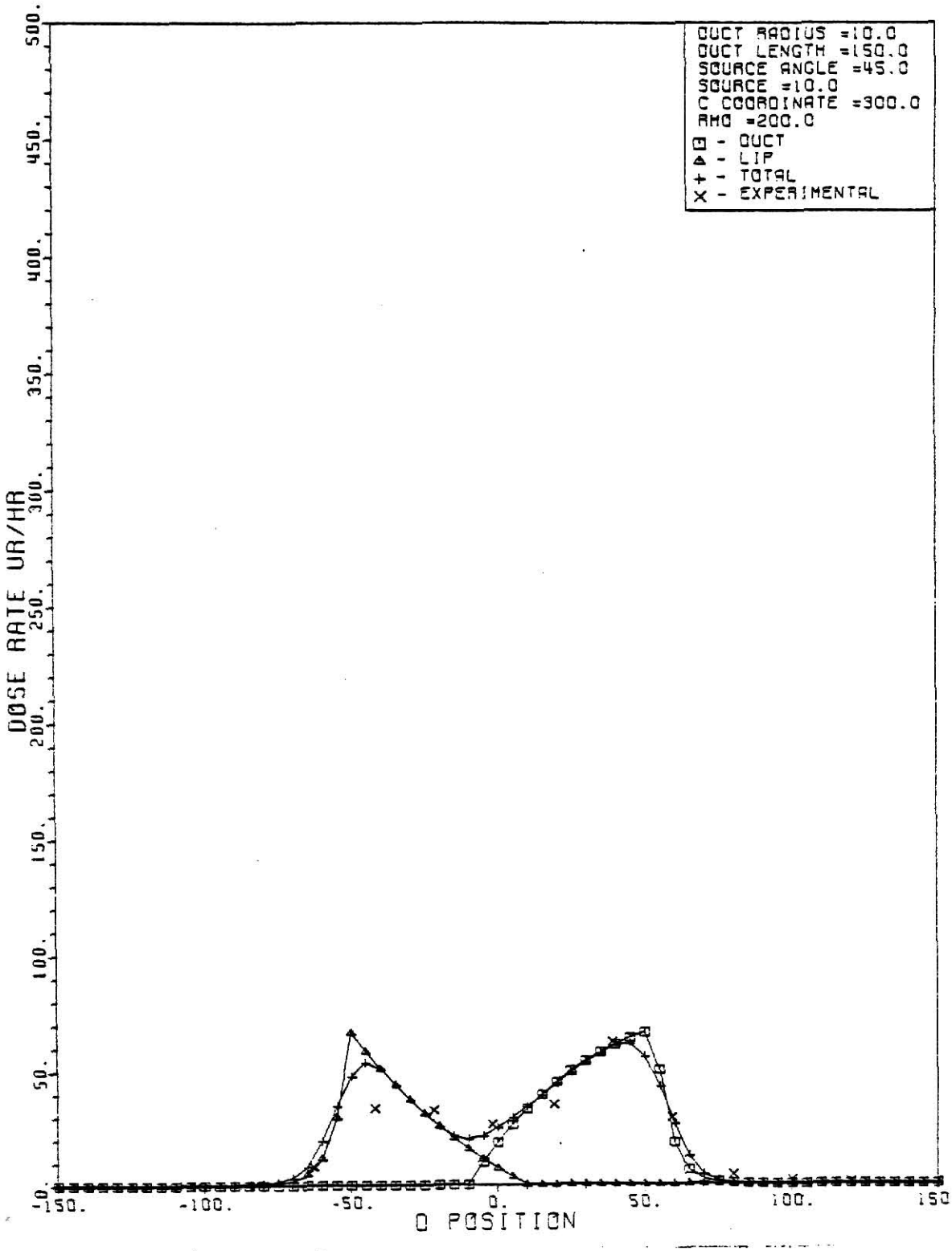
DUCT RADIUS =10.0
DUCT LENGTH =150.0
SOURCE ANGLE =45.0
SOURCE =10.0
C COORDINATE =300.0
RMD =200.0
□ - DUCT
△ - LIP
+ - TOTAL
X - EXPERIMENTAL
DOSE RATE UR/HR
0.
50.
100.
150.
200.
250.
300.
350.
400.
450.
500.
-150.
-100.
-50.
0.
50.
100.
150
D POSITION

Fig. B.14.

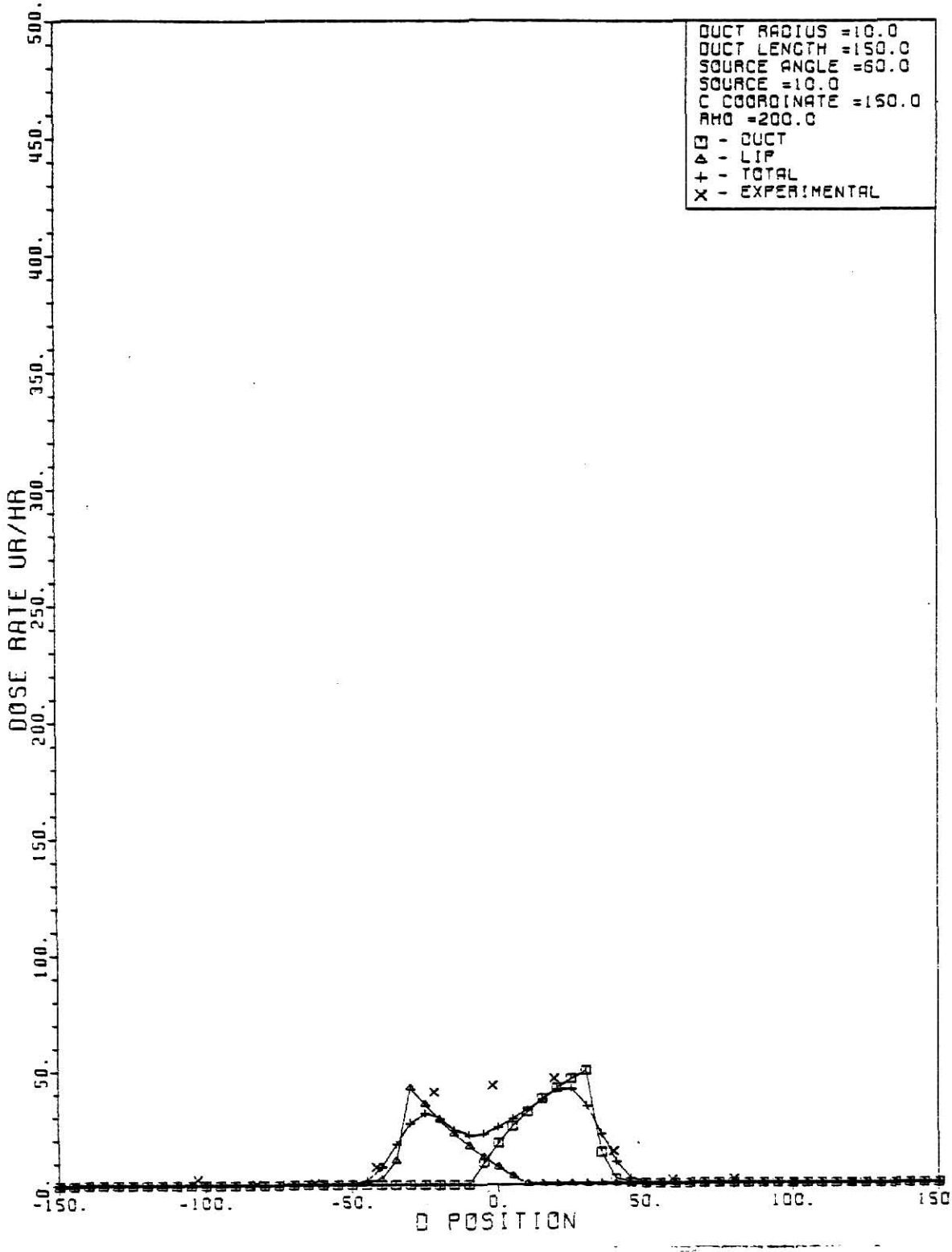
DUCT RADIUS =10.0
DUCT LENGTH =150.0
SOURCE ANGLE =60.0
SOURCE =10.0
C COORDINATE =150.0
RHO =200.0
□ - DUCT
△ - LIP
+ - TOTAL
× - EXPERIMENTAL
DOSE RATE UR/HR
0.
50.
100.
150.
200.
250.
300.
350.
400.
450.
500.
-150.
-100.
-50.
0.
50.
100.
150
D POSITION

Fig. B.15.

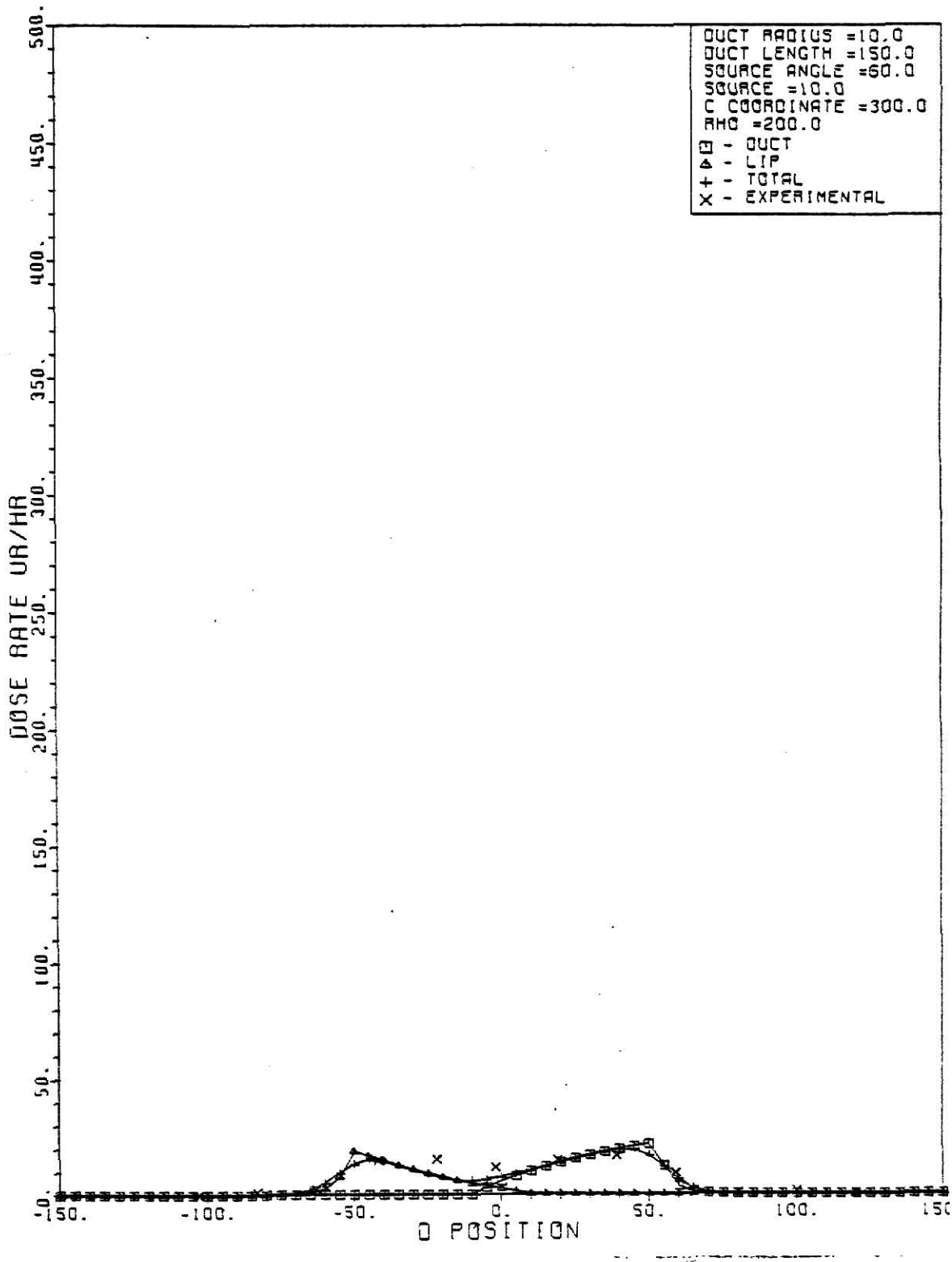
DUCT RADIUS =10.0
DUCT LENGTH =150.0
SOURCE ANGLE =60.0
SOURCE =10.0
C COORDINATE =300.0
RHO =200.0
□ - DUCT
Δ - LIP
+ - TOTAL
× - EXPERIMENTAL
DOSE RATE UR/HR
500.
450.
400.
350.
300.
250.
200.
150.
100.
50.
0.
-150.
-100.
-50.
0.
50.
100.
150
Θ POSITION

Fig. B.16.

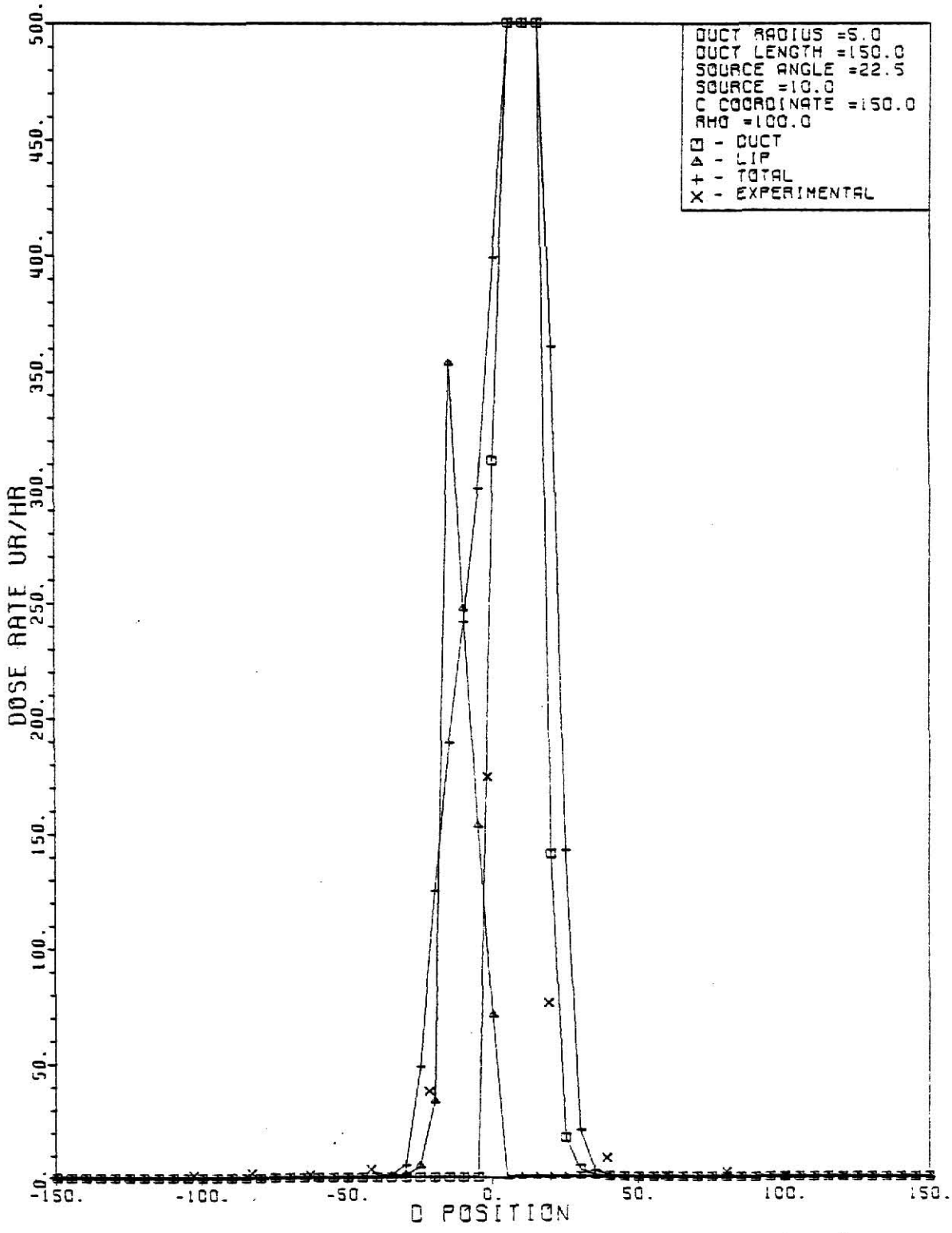
DUCT RADIUS =5.0
DUCT LENGTH =150.0
SOURCE ANGLE =22.5
SOURCE =10.0
C COORDINATE =150.0
RHO =100.0
□ - DUCT
△ - LIP
+ - TOTAL
X - EXPERIMENTAL
DOSE RATE UR/HR
0.
50.
100.
150.
200.
250.
300.
350.
400.
450.
500.
-150.
-100.
-50.
0.
50.
100.
150.
D POSITION

Fig. B.17.

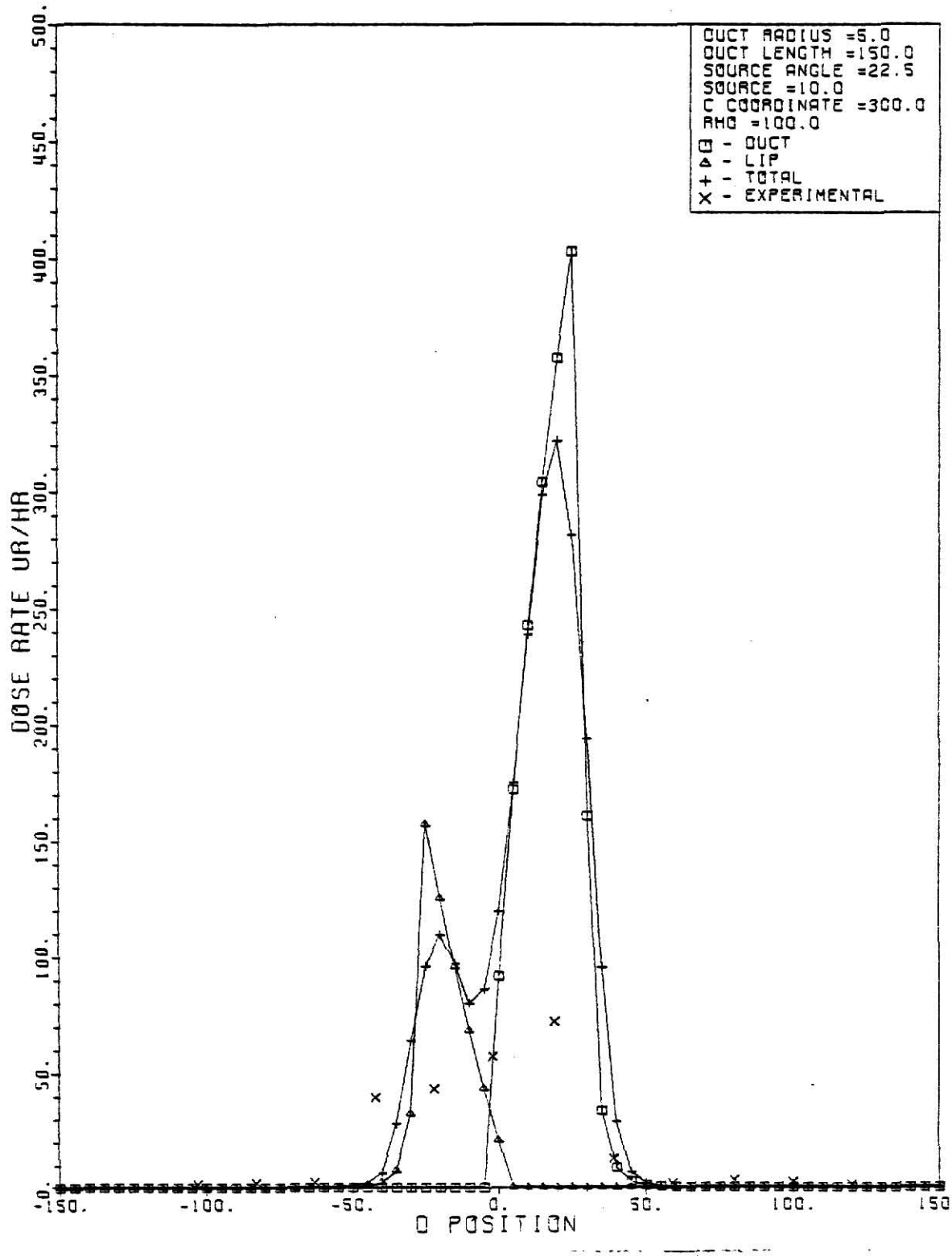
DUCT RADIUS =5.0
DUCT LENGTH =150.0
SOURCE ANGLE =22.5
SOURCE =10.0
C COORDINATE =300.0
RHO =100.0
□ - DUCT
△ - LIP
+ - TOTAL
× - EXPERIMENTAL
DOSE RATE UR/HR
0. 50. 100. 150. 200. 250. 300. 350. 400. 450. 500.
-150. -100. -50. 0. 50. 100. 150.
Θ POSITION

Fig. B.18.

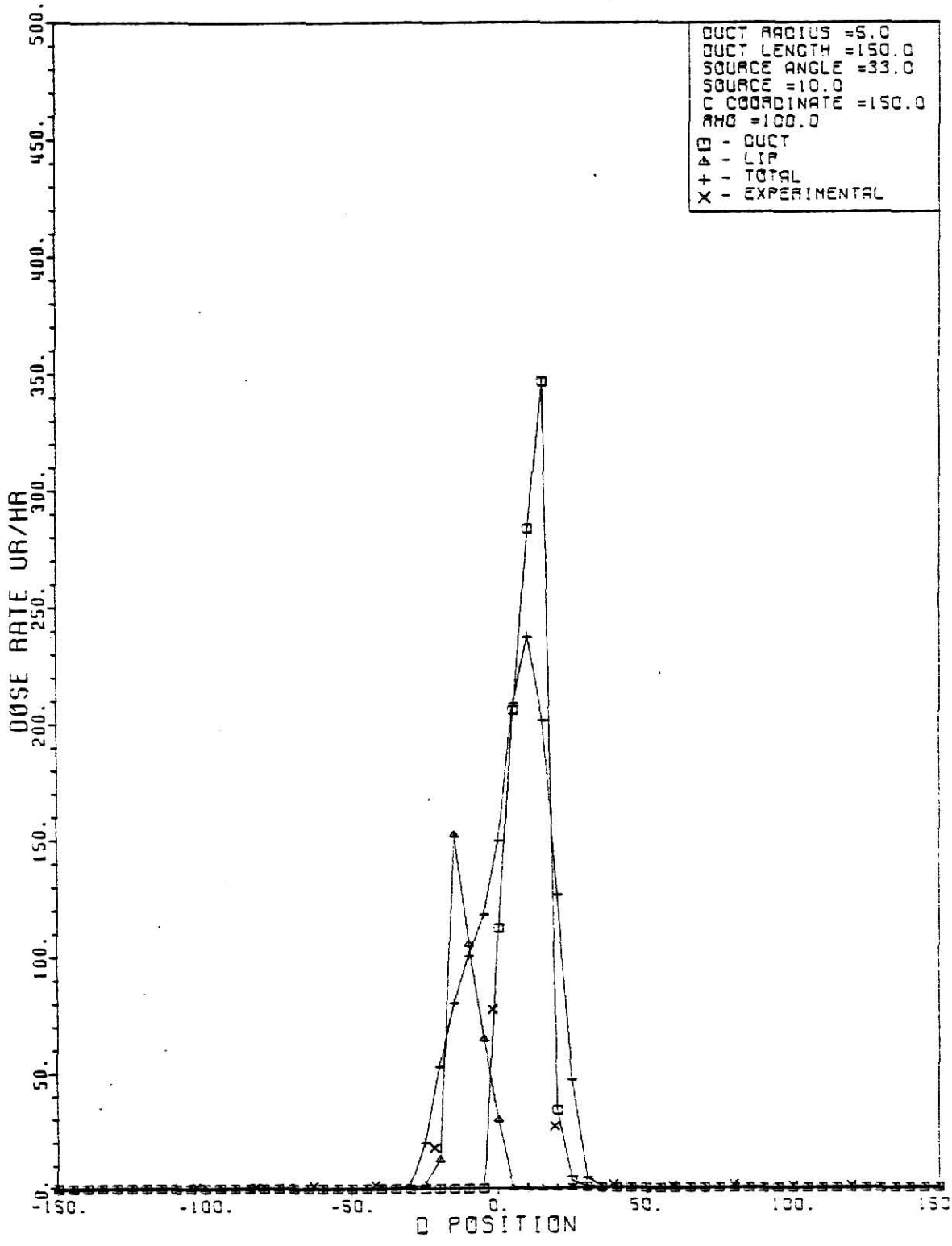
DUCT RADIUS =5.0
DUCT LENGTH =150.0
SOURCE ANGLE =33.0
SOURCE =10.0
C COORDINATE =150.0
AMG =100.0
⊡ - DUCT
△ - LIP
+ - TOTAL
X - EXPERIMENTAL
DOSE RATE UR/HR
0.
50.
100.
150.
200.
250.
300.
350.
400.
450.
500.
-150.
-100.
-50.
0.
50.
100.
150.
D POSITION

Fig. B.19.

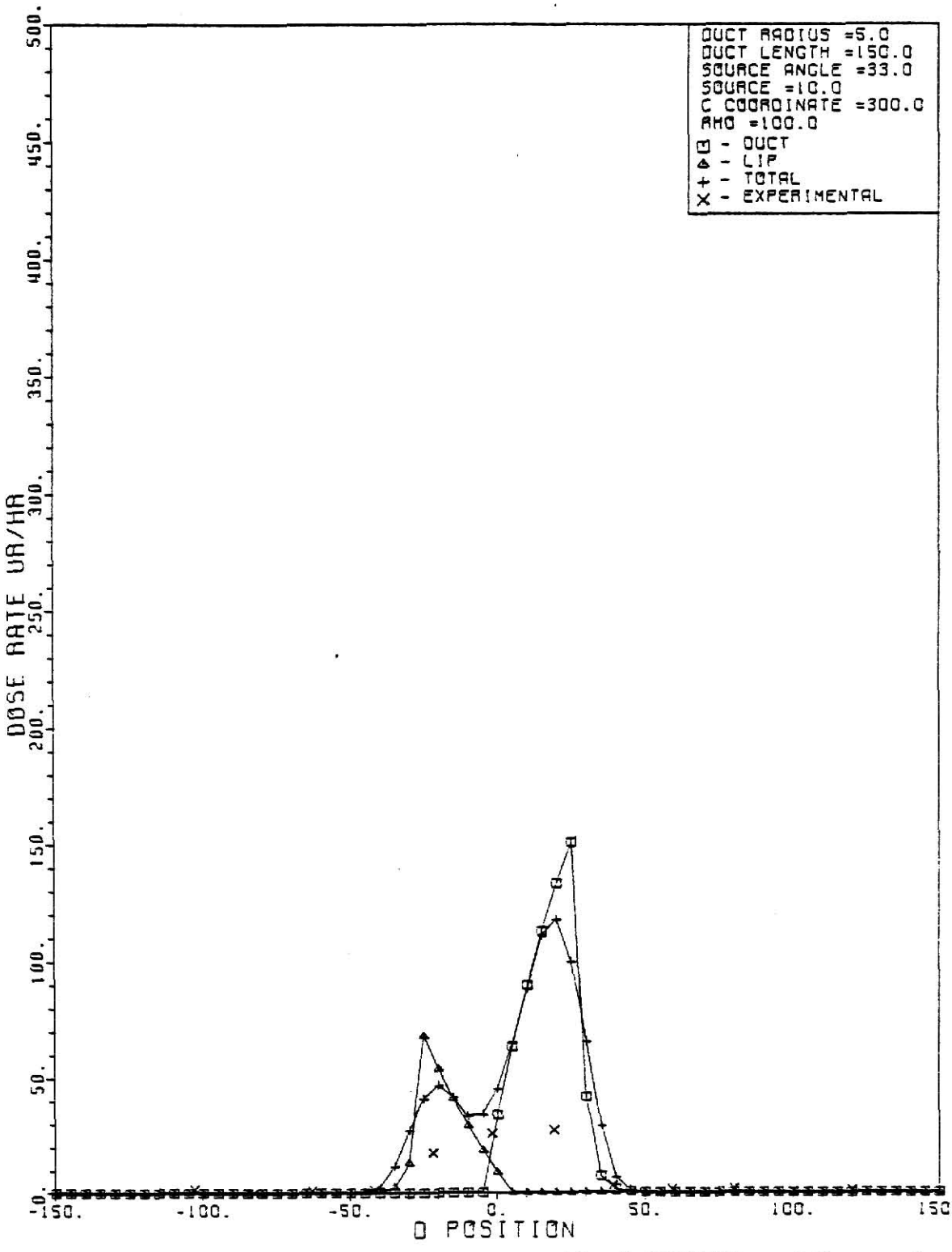
DUCT RADIUS =5.0
DUCT LENGTH =150.0
SOURCE ANGLE =33.0
SOURCE =10.0
C COORDINATE =300.0
RHO =100.0
□ - DUCT
Δ - LIP
+ - TOTAL
X - EXPERIMENTAL
DOSE RATE UR/HR
0. 50. 100. 150. 200. 250. 300. 350. 400. 450. 500.
-150. -100. -50. 0. 50. 100. 150.
D POSITION

Fig. B.20.

APPENDIX C

Presented in this section are the actual FORTRAN computer codes used to calculate the results presented earlier. CGRS (Conversational Gamma Ray Streaming) was the code that resulted from the analytical developments presented in Chapter 2. This code was written for the Kansas State University's ITEL System 370 (similar to IBM 370/158) in the FORTRAN related language of WATFIV. WATFIV was used because it readily allows user conversational programs. CGRS is, however, to the best knowledge of the author, fully FORTRAN compatible. The source listing for CGRS is presented as Fig. C.1 with a sample printed output (unit 8) presented as Fig. C.2. CGRS also produces a punched output (unit 7) that was used to supply data for the plotting routine. The input to CGRS comes from two sources. The parameters that are frequently varied, i.e., the duct radius and the source angle are entered conversationally at a remote terminal. The remaining parameters are read as standard data cards on unit 5. An abbreviated output appears at the terminal subsequent to entering the conversational parameters that completely describe the parameters of the problem presented in that run.

Figure C.3 presents the Calcomp plotting routine used to generate appropriate plots of data presented. Examples of this plotting routine appear in appendices A and B. This routine reads a tagword identifying the data set, then the calculated data set, and then the experimental data set corresponding to the calculated. The plots generated are all of a fixed axis, therefore calculated points greater than 500 μR/h are truncated to plot as 500.0 μR/h and a message is generated on the output listing to alert the user that truncations have occurred.

```
    $JOB
 1        COMMON E,PI
 2        DIMENSION C(3),D(62),DOSE(62,3),DOSEL(62,3)
 3        DIMENSION TTLDSE(62,3),REDUCE(62,3),DTTLS(62,3)
 4        REAL L,N,NIN,KE,MU
 5        REAL L1SQ,L2SQ,L2,K1,K2,K3,K4,NINL,KEL
 6        READ(5,1000)L,RHO,S,N,BFC,E,RHOCON
 7        READ(5,1000)DINT,DSLOPE,CINT,CSLOPE
 8   1000 FORMAT(F16.8)
 9        WRITE(9,3000)
10   3000 FORMAT(1X,'ENTER DUCT RADIUS IN CENTIMETERS')
11        READ(9,*)R
12        WRITE(9,3001)
13   3001 FORMAT(1X,'ENTER SOURCE ANGLE IN DEGREES')
14        READ(9,*)SORESA
15        WRITE(9,8000)
16        WRITE(9,1001)RHO,SORESA,L,R,S,N,E,RHOCON
17   1001 FORMAT(10X,'INPUT PARAMETERS',//,5X,'RHO =',E16.8,' CM.',/,5X,'SOU
          1RCE ANGLE =',E16.8,' DEGREES.',/,5X,'DUCT LENGTH =',E16.8,' CM.',/
          2,5X,'DUCT RADIUS =',E16.8,' CM.',/,5X,'SOURCE STRENGTH =',E16.8,'
          3 CURIES WITH ',F6.1,' GAMMAS PER DISINTEGRATION.',/,
          45X,'EFFECTIVE SOURCE ENERGY =',E16.8,' MEV.',/,5X,
          5'CONCRETE DENSITY =',E16.8,' GM PER CM3.',///)
18        PI=3.141592654
19        THETAS=SORESA*PI/180.0
20        C1=132.4606
21        C2=-1.953935801
22        C3=0.89330964
23        C4=1.144216E-2
24        FOP=C1*(R**C2)*(THETAS**(C3+C4*R))
25        A=RHO*COS(THETAS)
26        B=RHO*SIN(THETAS)
27        ZAA=0.5*6.023E23
28        TTM=ATAN((2.0*R)/(L-(A*R/B)))
29        DO 1 J=1,3
30   8000 FORMAT(///)
31   8001 FORMAT(6X,'DETECTOR POSITION',7X,11('.'),' DOSE RATE CONTRIBUTORS
          1 ',28('.'),/)
32   8003 FORMAT(6X,'CM.',7X,'CM.',11X,'UR/HR',13X,'UR/HR',13X,'UR/HR',8X,'U
          1R.M**2/HR.CI',//)
     C
     C    END INITIALIZATION
     C
33        DO 1 I=1,61
34        C(J)=CINT+CSLOPE*J
35        IF(C(J).EQ.200.0) C(J)=250.0
36        D(I)=DINT+DSLOPE*I
     C
     C    CALCULATE DUCT SCATTERED CONTRIBUTION
     C    IF D .LT. -R SCATTERING IS THROUGH WALL AND NEGLIGIBLE.
     C
37        IF((D(I)+R).LE.0.0) GO TO 200
38        NIN=3.7E10*S*N*(R**2)*(A/B)/(4.0*(RHO**2))
39        THETAT=ATAN((R+D(I))/(C(J)+L-(A*R/B)))
40        KE=FTEXP(ESCAT(THETAS,THETAT))
41        CALL KLEIN(THETAS,THETAT,CROSS)
42        FINA=(C(J)+L-(A*R/B))**2+(R+D(I))**2
43        FINB=MU(E)/SIN(THETAS)+MU(ESCAT(THETAS,THETAT))/SIN(THETAT)
44        FIN=(1.0/FINA)*(1.0/FINB)
45        DOSE(I,J)=NIN*CROSS*ZAA*KE*FIN*BFC
```

Fig. C.1 CGRS Source Listing (P. 1)

```
46          DOSE(I,J)=DOSE(I,J)*FOP+DOSE(I,J)
      C
      C     DOSE = THE DUCT SCATTERED CONTRIBUTION
      C
47          IF(THETAT.GT.TTM)GO TO 300
48          GO TO 201
      C
      C     CORRECT THE DUCT SCATTERED COMPONENT FOR BUILDUP IN THE FAR LIP.
      C
49        300 P=(L-(A*R/B)-((2.0*R)/TAN(THETAT)))/COS(THETAT)
50          EST=ESCAT(THETAS,THETAT)
51          RDCT=RHOCON*P*MU(EST)
52          DOSE(I,J)=DOSE(I,J)*EXP(-1.0*RDCT)*BUF(RDCT,EST)
53          GO TO 201
54        200 DOSE(I,J)=0.0
55        201 CONTINUE
56          ST1=ATAN((B-R)/A)
57          ST3=ATAN((B+R)/(A+L))
58          IF(ST3.GE.ST1) GO TO 999
      C
      C     CALCULATE THE LIP SCATTERED COMPONENT.
      C
59          L1SQ=A**2+(B-R)**2
60          L2SQ=(L+C(J))**2+(R-D(I))**2
61          L2=SQRT(L2SQ)
62          THETSL=ATAN((B-R)/A)
63          THETTL=ARCOS((L+C(J))/L2)
64          ALD=(R-D(I))/L2
65          GAMD=(L+C(J))/L2
66          AL=RHOCON*MU(E)/COS(THETSL)
67          THESCL=THETSL-THETTL
68          IF(D(I).LT.R) GO TO 600
69          PATHL=L/COS(THETTL)
70          ESCL=ESCAT(THETTL,THETSL)
71          CALL KLEIN(THETTL,THETSL,CROSSL)
72          FINL=1.00
73          GO TO 601
74        600 PATHL=L/GAMD-2.0*R/ALD
75          IF(PATHL.LT.0.0) PATHL=0.0
76          ESCL=ESCAT(THESCL,0.0)
77          CALL KLEIN(THESCL,0.0,CROSSL)
78          BET=RHOCON*MU(ESCL)/SIN(THETTL)
79          K1=0.615
80          K2=-0.466
81          K3=0.0812
82          K4=-0.848
83          T1L=K1*(E**K2)
84          T2L=1.0-(K3*EXP(K4*E))
85          FINL=((1.0/BET)+2.0*T1L/(BET*(T2L**3))+R+R*T1L/(T2L**2)
86          FINL=FINL/(AL*BET)
87        601 NINL=3.7E10*S*N/(4.0*L1SQ*L2SQ)
88          KEL=FTEXP(ESCL)*RHOCON
89          RL=RHOCON*PATHL*MU(ESCL)
90          DOSEL(I,J)=NINL*CROSSL*KEL*BUF(RL,ESCL)*EXP(-1.0*RL)*ZAA*FINL
91        8002 FORMAT(7X,'D',9X,'C',13X,'DUCT',15X,'LIP',13X,'TOTAL',11X,'REDUCE
             1',/,2X,92('*'))
92          1 TTLOSE(I,J)=DOSE(I,J)+DOSEL(I,J)
93            DO 2 J=1,3
94          2 CALL SMOOTH(TTLOSE,DTTLS,J)
95            DO 3 J=1,3
```

Fig. C.1 CGRS Source Listing (p. 2)

```
      WRITE(8,8000)
      WRITE(8,1001)RHO,SURESA,L,R,S,N,E,RHOCON
      WRITE(8,8001)
      WRITE(8,8002)
      WRITE(8,8003)
      IR=100000000*R
      IS=0
      IF(S.GT.1.0)IS=1
      IRHO=RHO/10
      IL=((L/50)-1)*100
      IC=(C(J)/10)*1000
      IA=(SURESA*10.0)*100000
      ITYPE=IR+IS+IRHO+IL+IC+IA
      WRITE(7,7654)ITYPE
 7654 FORMAT(I10)
      DO 3 I=1,61
      REDUCE(I,J)=DTTLS(I,J)*((RHO/100.0)**2)/S
      WRITE(7,6000)D(I),DOSE(I,J),DOSEL(I,J),DTTLS(I,J)
 6000 FORMAT(4(E16.8))
    3 WRITE(8,2001)D(I),C(J),DOSE(I,J),DOSEL(I,J),DTTLS(I,J),REDUCE(I,J)
 2001 FORMAT(2(2X,F8.2),4(2X,E16.8))
      STOP
  999 WRITE(9,9090)
 9090 FORMAT(' EXECUTION ABORTED ..... OPEN DUCT PRESENTED.')
      STOP
      END

      REAL FUNCTION MU(E)
      MU=0.0625/(E**0.467)
      RETURN
      END

      FUNCTION ESCAT(THETAS,THETAT)
      COMMON E,PI
      ALPHA=E/0.511
      ESCAT=E/(1.0+ALPHA*(1.0-COS(THETAS+THETAT)))
      RETURN
      END

      SUBROUTINE KLEIN(THETAS,THETAT,CROSS)
      COMMON E,PI
      Y=ESCAT(THETAS,THETAT)/E
      CROSS=(3.0E-24*0.665/(16.0*PI))*(Y**2)*((1.0/Y)+Y-(SIN(THETAS+THET
     1AT)**2))
      RETURN
      END

      FUNCTION BUF(R,E)
      REAL K1,K2,K3,K4
      K1=0.615
      K2=-0.466
      K3=0.0812
      K4=-0.848
      BUF=1.0+R*K1*(E**K2)*EXP(R*K3*EXP(K4*E))
      RETURN
      END

      SUBROUTINE SMOOTH(DT,DS,J)
      DIMENSION DT(62,3),DS(62,3)
      DS(1,J)=DT(1,J)

      DS(2,J)=DT(2,J)
      DS(60,J)=DT(60,J)
      DS(61,J)=DT(61,J)
      W1=0.1085753983
      W2=0.2456937985
      W3=0.2914616066
      W4=W2
      W5=W1
      DO 1 I=3,59
      IM2=I-2
      IM1=I-1
      IP1=I+1
      IP2=I+2
    1 DS(I,J)=DT(IM2,J)*W1+DT(IM1,J)*W2+DT(I,J)*W3+DT(IP1,J)*W4+DT(IP2,J
     1)*W5
      RETURN
      END

      FUNCTION FTEXP(E)
      FTEXP=1.90*E
      RETURN
      END
$ENTRY
```

Fig. C.1 CGRS Source Listing (p. 3)

INPUT PARAMETERS

RIN = 0.30000000E 03 CM.
SOURCE ANGLE = 0.13000000E 02 DEGREES.
DUCT LENGTH = 0.10000000E 03 CM.
DUCT RADIUS = 0.20000000E 02 CM.
SOURCE STRENGTH = 0.81169990E 01 CURIES WITH 2.0 GAMMAS PER DISINTEGRATION.
EFFECTIVE SOURCE ENERGY = 0.12500000E 01 MEV.
CONCRETE DENSITY = 0.22200000E 01 GM PER CM3.

DETECTOR POSITION		..... DOSE RATE CONTRIBUTORS			
D	C	DUCT	LIP	TOTAL	REDUCED
CM.	CM.	UR/HR	UR/HR	UR/HR	UR.M**2/HR.CI
-150.00	100.00	0.00000000E 00	0.46030110E 01	0.46030110E 01	0.51037440E 01
-145.00	100.00	0.00000000E 00	0.65031550E 01	0.65031550E 01	0.72105940E 01
-140.00	100.00	0.00000000E 00	0.91837670E 01	0.99496800E 01	0.11032040E 02
-135.00	100.00	0.00000000E 00	0.12968400E 02	0.14056310E 02	0.15585410E 02
-130.00	100.00	0.00000000E 00	0.18320480E 02	0.19872370E 02	0.22034160E 02
-125.00	100.00	0.00000000E 00	0.25906600E 02	0.28133190E 02	0.31193630E 02
-120.00	100.00	0.00000000E 00	0.36695120E 02	0.39912300E 02	0.44254110E 02
-115.00	100.00	0.00000000E 00	0.52105660E 02	0.56793600E 02	0.62971810E 02
-110.00	100.00	0.00000000E 00	0.74241860E 02	0.81142210E 02	0.89969170E 02
-105.00	100.00	0.00000000E 00	0.10626240E 03	0.11653690E 03	0.12921430E 03
-100.00	100.00	0.00000000E 00	0.15297540E 03	0.16846830E 03	0.18679500E 03
-95.00	100.00	0.00000000E 00	0.22180270E 03	0.24547350E 03	0.27217700E 03
-90.00	100.00	0.00000000E 00	0.32436050E 03	0.36096550E 03	0.40023260E 03
-85.00	100.00	0.00000000E 00	0.47902750E 03	0.53607250E 03	0.59438840E 03
-80.00	100.00	0.00000000E 00	0.71497160E 03	0.80346890E 03	0.89087320E 03
-75.00	100.00	0.00000000E 00	0.10777280E 04	0.12099140E 04	0.13415330E 04
-70.00	100.00	0.00000000E 00	0.16337010E 04	0.18036730E 04	0.19998840E 04
-65.00	100.00	0.00000000E 00	0.24566670E 04	0.24503660E 04	0.27169270E 04
-60.00	100.00	0.00000000E 00	0.35137390E 04	0.29255670E 04	0.32438220E 04
-55.00	100.00	0.00000000E 00	0.32478260E 04	0.31980940E 04	0.34351170E 04
-50.00	100.00	0.00000000E 00	0.29703840E 04	0.29656680E 04	0.32883070E 04
-45.00	100.00	0.00000000E 00	0.26860230E 04	0.26845100E 04	0.29765410E 04
-40.00	100.00	0.00000000E 00	0.23994500E 04	0.24010700E 04	0.26622680E 04
-35.00	100.00	0.00000000E 00	0.21152970E 04	0.21158410E 04	0.23505010E 04
-30.00	100.00	0.00000000E 00	0.18379720E 04	0.18432490E 04	0.20459820E 04
-25.00	100.00	0.00000000E 00	0.15714390E 04	0.16349740E 04	0.18128330E 04
-20.00	100.00	0.00000000E 00	0.13191050E 04	0.15456480E 04	0.17137490E 04
-15.00	100.00	0.49688180E 03	0.10837460E 04	0.15721620E 04	0.17431870E 04
-10.00	100.00	0.85653120E 03	0.86741740E 03	0.16635200E 04	0.18444840E 04
-5.00	100.00	0.11078640E 04	0.67146280E 03	0.17456310E 04	0.19244400E 04
0.00	100.00	0.12747210E 04	0.49652510E 03	0.17403750E 04	0.19302540E 04
5.00	100.00	0.13765460E 04	0.34264860E 03	0.16992100E 04	0.18840370E 04
10.00	100.00	0.14290310E 04	0.20929600E 03	0.16262810E 04	0.18031950E 04
15.00	100.00	0.14447120E 04	0.95510450E 02	0.15426420E 04	0.17104570E 04
20.00	100.00	0.14334840E 04	0.23666360E-04	0.14664460E 04	0.16259720E 04
25.00	100.00	0.14030840E 04	0.19402140E-04	0.14043280E 04	0.15570960E 04
30.00	100.00	0.13594910E 04	0.15689560E-04	0.13534580E 04	0.15007370E 04

Fig. C.2 Sample CGRS printed output (p. 1)

35.00	100.00	0.13072630E 04	0.12915860E-04	0.13036360E 04	0.14454910E 04
40.00	100.00	0.12496460E 04	0.98634180E-05	0.12475780E 04	0.13837170E 04
45.00	100.00	0.11877910E 04	0.76746320E-05	0.11892100E 04	0.13185780E 04
50.00	100.00	0.11289690E 04	0.59005980E-05	0.11293100E 04	0.12521600E 04
55.00	100.00	0.10687130E 04	0.44852580E-05	0.10696580E 04	0.11860640E 04
60.00	100.00	0.10099580E 04	0.33716150E-05	0.10113740E 04	0.11213950E 04
65.00	100.00	0.95332340E 03	0.25076030E-05	0.95501530E 03	0.10589050E 04
70.00	100.00	0.89920580E 03	0.18495580E-05	0.89398040E 03	0.99123120E 03
75.00	100.00	0.84783000E 03	0.13459670E-05	0.80700000E 03	0.89478850E 03
80.00	100.00	0.79412860E 03	0.97154400E-06	0.67985180E 03	0.75380830E 03
85.00	100.00	0.50732640E 03	0.69512210E-06	0.52207340E 03	0.57886640E 03
90.00	100.00	0.32509220E 03	0.49298520E-06	0.36210180E 03	0.40149260E 03
95.00	100.00	0.20180000E 03	0.34668080E-06	0.23229680E 03	0.25756680E 03
100.00	100.00	0.12454800E 03	0.24182380E-06	0.14434080E 03	0.16004260E 03
105.00	100.00	0.75234690E 02	0.16736350E-06	0.88462260E 02	0.98065510E 02
110.00	100.00	0.45762030E 02	0.11495790E-06	0.53528640E 02	0.59795190E 02
115.00	100.00	0.27863540E 02	0.78388430E-07	0.32839460E 02	0.36411830E 02
120.00	100.00	0.17001090E 02	0.53078180E-07	0.20017450E 02	0.22195020E 02
125.00	100.00	0.10399880E 02	0.35698690E-07	0.12226730E 02	0.13556800E 02
130.00	100.00	0.63789530E 01	0.23853190E-07	0.74867730E 01	0.83012130E 01
135.00	100.00	0.39230250E 01	0.15838240E-07	0.45963710E 01	0.50963630E 01
140.00	100.00	0.24186580E 01	0.10453130E-07	0.28290920E 01	0.31368510E 01
145.00	100.00	0.14945730E 01	0.68583110E-08	0.14945730E 01	0.16571580E 01
150.00	100.00	0.92545800E 00	0.44744750E-08	0.92545800E 00	0.10261320E 01

INPUT PARAMETERS

RHO = 0.30000000E 03 CM.
SOURCE ANGLE = 0.13000000E 02 DEGREES.
DUCT LENGTH = 0.10000000E 03 CM.
DUCT RADIUS = 0.20000000E 02 CM.
SOURCE STRENGTH = 0.81169990E 01 CURIES WITH 2.0 GAMMAS PER DISINTEGRATION.
EFFECTIVE SOURCE ENERGY = 0.12500000E 01 MEV.
CONCRETE DENSITY = 0.22200000E 01 GM PER CM3.

DETECTOR POSITION		DOSE RATE CONTRIBUTORS			
D	C	DUCT	LIP	TOTAL	REDUCED
CM.	CM.	UR/HR	UR/HR	UR/HR	UR.M**2/HR.CI
-150.00	150.00	0.00000000E 00	0.31081630E 02	0.31081630E 02	0.34462790E 02
-145.00	150.00	0.00000000E 00	0.41220770E 02	0.41220770E 02	0.45704910E 02
-140.00	150.00	0.00000000E 00	0.54809660E 02	0.58070550E 02	0.64387690E 02
-135.00	150.00	0.00000000E 00	0.73112500E 02	0.77605750E 02	0.86048000E 02
-130.00	150.00	0.00000000E 00	0.97904370E 02	0.10414740E 03	0.11547760E 03
-125.00	150.00	0.00000000E 00	0.13170450E 03	0.14045190E 03	0.15573080E 03
-120.00	150.00	0.00000000E 00	0.17811500E 03	0.19047250E 03	0.21119280E 03
-115.00	150.00	0.00000000E 00	0.24232640E 03	0.25990820E 03	0.28818180E 03
-110.00	150.00	0.00000000E 00	0.33185980E 03	0.35696800E 03	0.39580020E 03
-105.00	150.00	0.00000000E 00	0.45758100E 03	0.49333050E 03	0.54699650E 03
-100.00	150.00	0.00000000E 00	0.63496970E 03	0.68496240E 03	0.75947500E 03
-95.00	150.00	0.00000000E 00	0.88517940E 03	0.95134880E 03	0.10544400E 04
-90.00	150.00	0.00000000E 00	0.12337420E 04	0.13077690E 04	0.14500330E 04

Fig C.2 Sample CGRS printed output (p. 2)

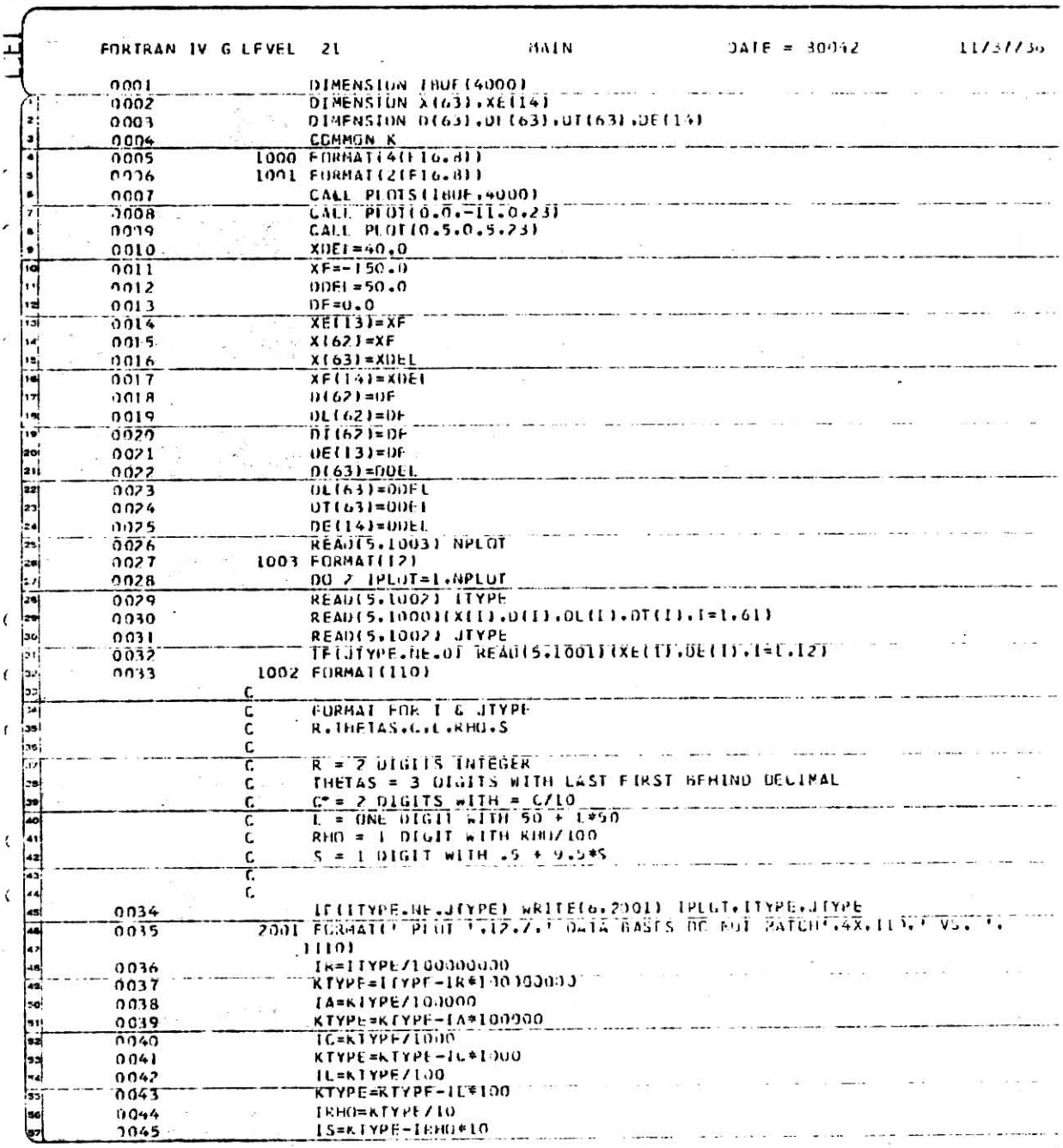

```
      FORTRAN IV G LEVEL  21                MAIN                DATE = 80042        11/37/36

0001                  DIMENSION IBUF(4000)
0002                  DIMENSION X(63),XE(14)
0003                  DIMENSION D(63),DL(63),DT(63),DE(14)
0004                  COMMON K
0005             1000 FORMAT(4(F16.8))
0006             1001 FORMAT(2(F16.8))
0007                  CALL PLOTS(IBUF,4000)
0008                  CALL PLOT(0.0,-11.0,3)
0009                  CALL PLOT(0.5,0.5,3)
0010                  XDEL=40.0
0011                  XF=-150.0
0012                  ODEL=50.0
0013                  DF=0.0
0014                  XE(1)=XF
0015                  X(62)=XF
0016                  X(63)=XDEL
0017                  XE(14)=XDEL
0018                  D(62)=DF
0019                  DL(62)=DF
0020                  DT(62)=DF
0021                  DE(1)=DF
0022                  D(63)=ODEL
0023                  DL(63)=ODEL
0024                  DT(63)=ODEL
0025                  DE(14)=ODEL
0026                  READ(5,1003) NPLOT
0027             1003 FORMAT(I2)
0028                  DO 7 IPLOT=1,NPLOT
0029                  READ(5,1002) ITYPE
0030                  READ(5,1000)(X(I),D(I),DL(I),DT(I),I=1,61)
0031                  READ(5,1002) JTYPE
0032                  IF(JTYPE.NE.0) READ(5,1001)(XE(I),DE(I),I=1,12)
0033             1002 FORMAT(I10)
                      C
                      C     FORMAT FOR I & JTYPE
                      C     R,THETAS,C,L,RHO,S
                      C
                      C     R = 2 DIGITS INTEGER
                      C     THETAS = 3 DIGITS WITH LAST FIRST BEHIND DECIMAL
                      C     C* = 2 DIGITS WITH = C/10
                      C     L = ONE DIGIT WITH 50 + L*50
                      C     RHO = 1 DIGIT WITH RHO/100
                      C     S = 1 DIGIT WITH .5 + 9.5*S
                      C
                      C
0034                  IF(ITYPE.NE.JTYPE) WRITE(6,2001) IPLOT,ITYPE,JTYPE
0035             2001 FORMAT(' PLOT ',I2,/,' DATA BASES DO NOT MATCH',4X,I10,' VS. ',
                     1I10)
0036                  IR=ITYPE/1000000000
0037                  KTYPE=ITYPE-IR*1000000000
0038                  IA=KTYPE/100000
0039                  KTYPE=KTYPE-IA*100000
0040                  IC=KTYPE/1000
0041                  KTYPE=KTYPE-IC*1000
0042                  IL=KTYPE/100
0043                  KTYPE=KTYPE-IL*100
0044                  IRHO=KTYPE/10
0045                  IS=KTYPE-IRHO*10
```

Fig. C.3 Calcomp Plotting Routine (p. 1)

```
FORTRAN IV G LEVEL  21                MAIN              DATE = 80042        11/37/36

0046                SOURCE=0.5+9.5*IS
0047                RHO=IRHO*100.0
0048                RADIUS=IR
0049                ANGLE=JA/10.0
0050                C=IC*10
0051                WL=50+50*IL
0052                K=0
0053                DO 1 I=1,61
0054                J=1
0055                IF(D(I).GT.500.0) CALL TRUNC(X(I),D(I),J)
0056                J=2
0057                DL(I)=D(I)
0058                IF(DL(I).GT.500.0) CALL TRUNC(X(I),DL(I),J)
0059                J=3
0060                DT(I)=DL(I)
0061                IF(DT(I).GT.500.0) CALL TRUNC(X(I),DT(I),J)
0062              1 DT(I)=DT(I)
0063                IF(K.NE.0) WRITE(6,2000) K
0064             2000 FORMAT(' TOTAL TRUNCATIONS =',I2)
0065                CALL DAXIS(0.0,0.0,10.0,90.0,0.0,20.5)
0066                CALL SAXIS(DF,50.0,0.0,2.5,'DCSE RATE GR/HR',15)
0067                CALL DAXIS(0.0,0.0,7.50,0.0,0.250,-5)
0068                CALL SAXIS(XF,50.0,0.0,1.,-5,'D POSITION',10)
0069                CALL PLOT(7.5,0.0,3)
0070                CALL PLOT(7.5,10.0,2)
0071                CALL PLOT(0.0,10.0,2)
0072                CALL SYMBOL(5.5,9.85,0.10,'DUCT RADIUS =',0.0,13)
0073                CALL NUMBER(999.0,999.0,0.10,RADIUS,0.0,1)
0074                CALL SYMBOL(5.5,9.7,0.10,'DUCT LENGTH =',0.0,13)
0075                CALL NUMBER(999.0,999.0,0.10,WL,0.0,1)
0076                CALL SYMBOL(5.5,9.55,0.10,'SOURCE ANGLE =',0.0,14)
0077                CALL NUMBER(999.0,999.0,0.10,ANGLE,0.0,1)
0078                CALL SYMBOL(5.5,9.40,0.10,'SOURCE =',0.0,8)
0079                CALL NUMBER(999.0,999.0,0.10,SOURCE,0.0,1)
0080                CALL SYMBOL(5.5,9.25,0.10,'C COORDINATE =',0.0,14)
0081                CALL NUMBER(999.0,999.0,0.10,C,0.0,1)
0082                CALL SYMBOL(5.5,9.1,0.10,'RHO =',0.0,5)
0083                CALL NUMBER(999.0,999.0,0.10,RHO,0.0,1)
0084                CALL SYMBOL(5.5,8.95,0.10,0.0,0.0,-1)
0085                CALL SYMBOL(999.0,999.0,0.10,'- DUCT',0.0,6)
0086                CALL SYMBOL(5.5,8.8,0.10,2.0,0.0,-1)
0087                CALL SYMBOL(999.0,999.0,0.10,'- LIP',0.0,5)
0088                CALL SYMBOL(5.5,8.65,0.10,3.0,0.0,-1)
0089                CALL SYMBOL(999.0,999.0,0.10,'- TOTAL',0.0,7)
0090                CALL SYMBOL(5.5,8.5,0.10,4.0,0.0,-1)
0091                CALL SYMBOL(999.0,999.0,0.10,'- EXPERIMENTAL',0.0,14)
0092                CALL PLOT(5.375,10.0,3)
0093                CALL PLOT(5.375,8.375,2)
0094                CALL PLOT(7.50,8.375,2)
0095                CALL LINE(X,0.0,61,1,1,0)
0096                CALL LINE(X,DL,61,1,1,2)
0097                CALL LINE(X,DT,61,1,1,3)
0098                IF(JTYPE.EQ.0) GO TO 2
0099                CALL LINE(XE,DE,12,1,-1,4)
0100              2 CALL PLOT(12.0,0.0,-3)
0101                CALL PLOT(0.0,0.0,999)
0102                STOP
0103                END
```

Fig. C.3 Calcomp Plotting Routine (p. 2)

```
FORTRAN IV G LEVEL 21          TRUNC          DATE = 82042          11/37/36

0001            SUBROUTINE TRUNC(X,D,J)
0002            COMMON K
0003            IF(K.EQ.0) WRITE(6,1000)
0004            K=K+1
0005       1000 FORMAT(' DATA POINTS TRUNCATED IN PLOT')
0006            FH=500.0
0007            IF(J.EQ.3) GO TO 10
0008            IF(J.EQ.2) GO TO 20
0009         30 WRITE(6,1001) X,D,X,FH
0010       1001 FORMAT(' DUCT SCATTER POINT  ',F8.2,',',F8.2,'  TRUNCATED TO PLOT
           1 ',F8.2,',',F8.2)
0011            D=FH
0012            RETURN
0013         20 WRITE(6,1003) X,D,X,FH
0014       1003 FORMAT(' LIP SCATTER POINT  ',F8.2,',',F8.2,'  TRUNCATED TO PLOT'
           1,F8.2,',',F8.2)
0015            D=FH
0016            RETURN
0017         10 WRITE(6,1004)X,D,X,FH
0018       1004 FORMAT(' TOTAL DUCT POINT  ',F8.2,',',F8.2,'  TRUNCATED TO PLOT  '
           1,F8.2,',',F8.2)
0019            D=FH
0020            RETURN
0021            END
```

Fig. C.3 Calcomp Plotting Routine (p. 3)

MEASUREMENTS AND ANALYSIS OF GAMMA-RAY STREAMING THROUGH CONCRETE LINED DUCTS

by

DAVID LEE STUCKER

B.S., Nuclear Engineering
Kansas State University
Manhattan, Kansas
1977

AN ABSTRACT OF A MASTER'S THESIS

submitted in partial fulfillment of the

requirements of the degree

MASTER OF SCIENCE

Department of Nuclear Engineering
KANSAS STATE UNIVERSITY
Manhattan, Kansas

1980

ABSTRACT

The design and operation of a unique facility for measuring the streaming of gamma radiation through ducts is described. Of particular note is a special automatic traversing mechanism constructed for remotely measuring the radiation field behind the duct wall. With this facility a major benchmark experiment was performed to obtain detailed information about the spatial distribution of the exposure rate resulting from ^{60}Co gamma photons that penetrate straight, concrete-lined ducts. A large variety of duct length-to-diameter ratios and incident photon directions on the duct mouth were considered. The complete set of experimental data is presented. While the data obtained in this study could be used directly for the analysis of ducts, they are intended to serve primarily as benchmarks against which simplified models for duct penetration of radiation can be tested.

Additionally, semi-empirical models for the scattering phenomena within the duct are presented. These models are one pass, analytically simple calculations of a size and complexity such that it is feasible to execute them on a small programmable calculator. The models consist of semi-empirical point scattering kernal modelling for a point detector designed to provide accurate prediction within a factor of two. Alterations for non-point detector behavior are also presented.